NONEQUILIBRIUM STEADY-STATE SOLUTIONS OF DRIVEN-DISSIPATIVE SPIN SYSTEMS

By

Mostafa Ali

A DISSERTATION

Submitted to
Michigan State University
in partial fulfillment of the requirements
for the degree of

Physics—Doctor of Philosophy

2026

ABSTRACT

The study of driven open quantum systems offers a rich frontier for discovering phases of matter that exist strictly far from thermal equilibrium. In these systems, coherent many-body dynamics compete with environmental noise, a process that typically suppresses quantum correlations and drives the system toward a classical mixed state. This thesis investigates the nonequilibrium steady states and dynamics of driven-dissipative quantum spin models, demonstrating that steady states can exhibit signatures of ground-state criticality and host genuine quantum phase transitions.

In this thesis, we establish a powerful analytical framework for short-range driven-dissipative quantum Ising chains. Although exact solutions are available for the Ising model, the introduction of dissipation renders standard analytical methods largely inadequate. Here, we demonstrate that the dynamics in the weak-dissipation limit can be described in terms of a time-evolving generalized Gibbs ensemble composed of non-interacting fermions. We subsequently break this free-fermion integrability by introducing next-nearest-neighbor interactions. We argue that the dissipative dynamics subject to the non-integrable Hamiltonian effectively thermalize the system to a standard Gibbs ensemble at a finite effective temperature. Remarkably, we find that the nonequilibrium steady states in both the integrable and chaotic regimes show distinct signatures of the underlying ground-state quantum phase transitions.

Next, we extend our analysis to long-range quantum Ising models subject to spatially correlated dissipation, which generically arise in modern quantum simulators. To capture the complex many-body dynamics, we develop a systematic Keldysh functional integral formalism that transcends standard mean-field approximations. In stark contrast to their short-range counterparts, the steady states of these long-range models could host phase transitions. Specifically, while the mean-field merely signals bistability regions, our framework uncovers a genuine first-order driven-dissipative phase transition. By mapping the exact phase boundaries of the nonequilibrium steady state, we identify a tricritical point where the transition is characterized by an anomalous critical scaling.

Finally, we analyze the dynamics of the driven-dissipative spin-boson model. While exact matrix product state simulations reveal a localization transition in the spin-$1/2$ case, we investigate an

alternative model with a macroscopic large-spin that represents a mean-field analog. We identify a quantum-to-classical crossover at sufficiently large spin, highlighting the role of strong quantum fluctuations in stabilizing the localization transition in the presence of Markovian dissipation.

Together, these results advance our fundamental understanding of dissipation-induced critical phenomena in many-body quantum systems. The analytical and numerical frameworks developed herein provide a robust theoretical blueprint for identifying and exploring exotic nonequilibrium phases in modern noisy intermediate-scale quantum (NISQ) simulators.

ACKNOWLEDGMENTS

I would like to express my deepest gratitude to my advisor, Mohammad Maghrebi. Thank you for your unwavering guidance, patience, and support. Your mentorship has been instrumental not only in shaping this thesis but in shaping me as a physicist. I am also incredibly grateful to my guidance committee: Prof. Jonas Becker, Prof. Dean Lee, Prof. Carlo Piermarocchi, and Prof. Scott Pratt. Thank you for your time, your feedback, and the diverse perspectives you brought to my research.

I also want to acknowledge the undergraduate and early graduate professors who first fostered my curiosity in physics. Thank you for challenging me to ask the right questions and giving me the foundation to tackle them.

To the friends who made Lansing feel like home. To Roy, Jeremiah, Emily, Artemis, Tawfik, James, Julia, Mo, Stefanie, Mahmoud, and Austin, alongside the rest of my colleagues: your camaraderie and some much-needed coffee breaks kept me grounded. Thank you for putting up with my more eccentric moments, for the heavy lifting when it mattered most, for confiding in me, and for simply being there through it all. Even as I pack up for the next chapter, I am profoundly grateful our paths crossed here. Earning this degree is a milestone, but walking away with your friendships is the true reward.

I owe everything to my family. To my brother: thank you for always pushing me to pursue my passion for physics. To my mom: thank you for your endless sacrifices and unconditional love. Even with an ocean between us for so much of this journey, you were with me every step of the way. Your belief in me made this possible, and this milestone is as much yours as it is mine.

Finally, to my fiancée, Maggie. Thank you for your boundless patience, and your constant encouragement. You have been my anchor through the most demanding stretches of this Ph.D. (And a special mention to Braveheart, for his constant company and his occasional attempts to walk across my keyboard.)

Thank you all.

TABLE OF CONTENTS

LIST OF TABLES

LIST OF FIGURES

LIST OF ABBREVIATIONS

BKT Berezinskii-Kosterlitz-Thouless

DDPT driven-dissipative phase transition

DMRG density matrix renormalization group

ED exact diagonalization

FDT fluctuation-dissipation theorem

GE Gibbs ensemble

GGE generalized Gibbs ensemble

GKSL Gorini–Kossakowski–Sudarshan–Lindblad

HS Hubbard-Stratonovich

HP Holstein-Primakoff

JW Jordan-Wigner

MCWF Monte Carlo wave function

NESS nonequilibrium steady state

NISQ noisy intermediate-scale quantum

QCF quantum critical fan

QCP quantum critical point

QPT quantum phase transition

RWA rotating-wave approximation

TEBD time-evolving block decimation

TFIM transverse-field Ising model

CHAPTER 1

INTRODUCTION: NON-EQUILIBRIUM MANY-BODY SYSTEMS

Modern physics increasingly confronts phenomena where the idealized constraints of thermal equilibrium are inadequate. While equilibrium statistical mechanics offers a rigorous description for systems satisfying detailed balance—the condition where net probability currents vanish—many processes in condensed matter, high-energy physics, quantum information science, and biology are characterized by their inherent irreversibility. This irreversibility usually manifests as the transient relaxation towards equilibrium, where entropy production eventually ceases and detailed balance is restored. However, in driven-dissipative systems, the continuous exchange of energy, information, and entropy with an external environment explicitly breaks detailed balance. This persistent driving stabilizes a nonequilibrium steady state (NESS), where entropy is constantly produced and pumped into the environment [1, 2]. The fields of nonequilibrium statistical mechanics and open quantum systems provide the necessary framework to study driven-dissipative phenomena by capturing the interplay of coherent drive and dissipation. This chapter provides a brief review of the theoretical landscapes of the field, tracing their development from 19th-century kinetic foundations to the modern formalism of quantum master equations.

1.1 Foundations of Statistical Physics

The genesis of nonequilibrium theory and the kinetic foundations—The formal study of nonequilibrium processes finds its origins in the efforts to reconcile the time-reversible laws of microscopic mechanics with the macroscopic irreversibility of thermodynamics. The founding of statistical mechanics is generally attributed to Boltzmann, Maxwell, and Gibbs, who sought to explain macroscopic properties such as temperature and pressure in terms of fluctuating microscopic parameters. Boltzmann's seminal 1872 paper [3] established the modern subject by extending Maxwell's kinetic theory [4] to include intermolecular interactions, typically modeled as hard-sphere collisions or short-range repulsive forces, leading to the formulation of the Boltzmann transport equation.

The transition from the exact, reversible N-body description to a tractable nonequilibrium the-

ory is realized through the Bogoliubov–Born–Green–Kirkwood–Yvon (BBGKY) hierarchy [5–8]. By integrating the Liouville equation—which describes the incompressible flow of a probability density in a $6N$-dimensional phase space—over the degrees of freedom of $N - s$ particles, one obtains a chain of coupled integro-differential equations where the evolution of the s-particle distribution function f_s depends on the $(s+1)$-particle distribution f_{s+1}. The hierarchy is fundamentally exact but not closed to low orders, as solving for the one-particle distribution f_1 requires knowledge of the two-particle correlations f_2. The derivation of the Boltzmann transport equation—the first true description of nonequilibrium processes—requires a truncation of this hierarchy. In the dilute gas limit, Boltzmann introduced the ''molecular chaos'' hypothesis, which assumes that the velocities of two particles are uncorrelated before they collide [9]. This approximation allows the two-particle distribution to be factorized as $f_2(\mathbf{x}_1, \mathbf{x}_2, t) \approx f_1(\mathbf{x}_1, t) f_1(\mathbf{x}_2, t)$, closing the hierarchy at the first level and yielding a non-linear integro-differential equation for f_1. This step introduces the ''arrow of time'' into the dynamics, as demonstrated by Boltzmann's H-theorem, which states that a quantity H (related to negative entropy) must monotonically decrease until the distribution relaxes to the Maxwellian equilibrium state. This reconciliation of reversible mechanics with irreversible relaxation remains a central theme, often referred to as the Loschmidt paradox [10, 11].

Brownian motion and the stochastic revolution—The early twentieth century witnessed a shift from the purely kinetic description of gases to the stochastic modeling of particles in fluids. Albert Einstein (1905) and Marian Smoluchowski (1906) derived the relationship between the diffusion coefficient and the mobility of a free Brownian particle [12–14], linking the microscopic erratic motion observed under a microscope to macroscopic transport properties. This Einstein-Smoluchowski relation is expressed as

$$D = \mu k_B T, \tag{1.1}$$

where D is the diffusion coefficient, μ is the mobility, k_B is the Boltzmann constant, and T is the absolute temperature. This was a foundational milestone because it demonstrated that the same molecular impacts responsible for the dissipative drag on a particle also provide the fluctuating

force that drives its random walk. Paul Langevin formalized this duality in 1908 by introducing the Langevin equation [15], which decomposes the force on a particle into a systematic frictional component and a stochastic random force

$$m\frac{\mathrm{d}v}{\mathrm{d}t} = -\gamma v + \xi(t). \tag{1.2}$$

In this framework, γ represents the friction coefficient and $\xi(t)$ is a Gaussian white noise term satisfying $\langle \xi(t) \rangle = 0$. The strength of the noise fluctuations is directly proportional to the dissipation via the relation $\langle \xi(t)\xi(t') \rangle = 2\gamma k_B T \delta(t - t')$. Rather than treating friction and noise as independent phenomena, this approach mathematically binds the macroscopic drag to the variance of the stochastic force, providing the first concrete realization of the fluctuation-dissipation theorem (FDT).

1.2 The Near-Equilibrium Regime

Reciprocity and symmetry in near-equilibrium conditions—A central pillar of nonequilibrium thermodynamics is Lars Onsager's reciprocity relations [16–18], published in 1931. Onsager established that the cross-coefficients coupling different fluxes and forces in a linear response regime must be symmetric. For example, in a thermoelectric system, the fluxes of heat ($\mathbf{J}_Q$) and electric charge ($\mathbf{J}_E$) are linearly coupled to temperature gradients ($\boldsymbol{\nabla} T$) and electric fields ($\mathbf{E}$) via a matrix of phenomenological coefficients L_{ij}. While the diagonal terms describe standard direct transport—like Ohm's law—the off-diagonal terms capture the ability of a thermodynamic force to drive a flux of an entirely different nature such as the Seebeck and Peltier effects. Onsager's relations dictate that these cross-coefficients are strictly symmetric ($L_{QE} = L_{EQ}$), meaning the electrical current driven by a thermal gradient is governed by the same coefficient as the heat flux driven by an electric field. This macroscopic symmetry emerges directly from the time-reversal invariance of the underlying microscopic equations of motion. Crucially, Onsager's regression hypothesis links these transport laws to thermal fluctuations by postulating that the macroscopic relaxation of a system after a small perturbation obeys the same dynamical equations as the regression of spontaneous microscopic fluctuations.

The fluctuation-dissipation theorem and the linear response theory—

The fluctuation-dissipation theorem stands as one of the most powerful results in statistical physics, bridging the gap between systems in thermal equilibrium and those subjected to small external perturbations. Proven by Herbert Callen and Theodore Welton in 1951 [19] and expanded by Ryogo Kubo [20, 21], the theorem states that the linear response of a system to an external force is determined by the correlation functions of its variables in equilibrium. The physical insight of the FDT is that the mechanism by which a system dissipates energy (e.g., through friction or resistance) is the same mechanism that governs the decay of spontaneous thermal fluctuations. In the frequency domain, the theorem relates the imaginary part of the susceptibility $\chi''(\omega)$ to the power spectrum of fluctuations $S(\omega)$

$$S(\omega) = \frac{2k_B T}{\omega}\chi''(\omega). \tag{1.3}$$

System / Domain	**Dissipative Process**	**Fluctuating Process (Noise)**
Mechanical	Viscous Drag / Friction	Brownian Motion
Electrical Conductors	Electrical Resistance	Johnson-Nyquist Noise
Electromagnetic	Optical Absorption	Thermal Radiation
Magnetic Materials	Magnetic Damping	Spin Fluctuations

Table 1.1 Physical applications of the fluctuation-dissipation theorem (FDT) across diverse physical systems, illustrating the universal link between macroscopic dissipation and microscopic fluctuations.

In the quantum regime, the theorem must account for zero-point fluctuations. Callen and Welton extended the Nyquist–Johnson relation [22, 23] to provide a generalized quantum FDT. For a system observable $\hat{A}$ in thermal equilibrium, the symmetrized power spectral density $S(\omega)$ is related to the dissipative part of the retarded susceptibility $\chi''(\omega)$ by

$$S(\omega) = \hbar \coth\left(\frac{\hbar\omega}{2k_B T}\right)\chi''(\omega), \tag{1.4}$$

where $S(\omega) = \frac{1}{2}\int dt e^{i\omega t}\langle\hat{A}(t)\hat{A}(0) + \hat{A}(0)\hat{A}(t)\rangle$, and the dissipative response is governed by the commutator, $\chi''(\omega) = \frac{1}{2\hbar}\int dt e^{i\omega t}\langle\hat{A}(t)\hat{A}(0) - \hat{A}(0)\hat{A}(t)\rangle$. This formulation encapsulates both thermal and zero-point (vacuum) noise through the hyperbolic cotangent factor. In the classical

limit ($k_B T \gg \hbar\omega$), $\coth(x) \approx 1/x$, and the expression reverts to the classical FDT in Eq. (1.3). Conversely, at absolute zero temperature ($T = 0$), the fluctuations persist as $S(\omega) = \hbar\chi''(\omega)$, representing purely quantum noise. This relationship is perhaps most famously recognized in the context of electromagnetic radiation, where the energy spectrum $u(\omega, T)$ of a single mode explicitly captures both the Planck thermal distribution and the residual quantum fluctuations

$$u(\omega, T) = \frac{\hbar\omega}{2} \coth\left(\frac{\hbar\omega}{2k_B T}\right) = \frac{\hbar\omega}{\exp\left(\frac{\hbar\omega}{k_B T}\right) - 1} + \frac{\hbar\omega}{2}. \tag{1.5}$$

The inclusion of the $\frac{\hbar\omega}{2}$ term leads to the ''vacuum catastrophe'', where the total energy associated with spectral density diverges at high frequencies—a problem addressed by imposing ultraviolet cutoffs on realistic physical baths.

Far-from-equilibrium dynamics and fluctuation theorems—While fluctuation-dissipation relations successfully bridge dissipation and microscopic noise in the linear response regime, a major breakthrough achieved in the 1990s was the discovery of exact equalities that hold even when a system is driven far from equilibrium [24, 25]. The Jarzynski equality and the Crooks fluctuation theorem extended the second law of thermodynamics into the regime of large fluctuations. The Jarzynski equality [26] relates the work W performed during a nonequilibrium process to the equilibrium free energy difference ΔF

$$\langle \exp(-\beta W) \rangle = \exp(-\beta \Delta F). \tag{1.6}$$

The profound significance of this equality lies in its ability to extract exact equilibrium thermodynamic information from a system driven arbitrarily far and arbitrarily fast out of equilibrium. This equality implies that while the average work is greater than or equal to the free energy change ($\langle W \rangle \geq \Delta F$), there exist rare trajectories where the work performed is less than the free energy change—effectively violating the second law on short timescales. The Crooks theorem [27] further quantifies this by relating the probability distribution of work in a forward process $P_F(W)$ to the distribution in the time-reversed process $P_R(-W)$

$$\frac{P_F(W)}{P_R(-W)} = \exp(\beta(W - \Delta F)). \tag{1.7}$$

These theorems have been verified experimentally using single-molecule stretching and optical tweezers, providing a deep link between irreversibility and information theory [28, 29].

1.3 The Open Quantum Systems Framework

While the classical description of nonequilibrium processes (e.g., Boltzmann's equation) relies on probability distributions in phase space, quantum systems require a description based on the density matrix $\hat{\rho}$. An open quantum system is defined as a system of interest (S) coupled to an external environment or bath (B). The total system $S + B$ is treated as a closed system evolving unitarily under the total Hamiltonian $\hat{H} = \hat{H}_S + \hat{H}_B + \hat{H}_I$, where $\hat{H}_I$ encodes the interaction. The objective of the theory of open quantum systems is to derive a reduced description for the system S alone by tracing out the bath degrees of freedom

$$\hat{\rho}_S(t) = \mathrm{Tr}_B\, \hat{\rho}. \tag{1.8}$$

This process leads to the emergence of decoherence (the loss of phase information) and dissipation (the loss of energy), which are critical hurdles in the development of quantum computers and the maintenance of quantum entanglement.

Modeling quantum dissipation—To understand the specific mechanisms of decoherence [30], two paradigmatic models serve as the workhorses of the field.

- *The Caldeira-Leggett model*—Introduced in Refs. [31, 32], the Caldeira-Leggett model describes a single quantum particle (the system) linearly coupled to a bath of independent quantum harmonic oscillators. It was introduced to justify the emergence of classical-like Brownian motion from a purely Hamiltonian starting point. By integrating out the infinite oscillators of the bath, one recovers effective dynamics that include both friction and fluctuating forces. This model is essential for studying the transition from quantum to classical behavior, proving that environmental coupling ''smears out'' quantum interference, a process known as decoherence. A key feature of this model is its ability to handle ''Ohmic''

dissipation, where the bath's influence mimics the standard viscous drag found in fluids and electrical circuits.

- *The spin-boson model*—The spin-boson model [33] applies similar principles to a discrete two-level system (a spin) interacting with a bosonic environment. Introduced to study impurity problems, this model is the primary tool for understanding the decoherence of qubits in quantum computers and the dynamics of state decay in atoms. It is particularly useful for modeling processes where a system can hop between two distinct configurations, such as chemical reactions or exciton transport in photosynthesis [34, 35]. Depending on how strongly the spin is coupled to the environment, the model predicts a dramatic transition: at low coupling, the spin can oscillate between its two states, but beyond a critical threshold, the environment ''traps'' the spin in a given state, illustrating a quantum phase transition driven by dissipation.

Both models are fundamentally different from ''axiomatic'' Markovian descriptions like the Lindblad equation. While the Lindblad formalism assumes the environment is memoryless—instantly returning to equilibrium after every interaction—the Caldeira-Leggett and spin-boson models are more physically complete. Because they start from a microscopic ''system-plus-bath'' Hamiltonian, they naturally capture memory effects (non-Markovianity) where the future state of the system depends on its past history.

The Born-Markov approximation and the Lindblad master equation—The derivation of a time-local master equation for the reduced density matrix $\hat{\rho}_S(t)$ typically begins with the exact unitary evolution of the total system and reservoir. To obtain a tractable description, three standard approximations are applied

- **Born approximation:** Assumes weak system–environment coupling such that the total state remains approximately factorized ($\hat{\rho}_{SB} \approx \hat{\rho}_S \otimes \hat{\rho}_B$). This implies that the system's influence on the bath is negligible.

- **Markov approximation:** Assumes that bath correlations decay rapidly compared to the system's relaxation timescale. This makes the dynamics memoryless, as the rate of change of the system depends only on its current state.

- **Secular (rotating wave) approximation:** Neglects rapidly oscillating non-resonant terms that average to zero over the relaxation time, ensuring the equation takes a mathematically consistent form.

These steps culminate in the Gorini–Kossakowski–Sudarshan–Lindblad (GKSL) equation [36–38], the most general time-local master equation that preserves trace and complete positivity of the density matrix

$$\frac{\mathrm{d}\hat{\rho}_S}{\mathrm{d}t} = -i\left[\hat{H}_S, \hat{\rho}_S\right] + \sum_k \gamma_k \left(\hat{L}_k \hat{\rho}_S \hat{L}_k^\dagger - \frac{1}{2}\left\{\hat{L}_k^\dagger \hat{L}_k, \hat{\rho}_S\right\}\right). \tag{1.9}$$

The operators $\hat{L}_k$ are the Lindblad (jump) operators, which describe incoherent processes such as spontaneous emission, and γ_k are the associated transition rates. In the absence of an external drive, these jump operators typically induce transitions between the energy eigenstates of the system. In this un-driven regime, the transition rates γ_k inherently satisfy detailed balance, guaranteeing that the dissipative dynamics will ultimately relax the system to a standard thermal equilibrium state rather than a nonequilibrium steady state.

However, this time-local formulation relies strictly on the rapid decay of bath correlations. The GKSL equation is only expected to be valid after an initial non-Markovian transient period, during which the system and bath establish mutual correlations and the evolution remains sensitive to its initial preparation [39–42]. While many systems quickly relax into this memoryless regime, environments with structured spectral densities—such as those encountered in the spin-boson model—can sustain persistent memory effects that transcend the Lindbladian framework entirely.

1.4 Quantum Driven-Dissipative Systems

The integration of driving and dissipation into quantum theory traces its roots to the early development of quantum electrodynamics and the study of light-matter interaction. A pivotal moment

was Willis Lamb's 1947 measurement of the Lamb shift, which demonstrated that vacuum fluctuations shift atomic energy levels, forcing a revision of the Dirac equation. This realization that a system is never truly isolated from the electromagnetic vacuum was later formalized in the theory of the optical maser and laser by Lamb [43] and Haken [44, 45]. The laser serves as the canonical blueprint for driven-dissipative systems: it relies on a persistent external pump (the drive) to overcome inevitable cavity photon leakage (the dissipation). Haken's introduction of ''Synergetics'' formalized the laser threshold as a true nonequilibrium phase transition, demonstrating how a macroscopic order parameter (coherent light) can emerge from a driven, noisy ensemble.

While Haken established the phenomenology of these steady states, the rigorous mathematical treatment of the external ''drive'' itself required new theoretical tools. Because quantum driving is typically achieved via periodic electromagnetic fields, J. H. Shirley established the basis for analyzing these systems using Floquet theory [46, 47]. By mapping time-dependent periodic dynamics onto an effective time-independent framework, Floquet theory provided the ability to calculate ''quasi-energies'' and characterize the steady-state populations of many-body systems subjected to strong, continuous driving.

Modern interest in these phenomena shifted towards the active control of dissipation, leading to the paradigm of quantum reservoir engineering [48, 49]. This approach recontextualizes environmental coupling: rather than a source of decoherence to be suppressed, the environment is treated as a resource to be engineered for the preparation of specific quantum states, such as entangled Bell or Greenberger–Horne–Zeilinger (GHZ) states [50, 51]. This direction was expanded into the engineering of nonequilibrium quantum phases [52, 53], where it was demonstrated that local dissipation could sustain long-range order in cold atomic gases, realizing phase transitions that are fundamentally driven by a persistent balance between coherent gain and dissipative loss. Crucially, in these setups, the detailed balance between the coherent drive—typically captured by an effective Hamiltonian in a rotating frame—and the engineered dissipation is explicitly broken, stabilizing a true nonequilibrium steady state.

Since these foundational works, the rapid advancement of programmable quantum simulators

has revolutionized the study of driven-dissipative phenomena [54]. Platforms ranging from atomic, molecular, and optical (AMO) setups—such as trapped ion simulators [50, 55] and Rydberg atom arrays [56, 57]—to solid-state superconducting circuit architectures [58, 59] offer unprecedented, site-resolved control over both coherent Hamiltonian dynamics and engineered local dissipation. These highly tunable platforms serve as premier experimental testbeds for simulating complex spin models and observing nonequilibrium quantum phases [60–64]. Consequently, theoretical predictions regarding the steady-state properties of driven-dissipative spin chains can now be directly benchmarked against state-of-the-art experiments, bridging the gap between exact many-body theory and observable quantum phenomena [65–72].

Finally, the formulation of open quantum systems has taken on renewed urgency in the era of the noisy intermediate-scale quantum (NISQ) devices [73]. Current quantum hardware consists of arrays of qubits that lack the operational fidelity required for full-scale quantum error correction [74–76]. Consequently, these devices operate as inherently driven-dissipative many-body systems [77]. Understanding the precise microscopic mechanisms of decoherence and dissipation is no longer merely a theoretical exercise but the central engineering bottleneck of modern quantum technology [72]. As NISQ devices scale, the complexity of their environmental coupling necessitates advanced theoretical techniques to model how local noise may lead into macroscopic decoherence, and how dissipation might be mitigated or even exploited [49].

Thesis Overview— The theoretical foundations discussed in this chapter provide an overview of the development of nonequilibrium quantum physics, and establish the conceptual toolkit required to analyze driven-dissipative quantum systems. This thesis is structured as follows: Chapter 2 establishes the theoretical foundations of criticality across classical, quantum, and dissipative regimes. We provide a rigorous overview of the mechanisms driving phase transitions—ranging from thermal and quantum fluctuations to the competition between coherent dynamics and environmental dissipation in open systems. A central focus is placed on identifying robust signatures of quantum phase transitions both in and out of equilibrium. This chapter serves as a conceptual guide for the

subsequent chapters, providing the fundamental principles required to distinguish between trivial thermalization and the emergence of fundamentally non-thermal, quantum-correlated steady states in driven-dissipative many-body systems.

In Chapter 3, we establish the theoretical and mathematical foundation for the study of open quantum many-body systems. We begin by defining the density matrix formalism and the GKLS master equation, providing a rigorous framework for Markovian dissipative dynamics. To address the complexity of many-body Liouville space, we introduce the method of *vectorization*, which maps matrix-valued operators onto a vector in a doubled Hilbert space. Building on this, in Chapter 4, we discuss tractable methods applicable to quadratic (Gaussian) systems. Using the spin-wave approximation of the transverse field Ising model (TFIM) as a example, we provide a comparative review of three distinct formalisms: the stochastic Heisenberg-Langevin approach, the algebraic third quantization method, and the field-theoretic Keldysh path integral. This comparative analysis demonstrates the mathematical equivalence of these methods, identifying the ‘‘hard-core’’ constraints that lead to the breakdown of Gaussian approximations near the quantum critical point.

In Chapter 5, we establish the hierarchical numerical toolkit required to simulate the nonequilibrium dynamics of open quantum many-body systems. We begin with exact diagonalization (ED) which provides full spectral information for small systems, then transition to the method of quantum trajectories, i.e., Monte Carlo wave function (MCWF). To circumvent the exponential scaling of the Hilbert space dimension in many-body systems, we discuss matrix product states (MPS) as a polynomial-scaling representation of 1D quantum states. We detail the optimization of steady states via the density matrix renormalization group (DMRG) and the tracking of dissipative dynamics through time-evolving block decimation (TEBD) algorithms. In Chapter 6, we present a case study in which we utilize ED and MCWF methods to model decoherence in experimental trapped-ion simulators.

In Chapter 7, we develop an asymptotically exact analytical framework to describe the steady state of the driven-dissipative transverse-field quantum Ising chain. Exploiting the free-fermion integrability of the underlying Hamiltonian, we utilize a generalized Gibbs ensemble (GGE) ansatz in

the weak-dissipation limit, where we derive exact integro-differential kinetic equations that govern the excitations' momentum distributions. This analytical treatment reveals that the nonequilibrium steady state retains distinct signatures of the underlying ground-state phase transition, most notably the steady state shows a robust enhancement of the spatial correlation length near the quantum critical point. In order to address the *universality* of these nonequilibrium phenomena, we extend this investigation to systems with non-integrable Hamiltonians in Chapter 8. By introducing next-nearest-neighbor (NNN) interactions, we explicitly break the free-fermion integrability of the Hamiltonian, transitioning the internal closed-system dynamics from GGE relaxation to chaotic thermalization governed by the eigenstate thermalization hypothesis (ETH). Employing advanced numerical techniques—including matrix product states (MPS) simulations of the Lindblad master equation, finite-size scaling, and Binder cumulant analysis—we explore the complex competition between chaotic coherent dynamics and dissipation. We demonstrate that the steady-state signatures of criticality found in the integrable model robustly survive the breaking of integrability. We show that the steady state of a chaotic Ising Hamiltonian under weak local Markovian dissipation that preserves the Ising symmetry is identical to that obtained by quench dynamics in the absence of dissipation. This intriguing connection then allows us to draw on recent findings about quantum phase transition signatures in quench dynamics.

In Chapter 9, we investigate the nonequilibrium steady states of a long-range quantum Ising model subjected to collective dissipation. We develop a rigorous Keldysh functional integral formalism to isolate the critical fluctuations, deriving an effective potential that captures the steady-state criticality and reveals the onset of a nonequilibrium bistability regime. This field-theoretic approach enables us to map the first-order phase boundaries and identify a novel nonequilibrium tricritical point characterized by an anomalous critical scaling exponent of $\beta = 1/4$.

In Chapter 10, we investigate the critical dynamics of the driven-dissipative spin-boson model, demonstrating that frequency-dependent Markovian dissipation can remarkably stabilize, rather than destroy, a robust quantum phase transition. Through variational methods and time-evolving block decimation (TEBD) simulations, we show that the single spin-$1/2$ impurity model undergoes

a localization transition characterized by a nontrivial purification of the nonequilibrium steady state. To highlight the strongly interacting, highly quantum nature of this phenomenon, we systematically contrast it with a macroscopic large-spin mean-field analog. Utilizing Keldysh field theory and third quantization on a mapped one-dimensional lattice, we rigorously prove that, unlike the spin-$1/2$ case, the macroscopic limit is invariably driven into an effectively classical, highly mixed state at criticality, completely devoid of quantum entanglement.

CHAPTER 2

OVERVIEW OF THE ISING MODEL IN AND OUT OF EQUILIBRIUM

The study of phases and phase transitions forms the bedrock of statistical mechanics and condensed matter physics. At the most fundamental level, a phase transition is identified by the non-analytic behavior of a system's thermodynamic potential in the thermodynamic limit, where the number of constituents $N \to \infty$ [78, 79]. Traditionally, these transitions have been classified through the Landau paradigm, which posits that transitions are driven by the competition between different energy scales and symmetries [80, 81]. In the classical regime, transitions are primarily driven by thermal fluctuations, where entropy competes with internal energy to determine the most favorable state of the system. However, as the temperature is reduced to absolute zero, thermal fluctuations vanish, and the physics is instead dominated by quantum fluctuations rooted in the Heisenberg uncertainty principle [82]. This transition from classical to quantum descriptions of criticality marks a significant conceptual shift, extending the notion of phases from macroscopic thermodynamic ensembles to the properties of many-body wavefunctions [83]. In recent decades, the paradigm has expanded further to include driven-dissipative phase transitions (DDPTs) in open quantum systems. These systems are no longer isolated; rather, they are subjected to coherent external driving fields and environmental loss mechanisms. The competition in these systems is not between energy and entropy, but between coherent unitary evolution and incoherent dissipative processes. This chapter provides a theoretical overview of these three classes of transitions. Utilizing the Ising model as a prototypical framework, we elucidate their underlying mathematical structures, scaling properties, and universal features. We discuss the transition from Landau-Ginzburg phenomenological theories to the exact results of the renormalization group, and finally to the spectral theory of the Liouvillian super-operator that governs the physics of open quantum systems.

2.1 Classical Phase Transitions

Classical phase transitions occur at finite temperatures and are governed by the interplay of temperature, pressure, and chemical potential [84, 85]. The cornerstone of our understanding of these transitions is the Landau theory of second-order phase transitions, which assumes that the

free energy of a system can be expressed as an analytic function of an order parameter near the critical point [86].

2.1.1 Landau-Ginzburg Theory and Mean-Field Approximations

The order parameter, denoted as M, is a macroscopic variable that vanishes in the symmetric, disordered phase and becomes non-zero in the ordered phase. For a system with $\mathbb{Z}_2$ symmetry ($M \to -M$) in the absence of an external field, such as the unperturbed Ising model, the free energy density $f(M,T)$ can be expanded in a Taylor series containing only even powers of M. Coupling the system to an external conjugate field h explicitly breaks this symmetry, introducing a linear term

$$f(M,T) = f_0(T) + a(T)M^2 + b(T)M^4 + \cdots - hM \tag{2.1}$$

The coefficient $a(T)$ is the primary driver of the transition, assumed to take the form $a(T) = a_0(T - T_c)$ near the critical temperature T_c.

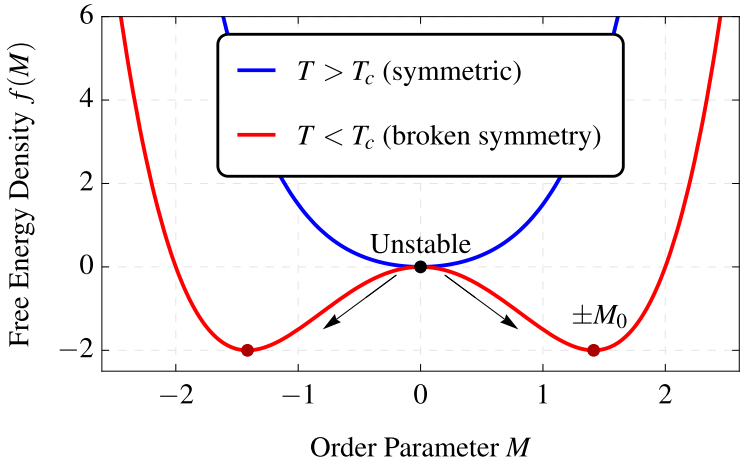

Figure 2.1 Landau free energy density $f(M) = aM^2 + bM^4$ in the absence of an external field for the symmetric ($a > 0$, blue) and broken symmetry ($a < 0$, red) phases. In the ordered phase ($T < T_c$), the local maximum at $M = 0$ represents an unstable equilibrium, while the spontaneous magnetization $M = \pm M_0 = \pm\sqrt{-a/2b}$ corresponds to the new stable equilibrium states. The emergence of these non-zero minima characterizes the onset of long-range order in the thermodynamic limit.

For the system to remain stable, the coefficient $b(T)$ must be positive. By minimizing the free

energy with respect to M, we obtain the equilibrium equation of state

$$\frac{\partial f}{\partial M} = 2a_0(T - T_c)M + 4bM^3 - h = 0 \tag{2.2}$$

In the absence of an external field ($h = 0$), for $T > T_c$, the only real solution is $M = 0$. For $T < T_c$, two non-trivial solutions emerge, $M = \pm\sqrt{-a/2b} \propto (T_c - T)^{1/2}$, yielding the mean-field critical exponent $\beta = 1/2$ [87]. This mean-field approach essentially averages out the microscopic fluctuations, assuming that every constituent of the system experiences an effective ''molecular field'' produced by the average state of its neighbors [88]. As shown in Fig. 2.1, the transition from a single-well to a double-well potential provides a geometric interpretation of the Ginzburg-Landau functional.

Beyond the molecular field limit, the spatial dependence of the order parameter is introduced in the Ginzburg-Landau functional [84] by adding a gradient term that penalizes spatial variations

$$\mathcal{F}[M(\mathbf{r})] = \int d^d\mathbf{r} \left[aM(\mathbf{r})^2 + bM(\mathbf{r})^4 + c|\nabla M(\mathbf{r})|^2 - h(\mathbf{r})M(\mathbf{r})\right] \tag{2.3}$$

From this functional, we derive the correlation length ξ, which characterizes the distance over which fluctuations of the order parameter are correlated [87, 89]. Near T_c, the correlation length diverges as $\xi \propto |T - T_c|^{-1/2}$, yielding the exponent $\nu = 1/2$. The validity of this mean-field description is governed by the Ginzburg criterion, which states that mean-field theory holds when the fluctuations in a correlation volume ξ^d are small compared to the square of the order parameter, $\langle(\delta M)^2\rangle_{\xi^d} \ll \langle M\rangle^2$. By comparing the scaling of these fluctuations to the mean-field exponents, this criterion defines an upper critical dimension, $d_u = 4$. Below this dimension, localized fluctuations diverge near T_c and overpower the mean field, leading to significant deviations from classical critical exponents [90].

2.1.2 The Renormalization Group and the Concept of Universality

The failure of mean-field theory in lower dimensions necessitated a more sophisticated approach: the renormalization group (RG). Developed by Wilson, RG provides a mathematical framework to understand how the parameters of a Hamiltonian change as we observe the system at increasingly larger length scales [92]. The process involves two fundamental steps: coarse-graining, where

Exponent	Quantity	Scaling Law	MFT Value	2D Ising
β	Order Parameter	$M \sim \lvert t\rvert^{\beta}$	1/2	1/8
γ	Susceptibility	$\chi \sim \lvert t\rvert^{-\gamma}$	1	7/4
ν	Correlation Length	$\xi \sim \lvert t\rvert^{-\nu}$	1/2	1
α	Specific Heat	$C_V \sim \lvert t\rvert^{-\alpha}$	0 (jump)	0 (log)
η	Correlation Decay	$G(r) \sim r^{-(d-2+\eta)}$	0	1/4

Table 2.1 Comparison of critical exponents between mean-field theory (MFT) and the exact solution of the 2D Classical Ising Model [91].

we integrate out the high-frequency (short-wavelength) degrees of freedom, and rescaling, where we restore the original length units of the system. This flow through the space of Hamiltonians reveals fixed points, which correspond to the thermodynamic phases of the system. Critical points are associated with unstable fixed points, where the correlation length is infinite and the system is scale-invariant [93]. The power of the RG approach lies in the discovery of universality classes: the observation that systems with vastly different microscopic interactions can exhibit identical critical behavior, provided they share the same spatial dimensionality and symmetry properties. The ϵ-expansion, where $\epsilon = 4 - d_u$, allows for the perturbative calculation of critical exponents near the upper critical dimension [90, 94]. As $\epsilon \to 0$, the exponents approach their mean-field values, while for $\epsilon > 0$, non-trivial corrections emerge. The RG flow for a coupling constant g can be expressed via the β-function

$$\beta(g) = \mu \frac{\partial g}{\partial \mu} \tag{2.4}$$

where μ is the momentum scale. A critical point occurs at g^* where $\beta(g^*) = 0$. The derivative of the β-function at this fixed point determines the critical exponents, establishing a direct link between the topological properties of the RG flow and the macroscopic observable scaling laws.

2.2 Quantum Phase Transitions

Quantum phase transitions (QPTs) are qualitatively different from their classical counterparts. They occur strictly at $T = 0$, driven by quantum fluctuations that persist even at the lowest possible energy state [82, 95]. These transitions are controlled by non-thermal parameters, such as an external magnetic field, or doping concentration.

2.2.1 The 1D Transverse-Field Ising Model (TFIM)

The 1D TFIM is paradigmatic model demonstrating a quantum phase transition. The standard Hamiltonian on a lattice of N spins is defined as

$$\hat{H}_{\text{TFIM}} = -J \sum_{i=1}^{N-1} \sigma_i^z \sigma_{i+1}^z - g \sum_{i=1}^{N} \sigma_i^x \tag{2.5}$$

where σ_i^z and σ_i^x are Pauli operators acting on site i [82, 96, 97]. The first term represents an ferromagnetic Ising interaction that favors the alignment of spins along the z-axis, while the second term is a transverse field that induces quantum tunneling between the spin-up and spin-down states. In the limit $g \ll J$, the ground state is two-fold degenerate and breaks the $\mathbb{Z}_2$ symmetry, resulting in long-range ferromagnetic order where $\langle \sigma^z \rangle \neq 0$. In the opposite limit $g \gg J$, the transverse field dominates, and the ground state is a unique product of spins aligned along the x-direction, resulting in a quantum paramagnetic phase where $\langle \sigma^z \rangle = 0$. The transition occurs at the quantum critical point $g_c = J$. This can seen by exactly solving the 1D TFIM using the Jordan-Wigner (JW) transformation [98], which maps the spin operators to spinless fermions ($\hat{c}_j$)

$$\hat{c}_j = \left(\prod_{l<j} \sigma_l^x \right) \frac{\sigma_j^z - i\sigma_j^y}{2} \tag{2.6}$$

Under the JW transformation, the Hamiltonian in Eq. (2.5) takes the form of a non-interacting fermionic model. After transforming to momentum space, the Hamiltonian reduces to a quadratic form

$$\hat{H}_{\text{TFIM}} = \sum_k \left[2(g - J\cos k)\hat{c}_k^\dagger \hat{c}_k + iJ \sin k (\hat{c}_k^\dagger \hat{c}_{-k}^\dagger + \hat{c}_k \hat{c}_{-k}) \right]. \tag{2.7}$$

The elementary excitations are Bogoliubov quasiparticles with energy

$$\epsilon_k = 2\sqrt{(J - g\cos k)^2 + g^2 \sin^2 k}. \tag{2.8}$$

At the critical point $g = J$, the energy gap ($\Delta = \epsilon_{k=0} = 2|J - g|$) closes, implying a divergent relaxation time $\tau \sim \Delta^{-1}$ and infinite-range spatial correlations.

2.2.2 Quantum-Classical Mapping and Dynamical Exponents

A central result in the field of quantum criticality is the mapping between a d-dimensional quantum system at $T = 0$ and a $(d+1)$-dimensional classical system [95, 99]. Using the Feynman path

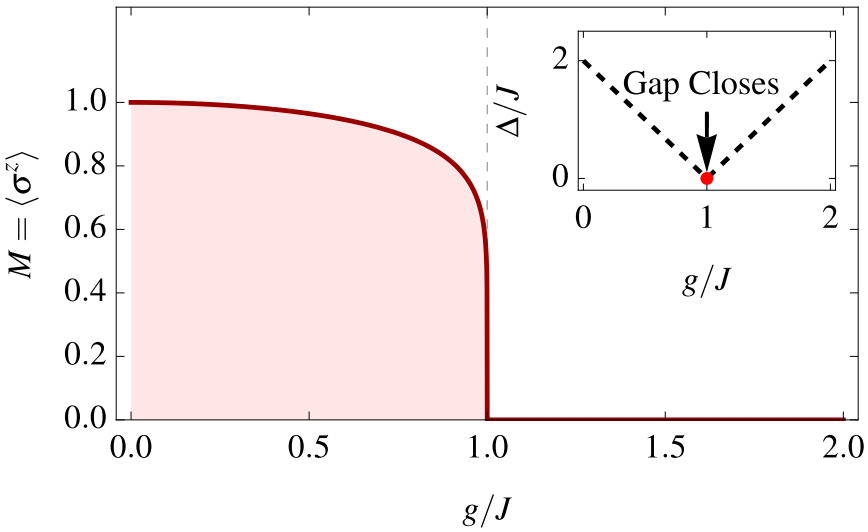

Figure 2.2 Longitudinal magnetization $M = \langle \sigma^z \rangle$ in the ground state of the 1D transverse-field Ising model (TFIM) as a function of the transverse field g/J. The system transitions from a ferromagnetic ordered phase ($g < J$) to a paramagnetic disordered phase ($g > J$) at the quantum critical point $g_c = J$. *Inset:* The excitation energy gap Δ/J vanishes linearly at the critical point, indicating the divergence of the correlation length and the onset of scale-invariant quantum criticality.

integral approach, the quantum partition function can be expressed as a functional integral over the configurations of a classical field in one higher dimension, where the additional dimension corresponds to imaginary time $\tau \in [0, \beta]$. For the 1D quantum Ising model discussed in Section 2.2.1, the mapping relates it to the 2D classical Ising model on a square lattice. The temporal dimension in the quantum system plays a role analogous to a spatial dimension in the classical system, but with an important distinction: space and time are not necessarily isotropic. This anisotropy is quantified by the dynamic critical exponent z, which relates the divergence of the correlation length ξ to the divergence of the correlation time ξ_τ

$$\xi_\tau \sim \xi^z \tag{2.9}$$

In the 1D TFIM, $z = 1$, meaning space and time enter the scaling relations in the same way, reminiscent of relativistic invariance. The energy gap vanishes as $\Delta \sim |g - g_c|^{z\nu}$, where ν is the correlation length exponent. The scaling laws of the quantum system are thus determined by the combination $z\nu$.

2.2.3 The Dicke Model and the Superradiant Phase Transition

While the TFIM illustrates criticality driven by local, short-range interactions, the Dicke model replaces this local exchange with a global, all-to-all coupling mediated by a common bosonic mode. It serves as a paradigmatic example of collective matter-light interactions, describing N two-level systems (atoms) coupled to a single quantized mode of an electromagnetic field [100, 101]. In its fundamental Hamiltonian formulation, the interaction is characterized by the following operator structure

$$\hat{H}_{\text{Dicke}} = \omega_c \hat{a}^\dagger \hat{a} + \omega_a \hat{S}_z + \frac{2\lambda}{\sqrt{N}}(\hat{a} + \hat{a}^\dagger)\hat{S}_x, \tag{2.10}$$

where $\hat{a}^\dagger$ ($\hat{a}$) are the photon creation (annihilation) operators and $\hat{S}_{x,z}$ are the collective spin operators of the N atoms. Under fast cavity dynamics ($\omega_c \gg \omega_a,\ \lambda$), the Dicke model reduces exactly to the Ising model. In this regime, the fast cavity field can be adiabatically eliminated, effectively integrating out the photonic degrees of freedom and mapping the Dicke Hamiltonian directly onto an infinite-range quantum Ising model [102].

In the thermodynamic limit ($N \to \infty$), the ground state of this model undergoes a second-order quantum phase transition at a critical coupling strength $\lambda_c = \sqrt{\omega_a \omega_c}/2$ [103]. Below the critical point ($\lambda < \lambda_c$), the system resides in a ''normal'' phase where the cavity is in a vacuum state and atoms are in their ground states. Above threshold ($\lambda > \lambda_c$), the system enters the ''superradiant'' phase, characterized by a macroscopic occupation of the cavity mode, where the photon number scales linearly with the number of atoms N. This transition involves the spontaneous breaking of a discrete $\mathbb{Z}_2$ parity symmetry ($\hat{a} \to -\hat{a},\ \hat{S}_x \to -\hat{S}_x$), leading to two possible steady states with opposite phases. Due to the collective, infinite-range nature of the atom-cavity coupling, the mean-field approximation becomes exact as $N \to \infty$, placing the critical behavior of the Dicke model strictly into the mean-field Ising universality class.

Unlike the 1D TFIM, the Dicke model also exhibits a thermal phase transition at finite temperatures ($T > 0$). Because thermal fluctuations counteract the collective ordering, a stronger coupling

is required to achieve superradiance. The temperature-dependent critical coupling is given by

$$\lambda_c(T) = \frac{\sqrt{\omega_a \omega_c}}{2} \sqrt{\coth\left(\frac{\omega_a}{2k_B T}\right)}. \tag{2.11}$$

As $T \to 0$, $\coth(\infty) \to 1$, recovering the quantum critical point. Because the mean-field approximation remains exact across all temperature regimes, both the zero- and finite-temperature transitions exhibit identical mean-field critical exponents for the order parameter ($\beta = 1/2$). However, their universal behaviors fundamentally differ in how the critical fluctuations scale. At $T = 0$, the transition is governed by quantum zero-point fluctuations; as the critical mode softens, the photon number diverges with a characteristic exponent of $\gamma = 1/2$. Conversely, at any finite temperature, classical thermal fluctuations dominate, altering the scaling of the divergent mode to $\gamma = 1$ [104]. This distinction in fluctuation scaling firmly places the finite-temperature transition into the classical mean-field Ising universality class.

Model	**Ordered Phase**	**Disordered Phase**	**Transition Point**
1D TFIM	Ferromagnetic ($g < J$)	Paramagnetic ($g > J$)	$g/J = 1$
Dicke Model	Superradiant ($\lambda > \lambda_c$)	Normal ($\lambda < \lambda_c$)	$\lambda_c = \frac{\sqrt{\omega_a \omega_c}}{2}$

Table 2.2 Examples of ground-state phase transitions in quantum many-body models. Notably, while thermal fluctuations destroy long-range order in the 1D TFIM, the Dicke model exhibits a finite-temperature phase transition.

2.2.4 Finite-Temperature Signatures of Quantum Criticality

The existence of a quantum critical point (QCP) is not merely a theoretical construct at $T = 0$; it leaves an indelible ‘‘fingerprint’’ on the finite-temperature phase diagram of strongly correlated systems, giving rise to an extended region in parameter space known as the quantum critical fan (QCF) [82]. In this regime, the physics is governed not by the ground-state properties of the adjacent phases, but by the critical quantum fluctuations echoing from the QCP [95, 105].

The $T > 0$ landscape is broadly partitioned by the competition between the thermal energy $k_B T$ and the characteristic energy gap $\Delta(g)$ of the system's excitations [82, 106]. When $T \ll \Delta$, thermal fluctuations are too weak to close the gap, and the system behaves either as a semiclassical ordered state (the renormalized classical regime) or a thermally ‘‘frozen’’ paramagnet (the quantum disor-

dered regime), depending on the tuning parameter g [82, 107]. However, at higher temperatures where $k_B T \gg \Delta$, the discrete excitation spectrum is thermally smeared. In this intermediate ‘‘quantum critical fan,’’ the underlying ground state becomes irrelevant, and the macroscopic dynamics are instead governed by a scale-invariant continuum of quantum fluctuations. Instead, observables exhibit universal scaling behavior determined solely by the critical exponents of the $T = 0$ fixed point [108, 109]. This universal behavior allows the QCF to act as a ‘‘magnifying lens’’ for the QCP, making critical fluctuations observable over a broad range of temperatures and control parameters.

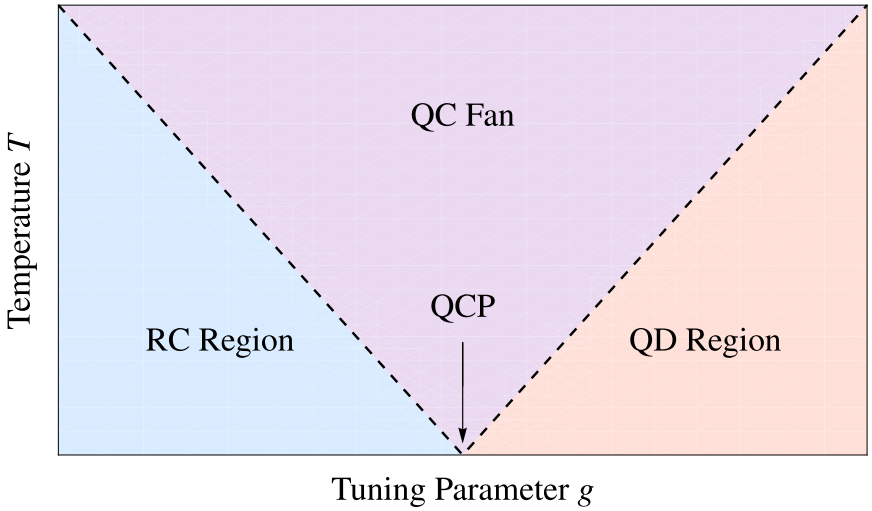

Figure 2.3 Adapted from Ref. [82]: finite-temperature phase diagram of the 1D TFIM near the QCP. The dashed lines denote crossover boundaries $T \sim |g - g_c|^{z\nu}$ (with $z = \nu = 1$) separating the renormalized classical (RC) and quantum disordered (QD) regimes from the scale-invariant quantum critical (QC) fan.

Prototypical experimental realizations of the quantum critical fan are found in heavy-fermion intermetallic compounds, such as $CeCu_{6-x}Au_x$ and $YbRh_2Si_2$ [110, 111]. These materials exhibit an ‘‘anomalous’’ temperature dependence of electrical resistivity, often showing T-linear behavior ($\rho \sim T$) within the fan, a hallmark of ‘‘strange metal’’ transport that violates the conventional T^2 scaling of Fermi liquids [111, 112]. This behavior is frequently associated with the breakdown of quasiparticle excitations near a Kondo-breakdown QCP [113, 114], where electrons scatter off collective critical fluctuations with a rate bounded by the ‘‘Planckian’’ timescale $\tau_{\mathrm{Pl}} = \hbar/k_B T$ [115, 116].

2.3 Probing Quantum Criticality in Nonequilibrium Dynamics

While quantum phase transitions (QPTs) are strictly defined by the non-analytic properties of the many-body ground state at absolute zero temperature, accessing these equilibrium states in experimental platforms is exceptionally challenging. Consequently, the focus of modern many-body physics has increasingly shifted toward identifying dynamical signatures of criticality [117].

2.3.1 Near Equilibrium: The Kibble-Zurek Mechanism

When a system is ramped through a critical point at a finite ''ramp rate'' $\nu = 1/\tau_Q$, the dynamics are governed by the Kibble-Zurek Mechanism (KZM) [118, 119]. The KZM provides a universal framework to understand how the system's relaxation time $\tau(g)$ eventually fails to keep pace with the changing control parameter $g(t)$ in the vicinity of a QCP, leading to a ''freeze-out'' of fluctuations. The mechanism predicts that the characteristic freeze-out time $\bar{t}$ and the resulting density of topological defects n scale universally with the quench time τ_Q:

$$\bar{t} \sim \tau_Q^{\frac{z\nu}{1+z\nu}}, \quad n \sim \tau_Q^{-\frac{d\nu}{1+z\nu}}, \tag{2.12}$$

where z and ν are the static critical exponents and d is the system dimensionality [120–122]. This scaling bridges the gap between static equilibrium properties and the dynamical response of a system driven across a phase boundary, providing a powerful experimental tool to extract critical exponents from nonequilibrium data.

The universality of KZM scaling has been verified across a wide array of experimental platforms. Early validations were performed in liquid crystals and superconductors [123, 124], while more recent breakthroughs have utilized highly controllable quantum simulators. These include the observation of defect scaling in trapped ion chains [125, 126], ultracold atomic gases [127], and strongly interacting Rydberg atom arrays [61]. Notably, experiments in the 1D transverse-field Ising model using programmable quantum devices have confirmed the predicted $n \sim \tau_Q^{-1/2}$ scaling for the $z = \nu = 1$ universality class [128].

2.3.2 Far from Equilibrium: Signatures of Quantum Phase Transitions in Quench Dynamics

Another ubiquitous protocol for probing QPT signatures is the quantum quench: a system is prepared in the ground state of an initial Hamiltonian $\hat{H}(g_i)$, and a control parameter is abruptly changed to a new value g_f. The resulting unitary evolution under $\hat{H}(g_f)$ drives the system out of equilibrium, yet the transient and asymptotic dynamics often robustly encode the universal properties of the underlying critical point, bypassing the need for perfect ground-state cooling.

A sudden global quench poses a conceptual challenge for observing criticality because it injects an extensive amount of energy into the system, effectively placing it in a highly excited state. From a thermodynamic perspective, this extensive energy density mimics an effective temperature [129]. Because thermal-like fluctuations generally cut off the long-range correlations associated with a QPT in 1D systems, one typically observes volume-law entanglement growth and the exponential decay of standard two-point correlation functions. Historically, this exponential decay—driven by the effective thermalization of the injected energy—was thought to wash out any signature of the underlying zero-temperature critical point [130–133]. However, a wave of recent studies has demonstrated that genuine quantum criticality may survive after a quench [134–137].

Instead of manifesting in traditional long-range spatial correlations, the QPT imprints robust signatures of criticality directly onto the dynamics of local, experimentally accessible observables. When a system is quenched across a quantum critical point, the time-averaged expectation values of short-range correlators and local bulk observables exhibit pronounced non-analyticities, such as kinks or cusps, as a function of the quench parameter [135, 136]. Furthermore, similar non-analytic signatures of the continuous QPT manifest in the macroscopic nonequilibrium energy absorbed by the system from the quenching pulse [134]. Beyond local observables, even when a quench along a critical line results in volume-law entropy and exponentially decaying two-point correlations, the quantum critical signatures are not destroyed; rather, they are ‘‘hidden’’ [137]. This emergent quantum criticality can be systematically uncovered by probing higher-order correlations via quantum information measures. Bipartite entanglement measures, such as the mutual information and the

logarithmic negativity between disjoint regions, retain their universal scale invariance, successfully revealing the underlying order-disorder phase transition despite the extensive energy injected by the quench.

These dynamical signatures of criticality have proven remarkably robust across a diverse array of theoretical models. Beyond exactly solvable or short-range systems, they have been shown to successfully identify topological gap closings [135], persist in long-range interacting spin models characterized by distinct nonequilibrium universality classes [129], and even survive at prethermal timescales in nearly integrable systems before the onset of full thermalization [136].

Experimentally, the observation of asymptotic steady-state signatures remains a challenge in many-body systems, as reaching a true steady state is often precluded by environmental decoherence, heating, or particle loss. Consequently, there has been a shift toward identifying transient temporal probes that capture the essence of the transition before the system thermalizes. Features of early-time dynamics have been experimentally shown to act as robust indicators of phase transitions [138–140].

2.4 Driven Dissipative Phase Transitions in Open Quantum Systems

Unlike classical or quantum phase transitions that occur in closed systems, driven-dissipative phase transitions (DDPTs) are properties of open systems that reach a nonequilibrium steady state (NESS) through the balance of coherent energy injection and dissipative decay [52]. The physics of these systems is described by the density matrix $\rho(t)$, whose evolution is governed by the Lindblad master equation [37].

2.4.1 The Lindbladian and Spectral Gap Theory

The master equation in the Schrödinger picture is given by:

$$\frac{\mathrm{d}\hat{\rho}}{\mathrm{d}t} = \hat{\mathcal{L}}[\hat{\rho}] = -i[\hat{H}, \hat{\rho}] + \sum_k \gamma_k \left(\hat{L}_k \hat{\rho} \hat{L}_k^\dagger - \frac{1}{2} \left\{ \hat{L}_k^\dagger \hat{L}_k, \hat{\rho} \right\} \right) \tag{2.13}$$

where $\hat{\mathcal{L}}$ is the Liouvillian super-operator, $\hat{H}$ is the system Hamiltonian, and $\hat{L}_k$ are the jump operators with associated rates γ_k. The steady state $\hat{\rho}_{ss}$ satisfies $\hat{\mathcal{L}}[\hat{\rho}_{ss}] = 0$, corresponding to the zero-eigenvalue of the Liouvillian. Here, the spectral properties of $\hat{\mathcal{L}}$ determine the stability and

relaxation dynamics of the system. Since $\hat{\mathcal{L}}$ is non-Hermitian, its eigenvalues λ_i are generally complex, satisfying $\mathrm{Re}(\lambda_i) \leq 0$. If we sort the eigenvalues λ_i of the Liouvillian by their real parts such that $0 = \mathrm{Re}(\lambda_0) \geq \mathrm{Re}(\lambda_1) \geq \mathrm{Re}(\lambda_2) \ldots$, the relaxation dynamics are dominated by the Liouvillian gap, defined as

$$\Delta_L = |\mathrm{Re}(\lambda_1)| \tag{2.14}$$

A DDPT is strictly associated with the closing of this Liouvillian gap in the thermodynamic limit ($N \to \infty$) [65–67, 141]. When $\Delta_L \to 0$, the relaxation time diverges, leading to critical slowing down—a hallmark of criticality that mirrors the diverging correlation lengths in equilibrium transitions. Furthermore, the imaginary part of the first excited eigenvalue, $\mathrm{Im}(\lambda_1)$, dictates the transient oscillatory dynamics.

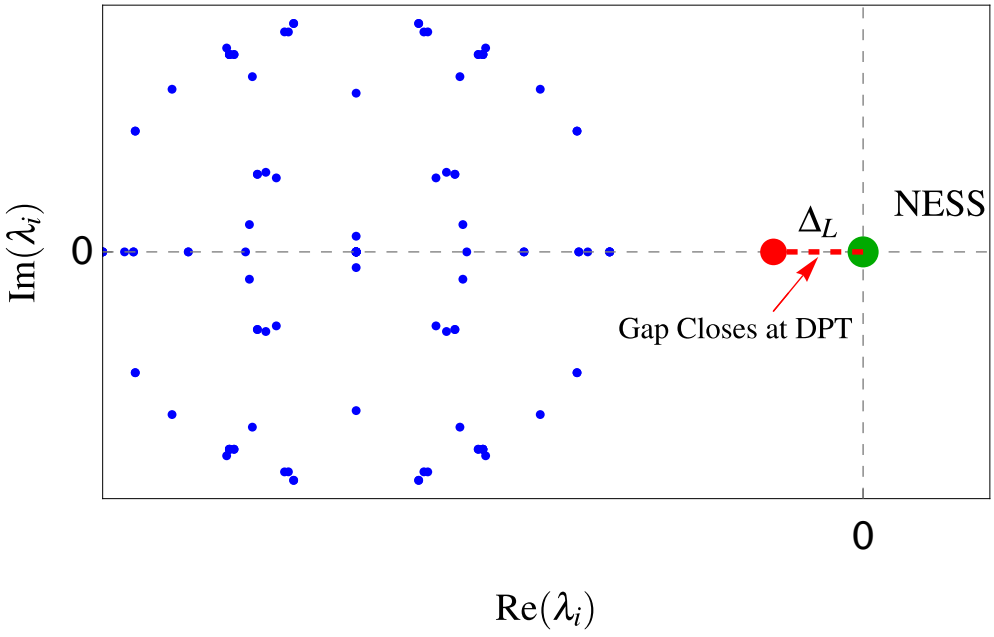

Figure 2.4 Liouvillian eigenvalues λ_i in the complex plane for a generic open quantum system. The steady state corresponds to the unique eigenvalue at the origin ($\lambda_0 = 0$). The Liouvillian gap Δ_L is defined as the absolute real part of the eigenvalue closest to the origin. A driven-dissipative phase transition occurs when $\Delta_L \to 0$ in the thermodynamic limit, leading to critical slowing down and the emergence of multiple steady states.

Much like their classical and quantum counterparts, driven-dissipative phase transitions are classified as either first- or second-order based on the nature of the non-analyticity in the steady state. First-order DDPTs involve a discontinuous jump in steady-state observables, accompanied

by an exponentially vanishing Liouvillian gap [142]. In finite systems, this severely suppressed relaxation rate manifests as pronounced metastability and bistability, with a prototypical example being the ''dim-to-bright'' transition in driven-dissipative nonlinear resonators [60]. Conversely, second-order DDPTs are characterized by an algebraic closing of the Liouvillian gap associated with the spontaneous breaking of a symmetry, which leads to a degenerate steady-state manifold. The archetypal example of such a continuous transition is the superradiant transition in the Dicke model, where a collective atomic state spontaneously develops a macroscopic dipole moment [66, 143].

2.4.2 The Superradiant Transition in the Dissipative Dicke Model

The Dicke model, introduced in Section 2.2.3, describes the collective coupling of N atoms to a single cavity mode. In the presence of photon loss κ, the system exhibits a second-order driven-dissipative phase transition (DDPT) as the atom-cavity coupling strength λ is tuned [100, 143]. As the coupling exceeds the critical value $\lambda_c = \sqrt{\omega_a(\omega_c^2 + \kappa^2/4)/4\omega_c}$, the nonequilibrium steady state (NESS) transitions from a normal phase, characterized by an empty cavity $\langle \hat{a}^\dagger \hat{a} \rangle = 0$, to a ''superradiant'' phase. In the superradiant regime, the $\mathbb{Z}_2$ symmetry of the Hamiltonian is spontaneously broken, and the system develops a macroscopic photon field $\langle \hat{a}^\dagger \hat{a} \rangle \propto N$ along with a collective atomic polarization [101, 104]. In the thermodynamic limit $N \to \infty$, the Liouvillian gap vanishes as $\Delta_L \sim |\lambda - \lambda_c|^{z\nu}$ near the critical point. Interestingly, at a generic critical point with finite dissipation, the dissipative Dicke transition is found to belong to the mean-field classical Ising universality class [104]. This highlights a profound feature of DDPTs: the stochastic nature of dissipation can play a role analogous to thermal fluctuations. Consequently, the presence of decay channels can effectively lead to behavior characteristic of a classical phase transition even when coupled to a bath at zero-temperature.

2.5 Summary

A comprehensive comparison of the three transition classes reveals a profound unity in the underlying scaling principles, despite their distinct driving mechanisms. The concept of the thermodynamic limit ($N \to \infty$) remains the essential requirement for all, as true non-analyticity and

spontaneous symmetry breaking may only emerge when local fluctuations are suppressed.

The mapping between quantum systems in d dimensions and classical systems in $d + z$ dimensions provides the rigorous bridge for understanding universality classes. In driven-dissipative systems, dissipation often serves as a stochastic fluctuation source analogous to a finite temperature. While this effect can drive the system toward an effectively thermal steady state—washing out quantum fluctuations—this mapping is not universal. Under specific conditions—such as engineered dissipation protocols may be designed or in the presence of long-range interactions—the system can circumvent this effective thermalization. In these regimes, the steady state remains fundamentally non-thermal, hosting purely quantum correlations and phase transitions that have no equilibrium analogues.

As experimental precision in quantum simulators continues to improve, the ability to observe exotic driven-dissipative phenomena across diverse physical platforms will allow for the verification of these theoretical paradigms and drive the discovery of novel states of matter that exist only far from equilibrium.

CHAPTER 3

THEORETICAL BACKGROUND

The study of quantum many-body dynamics is fundamentally transformed when a system is no longer treated as isolated. The primary objective of this chapter is to establish the rigorous mathematical foundation for describing such systems. We begin by introducing the density matrix formalism and the GKSL (Lindblad) master equation, which provides a standard Markovian framework for characterizing dissipation. We detail the fundamental properties of the Liouvillian superoperator, which preserve the physical integrity of the evolving density matrix, and present the method of vectorization, which maps matrix-valued operators onto vectors in a doubled Hilbert space. This structural ‘‘doubling’’ provides the technical bridge to the analytical methods that follow in Chapter 4.

3.1 The Density Matrix Formalism

Before detailing the dynamics of open quantum systems, it is necessary to establish the fundamental mathematical object used to describe them: the density matrix, or density operator, $\hat{\rho}$. While an isolated quantum system in a pure state can be fully described by a state vector $|\psi\rangle$ in a Hilbert space $\mathcal{H}$, realistically, physical systems are often in statistical mixtures of pure states due to classical uncertainty or entanglement with an external environment [144–148].

The density operator provides a complete statistical description of a quantum system and is defined as

$$\hat{\rho} = \sum_i p_i |\psi_i\rangle\langle\psi_i|, \tag{3.1}$$

where p_i represents the classical probability of the system being in the pure state $|\psi_i\rangle$. These probabilities must satisfy $p_i \geq 0$ and $\sum_i p_i = 1$.

In order to respect these constraints, the density matrix must strictly adhere to three mathematical properties [144, 149]:

1. **Hermiticity:** The density operator must be Hermitian, $\hat{\rho}^\dagger = \hat{\rho}$, ensuring that its eigenvalues (which correspond to physical probabilities) are strictly real.

2. **Unit trace:** The sum of the probabilities of all possible mutually exclusive measurement outcomes must equal unity. Therefore, the trace of the density matrix is conserved: $\mathrm{Tr}(\hat{\rho}) = \sum_i p_i \langle \psi_i | \psi_i \rangle = 1$.

3. **Positive semi-definiteness:** For any arbitrary state vector $|\phi\rangle$ in the Hilbert space $\mathcal{H}$, $\langle \phi | \hat{\rho} | \phi \rangle \geq 0$. This guarantees that the probability of finding the system in any state $|\phi\rangle$ is non-negative.

The expectation value of any observable, represented by a Hermitian operator $\hat{A}$, is naturally extracted by taking the trace of the observable with the density matrix [149]

$$\langle \hat{A} \rangle = \mathrm{Tr}(\hat{\rho}\hat{A}). \tag{3.2}$$

One of the most powerful features of the density matrix formalism is its ability to rigorously describe subsystems of a larger entangled state. In quantum mechanics, if two interacting systems are entangled, the composite system can be in a pure state while the individual subsystems exist in statistical mixtures. To illustrate this, consider a bipartite system composed of two qubits, A and B, prepared in the maximally entangled Bell state

$$|\Phi^+\rangle = \frac{1}{\sqrt{2}}(|0_A 0_B\rangle + |1_A 1_B\rangle). \tag{3.3}$$

The global density matrix for this composite pure state is simply $\hat{\rho}_{AB} = |\Phi^+\rangle\langle\Phi^+|$. While we possess maximal knowledge of the global system, any local measurement performed solely on subsystem A is oblivious to the quantum correlations shared with B. The effective local state of A is obtained by performing a partial trace over the unobserved degrees of freedom of B

$$\hat{\rho}_A = \mathrm{Tr}_B[\hat{\rho}_{AB}] = \langle 0_B | \hat{\rho}_{AB} | 0_B \rangle + \langle 1_B | \hat{\rho}_{AB} | 1_B \rangle. \tag{3.4}$$

Evaluating this partial trace yields

$$\hat{\rho}_A = \frac{1}{2}\left(|0_A\rangle\langle 0_A| + |1_A\rangle\langle 1_A|\right) = \frac{1}{2}\hat{I}. \tag{3.5}$$

Despite the global state $\hat{\rho}_{AB}$ being perfectly pure, the reduced state $\hat{\rho}_A$ is maximally mixed. The entanglement with an unmeasured subsystem manifests locally as classical entropy and loss of phase information [146].

This concept is the exact mechanism underlying the theory of open quantum systems. When evaluating reduced dynamics, the macroscopic environment E acts as the unobserved subsystem. The environment is traced out of the global system-environment state, leaving a reduced density matrix $\hat{\rho}_S = \mathrm{Tr}_E[\hat{\rho}_{SE}]$, which inherently captures the decoherence and dissipation that drive the primary system toward a nonequilibrium steady state [52, 150].

3.2 Open Quantum Systems and the Markov Approximation

In the density matrix formalism, the von Neumann equation prescribes unitary, time-reversible evolution [144]

$$\frac{\mathrm{d}\hat{\rho}_S}{\mathrm{d}t} = -i[\hat{H}_S, \hat{\rho}_S]. \tag{3.6}$$

Here, $\hat{H}_S$ is the system Hamiltonian. However, realistic physical systems are never perfectly isolated; they inevitably interact with a surrounding environment or thermal bath. Tracing out the environmental degrees of freedom yields effective dynamics that is generally non-unitary, irreversible, and characterized by the loss of energy (dissipation) and phase coherence (decoherence) [146, 147].

To obtain a tractable equation of motion for $\hat{\rho}_S(t)$, a series of approximations must typically be invoked. The most critical of these is the Markov approximation, which assumes that the environment is memoryless. Physically, this requires that the correlation time of the environment (τ_E) is strictly much shorter than the characteristic relaxation time of the system (τ_S). When combined with the Born approximation (weak system-bath coupling) and the secular approximation (averaging out rapidly oscillating terms), the system's dynamics can be described by a quantum dynamical semigroup [37, 38, 148, 151].

As introduced conceptually in Chapter 1, the most general generator of a quantum dynamical semigroup is the Gorini-Kossakowski-Sudarshan-Lindblad (GKSL) master equation, widely referred to as the Lindblad master equation [37, 38]. In a time-independent Markovian regime, the evolution of the system's density matrix $\hat{\rho}$ (dropping the subscript S) is given by

$$\frac{\mathrm{d}\hat{\rho}}{\mathrm{d}t} = \hat{\mathcal{L}}[\hat{\rho}] = -i[\hat{H}, \hat{\rho}] + \sum_k \gamma_k \left(\hat{L}_k \hat{\rho} \hat{L}_k^\dagger - \frac{1}{2}\{\hat{L}_k^\dagger \hat{L}_k, \hat{\rho}\} \right). \tag{3.7}$$

Here, $\hat{\mathcal{L}}$ is the Liouvillian superoperator. The first term on the right-hand side represents the coher-

ent evolution generated by the system Hamiltonian $\hat{H}$. The second term, representing the dissipator $\hat{\mathcal{D}}[\hat{\rho}]$, models the incoherent exchange of energy and information with the environment. The operators $\hat{L}_k$ are the Lindblad jump operators, which dictate specific dissipation channels, and $\gamma_k \geq 0$ are the associated decay rates.

The structural form of the GKSL equation guarantees that the solutions adhere to the foundational axioms of quantum mechanics [149]. Any physically permissible evolution must map density operators to valid density operators, strictly enforcing the following properties:

- **Trace preservation:** Probability conservation requires that $\mathrm{Tr}[\hat{\rho}(t)] = 1$ at all times. Taking the trace of the Liouvillian yields $\mathrm{Tr}(\hat{\mathcal{L}}[\hat{\rho}]) = 0$. The commutator vanishes under the cyclic property of the trace, and the dissipator sum cancels exactly: $\mathrm{Tr}(\hat{L}_k\hat{\rho}\hat{L}_k^\dagger) = \mathrm{Tr}(\hat{L}_k^\dagger\hat{L}_k\hat{\rho})$, ensuring $\frac{\mathrm{d}}{\mathrm{d}t}\mathrm{Tr}[\hat{\rho}] = 0$.

- **Hermiticity preservation:** The Liouvillian guarantees that if $\hat{\rho}(0)$ is Hermitian, $\hat{\rho}(t)$ remains Hermitian for all $t \geq 0$, ensuring the density matrix represents observable probabilities $(\hat{\mathcal{L}}[\hat{\rho}])^\dagger = \hat{\mathcal{L}}[\hat{\rho}^\dagger] = \hat{\mathcal{L}}[\hat{\rho}]$ [147, 149].

- **Complete positivity:** The dynamical map $\hat{\mathcal{E}}_t = \exp\left(\hat{\mathcal{L}}t\right)$ is completely positive (CP), ensuring that the eigenvalues of $\hat{\rho}(t)$ remain non-negative. This ensures that the GKSL equation is a generator of trace-preserving completely-positive (CPTP) maps.

3.2.1 Steady States and Driven-Dissipative Dynamics

A defining feature of Markovian open quantum systems is the tendency to relax toward a steady state, $\hat{\rho}_{ss}$, defined by the kernel of the Liouvillian: $\hat{\mathcal{L}}[\hat{\rho}_{ss}] = 0$. In the absence of an external drive, the bath leads the system toward a thermal Gibbs state. In typical driven-dissipative systems, however, an external field coherently pumps energy into the system, introducing an explicit time-dependence into the Hamiltonian. To analyze stationary properties, it is standard practice to transform into a rotating frame and apply the rotating wave approximation (RWA), which averages out rapidly oscillating terms to yield a time-independent effective Liouvillian. In this rotating

frame, the resulting dynamics breaks the detailed-balance symmetry. Eventually, the continuous competition between the coherent drive and local dissipation leads the systems into a nonequilibrium steady state (NESS) that can exhibit complex many-body correlations [49, 52]. The existence and uniqueness of the steady state in many-body systems are dictated by the spectral properties of this non-Hermitian Liouvillian superoperator [67, 70, 152].

A defining feature of Markovian open quantum systems is the tendency to relax toward a steady state, $\hat{\rho}_{ss}$, defined by the kernel of the Liouvillian: $\hat{\mathcal{L}}[\hat{\rho}_{ss}] = 0$. In the absence of an external drive, the bath leads the system toward a thermal Gibbs state. However, in driven-dissipative systems where external coherent driving competes with local dissipation, the resulting nonequilibrium steady states (NESS) can exhibit complex many-body correlations [49, 52]. The existence and uniqueness of the steady state in many-body systems are dictated by the spectral properties of the non-Hermitian Liouvillian superoperator [67, 70, 152].

3.2.2 Vectorization and Liouville Space

As mentioned in the introduction of this chapter, solving the Lindblad master equation for a many-body system is analytically and computationally demanding because the density matrix of a system with Hilbert space dimension N contains N^2 elements. In order to numerically solve for the nonequilibrium dynamics or to find the steady-state kernel $\hat{\mathcal{L}}[\hat{\rho}_{ss}] = 0$, it is highly advantageous to map the matrix equation (Eq. (3.7)) into a linear vector equation. This procedure is known as vectorization, or purification [147].

Vectorization maps the $N \times N$ density matrix (pure state) $\hat{\rho}$ onto a column vector $|\hat{\rho}\rangle\rangle$ residing in a larger space known as the Liouville space (or Hilbert-Schmidt space), which has dimension N^2. Utilizing the Choi-Jamiołkowski isomorphism [153, 154], a basis element $|i\rangle\langle j|$ is mapped to a tensor product of kets

$$|i\rangle\langle j| \longrightarrow |i\rangle \otimes |j\rangle \equiv |i, j\rangle\rangle. \tag{3.8}$$

Consequently, the density matrix is flattened into a state vector (where $\rho_{i,j}$ are scalar matrix ele-

ments)

$$\hat{\rho} = \sum_{i,j} \rho_{i,j} |i\rangle\langle j| \quad \longrightarrow \quad |\hat{\rho}\rangle\rangle = \sum_{i,j} \rho_{i,j} |i\rangle \otimes |j\rangle. \tag{3.9}$$

The power of this mapping lies in the tensor product identity, which dictates how standard operators act on the vectorized state. For any arbitrary matrices $\hat{A}$, $\hat{\rho}$, and $\hat{C}$, the matrix multiplication $\hat{A}\hat{B}\hat{C}$ vectorizes as

$$\hat{A}\hat{\rho}\hat{C} \longrightarrow (\hat{A} \otimes \hat{C}^T)|\hat{\rho}\rangle\rangle, \tag{3.10}$$

where $\hat{C}^T$ is the transpose of $\hat{C}$.

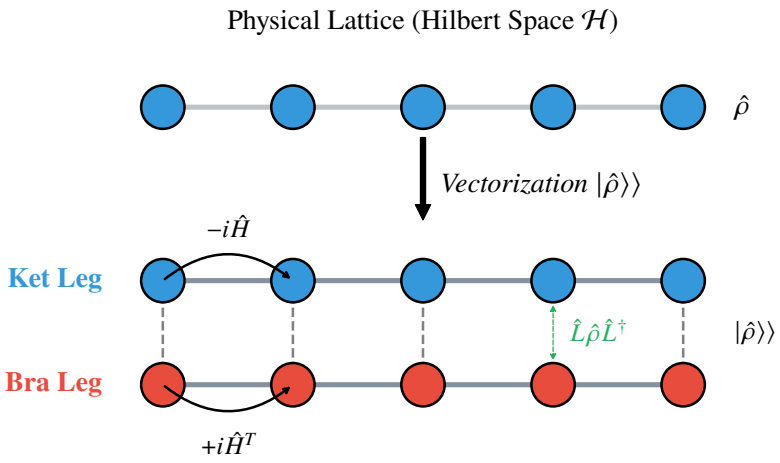

Figure 3.1 Schematic representation of vectorization. A 1D physical lattice (top) is described by a density matrix $\hat{\rho}$ acting on the state space $\mathcal{H}$. Vectorization flattens this operator into a state vector $|\hat{\rho}\rangle\rangle$ residing in the Liouville space $\mathcal{H} \otimes \mathcal{H}^*$ (bottom). This mathematical transformation maps the original spatial system onto an effective two-leg ''doubled'' lattice geometry. The upper (ket) and lower (bra) legs encode the left- and right-action of operators on the density matrix, respectively. Coherent Hamiltonian interactions dictate horizontal dynamics along the independent legs, whereas local Lindblad jump operators act as vertical rungs, explicitly coupling the ket and bra degrees of freedom at each physical site.

Applying the identity in Eq. (3.10) to the GKSL master equation allows us to represent the Liouvillian superoperator $\hat{\mathcal{L}}$ as an $N^2 \times N^2$ non-Hermitian matrix $\hat{\mathbb{L}}$. The coherent commutator term $-i[\hat{H}, \hat{\rho}]$ transforms as

$$-i(\hat{H}\hat{\rho} - \hat{\rho}\hat{H}) \longrightarrow -i(\hat{H} \otimes \hat{I} - \hat{I} \otimes \hat{H}^T)|\hat{\rho}\rangle\rangle. \tag{3.11}$$

Similarly, the dissipator transforms by applying Eq. (3.10) to the jump operators $\hat{L}_k$. The action of the jump operators on both sides of the density matrix, $\hat{L}_k\hat{\rho}\hat{L}_k^\dagger$, vectorizes to $(\hat{L}_k \otimes (\hat{L}_k^\dagger)^T)|\hat{\rho}\rangle\rangle$.

Noting that the transpose of the Hermitian conjugate is simply the complex conjugate, this term simplifies to

$$(\hat{L}_k \otimes \hat{L}_k^*)|\hat{\rho}\rangle\rangle. \tag{3.12}$$

The anti-commutator terms involving $\hat{L}_k^\dagger \hat{L}_k$ multiply the density matrix from the left and right, transforming into $-\frac{1}{2}(\hat{L}_k^\dagger \hat{L}_k \otimes \hat{I})|\hat{\rho}\rangle\rangle$ and $-\frac{1}{2}(\hat{I} \otimes (\hat{L}_k^\dagger \hat{L}_k)^T)|\hat{\rho}\rangle\rangle$, respectively.

Collecting the coherent and dissipative components, the master equation is thus recast into a system of linear differential equations

$$\frac{\mathrm{d}}{\mathrm{d}t}|\hat{\rho}\rangle\rangle = \hat{\mathbb{L}}|\hat{\rho}\rangle\rangle, \tag{3.13}$$

where the explicit algebraic form of the Liouvillian matrix $\hat{\mathbb{L}}$ is given by

$$\hat{\mathbb{L}} = -i(\hat{H} \otimes \hat{I} - \hat{I} \otimes \hat{H}^T) + \sum_k \gamma_k \left[\hat{L}_k \otimes \hat{L}_k^* - \frac{1}{2}\left(\hat{L}_k^\dagger \hat{L}_k \otimes \hat{I} + \hat{I} \otimes (\hat{L}_k^\dagger \hat{L}_k)^T\right)\right]. \tag{3.14}$$

This vectorized form is the standard starting point for exact diagonalization techniques [155–157]. Beyond numerical methods, this representation is also convenient for analytical methods (such as the Keldysh field theory [68]), and it is the necessary framework for solving quadratic models in the language of third quantization [158, 159], allowing for the exact resolution of the nonequilibrium spectrum.

Within this dual-space structure, the trace operation $\mathrm{Tr}\left(\hat{A}\right)$ is represented as an inner product. We define the ‘‘identity’’ or ‘‘trace state’’ as

$$\langle\langle \hat{I}| = \sum_i \langle i| \otimes \langle i|. \tag{3.15}$$

This allows us to write the trace of any operator $\hat{A}$ as $\mathrm{Tr}\left(\hat{A}\right) = \langle\langle \hat{I}|\hat{A}\rangle\rangle$. Importantly, physical observables are calculated as expectation values through the Liouville-space inner product

$$\langle \hat{O} \rangle = \mathrm{Tr}\left(\hat{O}\hat{\rho}\right) = \langle\langle \hat{I}|\hat{O}|\hat{\rho}\rangle\rangle. \tag{3.16}$$

With these theoretical background covered, Chapters 4 and 5 will leverage this dual-space framework to survey exact and numerical solution of open quantum systems.

CHAPTER 4

A SURVEY OF ANALYTICAL APPROACHES TO QUADRATIC OPEN QUANTUM SYSTEMS

A central challenge in many-body physics is the exponential growth of the Hilbert space, a problem that is even more conspicuous in the density matrix formalism. An exception to this rule, models characterized by quadratic Hamiltonians and linear Lindblad jump operators are analytically tractable. The exact solvability of these systems provides a crucial analytical foothold for understanding dissipation-induced phenomena. In this chapter, we outline three primary analytical frameworks used to solve such systems: the Heisenberg-Langevin operator formalism [160, 161], the third quantization superoperator method [158, 159], and the Keldysh nonequilibrium path integral [68]. To provide a concrete comparison of these methods, we will apply them to the spin-wave approximation of the driven-dissipative transverse-field Ising chain [162], a model that will be explored extensively in subsequent chapters (e.g., Chapters 7 and 8). The Hamiltonian for this model is given by

$$\hat{H}_{\text{TFIM}} = \sum_{m,n=1}^{L} J_{m,n}\sigma_m^x\sigma_n^x + h\sum_{m=1}^{L}\sigma_m^z, \tag{4.1}$$

where h is the transverse-field, and $J_{m,n}$ is the Ising interaction matrix. The chain is subject to local Markovian dissipation described by the jump operators $\hat{L}_i = \sqrt{\Gamma}\sigma_i^-$. To cast this into a quadratic form, we apply the Holstein-Primakoff (HP) approximation [163]: $\sigma_m^- \to \hat{b}_m$, $\sigma_m^+ \to \hat{b}_m^\dagger$, and $\sigma_m^z \to 2\hat{b}_m^\dagger\hat{b}_m - 1$. While this is strictly valid when $h \gg 1$, the resulting model provides a pedagogical example to demonstrate the techniques discussed in this chapter.

Assuming periodic boundary conditions and transforming to momentum space representation, the Hamiltonian in the bosonic basis, $\hat{H}_b$, decomposes into decoupled momentum sectors $\hat{H}_b = \sum_k \hat{H}_k + \text{const}$, where

$$\hat{H}_k = \begin{pmatrix} \hat{b}_k^\dagger \\ \hat{b}_{-k} \end{pmatrix}^T \begin{pmatrix} J_k + h & J_k \\ J_k & J_k + h \end{pmatrix} \begin{pmatrix} \hat{b}_k \\ \hat{b}_{-k}^\dagger \end{pmatrix}, \tag{4.2}$$

with $J_k \equiv \sum_{n-m>0} J_{m,n}\cos(k(n-m))$. The dissipator simultaneously maps to a bi-linear bosonic

form

$$\mathcal{D}_b(\hat{\rho}) = \Gamma \sum_k \left(\hat{b}_k \hat{\rho} \hat{b}_k^\dagger - \frac{1}{2} \hat{b}_k^\dagger \hat{b}_k \hat{\rho} - \frac{1}{2} \hat{\rho} \hat{b}_k^\dagger \hat{b}_k \right). \tag{4.3}$$

4.1 The Heisenberg-Langevin Formalism

The Heisenberg-Langevin formalism stems from the necessity to reconcile macroscopic dissipation with the fundamental axioms of quantum mechanics. In classical statistical mechanics, open system dynamics are phenomenologically modeled using the Langevin equation [15], which supplements the Newtonian equations of motion with a macroscopic viscous drag term and a classical stochastic fluctuating force. However, naively appending a damping rate to the quantum Heisenberg equations of motion leads to a fundamental physical violation. If a quantum harmonic oscillator simply loses energy via a generic friction term ($dv\hat{a}t = -i\omega\hat{a} - \frac{\gamma}{2}\hat{a}$), its canonical commutation relations ($[\hat{a}(t), \hat{a}^\dagger(t)] = e^{-\gamma t}$) will exponentially decay to zero [160]. This implies that an open system would eventually reach a state with zero zero-point energy, explicitly violating the Heisenberg uncertainty principle.

To resolve this, pioneers such as Senitzky, Lax, Ford, Kac, and Mazur in the 1960s demonstrated that any dissipative drag must be rigorously accompanied by a fluctuating *quantum* operator [164–166]. This operator noise acts as a continuous source of quantum fluctuations, perfectly balancing the dissipative losses—a direct operational manifestation of the quantum fluctuation-dissipation theorem. Building on this principle, the modern Heisenberg-Langevin approach evaluates open quantum dynamics strictly in the Heisenberg picture, where the physical operators carry the time dependence while their commutation algebra remains perfectly preserved for all $t > 0$. The irreversible nature of the open system is captured by appending both the deterministic damping term and the stochastic noise operator to the standard Heisenberg equation of motion.

For our bosonic modes in Eqs. (4.2) and (4.3), the Heisenberg-Langevin equations are given by [161]

$$\begin{aligned} \frac{\mathrm{d}\hat{b}_k(t)}{\mathrm{d}t} &= 2i[\hat{H}_k, \hat{b}_k(t)] - \frac{\Gamma}{2}\hat{b}_k(t) + \sqrt{\Gamma}\hat{b}_k^{in}(t), \\ \frac{\mathrm{d}\hat{b}_{-k}^\dagger(t)}{\mathrm{d}t} &= 2i[\hat{H}_k, \hat{b}_{-k}^\dagger(t)] - \frac{\Gamma}{2}\hat{b}_{-k}^\dagger(t) + \sqrt{\Gamma}\hat{b}_{-k}^{\dagger in}(t). \end{aligned} \tag{4.4}$$

Here, the environment is modeled via the input noise operators $\hat{b}_k^{in}(t)$, which satisfy the Markovian white-noise correlation condition $\langle \hat{b}_k^{in}(t)\hat{b}_{k'}^{\dagger in}(t')\rangle = \delta_{k,k'}\delta(t-t')$, with all other correlators vanishing, $\langle \hat{b}_k^{in}(t)\hat{b}_{k'}^{in}(t')\rangle = 0$. Because the dynamics are strictly linear, these equations can be elegantly packaged into a compact matrix-vector form

$$\frac{\mathrm{d}\hat{f}(t)}{\mathrm{d}t} = \mathcal{M}\hat{f}(t) + \hat{m}(t), \tag{4.5}$$

where $\hat{f}(t) = (\hat{b}_k, \hat{b}_{-k}^{\dagger})^T$, $\hat{m}(t) = (\sqrt{\Gamma}\hat{b}_k^{in}, \sqrt{\Gamma}\hat{b}_{-k}^{\dagger in})^T$, and the dynamic drift matrix $\mathcal{M}$ is defined as

$$\mathcal{M} = \begin{pmatrix} -2i(J_k + h) - \frac{\Gamma}{2} & -2iJ_k \\ 2iJ_k & 2i(J_k + h) - \frac{\Gamma}{2} \end{pmatrix}. \tag{4.6}$$

The formal solution is obtained by integrating the Green's function propagator $\exp(\mathcal{M}t)$, yielding $\hat{f}(t) = e^{\mathcal{M}t}\hat{f}(0) + \int_0^t e^{\mathcal{M}(t-t')}\hat{m}(t')dt'$. In the long-time limit ($t \to \infty$), the first term being transient decays to zero, and the steady state is entirely determined by the integral. Writing the matrix exponential $e^{\mathcal{M}\tau}$ on the general form

$$e^{\mathcal{M}\tau} = \begin{pmatrix} g_1(\tau) & g_2(\tau) \\ g_2^*(\tau) & g_1^*(\tau) \end{pmatrix}, \tag{4.7}$$

the asymptotic solution ($t \to \infty$) takes the exact form

$$\hat{f}(t) = \sqrt{\Gamma}\int_0^t dt' \begin{pmatrix} g_1(t-t')\hat{b}_k^{in}(t') + g_2(t-t')\hat{b}_{-k}^{\dagger in}(t') \\ g_1^*(t-t')\hat{b}_{-k}^{\dagger in}(t') + g_2^*(t-t')\hat{b}_k^{in}(t') \end{pmatrix}. \tag{4.8}$$

In our model, by introducing the auxiliary dispersion variables,

$$\begin{aligned} \epsilon_k &= 2(J_k + h), \\ \eta_k &= 2J_k, \\ \xi_k &= \sqrt{\epsilon_k^2 - \eta_k^2}, \end{aligned} \tag{4.9}$$

the Green's functions $g_1(\tau)$ and $g_2(\tau)$ can be evaluated explicitly

$$\begin{aligned} g_1(\tau) &= e^{-\frac{\Gamma}{2}\tau}\left[\cos(\tau\xi_k) - i\epsilon_k\frac{\sin(\tau\xi_k)}{\xi_k}\right], \\ g_2(\tau) &= -i\eta_k e^{-\frac{\Gamma}{2}\tau}\frac{\sin(\tau\xi_k)}{\xi_k}. \end{aligned} \tag{4.10}$$

The full spectrum of bosonic correlation functions in the nonequilibrium steady state can thus be extracted analytically from Eq. (4.8).

Returning to the spin degrees of freedom via the HP approximation, the transverse spin correlations at a spatial separation r are given by

$$\langle \sigma_j^x(t)\sigma_{j+r}^x(t)\rangle = \langle \hat{b}_j^\dagger(t)\hat{b}_{j+r}(t)\rangle + \langle \hat{b}_j(t)\hat{b}_{j+r}(t)\rangle + \text{c.}c. \tag{4.11}$$

To evaluate this in the steady-state limit ($t \to \infty$), we first express the local real-space operators in terms of their momentum-space counterparts via the Fourier transform, $\hat{b}_j = \frac{1}{\sqrt{L}}\sum_k e^{ikj}\hat{b}_k$. By invoking translation invariance, and passing to the thermodynamic limit, the spatial correlators become continuous integrals over the Brillouin zone

$$\langle \hat{b}_j^\dagger \hat{b}_{j+r}\rangle_{\text{SS}} = \frac{1}{2\pi}\int_{-\pi}^{\pi} dk\, e^{ikr}\langle \hat{b}_k^\dagger \hat{b}_k\rangle_{\text{SS}}, \tag{4.12a}$$

$$\langle \hat{b}_j \hat{b}_{j+r}\rangle_{\text{SS}} = \frac{1}{2\pi}\int_{-\pi}^{\pi} dk\, e^{ikr}\langle \hat{b}_k \hat{b}_{-k}\rangle_{\text{SS}}. \tag{4.12b}$$

The steady-state momentum expectation values are obtained by taking the noise average of the asymptotic solution in Eq. (4.8). Using the Markovian noise condition, these spatial correlations take the form

$$\langle \sigma_j^x\sigma_{j+r}^x\rangle_{\text{SS}} = \frac{1}{2\pi}\int_{-\pi}^{\pi} dk\ \cos(kr)\ \frac{\eta_k\ (\eta_k - \epsilon_k)}{(\frac{\Gamma}{2})^2 + \xi_k^2} + \frac{1}{2\pi}\int_{-\pi}^{\pi} dk\ \sin(kr)\ \frac{\eta_k\ (\frac{\Gamma}{2})}{(\frac{\Gamma}{2})^2 + \xi_k^2}. \tag{4.13}$$

This integral can be evaluated by analytically continuing the momentum k into the complex plane via the substitution $z = e^{ik}$. This maps the integration path onto the unit circle, transforming the correlation function into a contour integral. In the case of the nearest-neighbor TFIM considered in Chapter 7, this takes the form

$$\langle \sigma_j^x\sigma_{j+r}^x\rangle_{\text{SS}} = \frac{1}{4\pi i}\oint_{|z|=1} dz \frac{(z+z^{-1})(z^r+z^{-r})}{z^2 - \left[\frac{\Gamma^2+16h^2}{16h}\right] z + 1}. \tag{4.14}$$

The integrand in the expression above has two non-trivial poles, $Z_\pm$, which are the roots of the quadratic denominator $D(z) = z^2 - 2\mathcal{A}z + 1$ with $\mathcal{A} = (\Gamma^2 + 16h^2)/32h$. These poles take the form

$$Z_\pm = \mathcal{A} \pm \sqrt{\mathcal{A}^2 - 1}. \tag{4.15}$$

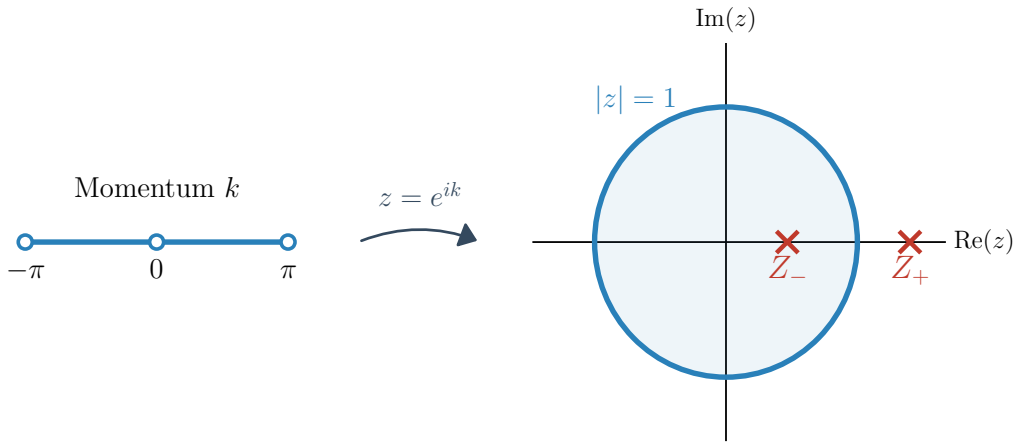

Figure 4.1 Schematic representation of the analytical continuation of momentum modes to the complex unit disk. The correlation length of the nonequilibrium steady state is dictated by the pole Z_- that lies strictly within $|z| \leq 1$.

Because these roots are reciprocal ($Z_+Z_- = 1$), it follows that $|Z_-| \leq 1 \leq |Z_+|$. According to Cauchy's residue theorem, only the pole Z_- lying strictly within the unit disk contributes to the contour integral, as Z_+ resides outside the boundary. The resulting correlation length ξ, which dictates the exponential spatial decay of the nonequilibrium steady state, is then elegantly given by $\xi = -1/\log|Z_-|$ [162]. This result in discussed later in Fig. 7.3.

4.2 Third Quantization

The third quantization approach provides an algebraic structure to solve the Lindblad equation directly in the Schrödinger (Liouville) picture. This method extends the concept of vectorization into a fully-fledged canonical quantization over operator spaces [158, 159]. Recall from Section 3.2.2 that vectorization maps the density matrix $\hat{\rho}$ to a state vector $|\hat{\rho}\rangle\rangle$. In third quantization, the left- and right-multiplication by the real-space bosonic operators $\hat{b}_j$ and $\hat{b}_j^\dagger$ are replaced by left- and right-action maps

$$\hat{b}_j\hat{\rho} \to |\hat{b}_j\hat{\rho}\rangle\rangle = \hat{b}_j^L|\hat{\rho}\rangle\rangle, \tag{4.16a}$$

$$\hat{\rho}\hat{b}_j \to |\hat{\rho}\hat{b}_j\rangle\rangle = \hat{b}_j^R|\hat{\rho}\rangle\rangle. \tag{4.16b}$$

While one could attempt to construct a Liouville-Fock space directly using these left- and right-action maps, it is more instructive to introduce a change of basis—a transformation from the pure

left/right action maps to a set of ‘‘unprimed’’ ($\hat{\beta}$) and ‘‘primed’’ ($\hat{\beta}'$) operators. For a given spatial site j, these are defined as

$$\begin{aligned} \hat{\beta}_{0,j} &= \hat{b}_j^L, \quad \hat{\beta}_{1,j} = \hat{b}_j^{\dagger R}, \\ \hat{\beta}'_{0,j} &= \hat{b}_j^{\dagger L} - \hat{b}_j^{\dagger R}, \quad \hat{\beta}'_{1,j} = \hat{b}_j^R - \hat{b}_j^L. \end{aligned} \tag{4.17}$$

This specific linear combination achieves two critical mathematical objectives for solving open quantum systems:

First, the primed maps $\hat{\beta}'$ are explicitly constructed as the exact difference between left and right actions. Taking the trace of such operators inherently vanishes. Consequently, these primed maps strictly left-annihilate the trace identity state: $\langle\langle\hat{\mathbb{I}}|\hat{\beta}'_{\nu,j} = 0$. By ensuring that the corresponding Liouvillian is written such that the primed operators appear on the left in each term, the trace-preserving nature of the Lindblad flow is manifestly hardcoded into the algebra.

Second, this transformation ensures that the new maps satisfy an essential algebraic structure

$$[\hat{\beta}_{\nu,j}, \hat{\beta}'_{\mu,k}] = \delta_{\nu,\mu}\delta_{j,k}, \quad [\hat{\beta}_{\nu,j}, \hat{\beta}_{\mu,k}] = [\hat{\beta}'_{\nu,j}, \hat{\beta}'_{\mu,k}] = 0 \tag{4.18}$$

These are referred to as ‘‘almost-canonical commutation relations’’ (almost-CCR). The ‘‘almost’’ reflects the fact that $\hat{\beta}'$ is not the strict Hermitian conjugate of $\hat{\beta}$. This mathematical structure accommodates the non-unitary, dissipative nature of the dynamics, while simultaneously preserving the bosonic commutation algebra.

To represent the full Liouvillian, we collect the complete set of $4L$ maps for all physical sites $j \in \{1, \ldots, L\}$ into a single multiparticle vector

$$\underline{\hat{\beta}} = (\underline{\hat{\beta}}_0, \underline{\hat{\beta}}_1, \underline{\hat{\beta}}'_0, \underline{\hat{\beta}}'_1)^T, \tag{4.19}$$

where each component is itself an L-dimensional vector (e.g., $\underline{\hat{\beta}}_0 = (\hat{\beta}_{0,1}, \hat{\beta}_{0,2}, \ldots, \hat{\beta}_{0,L})$). By packaging the operators in this way, the vectorized Liouvillian $\hat{\mathbb{L}}$ takes a non-Hermitian quadratic form in Liouville space

$$\hat{\mathbb{L}} = \underline{\hat{\beta}} \cdot S\underline{\hat{\beta}} - S_0\hat{\mathbb{I}}, \tag{4.20}$$

where S is a complex symmetric matrix. The matrix S dictates the entirety of the open system dynamics and is partitioned into two fundamental sub-blocks, X and Y

$$S = \begin{pmatrix} 0 & -X \\ -X^T & Y \end{pmatrix}. \tag{4.21}$$

The sub-matrix X functions as the deterministic drift matrix. It governs the dynamical coupling between the primed and unprimed maps, thereby fully determining the spectrum of the open system. In Eq. (4.20) , $S_0 = \mathrm{Tr}\, X$ is a scalar arising from map reordering (notice that Eq. (4.20) allows for $\beta\beta'$ as well as $\beta'\beta$ terms).

The matrix X is constructed from the complete coherent Hamiltonian—including both the particle-conserving interactions and the anomalous pairing terms—alongside the incoherent decay/pump rates. Assuming X is diagonalizable, its eigenvalues are the complex rapidities of the open system, dictating the relaxation timescales and coherent oscillations[1]. Conversely, the symmetric sub-matrix $Y = Y^T$ isolates the terms that are strictly quadratic in the primed maps ($\underline{\hat{\beta}}' \cdot Y \underline{\hat{\beta}}'$), representing pair creation in the Liouville space.

By performing a symplectic transformation that diagonalizes S, the Liouvillian is mapped into a normal form of decoupled master-modes

$$\hat{\mathbb{L}} = -2 \sum_{\mu} \beta_\mu \hat{\eta}'_\mu \hat{\eta}_\mu, \tag{4.22}$$

where β_μ are the rapidities, and $\hat{\eta}_\mu, \hat{\eta}'_\mu$ are the normal master-mode superoperators. The unique nonequilibrium steady state (NESS) corresponds to the ‘‘vacuum’’ state of these master-mode superoperators, meaning it is annihilated by all $\hat{\eta}_\mu$ (i.e., $\hat{\eta}_\mu |\mathrm{NESS}\rangle\rangle = 0$).

Because the Liouvillian is strictly quadratic, the resulting NESS is a Gaussian state [168]. A defining feature of Gaussian states is that they are entirely characterized by their two-point correlation functions, which are compactly encoded in the covariance matrix Z. The equation of motion

[1] While the matrix structure in Eq. (4.21) is somewhat reminiscent of a Keldysh action, the mapping is not strictly one-to-one in this formulation. Importantly, the top-left block in S is zero. This makes the physical Lindbladian traceless, which guarantees the conservation of the total probability, similar to the zero cc block in a Keldysh action. For an approach that aligns third quantization with Keldysh field theory language, see Ref. [167].

for the covariance matrix is given by [169]

$$\dot{Z}(t) = -X^T Z(t) - Z(t)X + Y. \tag{4.23}$$

To determine this matrix analytically in the steady state, one does not need to perform time-evolution integration. Instead, Z is obtained as the unique exact solution to the continuous algebraic Lyapunov equation [170] (also known as the Sylvester equation) defined by the Liouvillian sub-blocks

$$X^T Z + ZX = Y. \tag{4.24}$$

Solving this algebraic equation yields Z, which encapsulates all steady-state two-point correlation functions of the system. Specifically, for a lattice of L bosonic modes, Z is structured as a $2L \times 2L$ block matrix

$$Z = \begin{pmatrix} \langle \underline{\hat{b}} \otimes \underline{\hat{b}} \rangle & \langle : \underline{\hat{b}} \otimes \underline{\hat{b}}^\dagger : \rangle \\ \langle \underline{\hat{b}}^\dagger \otimes \underline{\hat{b}} \rangle & \langle \underline{\hat{b}}^\dagger \otimes \underline{\hat{b}}^\dagger \rangle \end{pmatrix}, \tag{4.25}$$

where $\langle : \hat{O} : \rangle$ is the expectation value of the normal-ordered operator, and $\underline{\hat{b}} = (\hat{b}_1, \hat{b}_2, ..., \hat{b}_L)^T$. Once Z is known, any higher-order physical observables and correlations can be immediately extracted using Wick's theorem. This offers a highly efficient algebraic alternative to the Heisenberg-Langevin formalism, directly targeting the asymptotic correlations through linear algebra rather than integrating noise over time. This approach has also been extended beyond quadratic models with computation costs polynomial in the system size in certain cases [169].

4.3 Keldysh Nonequilibrium Path Integral

To move beyond operator equations, the Keldysh formalism maps the Lindblad master equation directly onto a continuous field theory [68, 171]. By constructing a functional path integral over a closed-time contour, this approach naturally yields the nonequilibrium response functions and steady-state correlations. It serves as an indispensable framework when transitioning from exactly solvable quadratic models to those with many-body interactions where diagrammatic expansion becomes necessary.

4.3.1 Historical Background and the Closed-Time Contour

Standard equilibrium path integrals are typically defined on a linear time contour from $t_0 \to -\infty$ (the Feynman contour) [172, 173] or on an imaginary-time Matsubara axis [174, 175]. The zero-temperature Feynman approach relies fundamentally on the Gell-Mann and Low theorem [176]. In this standard S-matrix formulation, it is assumed that if an interaction is adiabatically turned on from the infinite past and turned off in the infinite future, a system prepared in the free vacuum state $|\Psi_0\rangle$ at $t = -\infty$ will adiabatically return to $|\Psi_0\rangle$ at $t = +\infty$, up to a global phase factor.

This adiabatic assumption is the mathematical bedrock of equilibrium field theory. It allows time-ordered expectation values to be evaluated via a single, linear time contour by projecting the future state onto the known past state

$$\langle\Omega|\,\{\hat{O}(t)\}\,|\Omega\rangle = \frac{\langle\Psi_0|\,\hat{U}(+\infty,t)\hat{O}(t)\hat{U}(t,-\infty)\,|\Psi_0\rangle}{\langle\Psi_0|\,\hat{U}(+\infty,-\infty)\,|\Psi_0\rangle}, \tag{4.26}$$

where the denominator—the vacuum-to-vacuum transition amplitude—elegantly cancels out disconnected vacuum diagrams.

However, for a system driven continuously out of equilibrium, this adiabatic projection completely fails. The system exchanges energy and entropy with its environment, evolving into a highly excited or mixed nonequilibrium steady state rather than returning to a known vacuum [171]. Because the asymptotic future state is unknown, the vacuum-to-vacuum denominator is undefined, rendering the linear Feynman contour inadequate. To calculate observables without relying on an asymptotic future state, one must return to the fundamental definition of the expectation value of an operator $\hat{O}$ at time t

$$\langle\hat{O}(t)\rangle = \mathrm{Tr}\big[\hat{\rho}(t)\hat{O}\big] = \mathrm{Tr}\big[\hat{U}(t,t_0)\hat{\rho}(t_0)\hat{U}^\dagger(t,t_0)\hat{O}\big]. \tag{4.27}$$

Translating this algebraic trace into a functional path integral geometrically dictates the structure of the time contour [68]. The forward time-evolution operator $\hat{U}(t,t_0)$ generates a path integral along a forward-time branch C_+. Conversely, the Hermitian conjugate operator $\hat{U}^\dagger(t,t_0)$, representing the evolution of the dual bra state, generates a path along a backward-time branch C_-. Because the trace operation circularly connects the left and right sides of the density matrix, the two time

branches must connect at the time t (or at $t \to +\infty$ if taken to the steady-state). This rigorously forces the integration over a closed ''Schwinger-Keldysh'' contour [177–179].

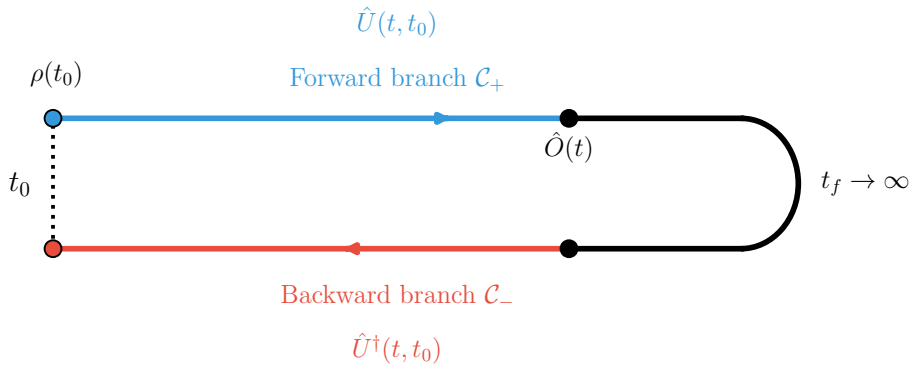

Figure 4.2 The Schwinger-Keldysh closed-time contour. The calculation of an expectation value $\langle \hat{O}(t) \rangle$ requires evolving the initial state forward from t_0 via $\hat{U}(t, t_0)$ along the upper branch C_+, and backward via $\hat{U}^\dagger(t, t_0)$ along the lower branch C_-. The trace operation connects the two branches, effectively closing the contour and circumventing the need to project onto an unknown asymptotic future state.

When mapping the Lindblad master equation onto this contour, the coherent Hamiltonian dynamics natively map to the independent forward and backward branches, while the dissipative jump operators act as explicit interaction vertices that couple C_+ and C_-. This geometric doubling of the branches is the exact continuous field-theoretic analog to the doubling of the Hilbert space into Liouville space discussed in Section 3.2.2.

4.3.2 Path Integral Construction and the Keldysh Rotation

To transition from the operator formalism to a continuous field theory, the time-evolution operators along the closed contour are discretized, and complete sets of coherent states are inserted at each infinitesimal time step [68, 171, 180]. For our specific bosonic model in Eqs. (4.2) and (4.3), this standard path-integral construction replaces the quantum operators $\hat{b}_k$ and $\hat{b}_k^\dagger$ acting on the forward branch C_+ with complex commuting fields $\phi_{+,k}(t)$ and $\bar{\phi}_{+,k}(t)$. Because the density matrix evolves bilaterally, the operators acting on the backward branch C_- map to an independent set of fields $\phi_{-,k}(t)$ and $\bar{\phi}_{-,k}(t)$. To account for the anomalous pairing terms in the TFIM, we group these fields into a Nambu vector $\Psi_{\pm,k} = (\phi_{\pm,k}, \bar{\phi}_{\pm,-k})^T$. While the theory can be formulated entirely in

this branch-indexed basis, doing so obscures the underlying causality structure. To explicitly reveal the physical content of the theory, it is standard practice to perform a Keldysh rotation'' to the classical (Ψ^c) and quantum (Ψ^q) components of the fields

$$\Psi_k^c = \frac{\Psi_{+,k} + \Psi_{-,k}}{\sqrt{2}}, \quad \Psi_k^q = \frac{\Psi_{+,k} - \Psi_{-,k}}{\sqrt{2}}. \tag{4.28}$$

The classical'' field Ψ_k^c represents the average, observable trajectory of the field and can often be interpreted as an order-parameter, while the ''quantum'' field Ψ_k^q isolates the quantum fluctuations and the stochastic noise induced by the environment.

For our quadratic spin-wave limit of the TFIM, the effective Keldysh action S in frequency-momentum space takes a highly structured matrix form

$$S = \int \frac{d\omega}{2\pi} \sum_k \begin{pmatrix} \bar{\Psi}_k^c & \bar{\Psi}_k^q \end{pmatrix}_\omega \begin{pmatrix} 0 & [G^{-1}]_k^{\mathrm{A}}(\omega) \\ [G^{-1}]_k^{\mathrm{R}}(\omega) & [G^{-1}]_k^{\mathrm{K}}(\omega) \end{pmatrix} \begin{pmatrix} \Psi_k^c \\ \Psi_k^q \end{pmatrix}_\omega . \tag{4.29}$$

The strict zero in the top-left entry of this inverse Green's function matrix is a direct mathematical consequence of probability conservation ($\mathrm{Tr}[\hat{\rho}(t)] = 1$). In the functional integral, this normalization requires that the partition function $Z = 1$ unconditionally. Consequently, if one considers the theoretical classical limit where quantum fluctuations and environmental noise are artificially suppressed—meaning the forward and backward histories are identical ($\phi_+ = \phi_-$) and the quantum fields vanish ($\phi^q = 0, \bar{\phi}^q = 0$)—the action itself must vanish: $S[\phi^c, 0] = 0$. This constraint physically mandates the absence of any pure $\bar{\Psi}^c\Psi^c$ term, thereby enforcing the structural zero. Inverting this action matrix yields the propagator matrix $\hat{G}$, which houses the three fundamental Green's functions characterizing the nonequilibrium dynamics

$$G = \begin{pmatrix} 0 & [G^{-1}]^{\mathrm{A}} \\ [G^{-1}]^{\mathrm{R}} & [G^{-1}]^{\mathrm{K}} \end{pmatrix}^{-1} = \begin{pmatrix} G^{\mathrm{K}} & G^{\mathrm{R}} \\ G^{\mathrm{A}} & 0 \end{pmatrix}. \tag{4.30}$$

Notice that the structural zero flips to the bottom-right corner upon inversion, meaning $G^{qq} = \langle \Psi^q \bar{\Psi}^q \rangle = 0$. This vanishing correlator is the strict mathematical manifestation of causality. It implies that purely quantum fluctuations cannot act as physical driving forces to causally source themselves; any quantum fluctuation must couple to the observable classical field to propagate and

physically affect the future state of the system. The properties of the remaining non-zero propagators are rigorously defined as follows:

- **The Retarded and Advanced Green's Functions ($G^{\mathbf{R}}, G^{\mathbf{A}}$):** Given by the off-diagonal elements G^{cq} and G^{qc}, these encode the spectrum and the causal response of the system. For a Markovian open quantum system, $[G^{\mathrm{R}}(\omega)]^{-1}$ is determined by both the coherent Hamiltonian and the dissipative decay rates, corresponding directly to the dynamic drift matrix $\mathcal{M}$ evaluated in the Heisenberg-Langevin equations of motion. The Advanced component is simply its Hermitian conjugate, $G^{\mathrm{A}} = [G^{\mathrm{R}}]^{\dagger}$.

- **The Keldysh Green's Function ($G^{\mathbf{K}}$):** Located in the cc-sector, $G^{\mathrm{K}} = \langle \phi^c \bar{\phi}^c \rangle$ encodes the occupation numbers, statistical fluctuations, and spatial correlations of the nonequilibrium steady state. It is an anti-Hermitian matrix governed by the local noise kernel $[G^{-1}]^{\mathrm{K}}$, which physically encapsulates the environmental noise injected by the Lindblad jump operators. For the case of a quadartic driven-dissipative systems, $[G^{-1}]^{\mathrm{K}}$ is mathematically equivalent to the covariance of the stochastic Langevin input noise vector in the Heisenberg-Langevin formalism.

The explicit functional relationship between these components is given by the Keldysh equation, a fundamental identity derived directly from the block-matrix inversion

$$G^{\mathrm{K}}_k(\omega) = -G^{\mathrm{R}}_k(\omega)[G^{-1}]^{\mathrm{K}}_k(\omega)G^{\mathrm{A}}_k(\omega). \tag{4.31}$$

The application of the Keldysh formalism to the spin-wave limit of the driven-dissipative TFIM was developed in Ref. [181]. Evaluating the steady-state using the Keldysh, Heisenberg-Langevin, and third quantization methods yields perfectly overlapping predictions. This exact agreement serves as a robust validation of the various approaches—stochastic, algebraic, and field-theoretic—demonstrating their underlying mathematical equivalence in the quadratic regime. While these frameworks provide a powerful baseline, the full many-body solution of the driven-dissipative Ising model is significantly more complex. A complete, exact treatment will be explored extensively in Chapters 7 and 8.

CHAPTER 5

NUMERICAL METHODS FOR OPEN QUANTUM SYSTEMS

While the analytical frameworks established in Chapter 4 can solve quadratic models, they are fundamentally limited to the non-interacting regime. In the presence of strong -body interactions, the Gaussian approximation often fails to capture the intricate correlations in the steady state (more discussion on this in Section 7.5). Solving these more complex scenarios requires advanced numerical approaches.

The primary obstacle in the numerical treatment of quantum -body systems is the exponential growth of the Hilbert space. For a system of L spins ($S = 1/2$), the dimension of the Hilbert space $\mathcal{H}$ scales as $N = 2^L$. In the context of open quantum systems, this complexity is squared; the density matrix $\hat{\rho}$ resides in the Liouville space $\mathcal{H} \otimes \mathcal{H}^*$ with dimension 4^L. This ‘‘curse of dimensionality’’ renders the exact numerical solution of the Lindblad master equation impossible even for moderately sized systems [182].

This chapter reviews the numerical techniques employed to bypass or mitigate this scaling, ranging from exact treatments of small clusters to tensor network methods. We begin with an overview of exact diagonalization (ED) and move toward quantum trajectories and matrix product states (MPS), detailing the specific algorithms used to extract nonequilibrium steady states.

5.1 Exact Diagonalization

Exact diagonalization provides a fundamentally unbiased numerical approach for solving the Lindblad equation. Unlike approximate methods, ED treats the full N^2-dimensional Liouville space without truncation, providing an unbiased window into the steady-state and dynamical properties of the system.

5.1.1 Spectral Properties of the Liouvillian

The power of ED lies in its ability to resolve the full spectral information of the Liouvillian superoperator $\hat{\mathcal{L}}$. After vectorization (see Section 3.2.2), the master equation becomes a linear algebraic problem: $\hat{\mathbb{L}}|\hat{\rho}\rangle\rangle = \beta|\hat{\rho}\rangle\rangle$. The complex eigenvalues β_μ are constrained by the requirement that the dynamical map be completely positive and trace-preserving (CPTP) [149]. Consequently,

all eigenvalues must satisfy $\mathrm{Re}(\beta_\mu) \leq 0$ [37, 148]. The spectrum typically follows a structured hierarchy:

- **The Steady State ($\beta_0 = 0$):** Every physical Liouvillian possesses at least one eigenvalue at the origin, corresponding to the nonequilibrium steady state (NESS), $|\hat{\rho}_{ss}\rangle\rangle$.
- **The Dissipative Gap (Δ):** Defined as $\Delta = \min_{\mu\neq 0} |\mathrm{Re}(\beta_\mu)|$, this gap determines the asymptotic relaxation timescale of the system, $\tau \sim 1/\Delta$. In the vicinity of a dissipative phase transition, this gap vanishes in the thermodynamic limit, $\Delta \to 0$ as $L \to \infty$ [65, 67].
- **Coherent Oscillations:** The imaginary parts $\mathrm{Im}(\beta_\mu)$ correspond to the characteristic frequencies of coherent oscillations during the relaxation process.

5.1.2 Symmetry Sector Decomposition

The primary bottleneck of ED is the 4^L scaling of the Liouvillian matrix. To mitigate this, one must exploit the physical symmetries of the Hamiltonian and the jump operators. If a symmetry operator $\hat{P}$ commutes with the Liouvillian ($[\hat{\mathcal{L}}, \hat{P}] = 0$), the Liouville space can be decomposed into independent symmetry sectors. For the driven-dissipative transverse-field Ising model (TFIM) discussed in Chapters 3 and 7, the $\mathbb{Z}_2$ parity symmetry ($P = \prod \sigma_i^z$) is preserved even under local σ^- dissipation. By working within a specific parity sector, the matrix dimension can be reduced by a factor of 4 (as the vectorization doubles the symmetry constraints), allowing for slightly larger L to be reached before memory exhaustion [183].

5.1.3 Iterative Solvers and Steady-State Extraction

Because the Liouvillian is typically a very sparse but non-Hermitian matrix, solving for the steady state does not require full diagonalization of the $4^L \times 4^L$ matrix. Instead, one utilizes iterative Krylov subspace methods, such as the Arnoldi algorithm or the Lanczos method for non-Hermitian matrices. These algorithms find the ''extremal'' eigenvalues—specifically the one closest to zero—by repeatedly applying $\hat{\mathbb{L}}$ to a trial vector. This reduces the computational complexity from $O((4^L)^3)$ for full diagonalization to $O(k \cdot (4^L)^2)$ for finding k eigenvalues. In practice, stan-

dard libraries, such as ‘‘the Quantum Toolbox in Python’’ (QuTiP) [155, 156] implement these algorithms, utilizing the ARPACK library [184] to efficiently target the eigenstates.

Despite these numerical optimizations, ED is strictly limited by the ‘‘memory wall.’’ For a system of $L = 10$ spins, the Liouvillian contains $4^{10} \approx 10^6$ rows and columns. A full double-precision complex matrix of this size requires approximately 16 TB of RAM just for storage. In reality, most Liouvillians are sparse matrices. On standard high-performance computing clusters, memory exhaustion typically occurs at $L \approx 12$ spins for a full density matrix treatment. Consequently, ED is most useful as a high-precision benchmark for small-scale clusters or for extracting the short-range physics that informs the more scalable methods discussed later in this chapter.

5.1.4 Time Evolution and Dynamical Integration

While exact diagonalization yields the full spectrum of the Liouvillian, utilizing the complete set of eigenvectors to compute the time evolution of the density matrix, $|\hat{\rho}(t)\rangle\rangle = \sum c_\mu e^{\beta_\mu t} |r_\mu\rangle\rangle$, is generally inefficient due to the $O((4^L)^3)$ scaling of matrix diagonalization.

Instead, when tracking the transient dynamics of the open system, the vectorized master equation is treated as a system of coupled ordinary differential equations (ODEs). The state vector is numerically propagated forward in time using standard ODE integration algorithms, such as Runge-Kutta or Adams-BDF methods [185]. In QuTiP, this is executed via the `mesolve` module [155, 156].

Because these integration routines rely purely on sparse matrix-vector multiplication at each time step, they scale as $O((4^L)^2)$, making them significantly faster than full diagonalization. However, because this approach still requires the storage of the full untruncated Liouville state vector in memory, it remains subject to the same memory wall as the steady-state solvers. In the literature, this exact state-vector integration is often colloquially grouped under the umbrella of ‘‘ED methods’’ to distinguish it from truncation-based approximations like tensor networks.

5.2 Quantum Trajectories and Stochastic Unravelling

To circumvent the crippling 4^L memory scaling of the full Liouville space, an alternative approach abandons the deterministic evolution of the density matrix in favor of the stochastic evolution

of individual pure states. This formalism, commonly known as the ‘‘quantum-trajectories’’ method or the Monte Carlo wave function (MCWF) approach, ‘‘unravels’’ the Lindblad master equation into an ensemble of stochastic state-vector trajectories [186–189]. Each trajectory $|\psi(t)\rangle$ represents a single, completely pure history of the quantum system conditioned on a specific sequence of discrete environmental measurements (quantum jumps) and the ‘‘null measurements’’ between them. Rather than simple unitary evolution, these null measurements correspond to the wave function evolving continuously and deterministically under an effective non-Hermitian Hamiltonian, defined as

$$\hat{H}_{\text{eff}} = \hat{H} - \frac{i}{2}\sum_{k} \hat{L}_k^{\dagger}\hat{L}_k. \tag{5.1}$$

Because $\hat{H}_{\text{eff}}$ is non-Hermitian, the norm of the state vector decays over time. The squared norm of this evolving state yields the exact probability that no quantum jump has occurred up to that point. When a jump $\hat{L}_k$ does stochastically occur, the state is abruptly projected and re-normalized. Because each individual trajectory resides entirely within the standard Hilbert space $\mathcal{H}$, the memory requirement drops exponentially from $O(4^L)$ back down to $O(2^L)$. The exact deterministic dynamics of the Lindblad master equation are recovered by performing an ensemble average over N_{traj} independent stochastic realizations

$$\hat{\rho}(t) = \lim_{N_{\text{traj}}\to\infty} \frac{1}{N_{\text{traj}}} \sum_{i=1}^{N_{\text{traj}}} |\psi_i(t)\rangle\langle\psi_i(t)|. \tag{5.2}$$

In numerical implementations, one never reconstructs the full density matrix $\hat{\rho}(t)$ using the equation above, as storing that dense $2^L \times 2^L$ matrix would immediately reintroduce the memory wall we sought to avoid. Instead, the expectation value of any physical observable $\hat{O}$ is computed ‘‘on the fly’’ as the statistical mean of the expectation values from the individual trajectories

$$\langle\hat{O}(t)\rangle = \frac{1}{N_{\text{traj}}} \sum_{i=1}^{N_{\text{traj}}} \langle\psi_i(t)|\hat{O}|\psi_i(t)\rangle. \tag{5.3}$$

By tracking only the state vectors and accumulating the scalar expectation values, the memory footprint remains strictly bounded at $O(2^L)$ throughout the entire simulation.

While substituting a deterministic matrix equation with a stochastic sampling process introduces a statistical standard error that scales as $1/\sqrt{N_{\text{traj}}}$, the trade-off is highly advantageous. The individual trajectories are completely uncorrelated, making the MCWF method an ‘‘embarrassingly parallel’’ algorithmic problem. The insurmountable memory bottleneck of exact diagonalization is thus successfully traded for a highly scalable CPU workload that can be distributed across modern high-performance computing clusters. With this scalable stochastic framework established, in Chapter 6 we will utilize the MCWF algorithm to benchmark and isolate the physical noise channels within state-of-the-art trapped-ion quantum simulators.

5.3 Matrix Product States

As demonstrated in the previous sections, both ED and MCWF eventually hit a hard computational wall due to the exponential growth of the Hilbert space. To push simulations of 1D chains beyond $L \approx 20$, a fundamental paradigm shift is required in how the quantum state is represented.

5.3.1 Area Law Entanglement and the MPS Ansatz

The full generic state of an L-site lattice of spin-1/2 particles may written as a superposition of all 2^L basis states

$$|\psi\rangle = \sum_{i_1,i_2,\ldots,i_L \in \{0,1\}} c_{i_1 i_2 \ldots i_L} |i_1 i_2 \ldots i_L\rangle. \tag{5.4}$$

Storing the rank-L tensor $c_{i_1 i_2 \ldots i_L}$ is what leads to the $O(2^L)$ memory scaling. However, physical quantum states—particularly ground states of local Hamiltonians and the steady states of typical dissipative systems—do not occupy this entire Hilbert space randomly. Instead, they occupy a minuscule, highly structured corner characterized by the *area law of entanglement* [190]. For 1D systems, the area law implies that the entanglement entropy between a subregion and the rest of the system is bounded by a constant, independent of the subregion’s size.

Matrix product states (MPS) exploit this physical restriction by decomposing the rank-L tensor into a sequential product of rank-3 local tensors [191]

$$c_{i_1 i_2 \ldots i_L} = \sum_{\alpha_1,\ldots,\alpha_{L-1}} A^{i_1}_{\alpha_1} A^{i_2}_{\alpha_1 \alpha_2} \ldots A^{i_L}_{\alpha_{L-1}}. \tag{5.5}$$

(a) Full generic state tensor: $O(d^L)$ parameters

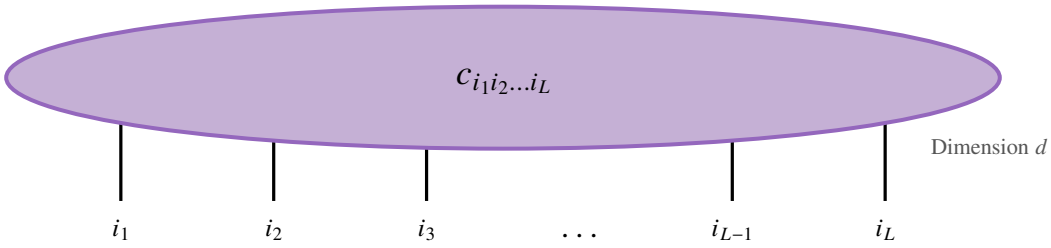

(b) Matrix product state (MPS): $O(L \cdot d \cdot \chi^2)$ parameters

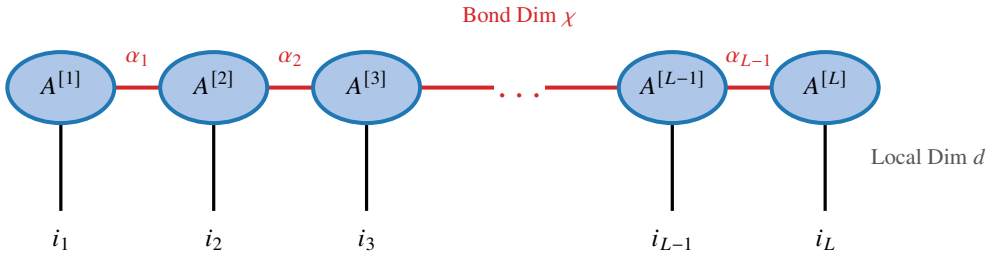

Figure 5.1 Illustration of matrix product states (MPS) decomposition. (a) The full generic state $|\psi\rangle$ is represented by a single rank-L coefficient tensor $c_{i_1 i_2 \ldots i_L}$, containing d^L coefficients which leads to an exponential scaling with system size L. (b) The MPS ansatz parameterizes the same state as a chain of local rank-3 tensors ($A^{[n]}$). Physical indices (i_n) descend with local dimension d, while neighboring tensors are connected by virtual (bond) indices (α_n) truncated to a maximum bond dimension χ. This reduces the parameter complexity to $O(L \cdot d \cdot \chi^2)$.

Here, i_n represents the physical dimension index of site n (with local dimension $d = 2$ for spins), while α_n are the internal, auxiliary (virtual)indices that connect neighboring tensors. The dimension of these virtual indices is truncated to a maximum value known as the *bond dimension*, χ. The bond dimension acts as a dial controlling the maximum amount of entanglement the state can represent. By truncating to a finite χ, the parameter space is drastically reduced from 2^L to $O(Ld\chi^2)$. For gapped 1D systems where entanglement is bounded, a modest χ provides an arbitrarily precise, numerically exact representation of the physical state. For a pedagogical introduction to the topic, see Ref. [192]

5.3.2 Density Matrix Renormalization Group (DMRG)

While originally formulated by Steven R. White in 1992 as a renormalization group procedure [193], the density matrix renormalization group (DMRG) is now understood fundamentally as a variational optimization over the MPS manifold [191]. The objective of DMRG is to find the MPS $|\psi\rangle$ that minimizes the energy functional $E = \frac{\langle\psi|\hat{H}|\psi\rangle}{\langle\psi|\psi\rangle}$ (or, for Liouvillians, the state that minimizes the eigenvalue magnitude). Rather than optimizing the entire network simultaneously, DMRG proceeds via a ''sweeping'' algorithm. In the standard two-site DMRG algorithm, two neighboring local tensors A^{i_n} and $A^{i_{n+1}}$ are merged into a single two-site tensor, denoted as Θ. The surrounding lattice is contracted, forming an ''effective environment.'' The algorithm then solves a local eigenvalue problem within this reduced, tractable subspace.

By treating the effective environment as a fixed background, the global optimization reduces to finding the optimal Θ that minimizes the energy locally. This is achieved by solving the effective eigenvalue equation, yielding a new two-site tensor that corresponds to the lowest eigenvalue. This optimized Θ completely replaces the previous configuration of the two sites.

Once the optimal Θ is found, it must be split back into two separate rank-3 tensors to restore the standard MPS structure and allow the algorithm to sweep to the next site. This splitting is accomplished using a singular value decomposition (SVD)

$$\Theta^{i_n i_{n+1}}_{\alpha_{n-1}\alpha_{n+1}} = \sum_{\alpha_n=1}^{d\chi^2} U^{i_n}_{\alpha_{n-1}\alpha_n} S_{\alpha_n\alpha_n} V^{i_{n+1}}_{\alpha_n\alpha_{n+1}}. \tag{5.6}$$

The singular values $S_{\alpha_n\alpha_n}$ directly relate to the bipartite entanglement spectrum. To maintain computational efficiency, the SVD is truncated by retaining only the χ largest singular values. The tensors U and V become the new updated A tensors, and the algorithm shifts one site to the right (or left). This seamlessly truncates the least entangled components of the state, ensuring the computational cost remains polynomial while maximizing fidelity. By sweeping back and forth across the 1D chain, the algorithm variationally converges to the true physical state.

In order to deploy this powerful algorithm for the open quantum systems studied in this thesis, a fundamental adaptation is required. Solving the Lindblad master equation often requires mapping

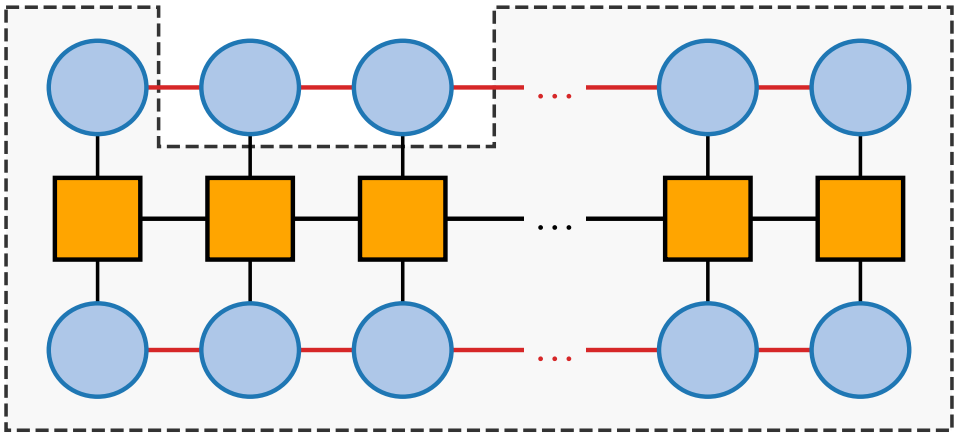

Figure 5.2 Effective environment for the two-site DMRG algorithm. The tensor network representation of the expectation value $\langle\psi|\hat{H}|\psi\rangle$. To perform a variational update on the local tensors at sites 2 and 3, the rest of the network is contracted together. The dashed boundary encloses this ‘‘effective environment,’’ which consists of the Hamiltonian MPO (orange squares), the ket MPS tensors (bottom blue circles), and the fixed bra MPS tensors (top blue circles) at all other sites. By treating this contracted environment as a constant tensor background, the global energy minimization simplifies into a tractable local eigenvalue problem for the active sites.

the density matrix onto a pure state via vectorization as discussed in Section 3.2.2. By reshaping the density matrix into a state vector $|\rho\rangle\rangle$, the system is promoted to a doubled Hilbert space (Liouville space), on which the Liouvillian superoperator $\mathbb{L}$ acts linearly. In this vectorized space, the nonequilibrium steady state is defined as the right eigenvector of the Liouvillian with a zero eigenvalue ($\hat{\mathbb{L}}|\rho_{\text{ss}}\rangle\rangle = 0$) [194]. Because the Liouvillian $\hat{\mathbb{L}}$ is non-Hermitian, standard energy-minimization DMRG cannot be applied natively. This can be resolved by using the $\hat{\mathbb{L}}^\dagger\hat{\mathbb{L}}$ operator method [195]. Constructing the squared operator $\hat{\mathbb{L}}^\dagger\hat{\mathbb{L}}$, results in a strictly Hermitian, positive semi-definite matrix. Effectively, the unique ground state of this squared operator (with an eigenvalue of exactly zero) corresponds to the physical steady state. This procedure maps the search for a nonequilibrium steady state into a standard ground-state DMRG optimization over an MPS ansatz. We utilize this powerful framework extensively to extract the nonequilibrium steady-state properties in Chapters 7 and 8.

5.4 Summary and Outlook

In this chapter, we have established a hierarchical numerical toolkit for the simulation of open -body quantum systems. While exact diagonalization (ED) provides unbiased spectral information at small system sizes, its exponential scaling necessitates more scalable approaches. By utilizing the Monte Carlo wave function (MCWF) algorithm, we successfully modeled decoherence in experimental trapped-ion simulators. However, in order to accommodate larger systems, we introduced matrix product states (MPS) as a polynomial-scaling representation of 1D quantum states and detailed the optimization of steady states via the density matrix renormalization group (DMRG).

With this numerical framework established, the remainder of this thesis pivots from methodology to physical application. In the following chapters, we deploy these algorithms, along with analytical methods, to investigate the dynamics and the steady-states properties of driven-dissipative spin systems.

CHAPTER 6

NOISE MODELING FOR A TRAPPED ION QUANTUM SIMULATOR: A CASE STUDY

The objective of modern quantum simulation platforms, such as trapped-ion chains, is to use a controllable quantum system to simulate many-body Hamiltonians that are otherwise classically intractable. The specific experiment, detailed in our recent publication in *Nature Communications* [196], utilizes a quantum simulator with single-spin resolution to investigate critical fluctuations after a quantum quench. The system consists of up to 50 $^{171}\mathrm{Yb}^{+}$ ions confined in a 3-layer linear Paul trap [197].

The quantum trajectories method provides a highly practical approach for modeling sources of dissipation in these setups at experimentally relevant system sizes. In trapped-ion chains, the dominant source of error typically stems from stray magnetic field fluctuations. In addition, implementing long-range Ising interactions often requires lowering the axial confinement of the trap [198], which makes the ions increasingly susceptible to background collisions and electric field noise [55]. Additional sources of decoherence include mode frequency drifts, spontaneous emission, and off-resonant motional excitations that generate residual spin-motion entanglement [199, 200].

The target dynamics of the simulator are governed by the long-range transverse-field Ising model (TFIM) Hamiltonian

$$\hat{H} = -\sum_{i<j}^{L} J_{ij}\sigma_i^x\sigma_j^x + B^z\sum_{i}^{L}\sigma_i^z, \tag{6.1}$$

where $\sigma_i^{x,y,z}$ are the Pauli matrices, B^z is the global transverse magnetic field, and J_{ij} represents the interaction strength. This interaction follows an approximate power-law decay, $J_{ij} \sim J/|i-j|^p$, with $p \approx 0.89$ [196].

To quantify the critical fluctuations during this evolution, the experiment measures the total spin $\hat{S}_x = \sum_i^L \sigma_i^x/2$ projected along the direction of interaction. The dynamics are then characterized by calculating the net correlator, defined as the variance of the total spin

$$\langle\hat{C}_x^2\rangle = \langle\hat{S}_x^2\rangle - \langle\hat{S}_x\rangle^2. \tag{6.2}$$

Because the initial state $|\downarrow\rangle^{\otimes L}$ and the Ising symmetry of the Hamiltonian keep the average mag-

netization $\langle \hat{S}_x \rangle$ at zero, this net correlator isolates the true critical fluctuations while removing any bias from imperfect single-qubit rotations in the experiment.

In reality, however, the simulator is an open quantum system subject to the decoherence channels mentioned above, which drive it away from ideal unitary evolution. To the lowest order, the cumulative effect of these environmental noises is phenomenologically modeled as an effective bit-flip error. The density matrix evolution is thus described by a Lindblad master equation incorporating uniform local σ^x jump operators

$$\frac{\mathrm{d}\hat{\rho}}{\mathrm{d}t} = -i[\hat{H}, \hat{\rho}] + \kappa \sum_{i=1}^{L} (\sigma_i^x \hat{\rho} \sigma_i^x - \hat{\rho}), \tag{6.3}$$

where $\hat{H}$ is the long-range Hamiltonian from Eq. (6.1) and κ represents the uniform single bit-flip rate across the spin chain.

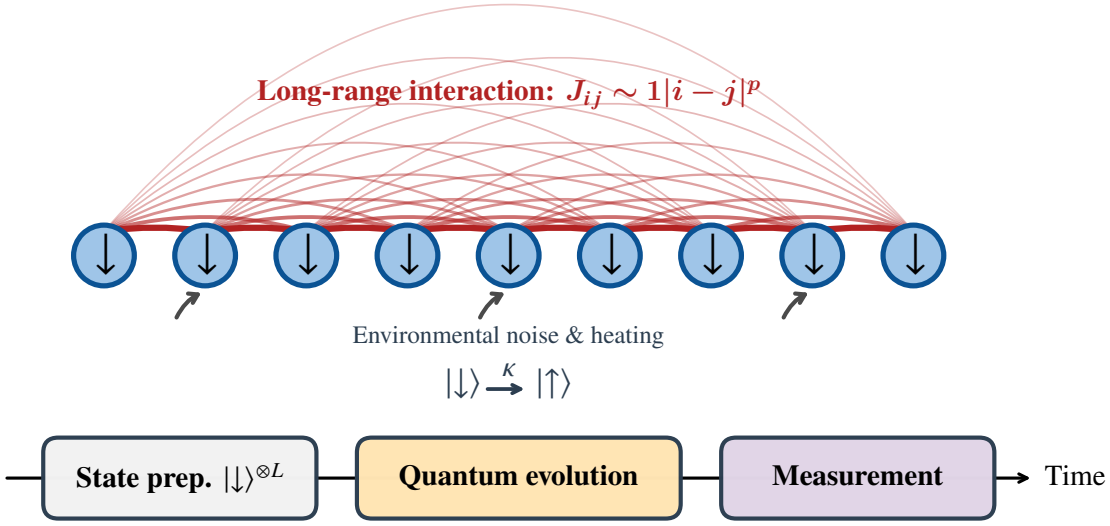

Figure 6.1 Trapped-ion quantum simulator and quench protocol: (Top) A linear chain of ions initialized in the $|\downarrow\rangle_z$ state. The curved red lines illustrate the coherent long-range transverse-field Ising interactions (J_{ij}). The accompanying bit-flips ($|\downarrow\rangle \xrightarrow{\sigma^x} |\uparrow\rangle$) denote the continuous action of environmental noise and motional heating during the system's evolution, modeled via the jump rate κ. (Bottom) The experimental timeline, depicting the sudden quench to the target Hamiltonian $\hat{H}$, followed by a projective measurement of the net correlator.

6.1 Diagnostic Optimization of Noise Channels

To advance beyond the computational limits of exact diagonalization and model the damped critical fluctuations of a chain of $L \geq 15$ ions, we employed the MCWF method. This allows us to bypass the extreme scaling of the full Liouvillian. Importantly, we utilize this algorithm as a diagnostic tool for isolating the dominant sources of experimental error. In our analysis, we numerically optimized the bit-flip rate κ in order to minimize the root-mean-square error (RMSE) between the trajectory simulation and the experimental measurements.

To confirm that bit-flip errors are the primary driver of decoherence, alternative noise models must be systematically ruled out. Investigating additional local σ^z dephasing channels (Γ) reveals that optimizing the dynamics under this extended equation returns an optimal value of $\Gamma \approx 0$ for most values of the transverse field B^z, suggesting that bit-flip errors are sufficient to capture the dissipative dynamics. Furthermore, modeling errors as static disorder in the interaction strength (J) by randomly scaling the J_{ij} matrix fails to reproduce the physical damping observed in the experiment, indicating that static disorder cannot explain the decay in oscillations. The dynamics under optimal κ and Γ are shown in Fig. 6.2 for $L = 10$. All parameters are normalized with respect to the Kac factor $\mathcal{J} = \frac{1}{L-1}\sum_{i,j} J_{ij}$ [201]. Incorporating only the optimized local bit-flip rate $\kappa(B^z)$ successfully matches the experimental data. As shown in Fig. 6.3, the optimized error rate results in the simulation accurately capturing both the observed damping rates and the frequencies of the underdamped coherent oscillations across the parameter space [196].

As a demonstration of scaling beyond the ED limit, we run the dynamics for the $L = 15$ system using the MCWF method averaged over 1000 independent trajectories [186, 187] in Fig. 6.4. This stochastic simulation successfully extracts the net correlator dynamics, $\langle \hat{C}_x^2 \rangle$. For a quench specifically to the critical point $B^z/\mathcal{J} = 1$ on the 15-spin chain, the optimum value of the bit-flip rate is found to be $\kappa/\mathcal{J} = 0.024$. This value is notably smaller than the optimized rate for $L = 10$ ($\kappa/\mathcal{J} = 0.082$), reflecting the variation in effective noise as the trap parameters are adjusted for different chain lengths. This trajectory-based approach can, in principle, be used to simulate even larger system sizes. However, optimizing the decoherence rate κ to fit the experimental data re-

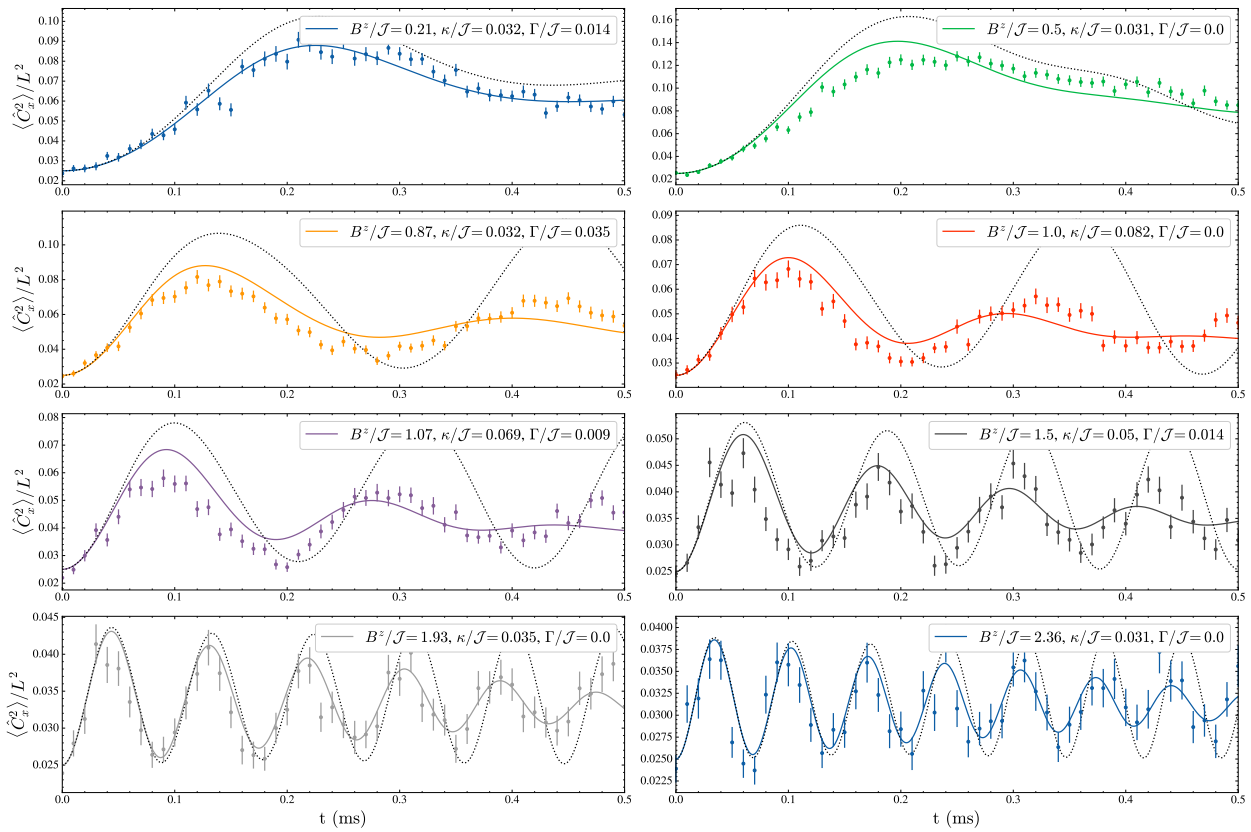

Figure 6.2 Evaluation of possible dissipation channels for $L = 10$. Exact Diagonalization (ED) of the Lindblad master equation incorporating both local σ^x and σ^z dephasing rates. The black dotted lines indicate the net correlator evaluated under unitary dynamics alone. The numerical optimization consistently returns $\Gamma \approx 0$ for the vast majority of the parameter space, confirming that the σ^x bit-flip channel alone is sufficient to reproduce the experimentally observed damping of the net correlator.

quires executing a large number of these simulations across a large parameter space. The necessary trajectories ensemble averaging, combined with the parameter search, severely limits our practical ability to scale to systems much larger than $L = 15$ in this case.

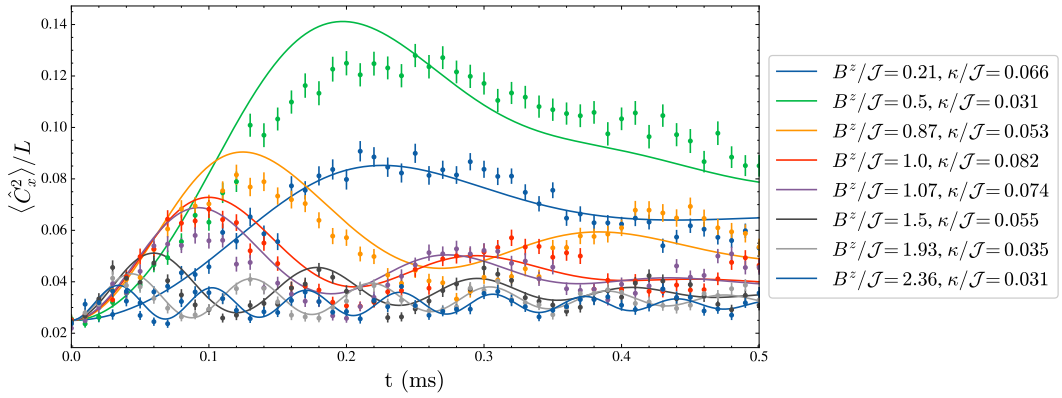

Figure 6.3 Net correlator dynamics across varying transverse fields for $L = 10$. Evolution of the experimental net correlator following a single quench, compared against exact numerical simulations of the dissipative dynamics. Different colors represent the evolution at different values of $B^z/\mathcal{J}$. The simulations strictly utilize the local σ^x noise channel, with the bit-flip rate κ optimized for each corresponding B^z value to minimize the simulation's root-mean-square error. The σ^x model successfully captures the damped amplitude.

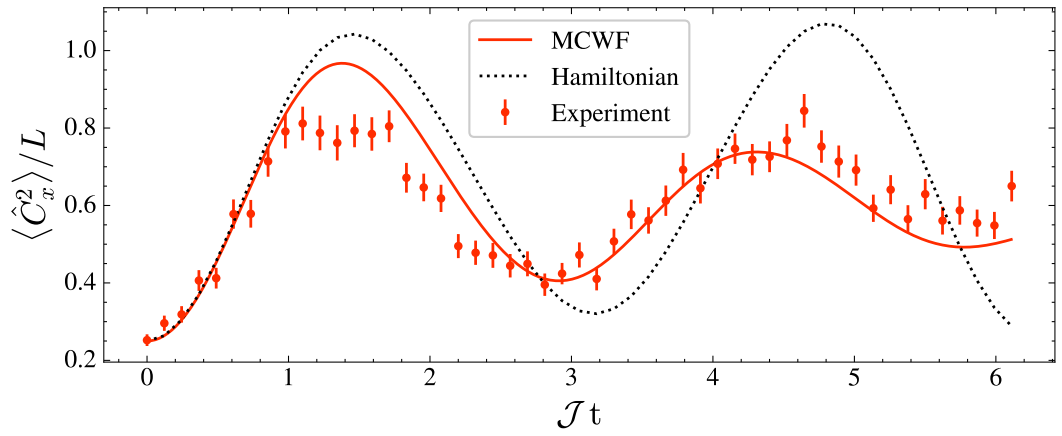

Figure 6.4 Net correlator dynamics for $L = 15$ ions. Evolution of the experimental net correlator following a single quench to the dynamical critical point $B^z/\mathcal{J} = 1$. The solid colored line represents the numerical simulation at the finite bit-flip rate $\kappa = 0.024$, obtained by averaging over 1000 quantum trajectories using the Monte Carlo wave function method. This is compared to the ideal, decoherence-free Hamiltonian dynamics shown in the dotted black line.

CHAPTER 7

ANALYTICAL SOLUTION OF THE DRIVEN-DISSIPATIVE ISING MODEL: PERTURBATIVE APPROACH AT WEAK DISSIPATION

The study of open driven quantum systems has established a exciting frontier for exploring the physics of nonequilibrium many-body systems, offering phenomena and phases of matter fundamentally distinct from their equilibrium counterparts [49, 52]. Experimentally, this paradigm is vigorously pursued across a diverse array of highly controllable quantum simulation platforms. These include, but are not limited to, exciton-polariton condensates in semiconductor microcavities [64, 202–206], trapped ions [207, 208], neutral atoms in optical tweezers and Rydberg gases [209–213], superconducting circuit quantum electrodynamics arrays [58, 60, 214], and can be efficiently realized in programmable quantum simulators [215–219]. In these systems, coherent Hamiltonian dynamics compete continuously with incoherent driving and environmental dissipation, steering the system toward a nonequilibrium steady state (NESS) rather than a thermal equilibrium state.

A central question in this domain is the fate of quantum correlations in the presence of dissipation. Generic Markovian dissipation is expected to induce decoherence and mixing, thereby washing out the delicate quantum correlations and entanglement that underlie ground-state quantum phase transitions [67, 69–71, 152]. While analytical solutions and exactly solvable models of open quantum systems have been developed [220–227], quantum spin systems subject to dissipation generally lack analytical solutions. In general, identifying the dynamics of quantum simulators subject to noise and decoherence remains a major conceptual and methodological challenge.

This chapter, detailing the central findings of our recent publication in *Physical Review Letters* [162], provides an exact analytical approach to the paradigmatic quantum Ising chain. In a perfectly isolated, dissipation-free setting, the transverse-field Ising model (TFIM) undergoes a famous continuous quantum phase transition at a critical field strength h_c, characterized by a diverging ground-state correlation length. We further consider spins subject to local dissipation in the form of spontaneous emission. In general, the steady state of this driven-dissipative model is mixed and disordered, not featuring a phase transition or a true divergence of the correlation length.

However, we demonstrate that the steady-state correlation length develops a pronounced peak near the ground state quantum critical point.

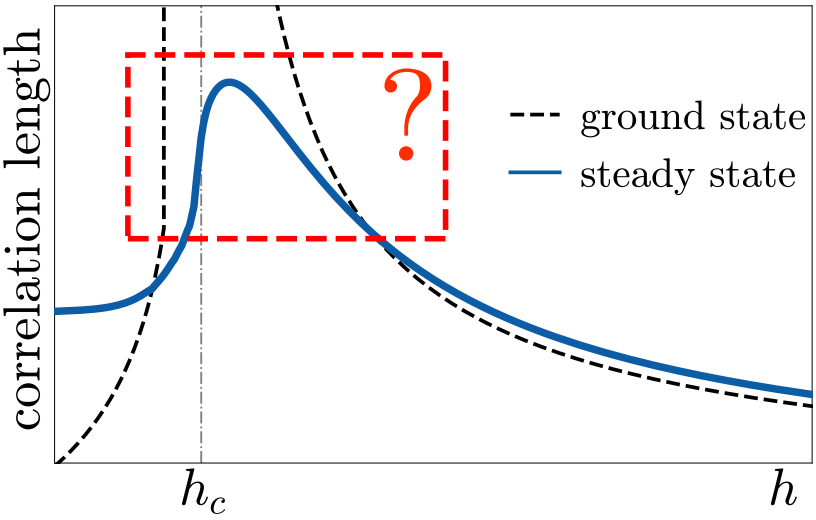

Figure 7.1 Schematic presentation of the correlation length in the steady state of a driven-dissipative Ising chain as a function of a tuning parameter h (e.g., an external field), compared to that of the ground state. While being very distinct, the steady state still features a peak close to the ground-state quantum critical point h_c. An analytical approach is lacking in the regime highlighted by the question mark.

To establish this result, we must overcome significant analytical hurdles. Standard approximation techniques, such as conventional spin-wave theory (discussed in Chapter 4) [161] or naive mappings to free-fermions, fail in the strongly correlated regime near the critical point [162]. This failure originates from the highly nonlinear, non-local string operators generated when local dissipative jump operators are mapped to the fermionic basis via the Jordan-Wigner transformation. To circumvent these limitations, we develop a versatile analytical framework that becomes asymptotically exact in the limit of weak dissipation ($\Gamma \to 0$ but at finite Γt). Inspired by the treatment of dissipative Bose gases [228], our approach relies on the construction of a generalized Gibbs ensemble (GGE). This formalism systematically accounts for the underlying free-fermion integrability of the coherent Hamiltonian dynamics while treating the dissipative Liouvillian superoperator perturbatively [228–239].

Through this GGE formalism, we gain a comprehensive and exact understanding of how signatures of quantum criticality are inherited by the NESS. Furthermore, we reveal that this phenomenon

exhibits a degree of *universality* which we further discuss in Chapter 8.

7.1 Model and Physical Realization

The effective Hamiltonian for the driven-dissipative Ising model is given by

$$\hat{H} = \sum_{i=1}^{L} -\sigma_i^x \sigma_{i+1}^x + h\sigma_i^z. \tag{7.1}$$

This time-independent form is derived by transforming a continuously driven system into a rotating frame and applying the rotating wave approximation (RWA). To explicitly demonstrate this, we derive the model starting from a driven Bose-Hubbard array [161, 240]. Such models naturally emerge in experiment [241–245].

Consider an array of coupled optical cavities, each possessing a strongly nonlinear medium. Photons can hop between adjacent cavities with an amplitude J, and the cavities are coherently driven by a two-photon pump field oscillating at frequency ω_p. The dynamics in the laboratory frame are governed by the Hamiltonian $\hat{H}_{\text{lab}} = \hat{H}_0 + \hat{H}_{\text{drive}}$, where

$$\hat{H}_0 = \sum_j \omega_c \hat{a}_j^\dagger \hat{a}_j - J \sum_j \left(\hat{a}_j^\dagger \hat{a}_{j+1} + \text{h.c.} \right) + \frac{U}{2} \sum_j \hat{a}_j^\dagger \hat{a}_j^\dagger \hat{a}_j \hat{a}_j, \tag{7.2}$$

and two-photon drive, which creates pairs of photons in adjacent sites, takes the form

$$\hat{H}_{\text{drive}} = \Omega \sum_j \left(\hat{a}_j^\dagger \hat{a}_{j+1}^\dagger e^{-i\omega_p t} + \text{h.c.} \right). \tag{7.3}$$

Here, $\hat{a}_j$ annihilates a photon at site j, ω_c is the bare cavity resonance, U is the onsite interaction strength, and Ω is the pump amplitude.

To remove the explicit time-dependence, we transform the system into a frame rotating at half the pump frequency, $\omega_p/2$, via the unitary operator $\hat{U}(t) = \exp\left(-i\frac{\omega_p}{2} t \sum_j \hat{a}_j^\dagger \hat{a}_j\right)$. Under this transformation, the effective rotating-frame Hamiltonian $\hat{H}_{\text{rot}} = \hat{U}^\dagger \hat{H}_{\text{lab}} \hat{U} - i\hat{U}^\dagger \partial_t \hat{U}$ becomes

$$\hat{H}_{\text{rot}} = \sum_j \delta \hat{a}_j^\dagger \hat{a}_j - J \sum_j \left(\hat{a}_j^\dagger \hat{a}_{j+1} + \text{h.c.} \right) + \frac{U}{2} \sum_j \hat{a}_j^\dagger \hat{a}_j^\dagger \hat{a}_j \hat{a}_j + \Omega \sum_j \left(\hat{a}_j^\dagger \hat{a}_{j+1}^\dagger + \text{h.c.} \right), \tag{7.4}$$

where $\delta = \omega_c - \omega_p$ is the detuning between the cavity resonance and the two-photon pump.

Next, we assume the system operates in the *photon blockade* regime [141], which occurs when the onsite nonlinearity is extremely large ($U \to \infty$). In this limit, the energetic cost of having two

photons in the same cavity is prohibitive, restricting the local Hilbert space of each cavity to zero or one photon. We can then map the hard-core bosonic operators to Pauli spin-1/2 operators

$$\hat{a}_j \to \sigma_j^-, \quad \hat{a}_j^\dagger \to \sigma_j^+, \quad \hat{a}_j^\dagger \hat{a}_j \to \frac{\sigma_j^z + 1}{2}. \tag{7.5}$$

Substituting these Pauli operators into $\hat{H}_{\text{rot}}$ and expressing the hopping and pairing terms in terms of σ^x and σ^y, we obtain the transverse field anisotropic XY model

$$\begin{aligned} \hat{H}_{\text{rot}} &= \frac{\delta}{2} \sum_j \sigma_j^z - \sum_j \left[\frac{J - \Omega}{2} \sigma_j^x \sigma_{j+1}^x + \frac{J + \Omega}{2} \sigma_j^y \sigma_{j+1}^y \right] \\ &= -J \sum_j \left[\frac{1 + \Delta}{2} \sigma_j^x \sigma_{j+1}^x + \frac{1 - \Delta}{2} \sigma_j^y \sigma_{j+1}^y - h \sigma_j^z \right], \end{aligned} \tag{7.6}$$

where we have defined the dimensionless transverse field $h = \delta/(2J)$ and the anisotropy parameter $\Delta = -\Omega/J$.

By tuning the pump strength such that $\Omega = -J$ (meaning $\Delta = 1$), the $\sigma^y \sigma^y$ terms vanish completely, recovering the exact pure Ising interaction. Setting $J = 1$, we arrive precisely at our target Hamiltonian

$$\hat{H} = \sum_{i=1}^{L} -\sigma_i^x \sigma_{i+1}^x + h \sigma_i^z. \tag{7.7}$$

Finally, accounting for the coupling to the environment, photons continuously leak out of the cavities into the surrounding vacuum at a specific rate. Since this is a single-photon loss process, it maps directly to the spin-lowering operator in the blockade limit, defined by the Lindblad jump operator $\hat{L}_i = \sqrt{\Gamma} \sigma_i^-$. The full nonequilibrium steady state is therefore governed by the Lindblad master equation

$$\frac{\mathrm{d}\hat{\rho}}{\mathrm{d}t} = -i\big[\hat{H}, \hat{\rho}\big] + \Gamma \sum_{i=1}^{L} \left(\sigma_i^- \hat{\rho} \sigma_i^+ - \frac{1}{2} \big\{ \sigma_i^+ \sigma_i^-, \hat{\rho} \big\} \right). \tag{7.8}$$

Thus, the ‘‘drive’’ is intrinsically baked into the time-independent Hamiltonian (7.1) via the two-photon parametric pumping terms, which manifest as the spin-spin interactions in the rotating frame. This elegant mapping establishes how the abstract driven-dissipative quantum Ising model corresponds to a highly realizable experimental architecture.

7.2 Mapping Hamiltonian to Free Fermions

Before addressing the full driven-dissipative dynamics, it is instructive to establish the exact solution of the isolated transverse-field Ising chain. The Hamiltonian governing the coherent evolution of the system is given by Eq. (7.7), where $h > 0$ represents the transverse magnetic field. Note that for convenience in the subsequent derivations, we have applied a global π rotation around the x-axis ($\sigma^{y,z} \to -\sigma^{y,z}$), which flips the sign of the transverse field term relative to standard conventions, and takes $\sigma_i^{\pm} \to \sigma_i^{\mp}$. The exact solution relies on mapping the interacting spin chain to a system of non-interacting fermions. This mapping is achieved via the Jordan-Wigner (JW) transformation [98, 246], which expresses the local Pauli operators in terms of spinless fermionic annihilation ($\hat{c}_i$) and creation ($\hat{c}_i^\dagger$) operators

$$\sigma_i^- = \prod_{l=1}^{i-1}(1 - 2\hat{c}_l^\dagger \hat{c}_l)\hat{c}_i^\dagger, \quad \sigma_i^+ = (\sigma_i^-)^\dagger, \quad \sigma_i^z = 1 - 2\hat{c}_i^\dagger \hat{c}_i. \tag{7.9}$$

Applying this transformation to the Hamiltonian, the bulk interaction terms map straightforwardly to local fermionic hopping and pairing terms [82, 247]. However, the periodic boundary conditions enforced in the spin basis ($\sigma_{L+1}^{x,y,z} = \sigma_1^{x,y,z}$) introduce a crucial subtlety. The boundary coupling term $\sigma_L^x \sigma_1^x$ generates a non-local string operator that spans the entire chain, $e^{i\pi\hat{N}}$, where $\hat{N} = \sum_{i=1}^{L} \hat{c}_i^\dagger \hat{c}_i$ is the total fermion number operator.

$$\hat{H} = -\sum_{i=1}^{L-1}(\hat{c}_i^\dagger - \hat{c}_i)(\hat{c}_{i+1} + \hat{c}_{i+1}^\dagger) - h\sum_{i=1}^{L}(\hat{c}_i\hat{c}_i^\dagger - \hat{c}_i^\dagger\hat{c}_i) - e^{i\pi\hat{N}}(\hat{c}_L - \hat{c}_L^\dagger)(\hat{c}_1 + \hat{c}_1^\dagger), \tag{7.10}$$

Consequently, the sign of the boundary term is explicitly determined by the total fermionic parity [247]. The Hamiltonian naturally block-diagonalizes into even and odd parity sectors, $\hat{H} = \hat{H}_\mathrm{e} \oplus \hat{H}_\mathrm{o}$, corresponding to an even or odd number of fermionic excitations. Because the Hamiltonian is parity-conserving, these two sectors are strictly independent under purely unitary dynamics. Within each sector, the Hamiltonian takes the quadratic form

$$\hat{H}_{\mathrm{e/o}} = -\sum_{i=1}^{L}(\hat{c}_i^\dagger - \hat{c}_i)(\hat{c}_{i+1} + \hat{c}_{i+1}^\dagger) - h\sum_{i=1}^{L}(\hat{c}_i\hat{c}_i^\dagger - \hat{c}_i^\dagger\hat{c}_i), \tag{7.11}$$

subject to the parity-dependent boundary conditions

$$\hat{c}_{L+1} = \mp\hat{c}_1. \tag{7.12}$$

Thus, the even sector obeys antiperiodic boundary conditions, while the odd sector obeys periodic boundary conditions. This mandates that the allowed momentum modes, k, be quantized differently in each sector. Applying a spatial Fourier transform, the allowed momenta are given by $k \in \frac{2\pi}{L}(\mathbb{Z}_L + \frac{1}{2}) \equiv \mathbb{Z}_{\text{ap}}$ for the even sector (antiperiodic), and $k \in \frac{2\pi}{L}\mathbb{Z}_L \equiv \mathbb{Z}_{\text{p}}$ for the odd sector (periodic).

Finally, the Hamiltonian in each sector can be diagonalized in momentum space by a standard Bogoliubov transformation [82, 247]. We define the Bogoliubov fermionic operators as

$$\hat{\alpha}_k = \cos\left(\frac{\theta_k}{2}\right)\hat{c}_k - i\sin\left(\frac{\theta_k}{2}\right)\hat{c}^\dagger_{-k}, \tag{7.13}$$

where the Bogoliubov angle θ_k is parameterized by $\tan\theta_k = \frac{\sin k}{h-\cos k}$. In this quasiparticle basis, the Hamiltonian takes its fully diagonal form

$$\hat{H}_{\text{e/o}} = \sum_{k\in\mathbb{Z}_{ap,p}} \epsilon_k[\hat{\alpha}^\dagger_k\hat{\alpha}_k - 1], \tag{7.14}$$

with the single-particle excitation spectrum given by $\epsilon_k = 2\sqrt{1 + h^2 - 2h\cos k}$.

This exact solution completely captures the free-fermion nature of the Hamiltonian. In the absence of dissipation, an initial state with a definite parity will remain within its respective momentum quantization sector indefinitely. As we will detail in the following sections, the local dissipative environment drastically alters this structure by explicitly breaking parity conservation, thereby coupling the distinct momentum grids of the even and odd sectors and introducing non-linear dynamics to the otherwise free fermions.

7.3 Emergence of the Generalized Gibbs Ensemble and the Weak Dissipation Limit

Although the Ising Hamiltonian is exactly solvable, a solution to the driven-dissipative model is simply not available. In order to develop an analytical solution, valid in the weak dissipation regime, $\Gamma \to 0$, it is necessary to rigorously examine the relaxation dynamics under the system Hamiltonian in the absence of dissipation. Consider an isolated, generic interacting many-body system evolving unitarily under its Hamiltonian $\hat{H}$ from a initial state $|\psi_0\rangle$. According to the eigenstate thermalization hypothesis (ETH) [130, 132, 248, 249], a system with a Hamiltonian effectively acts as its own heat bath. Consequently, in the thermodynamic limit and after a sufficiently long relaxation time,

the expectation values of any local observable $\hat{O}$ become indistinguishable from those evaluated in a thermal Gibbs ensemble (GE) [117, 132, 133, 250, 251]

$$\lim_{t\to\infty}\lim_{L\to\infty}\langle\psi(t)|\,\hat{O}\,|\psi(t)\rangle = \mathrm{Tr}\{\hat{\rho}_{\mathrm{GE}}\hat{O}\}, \tag{7.15}$$

where the standard thermal density matrix is $\hat{\rho}_{\mathrm{GE}} = Z^{-1}e^{-\beta\hat{H}}$, with the inverse temperature β fixed by the initial energy density.

However, as established in Section 7.2, the transverse-field Ising model is exactly solvable (integrable) and maps to non-interacting free fermions. An integrable model possess an extensive set of independent, mutually commuting conserved quantities. In our model, the occupation numbers of the Bogoliubov quasiparticle modes, $\hat{Q}_k = \hat{\alpha}_k^\dagger\hat{\alpha}_k$, constitute these constants of motion, satisfying $[\hat{H},\hat{Q}_k] = 0$. This extensive set of conserved quantities fundamentally violates the assumptions of ETH and precludes standard thermalization. Instead, the system undergoes *generalized thermalization*, where the long-time expectation values of local observables relax to those of a generalized Gibbs ensemble (GGE) [247, 252, 253]

$$\lim_{t\to\infty}\lim_{L\to\infty}\langle\psi(t)|\,\hat{O}\,|\psi(t)\rangle = \mathrm{Tr}\{\hat{\rho}_{\mathrm{GGE}}\hat{O}\}. \tag{7.16}$$

The GGE density matrix is constructed to maximize entropy while constraining all conserved charges, yielding $\hat{\rho}_{\mathrm{GGE}} = Z_{\mathrm{GGE}}^{-1}\exp\Big(-\sum_k \lambda_k\hat{Q}_k\Big)$. The generalized inverse temperatures (or Lagrange multipliers) λ_k are rigorously fixed by the initial state such that $\mathrm{Tr}\{\hat{\rho}_{\mathrm{GGE}}\hat{Q}_k\} = \langle\psi_0|\,\hat{Q}_k\,|\psi_0\rangle$. Furthermore, properly accounting for the independent parity sectors identified in the exact solution, the density matrix must respect the parity block-diagonal structure, decomposing into two distinct Gaussian operators associated with the two momentum quantization grids [228]

$$\hat{\rho}_{\mathrm{GGE}} = \prod_{k\in\mathbb{Z}_{\mathrm{ap}}}\hat{\rho}_k \oplus \prod_{k\in\mathbb{Z}_{\mathrm{p}}}\hat{\rho}_k. \tag{7.17}$$

We now pivot to the full driven-dissipative dynamics, where the continuous coupling to the environment is governed by the Lindblad master equation

$$\frac{\mathrm{d}\hat{\rho}}{\mathrm{d}t} = -i\big[\hat{H},\hat{\rho}\big] + \Gamma\sum_{j=1}^{L}\hat{\mathcal{D}}_j(\hat{\rho}). \tag{7.18}$$

The dissipative operators $\hat{\mathcal{D}}_j(\hat{\rho})$ are defined as

$$\hat{\mathcal{D}}_j(\hat{\rho}) = \sigma_j^- \hat{\rho} \sigma_j^+ - \frac{1}{2}\left\{\sigma_j^+ \sigma_j^-, \hat{\rho}\right\} \tag{7.19}$$

The introduction of the local dissipative jump operators—which, recalling the global π rotation from Section 7.2, take the form $\hat{L}_j = \sqrt{\Gamma}\sigma_j^+$—breaks the free-fermion integrability and explicitly violates fermionic parity conservation. Under generic conditions, this would completely destroy the GGE structure. However, we assume a strict timescale separation where the dissipation rate is significantly slower than the intrinsic relaxation rate of the Hamiltonian dynamics ($\Gamma \ll 1/\tau(\hat{H})$). Here, $\tau(\hat{H}) \sim J^{-1}$ represents the characteristic time for local observables to reach their generalized Gibbs ensemble (GGE) values under purely coherent evolution. In this regime, the rapid coherent dynamics continually project the system's density matrix back onto the GGE manifold. The dissipation therefore acts as a weak, secular perturbation that merely drives slow transitions *between* different GGE states [228, 229]. Figure 7.2 shows a schematic representation of this process.

Effectively, the Lagrange multipliers are promoted to slowly varying functions of time, $\lambda_k \to \lambda_k(t)$, meaning the density matrix retains a GGE form at any instantaneous moment. We formalize this by perturbatively expanding the density matrix in powers of the dissipation strength Γ

$$\hat{\rho}(t) = \hat{\rho}_{\mathrm{GGE}}(t) + \Gamma \hat{\rho}_1(t) + O(\Gamma^2). \tag{7.20}$$

Substituting this expansion into the master equation (7.18) and invoking $[\hat{H}, \hat{\rho}_{\mathrm{GGE}}] = 0$, we obtain

$$\frac{\mathrm{d}\hat{\rho}}{\mathrm{d}t} = -i\Gamma\left[\hat{H}, \hat{\rho}_1\right] + \Gamma \sum_{j=1}^{L} \hat{\mathcal{D}}_j(\hat{\rho}_{\mathrm{GGE}}) + O(\Gamma^2). \tag{7.21}$$

Truncating to leading order in Γ, we extract the equations of motion for the relevant physical observables—the quasi-conserved charges $Q_k(t) \equiv \mathrm{Tr}\{\hat{\rho}(t)\hat{Q}_k\}$

$$\frac{\mathrm{d}Q_k}{\mathrm{d}t} = \mathrm{Tr}\left\{\hat{Q}_k \frac{\mathrm{d}\hat{\rho}}{\mathrm{d}t}\right\} = \Gamma \sum_{j=1}^{L} \mathrm{Tr}\left\{\hat{\mathcal{D}}_j^\dagger(\hat{Q}_k)\hat{\rho}_{\mathrm{GGE}}\right\} - i\Gamma\,\mathrm{Tr}\{\hat{Q}_k\left[\hat{H}, \hat{\rho}_1\right]\}. \tag{7.22}$$

Using the cyclic property of the trace, the second term evaluates to $-i\Gamma\,\mathrm{Tr}\{\hat{\rho}_1[\hat{Q}_k, \hat{H}]\}$, which strictly vanishes because the charges commute with the Hamiltonian. Furthermore, by exploiting

the translational invariance of the Lindbladian, the sum over all lattice sites j simplifies to the contribution of a single site scaled by the total system size L. This yields the central kinetic equation that dictates the slow drift of the system through the GGE manifold [162]

$$\frac{\mathrm{d}Q_k}{\mathrm{d}t} = L\langle \hat{\mathcal{D}}_1^\dagger(\hat{Q}_k)\rangle_{\mathrm{GGE}}, \tag{7.23}$$

where $\hat{\mathcal{D}}_1^\dagger$ is the adjoint Lindblad superoperator acting on the first lattice site, explicitly defined as

$$\hat{\mathcal{D}}_1^\dagger(\hat{Q}_k) = \hat{L}_1^\dagger \hat{Q}_k \hat{L}_1 - \frac{1}{2}\left\{\hat{L}_1^\dagger \hat{L}_1, \hat{Q}_k\right\}. \tag{7.24}$$

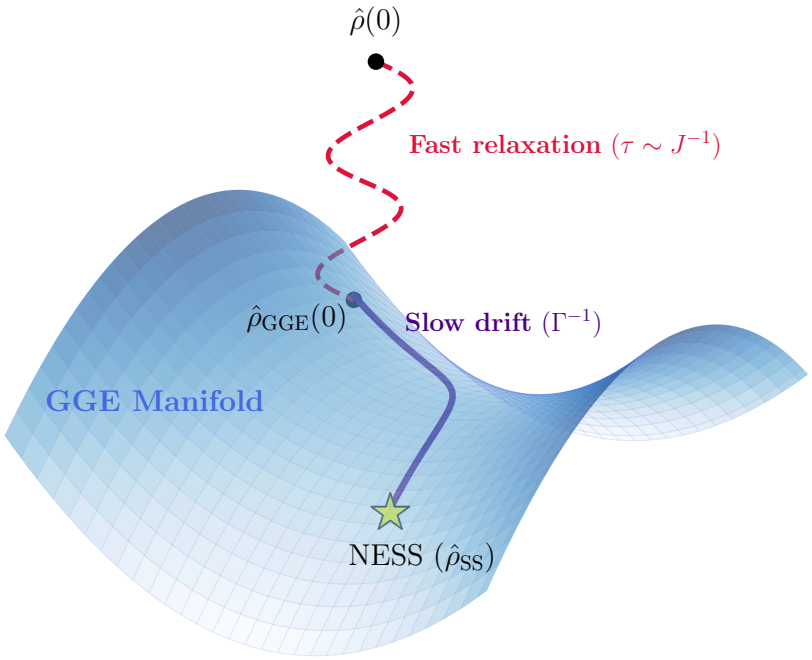

Figure 7.2 Schematic representation of the timescale separation in a weakly dissipative system with an integrable Hamiltonian. Starting from an arbitrary initial state $\hat{\rho}(0)$, fast coherent Hamiltonian dynamics ($\tau \sim J^{-1}$) quickly project the system onto the constrained (GGE) manifold, defining the initial generalized temperatures $\lambda_k(0)$. The local Markovian dissipation acts as a weak perturbation ($\Gamma \ll J$) that continuously breaks the integrability, driving a slow adiabatic drift (Γ^{-1}) strictly within the GGE manifold. The generalized temperatures become slowly varying functions of time, $\lambda_k(t)$, guiding the system to its final nonequilibrium steady state (NESS). In Eq. (7.7), we set the energy scale $J = 1$.

Crucially, the expectation value on the right-hand side of Eq. (7.23) is evaluated entirely with respect to the instantaneous, non-interacting Gaussian GGE state. This permits the application of

Wick's theorem to exactly compute the dissipative correlators, systematically bridging the microscopic integrability of the closed chain to the macroscopic driven-dissipative steady state.

7.4 Evaluating the Dissipative Dynamics

With the kinetic equation (7.23) established, our goal is to evaluate the right-hand side to obtain closed-form equations of motion for the fermionic correlators. Because the dissipator in Eq. (7.24) now acts exclusively on the first site ($j = 1$), the Jordan-Wigner string for the lowering operator simplifies entirely. The string operator $\prod_{l=1}^{i-1}(1-2\hat{c}_l^\dagger \hat{c}_l)$ evaluates to the identity for $i = 1$. Therefore, we can make the exact substitution $\hat{L}_1 = \sqrt{\Gamma}\sigma_1^+ \to \sqrt{\Gamma}\hat{c}_1$ and $\hat{L}_1^\dagger \to \sqrt{\Gamma}\hat{c}_1^\dagger$. This localized form significantly simplifies the subsequent analysis.

7.4.1 Basis Transformation

To evaluate $\langle \hat{\mathcal{D}}_1^\dagger(\hat{Q}_k)\rangle_{\mathrm{GGE}}$, we split the superoperator into two parts: the anticommutator term and the quantum jump term. Because the expectation value is taken with respect to the non-interacting, Gaussian GGE state, we can, in principle, utilize Wick's theorem to reduce four-point correlators into products of two-point correlators.

The anticommutator term, proportional to $\{\hat{c}_1^\dagger \hat{c}_1, \hat{Q}_k\}$, is straightforward to compute. The operator $\hat{c}_1^\dagger \hat{c}_1$ conserves the total number of fermions, meaning it preserves the parity of the state. Therefore, it does not mix the even and odd parity sectors, and Wick's theorem can be applied directly within a single momentum quantization grid.

In contrast, the jump term $\hat{c}_1^\dagger \hat{Q}_k \hat{c}_1$ presents a technical challenge. The operators $\hat{c}_1^\dagger$ and $\hat{c}_1$ add or remove a single fermion, thereby flipping the parity of the many-body state. As established in Section 7.2, a change in parity alters the boundary conditions (from antiperiodic to periodic, or vice versa), which in turn shifts the allowed quantization of the momentum modes. Specifically, if $\hat{Q}_k$ belongs to the antiperiodic sector ($k \in \mathbb{Z}_{\mathrm{ap}}$), the operators sandwiching it effectively project the state into the periodic sector ($p \in \mathbb{Z}_{\mathrm{p}}$).

To apply Wick's theorem to the jump term, we must therefore express the operators of one sector in terms of the operators of the opposite sector. Since both the periodic modes $\{\hat{c}_p\}$ and antiperiodic modes $\{\hat{c}_k\}$ form a complete basis for the single-particle Hilbert space on the ring, they are related

by a unitary basis transformation. We can relate the momentum eigenstates by computing their inner product

$$\langle p|k\rangle = \frac{1}{L}\sum_{j=1}^{L} e^{i(k-p)j}. \tag{7.25}$$

Recognizing this as a geometric series, we can evaluate the sum. Defining $z = e^{i(k-p)}$, the sum takes the form

$$\langle p|k\rangle = \frac{z}{L}\left[\frac{1-z^L}{1-z}\right]. \tag{7.26}$$

Crucially, because k and p belong to different parity sectors, their difference is a half-integer multiple of $2\pi/L$, ensuring that $k - p = \frac{2\pi}{L}(m + 1/2)$ for some integer m. This implies $z^L = e^{i(k-p)L} = e^{i2\pi(m+1/2)} = -1$. Substituting this back yields

$$\langle p|k\rangle = \frac{2}{L}\frac{z}{1-z} = -\frac{2}{L}\frac{1}{1-e^{-i(k-p)}}. \tag{7.27}$$

Inserting a complete set of states $|p\rangle$ from the periodic sector, we can express a state in the antiperiodic sector as $|k\rangle = \sum_{p\in\mathbb{Z}_{\mathrm{p}}} \langle p|k\rangle\,|p\rangle$. Identifying $|k\rangle = \hat{c}_k^\dagger|0\rangle$, we obtain the exact basis transformation relating the creation and annihilation operators of the two sectors [162, 234]

$$\hat{c}_k = -\frac{2}{L}\sum_{p\in\mathbb{Z}_{\mathrm{p}}} \frac{1}{1-e^{i(k-p)}}\hat{c}_p. \tag{7.28}$$

This transformation reveals that the local dissipative jump explicitly couples every momentum mode in one sector to every mode in the other. It is this non-local stringing of modes across parity sectors that introduces the fundamental non-linearities into the open-system dynamics, distinguishing the driven-dissipative steady state from a simple free-fermion model.

7.4.2 Application of Wick's Theorem and the Kinetic Equations

To explicitly evaluate the right-hand side of the kinetic equation (7.23), it is most convenient to work directly with the original fermions $\hat{c}_k, \hat{c}_k^\dagger$ rather than the Bogoliubov quasiparticles. The state of the system is fully characterized by the expectation values of the normal and anomalous momentum-space density operators, defined respectively as

$$\hat{A}_k = \frac{1}{2\pi}\mathbb{P}_k\hat{c}_k^\dagger\hat{c}_k, \qquad i\hat{B}_k = \frac{1}{2\pi}\mathbb{P}_k\hat{c}_k\hat{c}_{-k}, \tag{7.29}$$

where $\mathbb{P}_k$ enforces the projection onto the appropriate parity sector for a given momentum k. We aim to compute the corresponding scalar expectation values $A_k \equiv \langle \hat{A}_k \rangle$ and $B_k \equiv \langle \hat{B}_k \rangle$.

Because there is only a single independent conserved charge $\hat{Q}_k = \hat{\alpha}_k^\dagger \hat{\alpha}_k$ per momentum mode k, the functions A_k and B_k are not independent. The GGE ansatz constrains them together. By inverting the Bogoliubov transformation and expressing $\langle \hat{\alpha}_k^\dagger \hat{\alpha}_k \rangle$ in terms of A_k and B_k, we find that they must satisfy the algebraic constraint

$$C_k \equiv \sin k \, (A_k - 1/4\pi) - (h - \cos k) B_k = 0. \tag{7.30}$$

The full dynamics of these observables are governed by the dissipative jump operators, subject to the continuous enforcement of this constraint. We handle this analytically by introducing a Lagrange multiplier Λ_k. The coupled equations of motion are given by

$$\frac{1}{\Gamma}\frac{\mathrm{d}A_k}{\mathrm{d}t} = -F_A(k) + \Lambda_k \sin k, \tag{7.31a}$$

$$\frac{1}{\Gamma}\frac{\mathrm{d}B_k}{\mathrm{d}t} = -F_B(k) - \Lambda_k (h - \cos k), \tag{7.31b}$$

where the dissipative driving terms, $F_A(k)$ and $F_B(k)$, are derived from the explicit evaluation of the dissipator. We define these terms via the relation

$$-\frac{1}{L} F_A(k) \equiv \langle \hat{c}_1^\dagger \hat{A}_k \hat{c}_1 \rangle_{\mathrm{GGE}} - \langle \hat{c}_1^\dagger \hat{c}_1 \hat{A}_k \rangle_{\mathrm{GGE}}, \tag{7.32a}$$

$$-\frac{1}{L} F_B(k) \equiv \langle \hat{c}_1^\dagger \hat{B}_k \hat{c}_1 \rangle_{\mathrm{GGE}} - \langle \hat{c}_1^\dagger \hat{c}_1 \hat{B}_k \rangle_{\mathrm{GGE}}. \tag{7.32b}$$

We evaluate the terms on the rhs in Eq. (7.32a) and Eq. (7.32b) using Wick's theorem, exploiting the fact that the expectation values are taken with respect to the Gaussian GGE state. The second terms, stemming from the anticommutator, do not alter the fermionic parity. Substituting $\hat{c}_1 = \frac{1}{\sqrt{L}} \sum_q e^{iq} \hat{c}_q$ and applying Wick's theorem directly within the same momentum grid yields

$$\frac{L}{2\pi} \langle \hat{c}_1^\dagger \hat{c}_1 \hat{c}_k^\dagger \hat{c}_k \rangle_{\mathrm{GGE}} = nLA_k + A_k(1 - 2\pi A_k) + 2\pi B_k^2, \tag{7.33a}$$

$$\frac{L}{2\pi i} \langle \hat{c}_1^\dagger \hat{c}_1 \hat{c}_k \hat{c}_{-k} \rangle_{\mathrm{GGE}} = nLB_k + B_k(1 - 4\pi A_k), \tag{7.33b}$$

where $n = \int_{-\pi}^{\pi} dk \, A_k$ is the total fermionic density.

The first terms, representing the quantum jumps, require the basis transformation we derived in Eq. (7.28) because the operators $\hat{c}_1$ and $\hat{c}_1^\dagger$ alter the parity. Expanding $\hat{c}_k$ (and $\hat{c}_{-k}$) in the basis of the opposite parity sector and applying Wick's theorem produces a highly non-local expression involving all momentum modes in the corresponding target sector. For example, the term

$$\langle \hat{c}_1^\dagger \hat{A}_k \hat{c}_1 \rangle_{\mathrm{GGE}} = \frac{4}{L^2}\left(n \sum_\lambda \frac{2\pi A_\lambda}{|e^{ik} - e^{i\lambda}|^2} - \frac{1}{L}\left| \sum_\lambda \frac{2\pi A_\lambda}{e^{ik} - e^{i\lambda}} \right|^2 + \frac{1}{L}\left| \sum_\lambda \frac{2\pi B_\lambda}{e^{ik} - e^{i\lambda}} \right|^2 \right). \tag{7.34}$$

We then take the thermodynamic limit $L \to \infty$, converting the discrete sums over momentum grids into continuous integrals. To handle the apparent divergence when $\lambda \to k$, we isolate the singular part by adding and subtracting A_k (or B_k) in the numerator, generating a Cauchy principal value integral.

Combining the anticommutator and jump contributions, the full dissipative driving functions take the form

$$\begin{aligned} F_A(k) = A_k - 2\pi &\left(A_k^2 - \left| \frac{1}{\pi} \mathrm{P} \int d\lambda \frac{A_\lambda}{e^{ik} - e^{i\lambda}} \right|^2 \right) \\ &+ \frac{2n}{\pi} \mathrm{P} \int d\lambda \frac{A_k - A_\lambda}{|e^{ik} - e^{i\lambda}|^2} + 2\pi \left(B_k^2 - \left| \frac{1}{\pi} \mathrm{P} \int d\lambda \frac{B_\lambda}{e^{ik} - e^{i\lambda}} \right|^2 \right), \end{aligned} \tag{7.35}$$

and

$$\begin{aligned} F_B(k) = B_k - 2\pi &\left(2A_k B_k - \left[\mathrm{P} \int \frac{d\lambda}{\pi} \frac{A_\lambda}{e^{ik} - e^{i\lambda}} \mathrm{P} \int \frac{d\lambda'}{\pi} \frac{B_{\lambda'}}{e^{-ik} - e^{-i\lambda'}} + \mathrm{c.c.} \right] \right) \\ &+ \frac{2n}{\pi} \mathrm{P} \int d\lambda \frac{B_k - B_\lambda}{|e^{ik} - e^{i\lambda}|^2}, \end{aligned} \tag{7.36}$$

where P is the principal part of the integral. The resulting integro-differential equations can be written in a more suggestive and mathematically revealing form. We first observe that, by using the total fermion density $n = \int \frac{dk}{2\pi} A_k$ and the identity $\frac{1}{1-e^{i\lambda}} = \frac{1}{2}(1 + i \cot \frac{\lambda}{2})$, the absolute squared integral terms can be expanded as

$$\left| \mathrm{P} \int \frac{d\lambda}{\pi} \frac{A_\lambda}{e^{ik} - e^{i\lambda}} \right|^2 = \left(\frac{n}{2\pi} \right)^2 + \left| \mathrm{P} \int \frac{d\lambda}{2\pi} A_\lambda \cot\left(\frac{k - \lambda}{2} \right) \right|^2, \tag{7.37a}$$

$$\left| \mathrm{P} \int \frac{d\lambda}{\pi} \frac{B_\lambda}{e^{ik} - e^{i\lambda}} \right|^2 = \left| \mathrm{P} \int \frac{d\lambda}{2\pi} B_\lambda \cot\left(\frac{k - \lambda}{2} \right) \right|^2. \tag{7.37b}$$

Furthermore, the denominator in the final integral of Eq. (7.36) satisfies $|e^{ik} - e^{i\lambda}|^2 = 2(1 - \cos(k - \lambda))$. Thus, $F_A(k)$ becomes

$$F_A(k) = A_k + \frac{n^2}{2\pi} - 2\pi \left(A_k^2 - \left| \mathrm{P} \int \frac{d\lambda}{2\pi} A_\lambda \cot\left(\frac{k-\lambda}{2}\right) \right|^2 - B_k^2 + \left| \mathrm{P} \int \frac{d\lambda}{2\pi} B_\lambda \cot\left(\frac{k-\lambda}{2}\right) \right|^2 \right) + 2n\mathrm{P} \int \frac{d\lambda}{2\pi} \frac{A_k - A_\lambda}{1 - \cos(k-\lambda)}. \tag{7.38}$$

Crucially, we note the trigonometric identity $-\partial_k \cot\left(\frac{k-\lambda}{2}\right) = \frac{1}{1-\cos(k-\lambda)}$. This allows us to rewrite the last integral exactly as a Hadamard finite part, extracting the derivative with respect to momentum outside the principal value integral

$$\mathrm{P} \int \frac{d\lambda}{2\pi} \frac{A_k - A_\lambda}{1 - \cos(k-\lambda)} = \partial_k \mathrm{P} \int \frac{d\lambda}{2\pi} A_\lambda \cot\left(\frac{k-\lambda}{2}\right). \tag{7.39}$$

By defining the Hilbert transform on the unit circle as $(\mathcal{H}f)_k = \frac{1}{2\pi}\mathrm{P}\int_0^{2\pi} d\lambda\, f_\lambda \cot\left(\frac{k-\lambda}{2}\right)$, we can finally express these equations in their most compact form

$$F_A(k) = A_k + \frac{n^2}{2\pi} - 2\pi \left[A_k^2 - (\mathcal{H}A)_k^2 - B_k^2 + (\mathcal{H}B)_k^2 \right] + 2n(\mathcal{H}A)'_k, \tag{7.40a}$$

$$F_B(k) = B_k - 4\pi \left[A_k B_k - (\mathcal{H}A)_k (\mathcal{H}B)_k \right] + 2n(\mathcal{H}B)'_k, \tag{7.40b}$$

where the prime denotes the partial derivative with respect to k that arose naturally from Eq. (7.39). These non-local equations underscore the profound mixing of momentum modes generated by local Markovian dissipation.

7.4.3 Analytic Continuation to the Complex Plane

The integro-differential equations governing the dissipative driving terms, $F_A(k)$ and $F_B(k)$, exhibit a high degree of non-locality due to the principal value integrals (or equivalently, the Hilbert transforms). Recognizing that the momentum k defines a unit circle via e^{ik}, we can dramatically simplify the problem by analytically continuing our real distribution functions into the interior of the unit disk in the complex plane ($|z| \leq 1$).

We define the complex function $\mathcal{G}_A(z)$, corresponding to the normal momentum density A_k, via the Cauchy-like integral

$$\mathcal{G}_A(z) = \int_0^{2\pi} \frac{dk}{2\pi} A_k \frac{e^{ik} + z}{e^{ik} - z}. \tag{7.41}$$

By construction, $\mathcal{G}_A(z)$ is strictly analytic within the unit disk ($|z| < 1$). When we evaluate this function as we approach the boundary of the unit disk from the inside ($z \to e^{ik-0^+}$), the real part precisely recovers the physical momentum distribution

$$\mathrm{Re}\,\mathcal{G}_A(e^{ik-0^+}) = A_k. \tag{7.42}$$

Simultaneously, the imaginary part yields exactly the Hilbert transform that appeared in our evaluation of the dissipator. This establishes a fundamental Kramers-Kronig relation for the momentum density function

$$\mathrm{Im}\,\mathcal{G}_A(e^{ik-0^+}) = \mathrm{P}\int_0^{2\pi}\frac{d\lambda}{2\pi}A_\lambda \cot\left(\frac{k-\lambda}{2}\right) = (\mathcal{H}A)_k. \tag{7.43}$$

An entirely analogous analytic function, $\mathcal{G}_B(z)$, is defined corresponding to the anomalous correlator B_k.

With these powerful analytic properties established, we can map the non-local terms present in Eq. (7.40) directly to local operations on these complex functions. For instance, the combinations of squares in $F_A(k)$ naturally form the real part of the squared analytic function

$$A_k^2 - (\mathcal{H}A)_k^2 = \mathrm{Re}\left[\mathcal{G}_A(z = e^{ik-0^+})^2\right]. \tag{7.44}$$

Similarly, the Hadamard finite part, which we explicitly isolated as the derivative of the Hilbert transform, is elegantly recognized as the real part of a complex derivative weighted by z

$$\partial_k(\mathcal{H}A)_k = \mathrm{Re}\,\left[z\partial_z\mathcal{G}_A(z)\right]_{z=e^{ik-0^+}}. \tag{7.45}$$

By elevating the entire set of equations of motion Eq. (7.31) into the complex plane, we replace the coupled, non-local real equations with a set of local complex differential equations

$$\frac{1}{\Gamma}\frac{\mathrm{d}}{\mathrm{d}t}\mathcal{G}_A(t,z) = -\left[\mathcal{G}_A + \frac{n^2}{2\pi} - 2\pi\mathcal{G}_A^2 + 2\pi\mathcal{G}_B^2 + 2nz\partial_z\mathcal{G}_A\right] + \mathcal{G}_{\Lambda_1}(z), \tag{7.46a}$$

$$\frac{1}{\Gamma}\frac{\mathrm{d}}{\mathrm{d}t}\mathcal{G}_B(t,z) = -\left[\mathcal{G}_B - 4\pi\mathcal{G}_A\mathcal{G}_B + 2nz\partial_z\mathcal{G}_B\right] + \mathcal{G}_{\Lambda_2}(z). \tag{7.46b}$$

Here, the Lagrange multiplier term Λ_k has also been promoted to analytic functions corresponding to the physical constraints, specifically $\Lambda_1(k) = \Lambda_k \sin k$ and $\Lambda_2(k) = -\Lambda_k(h - \cos k)$.

To further decouple these dynamics, we introduce the linear combinations

$$\mathcal{G}_{\pm}(z) = \mathcal{G}_A(z) \mp i\mathcal{G}_B(z). \tag{7.47}$$

Combining the two equations in Eq. (7.46), we find a more symmetric form

$$\frac{1}{\Gamma}\frac{\mathrm{d}}{\mathrm{d}t}\mathcal{G}_{\pm}(t,z) = -\left[\mathcal{G}_{\pm} + \frac{n^2}{2\pi} - 2\pi\mathcal{G}_{\pm}^2 + 2nz\partial_z\mathcal{G}_{\pm}\right] \pm ih\mathcal{G}_{\Lambda}(z) \mp i\mathcal{G}_{\Lambda_{\pm}}(z), \tag{7.48}$$

where we have defined $\Lambda_{\pm}(k) \equiv e^{\pm ik}\Lambda_k$. Apart from the constraints enforced by the Lagrange multipliers, the equations for $\mathcal{G}_+$ and $\mathcal{G}_-$ are now decoupled.

We can systematically relate the multiplier functions explicitly using the parity properties of Λ_k. Since Λ_k is an odd function of k (while A_k is even and B_k is odd), we can show that $\mathcal{G}_{\Lambda_{\pm}}(z) = i\lambda_1 + z^{\pm 1}\mathcal{G}_{\Lambda}(z)$, where we define the integral over the multiplier as $\lambda_1 = \int dk\, \Lambda_k \sin k$.

This identification allows us to extract the decay rate of the total fermion density. Expanding Eq. (7.48) to the zeroth order in powers of z (i.e., evaluating the limits as $z \to 0$) yields the exact kinetic relation for the total density n

$$\dot{n} = -n + \lambda_1. \tag{7.49}$$

Substituting this relation back into the equations of motion allows us to absorb λ_1. This algebraic structure immediately motivates a convenient shift of variables for the complex functions

$$\mathcal{G}_{\pm} \to \mathcal{G}_{\pm} \pm \frac{n}{2\pi}. \tag{7.50}$$

Under this translation, the boundary terms and constants precisely cancel, and the final, simplified equations of motion in the complex plane take their ultimate form

$$\frac{1}{\Gamma}\frac{\mathrm{d}}{\mathrm{d}t}\mathcal{G}_{\pm} = -\left[\mathcal{G}_{\pm} \mp 2n\mathcal{G}_{\pm} - 2\pi\mathcal{G}_{\pm}^2 + 2nz\partial_z\mathcal{G}_{\pm}\right] \pm i(h - z^{\pm 1})\mathcal{G}_{\Lambda}(z). \tag{7.51}$$

7.4.4 Multipole Expansion and Numerical Solution

The representation in Eq. (7.51) provides a robust framework for obtaining the exact steady state and transient dynamics. Because A_k is an even function and B_k is an odd function of k, they can be expanded as standard Fourier series

$$A_k = \sum_{n=0}^{\infty} A_n \cos(nk), \qquad B_k = \sum_{n=1}^{\infty} B_n \sin(nk), \tag{7.52}$$

where the coefficients are given by the integrals $A_n = c_n \int_0^{2\pi} \frac{dk}{\pi} \cos(nk) A_k$ (with $c_0 = 1/2$ and $c_{n\geq 1} = 1$) and $B_n = \int_0^{2\pi} \frac{dk}{\pi} \sin(nk) B_k$.

In the complex plane, this corresponds exactly to a multipole (or Taylor) expansion of the analytic functions around $z = 0$

$$\mathcal{G}_A(z) = \sum_{n=0}^{\infty} A_n z^n, \qquad \mathcal{G}_B(z) = -i \sum_{n=1}^{\infty} B_n z^n. \tag{7.53}$$

The shifted functions $\mathcal{G}_\pm$ can similarly be expanded in terms of the real coefficients A_n and B_n

$$\mathcal{G}_+ = \sum_{n=1}^{\infty} (A_n - B_n) z^n, \qquad \mathcal{G}_- = 2A_0 + \sum_{n=1}^{\infty} (A_n + B_n) z^n, \tag{7.54}$$

where $A_0 = n/(2\pi)$.

The Lagrange multiplier $\mathcal{G}_\Lambda(z)$ in Eq. (7.51) enforces the GGE constraint continuously over time. To solve the system numerically, we eliminate $\mathcal{G}_\Lambda(z)$ entirely by taking an appropriate linear combination of the two equations for $\mathcal{G}_+$ and $\mathcal{G}_-$. Setting $\Gamma = 1$ for brevity, this yields a single equation free of the undetermined multipliers

$$\begin{aligned} \frac{\mathrm{d}}{\mathrm{d}t} \left[\left(-h + \frac{1}{z} \right) \mathcal{G}_+ - (h - z) \mathcal{G}_- \right] = &- \left(-h + \frac{1}{z} \right) \left[1 - 2\pi \mathcal{G}_+ - 2n + 2nz\partial_z \right] \mathcal{G}_+ \\ &+ (h - z) \left[1 - 2\pi \mathcal{G}_- + 2n + 2nz\partial_z \right] \mathcal{G}_-. \end{aligned} \tag{7.55}$$

Simultaneously, the GGE constraint from Eq. (7.30) must be satisfied at the level of the Fourier coefficients. Expanding the constraint $C_k = 0$ into its constituent harmonics links the coefficients A_n exclusively to B_n

$$A_0 - \frac{1}{4\pi} = -\sum_{m=1}^{\infty} B_{2m} + h \sum_{m=0}^{\infty} B_{2m+1}, \tag{7.56a}$$

$$A_n = -B_n - 2 \sum_{\substack{m>n \\ m+n \text{ even}}}^{\infty} B_m + 2h \sum_{\substack{m>n \\ m+n \text{ odd}}}^{\infty} B_m, \qquad (n \geq 1). \tag{7.56b}$$

By expanding Eq. (7.55) in powers of z and substituting for A_n using the constraints in Eq. (7.56), we obtain a infinite hierarchy of ordinary differential equations for the coefficients B_n. Truncating this hierarchy at a sufficiently large maximum order $n_{\max}$ allows us to efficiently time-evolve the system from an initial state—such as an infinite-temperature state where $A_0 = 1/(4\pi)$ and all other

coefficients are zero—directly to the nonequilibrium steady state. These steady-state coefficients completely determine all single-particle fermionic spatial correlations, from which the macroscopic spin-spin correlations can ultimately be reconstructed.

7.5 The Naive Free-Fermion Approximation

Before reconstructing the spin-spin correlation functions from the exact GGE solution, it is instructive to consider a simpler, naive approximation. This detour highlights exactly why the complex machinery developed in Section 7.4.2 is absolutely necessary to capture the physics of the driven-dissipative Ising model.

The mathematical complexity in our exact solution originates entirely from the Jordan-Wigner mapping of the local dissipative jump operators. Recall that the decay of a spin is represented by $\hat{L}_j = \sqrt{\Gamma}\sigma_j^+$. Under the JW transformation, this operator acquires a non-local parity-measuring string: $\hat{L}_j = \sqrt{\Gamma}\hat{c}_j \prod_{l=1}^{j-1}(1-2\hat{c}_l^\dagger \hat{c}_l)$. A naive approach to simplify such open quantum systems is to deliberately ignore this JW string, effectively assuming that the dissipation acts directly and locally as independent fermionic losses, $\hat{L}_j \approx \sqrt{\Gamma}\hat{c}_j$. By making this ''free-fermion'' approximation, the entire Liouvillian becomes strictly quadratic and the momentum modes completely decouple. Applying a Fourier transformation to the Hamiltonian, the problem reduces to a sum over independent momentum pairs $(k, -k)$

$$\hat{H}_{\text{free}} = 2\sum_{k>0}(h - \cos k)[\hat{c}_k^\dagger \hat{c}_k + \hat{c}_{-k}^\dagger \hat{c}_{-k}] - i \sin k\,[\hat{c}_k \hat{c}_{-k} + \hat{c}_k^\dagger \hat{c}_{-k}^\dagger]. \tag{7.57}$$

For any given momentum pair, the local Hilbert space is spanned by merely four states: the vacuum $|0,0\rangle$, the single-particle states $|k,0\rangle$ and $|0,-k\rangle$, and the fully occupied state $|k,-k\rangle$. In this isolated four-dimensional subspace, the Hamiltonian acts as a simple 4×4 matrix $\hat{h}_k$, and the dissipation acts strictly locally. We can therefore write a completely decoupled Lindblad master equation for the density matrix $\hat{\rho}_k$ of each mode

$$\frac{\mathrm{d}\hat{\rho}_k}{\mathrm{d}t} = -i\big[\hat{h}_k, \hat{\rho}_k\big] + \Gamma\left(\hat{c}_k\hat{\rho}_k\hat{c}_k^\dagger - \frac{1}{2}\left\{\hat{c}_k^\dagger\hat{c}_k, \hat{\rho}_k\right\} + \hat{c}_{-k}\hat{\rho}_k\hat{c}_{-k}^\dagger - \frac{1}{2}\left\{\hat{c}_{-k}^\dagger\hat{c}_{-k}, \hat{\rho}_k\right\}\right). \tag{7.58}$$

Because this equation is finite-dimensional and linear, we can algebraically solve for the steady state ($\frac{\mathrm{d}\hat{\rho}_k}{\mathrm{d}t} = 0$).

By defining the fermionic basis

$$\begin{aligned} |0,0\rangle &= (1,0,0,0)^T, \\ \hat{c}_k^\dagger |0,0\rangle &= |k,0\rangle = (0,1,0,0)^T, \\ \hat{c}_{-k}^\dagger |0,0\rangle &= |0,-k\rangle = (0,0,1,0)^T, \\ \hat{c}_{-k}^\dagger \hat{c}_k^\dagger |0,0\rangle &= |k,-k\rangle = (0,0,0,1)^T, \end{aligned} \tag{7.59}$$

the operators take the matrix form

$$\hat{c}_k = \begin{pmatrix} 0 & 1 & 0 & 0 \\ 0 & 0 & 0 & 0 \\ 0 & 0 & 0 & -1 \\ 0 & 0 & 0 & 0 \end{pmatrix}, \quad \hat{c}_{-k} = \begin{pmatrix} 0 & 0 & 1 & 0 \\ 0 & 0 & 0 & 1 \\ 0 & 0 & 0 & 0 \\ 0 & 0 & 0 & 0 \end{pmatrix}, \quad \hat{h}_k = 2 \begin{pmatrix} -(h-\cos k) & 0 & 0 & -i\sin k \\ 0 & 0 & 0 & 0 \\ 0 & 0 & 0 & 0 \\ i\sin k & 0 & 0 & (h-\cos k) \end{pmatrix}. \tag{7.60}$$

In the steady state, we find the only non-vanishing elements of the density matrix to be

$$\hat{\rho}_k(t \to \infty) = \begin{pmatrix} \rho_{11} & 0 & 0 & \rho_{14} \\ 0 & \rho_{22} & 0 & 0 \\ 0 & 0 & \rho_{33} & 0 \\ \rho_{14}^* & 0 & 0 & \rho_{44} \end{pmatrix}. \tag{7.61}$$

Finally, imposing the condition $\mathrm{Tr}\{\rho_k\} = 1$, we can determine these matrix elements yielding simple expressions for the steady-state momentum distributions at any finite Γ

$$A_k^{\text{free}} = \frac{1}{4\pi} \frac{\sin^2 k}{1 + h^2 - 2h\cos k + (\frac{\Gamma}{4})^2}, \tag{7.62a}$$

$$B_k^{\text{free}} = \frac{-1}{4\pi} \frac{\sin k (h - \cos k + \frac{i\Gamma}{4})}{1 + h^2 - 2h\cos k + (\frac{\Gamma}{4})^2}. \tag{7.62b}$$

To connect this back to our overarching analytical framework, we should take the weak dissipation limit ($\Gamma \to 0$).

One can recover the same result from the full integro-differential kinetic equations (Eqs. (7.35) and (7.36)), by deliberately discarding the non-linear terms from F_A and F_B. In this case, Eqs. (7.35)

and (7.36) reduce to

$$\frac{\mathrm{d}A_k^{\mathrm{linear}}}{\mathrm{d}t} = -A_k^{\mathrm{linear}} + \Lambda_k \sin\theta_k = 0, \tag{7.63a}$$

$$\frac{\mathrm{d}B_k^{\mathrm{linear}}}{\mathrm{d}t} = -B_k^{\mathrm{linear}} - \Lambda_k \cos\theta_k = 0, \tag{7.63b}$$

which, in the steady state, yields

$$A_k^{\mathrm{linear}} \cos\theta_k + B_k^{\mathrm{linear}} \sin\theta_k = 0. \tag{7.64}$$

Together with the constraint in Eq. (7.30), we can solve the two equations for A_k^{linear}, and B_k^{linear} in the steady state which yields

$$A_k^{\mathrm{linear}} = \frac{1}{2}\sin^2\theta_k, \qquad B_k^{\mathrm{linear}} = -\frac{1}{2}\sin\theta_k\cos\theta_k. \tag{7.65}$$

Upon substituting for θ_k in terms of h, we find

$$A_k^{\mathrm{linear}} = \frac{1}{4\pi}\frac{\sin^2 k}{1+h^2-2h\cos k}, \tag{7.66a}$$

$$B_k^{\mathrm{linear}} = \frac{-1}{4\pi}\frac{\sin k\,(h-\cos k)}{1+h^2-2h\cos k}. \tag{7.66b}$$

These equations simply reproduce Eq. (7.62) in the limit $\Gamma \to 0$.

Remarkably, the momentum distributions derived in Eq. (7.66) are mathematically identical to the state resulting from a sudden, purely unitary quench [254]. Specifically, it maps exactly to a quench originating from a completely uncorrelated product state with all spins pointing down (the ground state at $h_0 = \infty$) evolving under the the full Ising model with a transverse field h.

For such a quench, the macroscopic spin-spin correlation function has been exactly calculated [254]. In the ordered regime ($h \leq 1$), the correlations behave as $C_r \propto 2^{-r}\cos(r\arccos h)$. Conversely, in the disordered regime ($h > 1$), the correlations decay monotonically as $C_r \propto (2h)^{-r}$. Consequently, the correlation length extracted from this free-fermion approximation is strictly given by

$$\xi_{\mathrm{free}} = \begin{cases} 1/\log 2, & h \leq 1 \\ 1/\log(2h), & h \geq 1 \end{cases} \tag{7.67}$$

While it correctly predicts an oscillatory nature for the correlations below the critical point, the correlation length ξ_{free} strictly caps at $1/\log 2$ for all $h \leq 1$. It exhibits no enhancement near the quantum critical point ($h \to 1$). This rigorous step-by-step contrast highlights our core conclusion: the steady-state quantum criticality in the driven-dissipative Ising model is not a simple remnant of the free-fermion Hamiltonian. The full GGE framework succeeds because it faithfully preserves the essential dissipation-induced parity mixing and properly accounts for Jordan-Wigner strings.

7.6 Reconstructing Spin Correlations

The numerical integration of the truncated hierarchy described in Section 7.4.4 yields Fourier coefficients A_n and B_n in the steady state. However, the ultimate physical quantities of interest are the spin-spin correlation functions, which characterize the nonequilibrium state and encode the signatures of the underlying quantum phase transition. We must therefore reverse the mapping to express the spin correlators in terms of the solved fermionic distributions.

We are primarily interested in the two-point spatial correlation function in the x-direction, $\langle \sigma_i^x \sigma_{i+r}^x \rangle$, where r is the spatial separation between the spins. Under the Jordan-Wigner transformation, the Pauli σ^x operators are mapped to highly non-local strings of fermions. To systematically evaluate these strings, we introduce the Majorana fermionic operators [255]

$$\hat{M}_i \equiv \hat{c}_i^\dagger + \hat{c}_i, \qquad \hat{N}_i \equiv \hat{c}_i^\dagger - \hat{c}_i. \tag{7.68}$$

Using these operators, the product of two Pauli matrices separated by a distance r (assuming $r > 0$) cleanly absorbs the Jordan-Wigner string into a contiguous product of Majorana operators

$$\begin{aligned} \langle \sigma_i^x \sigma_{i+r}^x \rangle &= \langle \hat{N}_i \left(\prod_{l=i+1}^{i+r-1} \hat{M}_l \hat{N}_l \right) \hat{M}_{i+r} \rangle \\ &= \langle \hat{N}_i \hat{M}_{i+1} \hat{N}_{i+1} \dots \hat{M}_{i+r-1} \hat{N}_{i+r-1} \hat{M}_{i+r} \rangle. \end{aligned} \tag{7.69}$$

Because the steady state is described by a Gaussian GGE, this multi-point expectation value can be factored into products of two-point Majorana correlators using Wick's theorem. Since the functions A_k and B_k describing the steady state are entirely real, the normal and anomalous spatial fermionic correlators are also purely real. Consequently, the contractions between identical species

of Majorana fermions simplify trivially

$$\langle \hat{M}_i \hat{M}_j \rangle = \delta_{i,j}, \qquad \langle \hat{N}_i \hat{N}_j \rangle = -\delta_{i,j}. \tag{7.70}$$

The only non-trivial contractions arise from the cross-correlators between the $\hat{N}$ and $\hat{M}$ operators, which we define as $G_{i,j} \equiv \langle \hat{N}_i \hat{M}_j \rangle$.

Due to the vanishing of the identical-species contractions, the application of Wick's theorem to the Majorana string yields a Pfaffian that squares to an $r \times r$ determinant. Invoking the translational invariance of the steady state in the thermodynamic limit, the correlator depends only on the separation $l = j - i$, such that $G_{i,j} = G_{j-i} \equiv G_l$. The spin-spin correlation function is therefore given exactly by the Toeplitz determinant

$$\langle \sigma_i^x \sigma_{i+r}^x \rangle = \begin{vmatrix} G_{-1} & G_{-2} & \cdots & G_{-r} \\ G_0 & G_{-1} & \cdots & G_{-r+1} \\ \vdots & \vdots & \ddots & \vdots \\ G_{r-2} & G_{r-3} & \cdots & G_{-1} \end{vmatrix}. \tag{7.71}$$

The matrix elements G_l must now be expressed in terms of the numerically obtained multipole coefficients A_n and B_n. By expanding the Majorana operators back into the original complex fermions, we find

$$G_l = 2\mathrm{Re}\left[\langle \hat{c}_i^\dagger \hat{c}_{i+l} \rangle - \langle \hat{c}_i \hat{c}_{i+l} \rangle\right] - \delta_{l,0}. \tag{7.72}$$

The real-space fermionic correlators are simply the inverse Fourier transforms of the momentum-space density operators $\hat{A}_k$ and $i\hat{B}_k$. Using the multipole expansions defined in Section 7.4.4, these spatial correlators evaluate to

$$\langle \hat{c}_i^\dagger \hat{c}_{i+l} \rangle = 2\pi A_0 \delta_{l,0} + \pi \sum_{n=1}^{\infty} A_n \delta_{|l|,n}, \tag{7.73a}$$

$$\langle \hat{c}_i \hat{c}_{i+l} \rangle = \mathrm{sgn}(l)\, \pi \sum_{n=1}^{\infty} B_n \delta_{|l|,n}. \tag{7.73b}$$

Substituting these spatial relations back into the definition of the matrix elements yields the final, computable expressions for the elements of the Toeplitz determinant

$$G_0 = 4\pi A_0 - 1, \tag{7.74a}$$

$$G_l = 2\pi \left(A_{|l|} - \operatorname{sgn}(l) B_{|l|} \right) \qquad \text{for } l \neq 0. \tag{7.74b}$$

By populating the matrix in Eq. (7.71) with the elements computed via Eq. (7.74b), we can extract the macroscopic spin-spin correlations $\langle \sigma_i^x \sigma_{i+r}^x \rangle$ as a function of distance. The steady-state correlation length ξ, which exhibits the pronounced peak near the ground-state quantum critical point as discussed in the introduction, is subsequently extracted from the asymptotic exponential decay of this determinant for large r.

7.7 Steady-State Spin Correlations: GGE vs. Exact Numerics

With the analytical framework for evaluating the spin-spin correlations established, we benchmark the GGE predictions against exact numerical simulations. The validity of the GGE approach formally relies on the weak dissipation limit ($\Gamma \to 0$, taken strictly after the thermodynamic limit $L \to \infty$). To assess its robustness at finite dissipation and finite system size, we compare the GGE analytical solution to matrix product state (MPS) simulations of the Lindblad master equation for a chain of $L = 40$ spins at $\Gamma = 0.15$. We contrast these results with the predictions of the ‘‘free-fermion’’ approximation, which, as detailed in Section 7.5, treats the open system as a collection of non-interacting, parity-conserving momentum modes. We also compare them against the spin-wave analysis performed under the Holstein-Primakoff approximation in Chapter 4.

An analysis of the correlation length ξ extracted in the steady state is summarized in Fig. 7.3. Deep in the disordered regime ($h \gg 1$), the correlations decay rapidly. However, as the transverse field approaches the isolated quantum critical point ($h = 1$), the correlation length exhibits a peak, indicating that signatures of the underlying Hamiltonian criticality survive the non-unitary driven-dissipative dynamics.

Remarkably, the analytical GGE solution closely matches the exact MPS numerics across all

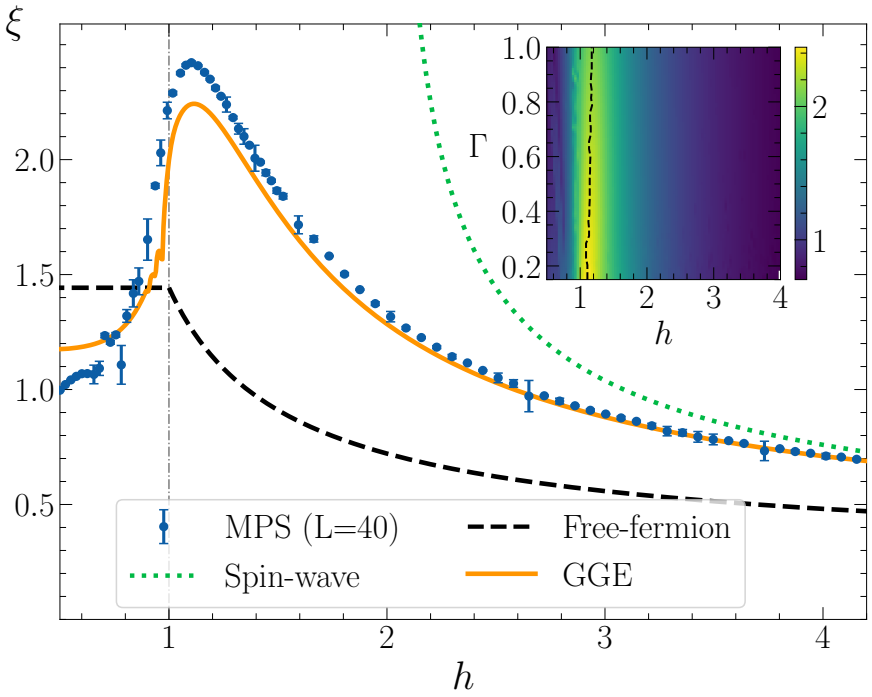

Figure 7.3 Correlation length ξ calculated in the steady state of the driven-dissipative Ising model. MPS, spin-wave theory, and the free-fermion jump calculations are done at $\Gamma = 0.15$. The solution that we developed, plotted as a solid line, is asymptotically exact in the limit $\Gamma \to 0$. The vertical dashed line marks the QCP. In the inset, we present MPS calculations for different h and Γ for $L = 40$ spins. The dashed line indicates the position of the maximum correlation length for a given value of Γ. The correlation length decays as Γ increases, but the peak remains close to the critical point.

investigated regimes. This agreement is particularly striking given that the MPS simulations are performed at a finite dissipation rate of $\Gamma = 0.15$, whereas the GGE framework is formally derived in the asymptotic weak-dissipation limit. Our results clearly reproduce a peak close to, but slightly above, the quantum critical point at $h_{peak} \approx 1.11$ in the limit $\Gamma \to 0$, thus confirming that $h_{peak} \gtrapprox 1$ is not an artifact of numerics at finite L or Γ. On the other hand, the spin-wave analysis (calculations performed in Chapter 4) predicts that $\xi \to \infty$ as $h \to 2$ in the limit $\Gamma \to 0$ and breaks down when $h \leq 2$, and thus fails to capture the physics except for large h. This benchmarking also illustrates the limitations of the free-fermion approximation. As mathematically predicted, this approach underestimates the correlation length near h_c, exhibiting a capping of the correlation length at $\xi \approx 1.44$. This contrast confirms that the steady-state correlations are driven by the non-local stringing of modes across parity sectors. By incorporating these non-linear, mode-mixing inter-

actions, the GGE successfully recovers the complex physics that simple Markovian free-fermion decay suppresses.

7.8 Conclusion

In this chapter, we have demonstrated that the steady state of the driven-dissipative transverse-field Ising model retains distinct, macroscopic signatures of the underlying Hamiltonian's quantum phase transition. By carefully treating the non-local, parity-mixing nature of the local dissipative jump operators under the Jordan-Wigner transformation, we can go beyond the naive free-fermion approximation. Utilizing the generalized Gibbs ensemble (GGE) ansatz in the weak-dissipation limit, we derived exact integro-differential kinetic equations for the momentum distributions, which we subsequently solved via analytic continuation to the complex plane and multipole expansion.

Through the exact evaluation of the Toeplitz determinant, we reconstructed the spatial spin-spin correlation functions and extracted the steady-state correlation length ξ. As summarized in Fig. 7.3, the exact GGE solution reveals a pronounced enhancement of the correlation length near the quantum critical point ($h_c = 1$). This peak is corroborated by finite-size MPS simulations at finite dissipation rates. Furthermore, while the linear spin-wave theory (derived in Chapter 4) captures the quantitative features of the steady state for $h \gg 1$, the GGE framework alone provides the exact description across all regimes, faithfully capturing the complex parity-mixing induced by the Markovian environment.

The success of the GGE approach relies fundamentally on the integrability of the TFIM Hamiltonian—specifically, the existence of an extensive set of conserved charges and the exact mapping to non-interacting Bogoliubov quasiparticles. However, physical realizations of quantum spin chains in synthetic quantum simulator platforms (such as Rydberg atom arrays [213] or trapped ions [207, 208]) often feature longer-range interactions that break this strict integrability.

This naturally raises an important question regarding the universality of our findings: do these dissipation-induced critical signatures survive the breaking of integrability? If the Hamiltonian is no longer reducible to free fermions, the closed system is expected to thermalize according to the eigenstate thermalization hypothesis (ETH) rather than relaxing to a GGE. How this chaotic internal

dynamics competes with the continuous measurements of the environment remains a highly non-trivial problem.

In the following chapter, we will address this question directly by introducing next-nearest-neighbor interactions to the Ising Hamiltonian. Moving beyond exactly solvable models, we explore the fate of the quantum phase transition in driven-dissipative quantum many-body systems with non-integrable Hamiltonians.

CHAPTER 8

BEYOND INTEGRABILITY: SIGNATURES OF QUANTUM PHASE TRANSITIONS IN DRIVEN DISSIPATIVE ISING MODELS

The analytical success of the GGE framework developed in Chapter 7 relies fundamentally on the underlying integrability of the nearest-neighbor transverse-field Ising model. The existence of an extensive set of conserved charges prevents the system from thermalizing, allowing the weak dissipation to simply drive transitions between non-interacting Gaussian states. The introduction of such next-nearest-neighbor (NNN) interactions explicitly breaks the free-fermion integrability. According to the eigenstate thermalization hypothesis (ETH) [131, 248, 249], the closed-system dynamics will become fully chaotic, effectively acting as its own heat bath and thermalizing to a standard Gibbs ensemble (GE). An important question therefore arises: do the dissipation-induced critical signatures observed in the integrable model survive when the internal coherent dynamics become chaotic?

By incorporating integrability-breaking interactions into the Hamiltonian, we observe that the correlation length peak not only persists but shifts even closer to the newly shifted quantum critical point of the chaotic model. To elucidate this, we map the weakly-dissipative steady state of our system to the infinite-time limit of a quantum quench in the corresponding isolated system. This equivalence allows us to translate recent, remarkable discoveries regarding signatures of quantum phase transitions in the transient dynamics of quantum quenches [129, 136, 137, 256] directly into the steady-state properties of driven-dissipative quantum simulators.

To address this, we introduce the non-integrable Ising Hamiltonian

$$\hat{H} = -\sum_{i=1}^{L} \left(J_1 \sigma_i^x \sigma_{i+1}^x + J_2 \sigma_i^x \sigma_{i+2}^x \right) + h \sum_{i=1}^{L} \sigma_i^z, \tag{8.1}$$

where $J_1 = 1$ and J_2 are the nearest and next-nearest-neighbor exchange couplings, respectively. We maintain the same homogeneous, local Markovian dissipation, described by the Lindblad master equation with jump operators $\hat{L}_i = \sqrt{\Gamma}\sigma_i^+$

$$\frac{\mathrm{d}\hat{\rho}}{\mathrm{d}t} = \mathcal{L}(\hat{\rho}) = -i\left[\hat{H}, \hat{\rho}\right] + \Gamma \sum_{i=1}^{L} \left(\sigma_i^+ \hat{\rho} \sigma_i^- - \frac{1}{2}\left\{\sigma_i^- \sigma_i^+, \hat{\rho}\right\} \right). \tag{8.2}$$

Because the system is no longer reducible to non-interacting quasiparticles, the infinite hierarchy of correlations cannot be closed exactly using Wick's theorem. We must instead rely on extensive numerical techniques, such as matrix product states (MPS) simulations.

8.1 Ground-State Criticality and Binder Cumulant Analysis

Before analyzing the nonequilibrium steady state, we must first establish the critical properties of the underlying Hamiltonian. While the inclusion of the NNN coupling J_2 explicitly breaks the free-fermion integrability of the TFIM, the ground state still undergoes a continuous quantum phase transition belonging to the Ising universality class. However, the location of the quantum critical point, h_c, is shifted from its integrable value of $h_c(J_2 = 0) = 1$ due to the additional interactions. To accurately locate this shifted critical point, we employ finite-size scaling of the Binder cumulant [257]. This is a highly sensitive numerical tool that allows us to pinpoint the phase transition without requiring prior knowledge of the correlation length.

The fourth-order cumulant (i.e., the Binder cumulant) for the total longitudinal magnetization $\hat{S}^x = \sum_{i=1}^{L} \sigma_i^x$ is defined as

$$U = 1 - \frac{\langle (\hat{S}^x)^4 \rangle}{3\langle (\hat{S}^x)^2 \rangle^2}. \tag{8.3}$$

In the thermodynamic limit ($L \to \infty$), the Binder cumulant takes distinct universal values depending on the phase. Deep in the ferromagnetic ordered phase ($h < h_c$), the spontaneous magnetization dominates, causing $\langle (\hat{S}^x)^4 \rangle \to \langle (\hat{S}^x)^2 \rangle^2$, which yields $U \to 2/3$. Conversely, deep in the paramagnetic phase ($h > h_c$), the fluctuations of the magnetization are purely Gaussian. By Wick's theorem, this leads to $\langle (\hat{S}^x)^4 \rangle \to 3\langle (\hat{S}^x)^2 \rangle^2$, resulting in $U \to 0$.

Near the phase transition, finite-size scaling dictates that the Binder cumulant behaves as a universal scaling function of the ratio L/ξ, where $\xi \propto |h - h_c|^{-\nu}$ is the correlation length [82]. Therefore, we can express the cumulant as

$$U(h, L) = \mathcal{F}\left((h - h_c) L^{1/\nu} \right). \tag{8.4}$$

Because $\mathcal{F}(0)$ is a universal constant independent of system size, plotting U as a function of the transverse field h for different lengths L produces curves that uniquely intersect exactly at the critical

point $h = h_c$.

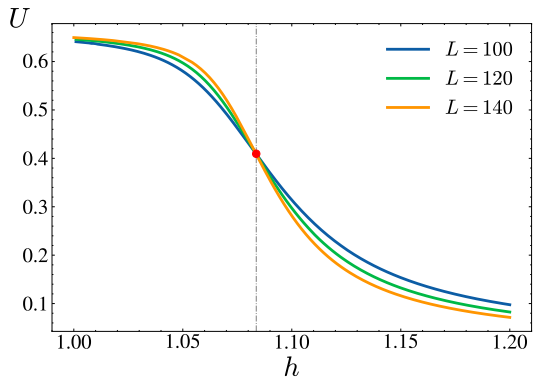

Figure 8.1 The Binder cumulant U calculated in the ground state of $\hat{H}$ with $J_2 = 0.05$ for multiple system sizes. The red dot marks h_c, the point where the curves cross.

Using density matrix renormalization group (DMRG) algorithms [191, 193], we compute the ground state of Eq. (8.1) for varying system sizes (e.g., $L = 100$ to 140) at a fixed non-integrable coupling J_2. By locating the crossing point of the resulting U curves, we identify the quantum critical point h_c of the ground state. Establishing this precise value is crucial, as it serves as the baseline for evaluating whether the dissipation-induced spatial correlations in the highly excited steady state are indeed anchored to the underlying ground-state criticality.

8.2 Exact Steady-State Energy Density

Before resorting to numerical methods to probe the complex spatial correlations of the steady state, it is instructive to ask what exact, analytical statements can be made about this generic, non-integrable driven-dissipative system. Remarkably, despite the complexity of the chaotic internal dynamics, we can derive an exact, closed-form expression for the steady-state energy density.

In the nonequilibrium steady state (NESS), the expectation value of any observable $\hat{O}$ must be stationary, $\frac{\mathrm{d}}{\mathrm{d}t}\langle\hat{O}\rangle_{\mathrm{SS}} = 0$. In this section, we apply this condition to the Hamiltonian itself, $\hat{O} = \hat{H}$. Consider a general transverse-field Ising Hamiltonian

$$\hat{H} = \sum_{i,j=1}^{L} J_{ij}\sigma_i^x\sigma_j^x + h\sum_{i=1}^{L}\sigma_i^z, \tag{8.5}$$

where J_{ij} is a real symmetric matrix with zero diagonal elements, with no other constraints on the range or structure of the Ising interactions. We start by considering the Lindblad master equation

in the steady state

$$0 = -i\left[\hat{H}, \hat{\rho}\right] + \sum_i \hat{L}_i \hat{\rho} \hat{L}_i^\dagger - 1/2\left\{\hat{L}_i^\dagger \hat{L}_i, \hat{\rho}\right\}. \tag{8.6}$$

Multiplying this equation by $\hat{H}$ from the left and taking the trace, we arrive at the condition [258]

$$0 = \mathrm{Re} \sum_i \left\langle \left[\hat{L}_i^\dagger, \hat{H}\right] \hat{L}_i \right\rangle_{\mathrm{SS}}, \tag{8.7}$$

where $\langle \hat{O} \rangle_{\mathrm{SS}} = \mathrm{Tr}\{\hat{O}\hat{\rho}_{\mathrm{SS}}\}$. Note that the condition in Eq. (8.7) is satisfied for any arbitrary Hamiltonian $\hat{H}$, and jump operators $\hat{L}_i$. In the case of the Hamiltonian in Eq. (8.5) and under bulk dissipation $\hat{L}_i = \sqrt{\Gamma}\sigma_i^-$ for $i \in \{1, \cdots, L\}$, this condition reduces to

$$0 = \mathrm{Re} \sum_i \left\langle \left[\sigma_i^+, \hat{H}\right] \sigma_i^- \right\rangle_{\mathrm{SS}}. \tag{8.8}$$

The previous equation can be simplified and put on the form

$$0 = -hL - \langle \hat{H} \rangle_{\mathrm{SS}} + \mathrm{Re}\left\{ i \sum_{i,j=1}^{L} J_{ij} \left\langle \sigma_i^x \sigma_j^y \right\rangle_{\mathrm{SS}} \right\}. \tag{8.9}$$

In the third term on the rhs of the previous equation, the operator $\sum_{ij} J_{ij} \sigma_i^x \sigma_j^y$ is Hermitian, making the third term purely imaginary (note that $J_{ii} = 0$). Therefore, we conclude that the energy density in the steady state of driven dissipative Ising models is always given by

$$\langle \hat{H} \rangle_{\mathrm{SS}}/L = -h. \tag{8.10}$$

This conclusion can be even further generalized to a wide class of $\mathbb{Z}_2$-symmetric models by considering the jump operators defined by $\hat{L}_i = \sqrt{\Gamma}\, \frac{\sigma_i^x - i e^{i\theta} \sigma_i^y}{2}$. Applying Eq. (8.7) to this case, we arrive at the condition

$$\langle \hat{H} \rangle_{\mathrm{SS}}/L = -h \cos\theta + \frac{1}{L} \sin\theta \sum_{i,j=1}^{L} J_{ij} \left\langle \sigma_i^x \sigma_j^y \right\rangle_{\mathrm{SS}}. \tag{8.11}$$

In the limit of weak dissipation, the steady state is expected to be symmetric under the action of the time-reversal operator ($\hat{K}\hat{\rho}\hat{K}^{-1} = \hat{\rho}$). Since the action of $\hat{K}$ on the Pauli matrices is simply complex conjugation ($\hat{K}\sigma_j^{x/y}\hat{K}^{-1} = \pm\sigma_j^{x/y}$), the second term on the rhs of Eq. (8.11) may be neglected. This

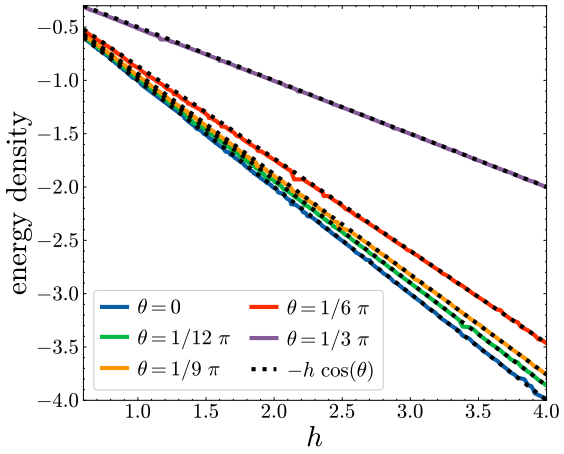

Figure 8.2 Energy density in the steady state $\langle \hat{H} \rangle_{\rm SS}/L$ as a function of the magnetic field h for multiple values of θ. The results are obtained using MPS simulations for $L = 40$, $\Gamma = 0.15$. The NNN coupling is set to $J_2 = 0.5$.

can be seen in the left panel of Fig. 8.2, where the energy in the steady state of the open NNN Ising model is shown to satisfy the predictions of Eq. (8.11) for $\Gamma = 0.15$ and for various values of θ.

Notably, the energy of the steady state is exactly equal to the expectation value of the Hamiltonian with respect to the product state, $\langle \psi_0 | \hat{H} | \psi_0 \rangle = -h$, where

$$|\psi_0\rangle = \bigotimes_{j=1}^{L} \left[i\sqrt{\frac{1-\cos\theta}{2}}\,|\uparrow\rangle_j + \sqrt{\frac{1+\cos\theta}{2}}\,|\downarrow\rangle_j \right]. \tag{8.12}$$

As we will explore in detail in subsequent sections, this exact formal equivalence provides a crucial mathematical bridge that will allow us to connect the steady-state properties of the driven-dissipative open system directly to the physics of unitary quench dynamics.

8.3 Numerical Analysis of Steady-State Correlations

To probe the spatial structure of the steady state, we evaluate the transverse spin-spin correlation function

$$C(r) = \langle \sigma_i^x \sigma_{i+r}^x \rangle_{\rm SS}. \tag{8.13}$$

Because the system is non-integrable, we compute $C(r)$ using matrix product states (MPS) algorithms adapted for open quantum systems [194, 259, 260]. We extract the correlation length ξ by fitting the spatial decay of the correlations to an exponential envelope, $C(r) \sim e^{-r/\xi}$.

Despite the effects of dissipation, the steady state exhibits pronounced spatial correlations. As the transverse field h is tuned across the phase diagram, the correlation length ξ does not remain

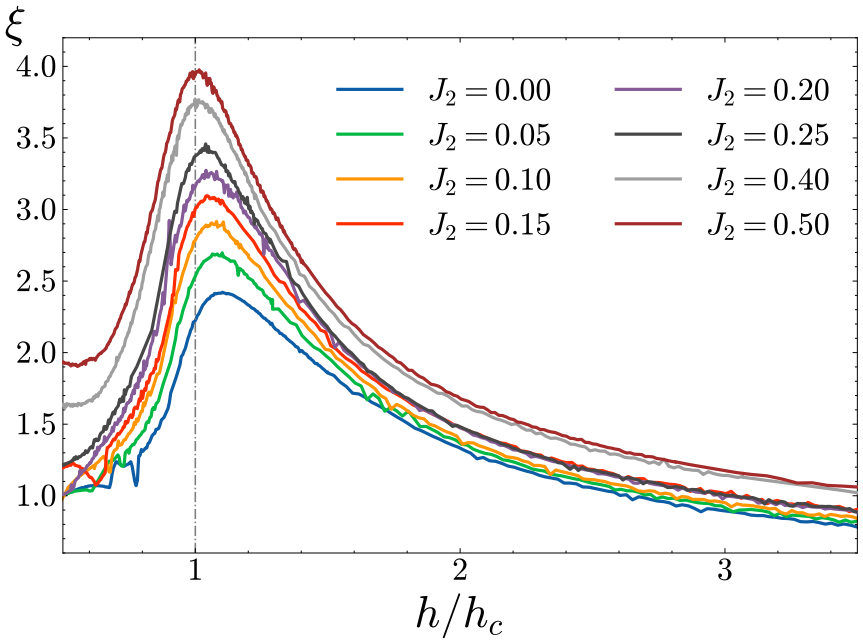

Figure 8.3 Correlation length ξ computed in the steady state of the driven-dissipative NNN Ising model ($\Gamma = 0.15$) obtained from MPS numerical results. The corresponding QCPs for $0 \leq J_2 \leq 0.5$ are at $1 \leq h_c \lessapprox 1.78$ as identified in Section 8.1.

flat or trivial. Instead, ξ exhibits a pronounced peak. Crucially, the location of this dissipation-induced peak aligns precisely with the shifted quantum critical point, h_c, which we independently identified via the Binder cumulant crossing in Section 8.1 for a large class of Ising models. While a phase transition is absent in our models, our observations suggest a form of *universality*, where pronounced features appear even closer to criticality despite increasing integrability breaking perturbations. Thus, the sensitivity to the QCP is not tied to integrability, and should be understood in a more general setting.

8.4 Relation to Unitary Quench Dynamics

To understand the physical origin of these persistent critical signatures in the non-integrable model, we must examine the nature of the steady state in the asymptotic weak-dissipation limit ($\Gamma \to 0$). We can establish an intriguing connection between the nonequilibrium steady state of the driven-dissipative system and the quench dynamics of an isolated, chaotic system by highlighting three key facts:

1. **Thermalization following a quantum quench:** While the integrable Hamiltonian relaxes

to a GGE, breaking integrability drastically alters the internal relaxation dynamics. It is well established that the unitary evolution under a chaotic Hamiltonian drives an isolated quantum system (in the absence of any dissipation) toward thermal equilibrium [131]. This behavior is underpinned by the eigenstate thermalization hypothesis (ETH) [130, 132, 248, 249]. Because the inclusion of the next-nearest-neighbor coupling J_2 explicitly breaks integrability, the eigenstates of the Hamiltonian effectively act as their own thermal baths. Consequently, if the isolated system is prepared in some initial state, the infinite-time average of its coherent dynamics—known as the diagonal ensemble—will cause the expectation values of local observables to relax precisely to the values predicted by a standard thermal Gibbs ensemble (GE), $\hat{\rho}_{\text{th}} \propto e^{-\beta_{\text{eff}}\hat{H}}$. The effective inverse temperature β_{eff} of this resulting state is fixed by the energy density of the initial state.

2. **Dissipative relaxation to the Gibbs ensemble:** Recent work has demonstrated that when a chaotic Hamiltonian is subject to bulk dissipation, the driven-dissipative steady state is also described by a thermal GE in the limit $\Gamma \to 0$ (taken after the infinite-time limit $t \to \infty$) [230, 258, 261–263]. This effectively extends our theoretical treatment from the integrable GGE ansatz to a standard GE. Importantly, while neither the isolated chaotic evolution nor the weakly dissipative system involves an intrinsic temperature originating from an external reservoir, their steady states are fully characterized by an effective temperature that is set by their energy densities.

3. **Identical energy densities:** Finally, as we proved analytically in Section 8.2, for a general Ising Hamiltonian subject to $\mathbb{Z}_2-$symmetric local Markovian dissipation, the steady state's energy density evaluates to exactly $\langle\hat{H}\rangle_{\text{SS}}/L = -h$, completely independent of the exchange couplings J_1 and J_2. Crucially, for $\theta = 0$ (i.e.,$\hat{L}_i\sigma_i^-$), this energy density is mathematically identical to the expectation value of the Hamiltonian with respect to the fully polarized initial product state $|\psi_0\rangle = |\downarrow\downarrow \ldots \downarrow\rangle$.

Combining these three points leads to a non-trivial conclusion: the steady state of the driven-

dissipative dynamics under a chaotic Ising Hamiltonian in the limit $\Gamma \to 0$ is exactly identical to the infinite-time average of unitary quench dynamics under the *same* Hamiltonian starting from the initial state $|\psi_0\rangle$. (More generally, for the θ-parameterized jump operators $\hat{L}_i = \sqrt{\Gamma}\,\frac{\sigma_i^x - ie^{i\theta}\sigma_i^y}{2}$, this corresponds to the generalized initial state introduced previously in Eq. (8.12)).

Having established this exact mapping, the generic sensitivity of the steady state to the quantum critical point becomes clear. While it is not immediately obvious why highly excited chaotic systems should retain memories of ground-state criticality, recent studies on quantum quenches in chaotic Ising-type models have identified robust signatures of quantum phase transitions. Specifically, when a system is quenched from a fixed, highly polarized initial state (such as $|\psi_0\rangle$) to the vicinity of the QCP, the long-time spin correlators develop pronounced peaks [256].

Therefore, by leveraging this equivalence, we conclude that the pronounced correlation peak observed in our steady-state MPS numerics is a direct manifestation of the signatures of quantum criticality that may be observed following a quench. The dissipation does not simply heat the system into a featureless state; instead, it acts to drive the chaotic system into a thermal Gibbs ensemble with effective temperature set by a corresponding quantum quench protocol, which in turn encodes the Hamiltonian's underlying criticality.

We can explicitly control this effective temperature by tuning the parameter θ in our generalized jump operators. However, as θ increases, the steady state is driven to higher energies, corresponding to higher effective temperatures. This thermalization process is vividly confirmed by our MPS numerical simulations, shown in Fig. 8.4, which illustrates the direct consequence of this energy injection on the spatial structure of the steady state. For pure loss ($\theta = 0$), the system sits at its lowest effective temperature, and the dissipation-induced correlation length peak remains highly pronounced near the critical point h_c. However, as θ increases toward $\pi/2$, the jump operators become strictly Hermitian, the energy approaches zero, and $T_{\text{eff}} \to \infty$. As we effectively heat the system, the NESS clearly shows a systematic suppression of the correlation length ξ across the entire phase diagram. At the extreme $\theta = \pi/2$ limit, the state approaches a featureless infinite-temperature GE, completely washing out any residual signatures of the underlying quantum phase

transition.

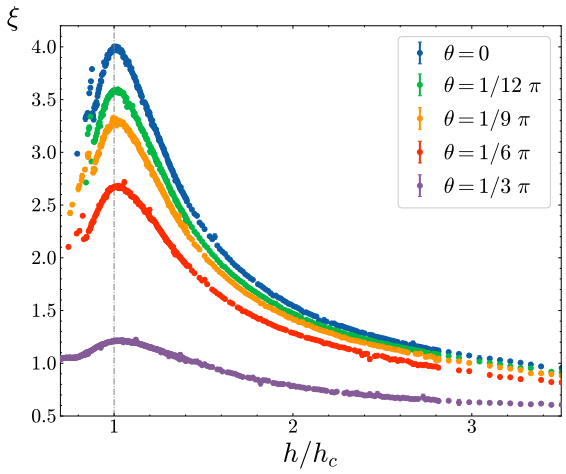

Figure 8.4 Correlation length ξ in the steady state as a function of h for multiple values of θ. The results are obtained using MPS simulations for $L = 40$, $\Gamma = 0.15$, and a next-nearest-neighbor coupling $J_2 = 0.5$. Although the steady state maps to a quench for any value of θ, increasing θ drives the macroscopic energy toward zero, which effectively heats the system toward infinite temperature and systematically suppresses the critical correlations.

8.5 Conclusion

In this chapter, we have investigated signatures of quantum criticality in driven-dissipative open quantum systems. By extending the TFIM to include integrability-breaking NNN interactions, we systematically tested whether the dissipation-induced critical signatures studied in Chapter 7 can survive the onset of fully chaotic Hamiltonian dynamics.

Our numerical results demonstrate a manifestation of these quantum features even in the non-integrable regime. Through extensive MPS simulations, we revealed that the spatial correlations not only survive but exhibit a pronounced peak that systematically tracks the shifted ground-state quantum critical point, h_c, of the underlying non-integrable Hamiltonian. To understand this, we established a nontrivial connection to quench dynamics. We demonstrated that in the weak-dissipation limit ($\Gamma \to 0$), the steady-state corresponds to a diagonal ensemble that is mathematically identical to the stationary state of a unitary quantum quench originating from a product state. The local Markovian dissipation does not simply heat the system into a featureless mixture; rather, it effectively drives the chaotic system into a thermal GE with a finite effective temperature. This

finite temperature, uniquely pinned by the NESS energy in Eq. (8.10), is precisely what allows the nonequilibrium steady state to probe the quantum phase transition.

Ultimately, these findings suggest a form of *universality* in driven-dissipative spin chains. The fact that the correlation peak persists—and even remains intimately tied to the critical point—when integrability-breaking perturbations are introduced indicates that this sensitivity is not an artifact of free-fermion solvability. On a fundamental level, this establishes that certain quantum features can robustly survive the decohering effects of bulk dissipation. On a practical level, this framework opens a promising avenue for experimentally identifying signatures of quantum phase transitions in noisy, near-term programmable quantum simulators, where environmental dissipation is inevitable.

CHAPTER 9

BEYOND INFINITE-RANGE: FIELD THEORY APPROACH TO LONG-RANGE DRIVEN-DISSIPATIVE ISING MODEL

In the preceding chapters (Chapters 7 and 8), we established a comprehensive framework for understanding the nonequilibrium properties of driven-dissipative quantum Ising chains. The physical paradigms explored thus far were fundamentally constrained to short-range Hamiltonians—specifically nearest- and next-nearest-neighbor couplings—subject to strictly local, on-site Markovian dissipation. Our analysis revealed that while the nonequilibrium steady states of these models retain signatures of the underlying ground-state quantum phase transitions, they are themselves typically devoid of true critical behavior. Consequently, a natural and pressing question arises, which forms the central focus of the present chapter: can the introduction of long-range coherent interactions and spatially correlated, collective dissipation channels stabilize macroscopic order and induce genuine phase transitions directly within the nonequilibrium steady state?

In the preceding chapters (Chapters 7 and 8), we established a comprehensive framework for understanding the nonequilibrium properties of driven-dissipative quantum Ising chains. The physical paradigms explored thus far were fundamentally constrained to short-range Hamiltonians—specifically nearest- and next-nearest-neighbor couplings—subject to strictly local, on-site Markovian dissipation. Our analysis revealed that while the nonequilibrium steady states of these models retain signatures of the underlying ground-state quantum phase transitions, they are themselves typically devoid of true critical behavior. While it is well-established that infinite-range systems, such as the paradigmatic Dicke model, can stabilize macroscopic order and undergo genuine steady-state phase transitions, such models are typically amenable to standard mean-field treatments. Consequently, a more formidable technical question arises, which forms the central focus of the present chapter: how can we rigorously tackle Ising models featuring long-range interactions and/or long-range correlated dissipation? Here, we move beyond the infinite-range mean-field limit, by developing a systematic field-theoretical framework.

Addressing this question is directly motivated by the rapid advancements in modern quantum

simulation. A plethora of highly controllable experimental platforms, including trapped-ion quantum simulators [208, 264, 265], Rydberg atom arrays [56, 63], and cavity-QED setups [143, 266], provide a remarkably fertile ground for testing the complex physics of driven-dissipative quantum many-body systems. A defining, ubiquitous feature across these diverse experimental architectures is the native presence of long-range interactions. These interactions are typically mediated by global or quasi-global bosonic modes, such as transverse phonon modes in trapped ion crystals [264], delocalized cavity photons in cavity-QED [266], or guided optical modes in waveguide-QED systems [267, 268]. For example, in ordered atomic arrays, vacuum-mediated dipole-dipole interactions intimately link long-range coherent exchange with highly correlated collective dissipation. This interplay can remarkably suppress free-space spontaneous emission by stabilizing subradiant states that act as dark guided modes, underscoring how non-local dissipation can be harnessed to protect quantum coherence and profoundly reshape steady-state correlations [268].

Furthermore, in these platforms, combining the extended interaction profiles with collective dissipative processes can lead to emergent phenomena. Specifically, these systems can undergo driven-dissipative phase transitions that manifest macroscopic symmetry breaking, characterized by critical slowing down and the asymptotic closing of the Liouvillian spectral gap in the thermodynamic limit [66]. Notably, the nonequilibrium critical behavior of models with collective Hamiltonians, such as the open Dicke model, has been extensively studied, particularly in the regime dominated by independent (local) atomic dissipation [181, 269]. However, recent investigations have revealed that introducing non-local long-range dissipative profiles fundamentally alters both the dynamical scaling and the spreading of correlations compared to systems governed solely by short-range loss mechanisms [270, 271].

Meanwhile, the complex interplay between long-range (or infinite-range) coherent coupling and long-range, correlated collective dissipation constitutes a distinct and rich frontier. While theoretical treatments [104, 272, 273] and corresponding experimental observations [274] have established the emergence of nonequilibrium bistability and first-order phase transitions in the mean-field regime, these semiclassical approaches cannot be systematically extended to systems with spatial

structures, e.g., power-law interactions. Systematically developing a field theory that incorporates this spatial dependence is therefore imperative to characterize the critical nature of the NESS and to determine the validity bounds of the mean-field predictions.

The remainder of this chapter focuses specifically on the open Dicke model and its long-range generalizations, operating strictly within the dispersive, fast-cavity regime. In its standard formulation, the Dicke model describes an ensemble of N two-level atoms interacting collectively with a single quantized cavity mode. The coherent dynamics of this system are governed by the Dicke Hamiltonian

$$\hat{H}_{\text{Dicke}} = \omega_c \hat{a}^\dagger \hat{a} + \omega_a \hat{S}_z + \frac{2\lambda}{\sqrt{N}}(\hat{a} + \hat{a}^\dagger)\hat{S}_x, \tag{9.1}$$

where $\hat{a}^\dagger$ ($\hat{a}$) is the creation (annihilation) operator for a cavity photon with frequency ω_c, ω_a is the atomic transition frequency, and λ is the collective light-matter coupling strength. The atomic degrees of freedom are described by the collective spin operators $\hat{S}_\alpha = \frac{1}{2}\sum_{i=1}^{N} \sigma_i^\alpha$ for $\alpha \in \{x, y, z\}$, where σ_i^α are the standard Pauli matrices for the i-th atom. Crucially, as an open system, photons continuously leak from the cavity at a decay rate κ.

To engineer effective spin-spin interactions, the system must operate in a regime where the cavity field dynamics are significantly faster than those of the atomic degrees of freedom. This is achieved by having either a large detuning ($\Delta_c = \omega_c - \omega_a \gg \lambda$) or a sufficiently large cavity photon loss rate κ. This strict separation of timescales justifies the adiabatic elimination of the photonic degrees of freedom ($\hat{a}, \hat{a}^\dagger$) [102], tracing out the fast cavity to leave behind an effective model of spins interacting via cavity-mediated long-range forces.

By tracing out the cavity field, the effective dynamics of the remaining atomic subsystem are fundamentally transformed. In the idealized single-mode case, the virtual exchange of cavity photons mediates an effective, infinite-range (all-to-all) exchange interaction $\propto -\frac{J}{N}\sum_{i,j} \sigma_i^x \sigma_j^x$, where the effective coupling strength $J \propto \lambda^2 \Delta_c/(4\Delta_c^2 + \kappa^2)$ [269]. However, this framework naturally generalizes to yield distance-dependent long-range interactions, if the atomic ensemble is instead coupled to a continuum or a discrete multitude of bosonic modes—such as transverse phonon modes in a trapped-ion crystal, or a multimode cavity setup [275, 276]. In such systems, adiabatic elim-

ination of the bosonic mediator yields an effective Hamiltonian featuring a long-range interaction term proportional to $-\sum_{i\neq j} J_{ij}\sigma_i^x\sigma_j^x$, where the coupling J_{ij} typically decays algebraically with distance as $1/|r_i - r_j|^\alpha$. Concurrently, the inherent leakage of these mediating modes translates into a non-local, correlated dissipation channel acting across the spatial extent of the spin ensemble.

This reduction to an effective long-range driven-dissipative Ising model establishes a mapping between the superradiant transition of the full Dicke model and the macroscopic magnetic ordering of the spin ensemble. Within this framework, the nonequilibrium phase transition is governed by the spontaneous breaking of a global $\mathbb{Z}_2$ symmetry, with the collective magnetization serving as the primary order parameter.

By developing a Keldysh functional integral formalism, we derive an effective action that captures this interplay of distance-dependent long-range coherent dynamics and spatially correlated collective dissipation. We demonstrate that while the saddle-point equations predict a robust region of steady-state bistability—indicative of a first-order phase transition—incorporating interactions systematically via this field theory enables us to transcend the semiclassical picture. This rigorous approach allows us to calculate the critical scaling behavior in the vicinity of the nonequilibrium tricritical point, where the vanishing of the effective quartic coupling drives the system into a distinct universality class governed by higher-order interactions.

9.1 The Long-range Driven-Dissipative Ising Model

The dynamics of the microscopic spin system of interest are governed by the Lindblad master equation

$$\frac{\mathrm{d}\hat{\rho}}{\mathrm{d}t} = \hat{\mathcal{L}}_\sigma[\hat{\rho}] = -i[\hat{H}_\sigma, \hat{\rho}] + \hat{\mathcal{D}}_\sigma[\hat{\rho}], \tag{9.2}$$

where $\hat{\rho}$ is the density matrix of the spin ensemble. The coherent dynamics are dictated by the long-range quantum Ising Hamiltonian, which takes the form

$$\hat{H}_\sigma = -\sum_{i,j=1}^{N} J_{ij}\sigma_i^x\sigma_j^x + \Delta\sum_{i=1}^{N}\sigma_i^z, \tag{9.3}$$

where Δ is the single-atom excitation energy (or transverse field) and J_{ij} is a real, symmetric matrix characterizing the long-range interactions across the lattice.

The dissipative evolution of the system is modeled by a combination of local and correlated non-local jump operators. The general dissipative superoperator can be written as

$$\hat{\mathcal{D}}_\sigma[\hat{\rho}] = \sum_{i,j=1}^{N} \mathcal{K}_{ij}\left[\sigma_j^{\downarrow}\hat{\rho}\sigma_i^{\uparrow} - \frac{1}{2}\left\{\sigma_i^{\uparrow}\sigma_j^{\downarrow}, \hat{\rho}\right\}\right], \tag{9.4}$$

where $\mathcal{K}$ is a positive semi-definite Hermitian matrix ($\mathcal{K} = \mathcal{K}^\dagger$). Here, the operators $\sigma_i^{\uparrow} = \frac{1}{2}(\sigma_i^x + i\sigma_i^y)$ and $\sigma_i^{\downarrow} = \frac{1}{2}(\sigma_i^x - i\sigma_i^y)$ denote the local spin raising and lowering operators for the i-th site. Assuming that the matrix $\mathcal{K}$ possesses a minimum eigenvalue $\varepsilon > 0$, we can separate the dissipation matrix into a purely long-range component Γ_{ij} and a strictly local, on-site component $\varepsilon\delta_{ij}$, such that $\mathcal{K}_{ij} = \Gamma_{ij} + \varepsilon\delta_{ij}$. This assumption allows us to partition the full dissipator into non-local and local parts, $\hat{\mathcal{D}}_\sigma[\hat{\rho}] = \hat{\mathcal{D}}_{0,\sigma}[\hat{\rho}] + \hat{\mathcal{D}}_{1,\sigma}[\hat{\rho}]$, where:

$$\hat{\mathcal{D}}_{0,\sigma}[\hat{\rho}] = \sum_{i,j=1}^{N} \Gamma_{ij}\left[\sigma_j^{\downarrow}\hat{\rho}\sigma_i^{\uparrow} - \frac{1}{2}\left\{\sigma_i^{\uparrow}\sigma_j^{\downarrow}, \hat{\rho}\right\}\right], \tag{9.5a}$$

$$\hat{\mathcal{D}}_{1,\sigma}[\hat{\rho}] = \varepsilon \sum_{i=1}^{N} \left[\sigma_i^{\downarrow}\hat{\rho}\sigma_i^{\uparrow} - \frac{1}{2}\left\{\sigma_i^{\uparrow}\sigma_i^{\downarrow}, \hat{\rho}\right\}\right]. \tag{9.5b}$$

To facilitate a systematic field-theoretical treatment, we map the spin-$1/2$ algebra to a bosonic representation. We recast the system as a dissipative Bose-Hubbard model by replacing the spin lowering and raising operators with canonical bosonic annihilation and creation operators [270]: $\sigma_i^{\downarrow} \to \hat{a}_i$ and $\sigma_i^{\uparrow} \to \hat{a}_i^\dagger$. These operators satisfy the standard canonical commutation relations $[\hat{a}_i, \hat{a}_j^\dagger] = \delta_{ij}$ and $[\hat{a}_i, \hat{a}_j] = 0$. To faithfully enforce the Pauli exclusion principle of the original spin lattice, which prohibits multiple excitations on a single site, we introduce an infinite on-site hard-core repulsion term proportional to $U\hat{a}_i^\dagger\hat{a}_i(\hat{a}_i^\dagger\hat{a}_i - 1)$. In the limit where $U \gg \Delta, J_{ij}$, this penalty term effectively restricts the local bosonic Hilbert space to its lowest two levels, perfectly mirroring a two-level spin system.

Under this mapping, the equivalent bosonic Hamiltonian takes the explicit form

$$\hat{H}_b = 2\Delta \sum_{i=1}^{N} \hat{a}_i^\dagger\hat{a}_i + U \sum_{i=1}^{N} \hat{a}_i^\dagger\hat{a}_i(\hat{a}_i^\dagger\hat{a}_i - 1) - \sum_{i,j=1}^{N} J_{ij}(\hat{a}_i + \hat{a}_i^\dagger)(\hat{a}_j + \hat{a}_j^\dagger), \tag{9.6}$$

while the corresponding bosonic dissipator becomes $\hat{\mathcal{D}}_b[\hat{\rho}] = \hat{\mathcal{D}}_{0,b}[\hat{\rho}] + \hat{\mathcal{D}}_{1,b}[\hat{\rho}]$, governed by:

$$\hat{\mathcal{D}}_{0,b}[\hat{\rho}] = \sum_{i,j=1}^{N} \Gamma_{ij} \left[\hat{a}_j \hat{\rho} \hat{a}_i^\dagger - \frac{1}{2} \left\{ \hat{a}_i^\dagger \hat{a}_j, \hat{\rho} \right\} \right], \tag{9.7a}$$

$$\hat{\mathcal{D}}_{1,b}[\hat{\rho}] = \varepsilon \sum_{i=1}^{N} \left[\hat{a}_i \hat{\rho} \hat{a}_i^\dagger - \frac{1}{2} \left\{ \hat{a}_i^\dagger \hat{a}_i, \hat{\rho} \right\} \right]. \tag{9.7b}$$

This allows us to cleanly separate the total superoperator $\hat{\mathcal{L}}_b[\hat{\rho}]$ into non-local and local contributions

$$\hat{\mathcal{L}}_b[\hat{\rho}] = \hat{\mathcal{L}}_0[\hat{\rho}] + \hat{\mathcal{L}}_1[\hat{\rho}]. \tag{9.8}$$

Here, $\hat{\mathcal{L}}_1[\hat{\rho}]$ contains only the strictly local (on-site) terms proportional to Δ, ε, and U, while $\hat{\mathcal{L}}_0[\hat{\rho}]$ encapsulates all spatially extended coherent and dissipative interactions proportional to J_{ij} and Γ_{ij}. As we will demonstrate in the following section, this splitting is the necessary first step for constructing the Keldysh functional integral.

Finally, the full physical spin Lindbladian is then recovered by taking the infinite repulsion limit of this bosonic analog

$$\hat{\mathcal{L}}_\sigma[\hat{\rho}] = \lim_{U \to \infty} \hat{\mathcal{L}}_b[\hat{\rho}]. \tag{9.9}$$

9.2 Keldysh Field Theory for Long-Range Spin Models

While the Lindblad master equation (Eq. (9.2)) formally dictates the exact dynamics of the open quantum system, solving it exactly for a many-body lattice with long-range interactions is analytically and computationally intractable. To systematically investigate the nonequilibrium steady state—and importantly, to capture fluctuations and critical scaling beyond the mean-field level—we map the operator dynamics onto a Keldysh functional integral.

9.2.1 The Coherent State Path Integral

We begin by employing the vectorization isomorphism, often referred to as the Liouville space representation; see Section 3.2.2 for details. This maps the density matrix $\hat{\rho}$ to a state vector $|\hat{\rho}\rangle\rangle$ in a doubled Hilbert space [147]. In this representation, the linear Lindblad superoperator $\hat{\mathcal{L}}_b$ maps to a non-Hermitian matrix $\hat{\mathbb{L}}$ acting on $|\hat{\rho}\rangle\rangle$, and the trace operation corresponds to the overlap with the left-vector associated with the identity operator, $\langle\langle \hat{I}|$. The partition function of the spin system

is then recovered by taking the infinite repulsion limit of the bosonic analog: $Z_\sigma = \lim_{U\to\infty} Z_b$, where

$$Z_b = \mathrm{Tr}\{\hat{\rho}_b(t)\} = \mathrm{Tr}\left\{e^{t\hat{\mathbb{L}}_b}\hat{\rho}_0\right\} = \langle\langle \hat{I}|e^{t\hat{\mathbb{L}}_b}|\hat{\rho}_0\rangle\rangle. \tag{9.10}$$

However, because the local dissipation $\hat{\mathbb{L}}_1$ and the non-local coherent and dissipative interactions $\hat{\mathbb{L}}_0$ do not commute, they cannot be evaluated simultaneously. To isolate the local dynamics from the collective coupling, we apply the Suzuki-Trotter decomposition. Discretizing the total time into M intervals of length $\delta t = t/M$, we expand the evolution operator as

$$e^{t\hat{\mathbb{L}}_b} = \lim_{M\to\infty} (e^{\delta t\hat{\mathbb{L}}_0}e^{\delta t\hat{\mathbb{L}}_1})^M, \tag{9.11}$$

which is exact up to $O(\delta t^2)$ corrections.

At each time step n, we insert a resolution of the identity constructed from bosonic coherent states defined on the two branches of the doubled Hilbert space (the forward and backward legs of the Keldysh contour, labeled + and −, respectively) [153, 154]

$$|\boldsymbol{\eta}(t_n = n\delta t)\rangle\rangle = \left|\boldsymbol{\eta}^+(t_n)\right\rangle \times |\boldsymbol{\eta}^{-*}(t_n)\rangle, \tag{9.12}$$

where $\boldsymbol{\eta}_\pm = (\eta_1^\pm, \eta_2^\pm, ..., \eta_N^\pm)^T$ collectively labels the fields across all N lattice sites [68, 179].

By expanding the coherent state actions on both the forward (+) and backward (−) branches of the doubled Hilbert space, the non-local coherent and dissipative interactions exponentiate as

$$\begin{aligned}
&\langle\langle\boldsymbol{\eta}(t_n)|e^{\delta t\hat{\mathbb{L}}_0}e^{\delta t\hat{\mathbb{L}}_1}|\boldsymbol{\eta}(t_{n-1})\rangle\rangle = \langle\langle\boldsymbol{\eta}(t_n)| \\
&\exp\Bigg\{i\delta t\sum_{i,j=1}^{N}\Big[(2J_{ij}+i\Gamma_{ij}/2)\eta_i^{+*}(t_n)\eta_j^+(t_{n-1}) + (-2J_{ij}+i\Gamma_{ij}/2)\eta_j^-(t_n)\eta_i^{-*}(t_{n-1}) \\
&+ J_{ij}\big(\eta_i^{+*}(t_n)\eta_j^{+*}(t_n) - \eta_i^{-*}(t_{n-1})\eta_j^{-*}(t_{n-1}) + \eta_i^+(t_{n-1})\eta_j^+(t_{n-1}) - \eta_i^-(t_n)\eta_j^-(t_n)\big) \\
&- i\Gamma_{ij}\eta_j^+(t_{n-1})\eta_i^{-*}(t_{n-1})\Big]\Bigg\} \quad \times e^{\delta t\hat{\mathbb{L}}_1}|\boldsymbol{\eta}(t_{n-1})\rangle\rangle.
\end{aligned} \tag{9.13}$$

Assuming standard Keldysh continuity conditions where $\eta_i^\pm(t_{n-1}) = \eta_i^\pm(t_n) + O(\delta t)$, we can approximate the fields at t_{n-1} with those at t_n within the exponential. Rewriting the double sums in a compact matrix-vector notation over the spatial lattice (and dropping the time argument), the

matrix element simplifies to

$$\langle\langle \boldsymbol{\eta}(t_n)|e^{\delta t\hat{\mathbb{L}}_0}e^{\delta t\hat{\mathbb{L}}_1}|\boldsymbol{\eta}(t_{n-1})\rangle\rangle \approx \langle\langle \boldsymbol{\eta}(t_n)|\exp\Big\{i\delta t\Big[\boldsymbol{\eta}^{+\dagger}(2\boldsymbol{J}+i\boldsymbol{\Gamma}/2)\boldsymbol{\eta}^{+}+\boldsymbol{\eta}^{-\dagger}(-2\boldsymbol{J}+i\boldsymbol{\Gamma}/2)\boldsymbol{\eta}^{-}$$
$$-i\boldsymbol{\eta}^{-\dagger}\boldsymbol{\Gamma}\boldsymbol{\eta}^{+}+\boldsymbol{\eta}^{+\dagger}\boldsymbol{J}\boldsymbol{\eta}^{+*}+\boldsymbol{\eta}^{+T}\boldsymbol{J}\boldsymbol{\eta}^{+}-\boldsymbol{\eta}^{-\dagger}\boldsymbol{J}\boldsymbol{\eta}^{-*}-\boldsymbol{\eta}^{-T}\boldsymbol{J}\boldsymbol{\eta}^{-}\Big]\Big\}e^{\delta t\hat{\mathbb{L}}_1}|\boldsymbol{\eta}(t_{n-1})\rangle\rangle. \tag{9.14}$$

To express this non-local weight in a physically-suggestive form, we separate the complex coherent fields into their real and imaginary components by defining the real, c-number fields $S^{\alpha}_{\pm}(t_n)$ via $\eta_{j,\pm}(t_n) = \frac{1}{2}(S^{x}_{j,\pm}(t_n) - iS^{y}_{j,\pm}(t_n))$. Grouping these spatial vectors into a generalized Nambu spinor at each time step, $\vec{\boldsymbol{S}}(t_n) = (\boldsymbol{S}^{x}_{+}(t_n), \boldsymbol{S}^{y}_{+}(t_n), -\boldsymbol{S}^{x}_{-}(t_n), -\boldsymbol{S}^{y}_{-}(t_n))^T$, the matrix element evaluates to a compact Gaussian weight

$$\langle\langle \boldsymbol{\eta}(t_n)|e^{\delta t\hat{\mathbb{L}}_0}e^{\delta t\hat{\mathbb{L}}_1}|\boldsymbol{\eta}(t_{n-1})\rangle\rangle = \langle\langle \boldsymbol{\eta}(t_n)|\exp\Big\{\Big(i\delta t\vec{\boldsymbol{S}}^{T}(t_n)\boldsymbol{D}^{-1}\vec{\boldsymbol{S}}(t_n)\Big)\Big\}e^{\delta t\hat{\mathbb{L}}_1}|\boldsymbol{\eta}(t_{n-1})\rangle\rangle, \tag{9.15}$$

where the non-local matrix $\boldsymbol{D}^{-1}$ takes the form

$$\boldsymbol{D}^{-1} = \frac{1}{2}\begin{pmatrix} 8\boldsymbol{J}+i\boldsymbol{\Gamma} & 0 & i\boldsymbol{\Gamma} & -\boldsymbol{\Gamma} \\ 0 & i\boldsymbol{\Gamma} & \boldsymbol{\Gamma} & i\boldsymbol{\Gamma} \\ i\boldsymbol{\Gamma} & \boldsymbol{\Gamma} & -8\boldsymbol{J}+i\boldsymbol{\Gamma} & 0 \\ -\boldsymbol{\Gamma} & i\boldsymbol{\Gamma} & 0 & i\boldsymbol{\Gamma} \end{pmatrix}. \tag{9.16}$$

Here, $\boldsymbol{J}$ and $\boldsymbol{\Gamma}$ are the matrices with spatial elements J_{ij} and Γ_{ij}. In the last few steps, we have explicitly enforced reciprocity on the dissipation ($\boldsymbol{\Gamma} = \boldsymbol{\Gamma}^T$).

9.2.2 Hubbard–Stratonovich Transformation

The presence of the non-local matrices $\boldsymbol{J}$ and $\boldsymbol{\Gamma}$ in the Gaussian weight directly couples the degrees of freedom across the entire lattice, prohibiting a straightforward evaluation of the partition function. To decouple these spatial modes and reduce the problem to an effective single-site theory, we apply a Hubbard-Stratonovich (HS) transformation. First, we introduce four species of real, scalar auxiliary fields $\boldsymbol{m}^{\alpha}_{n,\pm}$ (yielding $4N$ fields in total) to decouple the interactions. Here, α labels the spin component

$$\alpha \in \{x, y\}. \tag{9.17}$$

Because the system is assumed to be translationally invariant, this decoupling is most naturally performed in Fourier space. We define the transforms $S^{\alpha}_{j,\pm} = \frac{1}{N}\sum_k e^{ikj} S^{\alpha}_{k,\pm}$ and diagonalize the interaction matrices to yield

$$J_k = \frac{1}{N}\sum_r J_r \cos kr, \tag{9.18a}$$

$$\Gamma_k = \frac{1}{N}\sum_r \Gamma_r \cos kr. \tag{9.18b}$$

While the matrix elements J_{ij} and Γ_{ij} are $O(1/N)$, J_r and Γ_r are $O(1)$, e.g., $J_{i,i+r} = J_r/N$

Applying the HS transformation to the non-local weight for a single momentum mode k yields the following structure

$$\exp\left\{\left(\frac{i\delta t}{4N}\vec{S}^T_{-k} D^{-1}(k)\vec{S}_k\right)\right\} = \int \mathcal{D}[\vec{m}_k] \exp\left(\frac{iN}{\delta t}\vec{m}^T_{-k} D(k)\vec{m}_k + i\vec{m}^T_{-k}\vec{S}_k\right). \tag{9.19}$$

Due to the Hamiltonian structure, one may expect HS to only diagonal couple the fields, i.e., introduce $m^{x/y}S^{x/y}$ terms. However, this can no longer be the case since the non-local jump term explicitly couple the S^x and S^y fields across the upper and lower Keldysh branches (as seen in the off-diagonal terms ($\propto \mathbf{\Gamma}$) of the $\boldsymbol{D}^{-1}$ matrix in Eq. (9.16)). We introduce the auxiliary spinor $\vec{m}_k$ ordered as $\vec{m}_k = (m^y_{k,+}, m^x_{k,+}, m^y_{k,-}, m^x_{k,-})^T$ purely as a mathematical convenience; it ensures the resulting matrix blocks of $D(k)$ maintain a symmetric structure and will help establish a transparent mapping to physical observables in Section 9.2.4.

The validity of this transformation can be readily verified, as evaluating the Gaussian integral over the auxiliary fields on the rhs straightforwardly recovers the original expression on the lhs. Finally, to absorb the temporal scaling and ensure a well-defined continuum limit, we rescale the auxiliary fields via $m^{\alpha}_{k,\pm} \to \delta t\, m^{\alpha}_{k,\pm}$.

Having decoupled the spatial modes, we can now absorb the linear terms ($\propto i\sum_k \vec{m}^T_{-k}(t_n)\vec{S}_k(t_n)$) back into the single-site operator. By applying the inverse Fourier transform to the linear terms, the coupling between the auxiliary fields and the physical variables is recast in real space as

$$i\sum_{j=1}^{N} \vec{m}^T_j(t_n)\vec{S}_j(t_n).$$

At this stage, we may restore the operator form, effectively replacing the c-numbers fields $\vec{S}_j(t_n)$ with their corresponding bosonic operators.

The full partition function can then be written compactly as

$$\begin{aligned} Z_b = \lim_{M\to\infty} \int \prod_{n=0}^{M} \mathcal{D}[\boldsymbol{\eta}^+(t_n), \boldsymbol{\eta}^{+*}(t_n)] \mathcal{D}[\boldsymbol{\eta}^-(t_n), \boldsymbol{\eta}^{-*}(t_n)] \left(\prod_k \mathcal{D}[\vec{m}_k(t_n)] \right) \\ \times \left(\prod_{n=1}^{M} \exp\left\{ i\delta t N \sum_k \vec{m}^T_{-k}(t_n) D(k) \vec{m}_k(t_n) \right\} \right) \times \langle\langle \hat{I} | \boldsymbol{\eta}(t_M) \rangle\rangle \\ \times \left[\prod_{n=1}^{M} \langle\langle \boldsymbol{\eta}(t_n) | e^{\delta t \sum_{j=1}^{N} \hat{\mathbb{T}}^b_j(t_n)} | \boldsymbol{\eta}(t_{n-1}) \rangle\rangle \right] \langle\langle \boldsymbol{\eta}(t_0) | \hat{\rho}_0 \rangle\rangle. \end{aligned} \tag{9.20}$$

The exponential functions are now independent of the fields $\eta^{\pm}$, and the complete coherent state basis can be simply replaced by identities. Here, the operator $\hat{\mathbb{T}}^b_j(t_n)$ acts only on a single lattice site j. It incorporates both the strictly local coherent and dissipative processes ($\hat{\mathbb{L}}_{1,j}$) and the dynamic, time-dependent coupling to the Hubbard-Stratonovich fields

$$\hat{\mathbb{T}}^b_j(t_n) = \hat{\mathbb{L}}_{1,j} + i \begin{pmatrix} m^y_{j,+}(t_n) \\ m^x_{j,+}(t_n) \\ m^y_{j,-}(t_n) \\ m^x_{j,-}(t_n) \end{pmatrix}^T \begin{pmatrix} 1 & 1 & 0 & 0 \\ i & -i & 0 & 0 \\ 0 & 0 & -1 & -1 \\ 0 & 0 & i & -i \end{pmatrix} \begin{pmatrix} \hat{a}_{j,+} \\ \hat{a}^\dagger_{j,+} \\ \hat{a}_{j,-} \\ \hat{a}^\dagger_{j,-} \end{pmatrix}, \tag{9.21}$$

where the contribution of the purely local bosonic Lindbladian is explicitly given by

$$\begin{aligned} \hat{\mathbb{L}}_{1,j} = &-2i\Delta(\hat{a}^\dagger_{j,+}\hat{a}_{j,+} - \hat{a}^\dagger_{j,-}\hat{a}_{j,-}) + \varepsilon \hat{a}_{j,+}\hat{a}_{j,-} - \frac{\varepsilon}{2}(\hat{a}^\dagger_{j,+}\hat{a}_{j,+} + \hat{a}^\dagger_{j,-}\hat{a}_{j,-}) \\ &- iU(\hat{a}^\dagger_{j,+}\hat{a}^\dagger_{j,+}\hat{a}_{j,+}\hat{a}_{j,+} - \hat{a}^\dagger_{j,-}\hat{a}^\dagger_{j,-}\hat{a}_{j,-}\hat{a}_{j,-}). \end{aligned} \tag{9.22}$$

In the preceding equations, we have utilized the standard notation $\hat{O}_+ = \hat{O} \otimes \hat{I}$ and $\hat{O}_- = \hat{I} \otimes \hat{O}$ for operators acting on the forward (upper) and backward (lower) branches of the Keldysh contour, respectively.

The mathematical and physical significance of the Hubbard-Stratonovich transformation lies in its ability to exactly reduce an interacting many-body problem into a single-body problem subjected to a fluctuating background field. By introducing the auxiliary fields $\vec{m}_k$ via the HS transformation, we mathematically trade these two-body spin-spin interactions for single-body operators coupled

linearly to the auxiliary fields. Physically, this implies that the spins no longer interact directly with one another; instead, every individual spin interacts locally with a shared, dynamically fluctuating field represented by m.

9.2.3 The Continuum Limit and the Effective Action

We proceed by taking the continuum limit ($\delta t \to 0$), which allows us to write the partition function as a functional integral over the auxiliary Hubbard-Stratonovich fields $\vec{m}_k(t)$

$$Z_b = \int \left(\prod_k \mathcal{D}[\vec{m}_k(t)] \right) e^{i\mathcal{S}_b}, \tag{9.23}$$

where the continuum action $\mathcal{S}_b$ consists of a free quadratic term and a non-local trace-log term

$$\mathcal{S}_b = \int_t \left[N \sum_k \vec{m}_{-k}^T D(k) \vec{m}_k \right] - i \sum_{j=1}^{N} \ln \mathrm{Tr} \left\{ \mathcal{T} e^{\int_t \hat{\mathbb{T}}_{b,j}(t)} \right\}, \tag{9.24}$$

with $\mathcal{T}$ denoting the time-ordering operator and the shorthand notation $\int_t = \int_{-\infty}^{\infty} dt$.

At this stage, we are uniquely positioned to revert from the bosonic mapping back to the exact spin representation. By explicitly taking the limit $U \to \infty$, the local bosonic states with two or more excitations are infinitely penalized and projected out of the dynamics. The single-site matrix $\hat{\mathbb{T}}_j^b(t)$ thus maps exactly onto the spin operator $\hat{\mathbb{T}}_j^\sigma(t)$, and the partition function becomes Z_σ.

Further, to clarify the physical meaning of the auxiliary fields, we perform a standard Keldysh rotation, decomposing the fields defined on the forward and backward contours into classical (c) and quantum (q) components

$$m_{k,c/q}^\alpha = \frac{1}{\sqrt{2}} (m_{k,+}^\alpha \pm m_{k,-}^\alpha). \tag{9.25}$$

Applying this rotation to the fields and the corresponding spin operators, the exact Keldysh action governing the long-range driven-dissipative Ising model is given in its final form by

$$\mathcal{S}_\sigma = \int_t \left[N \sum_k \vec{m}_{-k}^T D_k^{\mathrm{K}} \vec{m}_k \right] - i \sum_{j=1}^{N} \ln \mathrm{Tr} \left\{ \mathcal{T} e^{\int_t \hat{\mathbb{T}}_j^\sigma(t)} \right\}, \tag{9.26}$$

with the Keldysh spinor $\vec{m}_k = (m_{k,c}^y, m_{k,c}^x, m_{k,q}^y, m_{k,q}^x)^T$. Crucially, the upper-left 2×2 block of the free propagator matrix D_k^{K} evaluates to identically zero, reflecting the fundamental causality

structure inherent to the Keldysh formalism. The remaining blocks define the bare inverse retarded, advanced, and Keldysh propagators

$$D_k^{\mathrm{K}} = \frac{2}{\Gamma_k}\begin{pmatrix} 0 & 0 & 0 & -1 \\ 0 & 0 & 1 & -8J_k\Gamma_k^{-1} \\ 0 & 1 & 2i & -16iJ_k\Gamma_k^{-1} \\ -1 & -8J_k\Gamma_k^{-1} & -16iJ_k\Gamma_k^{-1} & 2i + 128iJ_k^2\Gamma_k^{-2} \end{pmatrix}, \tag{9.27}$$

where, the local operator $\hat{\mathbb{T}}_j^{\sigma}(t)$ couples the exact spin algebra to the dynamically fluctuating fields

$$\hat{\mathbb{T}}_j^{\sigma}(t) = \hat{\mathbb{L}}_{1,j}^{\sigma} + i\sum_k e^{ikj}\left[m_{k,c}^y\hat{\Sigma}_{j,q}^x + m_{k,q}^y\hat{\Sigma}_{j,c}^x + m_{k,c}^x\hat{\Sigma}_{j,q}^y + m_{k,q}^x\hat{\Sigma}_{j,c}^y\right], \tag{9.28}$$

where $\hat{\mathbb{L}}_{1,j}^{\sigma}$ is the time-independent, purely local Liouvillian superoperator in the spin representation

$$\hat{\mathbb{L}}_{1,j}^{\sigma} = -i\Delta(\sigma_{j,+}^z - \sigma_{j,-}^z) + \varepsilon\sigma_{j,+}^{\downarrow}\sigma_{j,-}^{\downarrow} - \frac{\varepsilon}{2}(\sigma_{j,+}^{\uparrow}\sigma_{j,+}^{\downarrow} + \sigma_{j,-}^{\uparrow}\sigma_{j,-}^{\downarrow}), \tag{9.29}$$

and the rotated spin operators are defined as

$$\hat{\Sigma}_{j,c/q}^{\alpha} = \frac{1}{\sqrt{2}}(\sigma_{j,+}^{\alpha} \pm \sigma_{j,-}^{\alpha\,T}). \tag{9.30}$$

By exactly reformulating the many-body master equation as a functional integral over the fields $\vec{m}_k$, Eq. (9.26) serves as the starting point for evaluating the dynamics leading to the nonequilibrium steady state.

9.2.4 Relevant Field-Spin Relations

Before we discuss the physics encapsulated in the effective action given in Eq. (9.26), we must establish a rigorous dictionary relating the auxiliary HS fields to the physical spin observables. To compute expectation values and correlation functions for the spin operators, we introduce generating source fields, which we label $\beta_{c/q}^{\alpha}$, directly into the Keldysh action.

Introducing these source fields effectively adds a linear driving term to the local matrix $\hat{\mathbb{T}}_j^{\sigma}(t)$

$$i\sum_k e^{ikj}\left(\beta_{k,c}^y\hat{\Sigma}_{j,q}^x + \beta_{k,q}^y\hat{\Sigma}_{j,c}^x + \beta_{k,c}^x\hat{\Sigma}_{j,q}^y + \beta_{k,q}^x\hat{\Sigma}_{j,c}^y\right). \tag{9.31}$$

To absorb these sources and restore $\hat{\mathbb{T}}_j^{\sigma}(t)$ to its original form, we perform a linear shift of the integration variables in the path integral

$$m^{\alpha}_{k,c/q} \to m^{\alpha}_{k,c/q} - \beta^{\alpha}_{k,c/q}. \tag{9.32}$$

Under this transformation, the source fields are shifted entirely into the quadratic part of the free action. The physical observables are then generated by taking functional derivatives of the partition function Z_{σ} with respect to the corresponding quantum or classical source fields and subsequently setting $\beta^{\alpha}_{c/q} \to 0$.

9.2.4.1 Magnetization

The expectation value of the magnetization $\langle \sigma^x_j(t) \rangle$, which serves as our primary order parameter, is obtained from the first functional derivative of the partition function with respect to the quantum source field $\beta^x_{j,q}$. In the Keldysh basis, this relates the physical spin expectation value directly to the classical component of the auxiliary field m^x_c

$$\langle \sigma^x_j(t) \rangle = -2\sqrt{2} \sum_k e^{ikj} \Gamma_k^{-1} \langle m^x_{k,c}(t) \rangle. \tag{9.33}$$

9.2.4.2 Symmetrized Correlation Function

To capture the steady-state fluctuations of the order parameter, we compute the symmetrized two-point correlation function, defined as $C_{ij}(t,t') = \langle \{ \sigma^x_i(t), \sigma^x_j(t') \} \rangle$. Taking the appropriate second functional derivatives reveals that this physical correlation function is a composite of both the classical-classical autocorrelations of the m^x field and cross-correlations involving the quantum components

$$\begin{aligned} \langle \{ \sigma^x_i(t), \sigma^x_j(t') \} \rangle = 16 \sum_k e^{-ik(i-j)} \Gamma_k^{-2} \Big[& \langle m^x_{-k,c}(t) m^x_{k,c}(t') \rangle \\ & + 2i \big(\langle m^y_{-k,q}(t) m^x_{k,c}(t') \rangle + \langle m^x_{-k,c}(t) m^y_{k,q}(t') \rangle \big) \\ & - 16 i J_k \Gamma_k^{-1} \big(\langle m^x_{-k,q}(t) m^x_{k,c}(t') \rangle + \langle m^x_{-k,c}(t) m^x_{k,q}(t') \rangle \big) \Big]. \end{aligned} \tag{9.34}$$

9.2.4.3 Response Function

Finally, the dynamical response of the system to external perturbations is characterized by the linear response function (the retarded Green's function), defined via the commutator $\chi_{ij}(t,t') = -i\theta(t-t')\langle[\sigma_i^x(t),\sigma_j^x(t')]\rangle$. In the Keldysh formalism, this causal response is strictly governed by the mixed quantum-classical correlations of the fields

$$\langle[\sigma_i^x(t),\sigma_j^x(t')]\rangle = 16\sum_k e^{-ik(i-j)}\Gamma_k^{-2}\Big[\langle m^x_{-k,q}(t)m^x_{k,c}(t')\rangle - \langle m^x_{-k,c}(t)m^x_{k,q}(t')\rangle\Big]. \tag{9.35}$$

With these relations, the properties of the physical spin system can be fully diagnosed by analyzing the Green's functions of the auxiliary fields.

9.2.5 Saddle-Point Solution and Bistability in the Steady State

With the exact Keldysh action and the field-spin dictionary established, we can now investigate the steady-state phase diagram. The decoupling of the momentum modes in the effective action allows us to obtain a saddle-point solution for the model. Physically, in the thermodynamic limit ($N \to \infty$), a saddle-point solution assumes that the path integral is overwhelmingly dominated by the extrema of the action.

Assuming the system relaxes into a spatially homogeneous steady state (preserving translational invariance), the classical fields become site-independent constants, $m^{x/y}_{j,c} = m_{x/y}$. By definition, the quantum fields must vanish at the saddle point in order to respect the causality structure of the action, $m^{x/y}_{j,q} = 0$. In momentum space, this configuration corresponds to a macroscopic occupation of solely the zero-momentum mode

$$m^{\alpha}_{k=0,c} = m_\alpha, \tag{9.36}$$

with all finite-momentum fields set identically to zero. We determine these stationary states by minimizing the action with respect to the quantum fields by demanding

$$\left.\frac{\delta\mathcal{S}_\sigma}{\delta m^x_{k,q}}\right|_{\mathrm{SP}} = 0, \quad \left.\frac{\delta\mathcal{S}_\sigma}{\delta m^y_{k,q}}\right|_{\mathrm{SP}} = 0. \tag{9.37}$$

The variation of the Gaussian part of the action is straightforward; it yields linear terms proportional to the classical fields $m_{x/y}$. The non-trivial contribution arises from the functional derivative of the trace-log part of the action, $-i\sum_{j=1}^N \ln \mathrm{Tr}\left[\mathcal{T}e^{\int_t \hat{\mathbb{T}}^\sigma_j(t)}\right]$.

Applying the chain rule, the variation of the logarithm introduces the unperturbed partition function in the denominator, while the functional derivative of the time-ordered exponential brings down the operator $\delta\hat{\mathbb{T}}_j^\sigma/\delta m^\alpha_{k=0,q}$ inside the trace. Evaluating this variation at the spatially homogeneous saddle point (where $m^\alpha_{j,c} = m_\alpha$ and $m^\alpha_{j,q} = 0$) over the time interval from t_i to t_f yields

$$\frac{\mathrm{Tr}\left[e^{(t_f-t)\hat{\mathbb{T}}_j^{\mathrm{SP}}}\left(\frac{\delta\hat{\mathbb{T}}_j^\sigma}{\delta m^\alpha_{k=0,q}}\right)e^{(t-t_i)\hat{\mathbb{T}}_j^{\mathrm{SP}}}\right]}{\mathrm{Tr}\left[e^{(t_f-t_i)\hat{\mathbb{T}}_j^{\mathrm{SP}}}\right]} = \langle\langle\hat{\mathbb{I}}|\left(\frac{\delta\hat{\mathbb{T}}_j^\sigma}{\delta m^\alpha_{k=0,q}}\right)|\mathrm{SS}\rangle\rangle. \tag{9.38}$$

Here, $\hat{\mathbb{T}}_j^{\mathrm{SP}}$ is the local effective Liouvillian $\hat{\mathbb{T}}_j^\sigma$ evaluated at the self-consistent classical saddle-point configuration. The crucial equality on the right-hand side is obtained by taking the asymptotic limit $t_i \to -\infty$. In this long-time limit, all transient dynamics decay, and the evolution is entirely dominated by the nonequilibrium steady state, denoted by $|\mathrm{SS}\rangle\rangle$. Mathematically, $|\mathrm{SS}\rangle\rangle$ is the unique right eigenvector of the local superoperator $\hat{\mathbb{T}}_j^{\mathrm{SP}}$ corresponding to the non-negative (zero) eigenvalue. Consequently, the trace operation formally collapses into a simple projection, evaluating the expectation value over this steady state of the effective single-site problem.

Furthermore, recalling the structure of the local operator $\hat{\mathbb{T}}_j^\sigma(t)$, the quantum auxiliary fields m_q^α couple exclusively to the classical components of the spin operators, $\hat{\Sigma}^\alpha_{j,c}$, in the Keldysh basis. Therefore, the variation with respect to m_q^α precisely extracts the steady-state expectation value of the physical spin. Equating these expectation values with the linear terms from the Gaussian variation (Eq. (9.37)) yields the coupled, non-linear algebraic equations governing the macroscopic steady state

$$0 = m_x + \frac{\Gamma_0(4\Delta m_y + \varepsilon m_x)}{\varepsilon^2 + 16\Delta^2 + 4(m_x^2 + m_y^2)}, \tag{9.39a}$$

$$0 = -m_y - 8\frac{J_0}{\Gamma_0}m_x + \frac{\Gamma_0(4\Delta m_x - \varepsilon m_y)}{\varepsilon^2 + 16\Delta^2 + 4(m_x^2 + m_y^2)}. \tag{9.39b}$$

These equations always admit the trivial paramagnetic solution, $m_x = m_y = 0$. However, depending on the competition between the transverse field Δ, the coherent coupling J_0, and the collective dissipation Γ_0, non-trivial symmetry-broken solutions may emerge. Defining the auxiliary

parameter $\Lambda = \sqrt{J_0^2\Delta^3(16J_0^2\Delta - \Gamma_0^2\Delta - 2J_0\Gamma_0\varepsilon)}$, the non-trivial roots are given by

$$m_x = \frac{s_1}{2\sqrt{2}}\sqrt{\frac{4s_2\Lambda + J_0\Delta[\Gamma_0(\varepsilon+\Gamma_0) - 16J_0\Delta]}{J_0^2}}, \tag{9.40a}$$

$$m_y = -s_1\frac{\left(4J_0^2\Delta^2 - s_2\Lambda\right)}{4J_0\Delta^2}|m_x|, \tag{9.40b}$$

where $s_1, s_2 \in \{+1, -1\}$ denote the distinct solution branches. Physical validity strictly requires that the fields remain real-valued ($m_{x/y} \in \mathbb{R}$). Utilizing the relation $\langle\sigma^x\rangle \propto m_x$ derived in Eq. (9.33), these roots map precisely onto the mean-field solutions derived independently via the Heisenberg equations of motion (as detailed in appendix 9A).

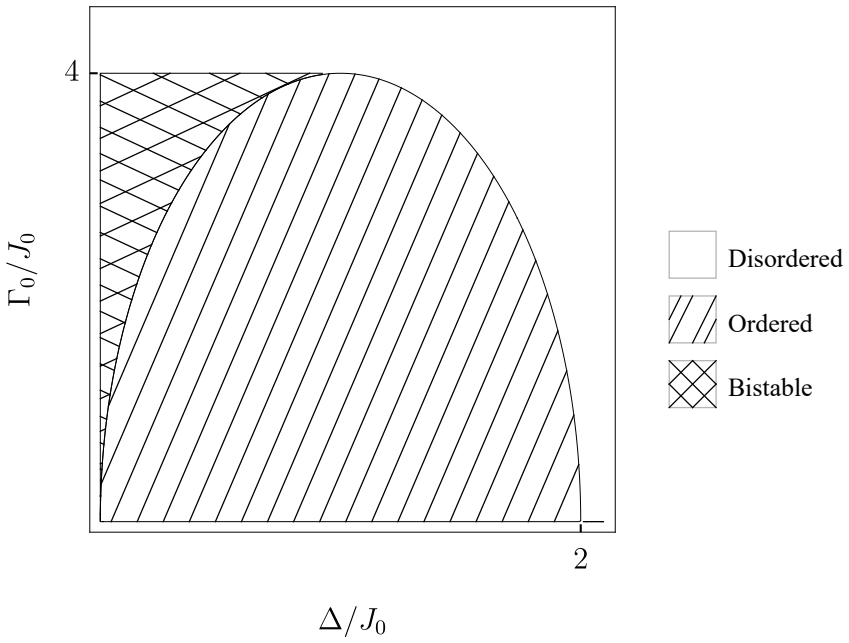

Figure 9.1 Mean-field phase diagram in the steady state taking the limit $\varepsilon \to 0$. The diagram highlights three distinct regimes: disordered (white), ordered (diagonal lines), and bistable (crossed lines).

Physically, mapping the boundaries where these real roots exist reveals a region of bistability, where all branches represent valid solutions. We discuss this in Fig. 9A.1. Specifically, in the limit $\varepsilon \to 0$ and for $\Delta < J_0$, the system enters a regime where two distinct stable attractors coexist: the disordered state ($m_x = m_y = 0$) and the ordered branch ($s_2 = 1$). The complementary branch ($s_2 = -1$) acts as an unstable saddle point separating the ordered and disordered basins of attrac-

tion. The structure, shown in Fig. 9.1, indicates that the magnetic transition becomes first-order (discontinuous) for $\Delta/J_0 < 1$ in the presence of collective dissipation Γ_0. Consequently, the point where the bistable region vanishes corresponds to a nonequilibrium *tricritical* point, marking the termination of the first-order transition line and the onset of the continuous second-order critical line.

9.2.6 Quadratic Action: Identifying the the Soft Mode

Having established the saddle-point solutions, we now turn our attention to the fluctuations around the trivial paramagnetic steady state, $m_{x/y} = 0$. In this regime, the local steady state of the non-interacting system reduces to the simple vacuum state, $|\mathrm{SS}\rangle\rangle_{m=0} = |\mathrm{vac}\rangle\rangle = |\downarrow\downarrow\rangle\rangle$. By expanding the exact Keldysh action to quadratic order in the fluctuation fields $\delta m^{x/y}_{k,c/q}$, we can systematically diagnose the dynamical stability of the system and identify the onset of critical slowing down.

The quadratic contribution to the effective action takes the form of a Gaussian field theory

$$\mathcal{S}^{(2)} = \frac{1}{2}\int_\omega \sum_k \vec{m}^T_{-k}(-\omega)\boldsymbol{\mathcal{S}}_2(k,\omega)\vec{m}_k(\omega), \tag{9.41}$$

where $\int_\omega$ is shorthand for $\frac{d\omega}{2\pi}$, and we have absorbed a factor of $\sqrt{N}$ into the definition of the fields. The frequency-domain fields are defined via the standard Fourier transform, $m^\alpha_{k,c/q}(\omega) = \int_t e^{i\omega t} m^\alpha_{k,c/q}(t)$.

The inverse propagator matrix $\boldsymbol{\mathcal{S}}_2(k,\omega)$ exhibits the fundamental Keldysh structure

$$\boldsymbol{\mathcal{S}}_2(k,\omega) = \begin{pmatrix} \mathbf{0} & P^{\mathrm{A}}(k,\omega) \\ P^{\mathrm{R}}(k,\omega) & P^{\mathrm{K}}(k,\omega) \end{pmatrix}. \tag{9.42}$$

The 2×2 blocks P^{R}, P^{A}, and P^{K} correspond to the inverse retarded, advanced, and Keldysh Green's functions, respectively, defined by the second-order functional derivatives with respect to the Keldysh spinors $\vec{m}_{k,c/q}(\omega) = (m^y_{k,c/q}(\omega), m^x_{k,c/q}(\omega))^T$.

$$P^{\mathrm{R}}(k,\omega) = [P^{\mathrm{A}}(k,\omega)]^\dagger = \frac{\delta \mathcal{S}_\sigma}{\delta \vec{m}_{-k,q}(-\omega)\delta \vec{m}^T_{k,c}(\omega)}, \tag{9.43a}$$

$$P^{\mathrm{K}}(k,\omega) = \frac{\delta \mathcal{S}_\sigma}{\delta \vec{m}_{-k,q}(-\omega)\delta \vec{m}^T_{k,q}(\omega)}. \tag{9.43b}$$

In the strictly global dissipation limit ($\varepsilon \to 0$), these matrices take the explicit forms

$$P^{\mathrm{R}}(k,\omega) = [P^{\mathrm{A}}(k,\omega)]^{\dagger} = \frac{4}{\Gamma_k}\begin{pmatrix} \frac{\Delta\Gamma_k}{4\Delta^2-\omega^2} & 1-\frac{i\omega\Gamma_k}{2(4\Delta^2-\omega^2)} \\ -\left[1-\frac{i\omega\Gamma_k}{2(4\Delta^2-\omega^2)}\right] & \frac{\Delta\Gamma_k}{4\Delta^2-\omega^2}-\frac{8J_k}{\Gamma_k} \end{pmatrix}, \tag{9.44a}$$

$$P^{\mathrm{K}}(k,\omega) = 8i\Gamma_k\begin{pmatrix} 1 & -\frac{8J_k}{\Gamma_k} \\ -\frac{8J_k}{\Gamma_k} & 1+\left(\frac{8J_k}{\Gamma_k}\right)^2 \end{pmatrix}. \tag{9.44b}$$

The dynamical response of the system and its relaxation timescales are entirely governed by the poles of the retarded Green's function $[P^{\mathrm{R}}(k,\omega)]^{-1}$. Solving for the roots of $\det P^{\mathrm{R}}(k,\omega) = 0$ yields two complex eigenfrequencies

$$\omega_1(k) = -\frac{i}{2}(\Gamma_k - \bar{\Gamma}_k), \tag{9.45a}$$

$$\omega_2(k) = -\frac{i}{2}(\Gamma_k + \bar{\Gamma}_k), \tag{9.45b}$$

where we have defined the parameter

$$\bar{\Gamma}_k = 4\sqrt{\Delta(2J_k - \Delta)}. \tag{9.46}$$

A continuous phase transition may occur when the system exhibits critical slowing down, corresponding to a closing of the Liouvillian spectral gap. This manifests as a pole approaching the real frequency axis, $\mathrm{Im}[\omega_1(k)] \to 0$. We therefore identify $\omega_1(k)$ as the frequency of the critical gapless (soft) mode, which dictates the macroscopic ordering, while $\omega_2(k)$ represents a massive, heavily damped gapped mode.

At the critical phase boundary, the collective dissipation satisfies $\Gamma_{k=0} = \bar{\Gamma}_{k=0} \equiv \Gamma_c$, and the static function $P^{\mathrm{R}}(k,\omega=0)$ becomes singular. The critical value Γ_c defines the dome in Fig. 9.1. To properly isolate the critical fluctuations from the massive background, we must diagonalize the static retarded matrix. Because the effective kernel $P^{\mathrm{R}}(k,\omega=0)$ is real and non-Hermitian, this diagonalization takes the form $P^{\mathrm{R}}(k,\omega=0) = U\Lambda U$ [181], where the diagonal matrix $\Lambda = \mathrm{diag}(0,-\delta)$ separates the zero eigenvalue of the soft mode from the mass $\delta = 2J_k/\Delta(\Delta - 2J_k)$ of the massive mode. The transformation matrix is explicitly given by

$$U = \frac{1}{\sqrt{2\Delta J_k}}\begin{pmatrix} \Delta & -\bar{\Gamma}_k/4 \\ \bar{\Gamma}_k/4 & \Delta \end{pmatrix}. \tag{9.47}$$

This rotation physically motivates a transformation from our original auxiliary fields $m^{x/y}$ to the eigenbasis of system near criticality, spanned by the gapless field ϕ_k and the gapped field ζ_k

$$\begin{pmatrix} \phi_c \\ \zeta_c \end{pmatrix}_k = U \begin{pmatrix} m_c^y \\ m_c^x \end{pmatrix}_k, \quad \text{and} \quad \begin{pmatrix} \phi_q \\ \zeta_q \end{pmatrix}_k = U^T \begin{pmatrix} m_q^y \\ m_q^x \end{pmatrix}_k . \tag{9.48}$$

By expressing the Keldysh action in terms of ϕ and ζ, we can formally integrate out the massive, fast-relaxing ζ fields to construct a low-energy effective field theory defined solely in terms of the gapless order parameter ϕ. This reduction is the essential prerequisite for executing the higher-order expansions needed to probe the phase transition.

9.2.7 Correlation and Response Functions

The physical observables are accessed directly via the correlation and response functions of the spin operators, which are intimately tied to the fluctuations of the auxiliary fields. Using the quadratic action in Eq. (9.41), we utilize the field-spin relations introduced in Section 9.2.4 to derive the symmetrized spin correlation function $C_{ij}(t-t')$ and the linear response function $\chi_{ij}(t-t')$ given by

$$\begin{aligned} C_{ij}(t-t') &= \left\langle \left\{ \sigma_i^x(t), \sigma_j^x(t') \right\} \right\rangle_{\text{SS}} \\ &= \sum_k e^{-ik(i-j)} C_k(t-t'), \end{aligned} \tag{9.49a}$$

$$\begin{aligned} \chi_{ij}(t-t') &= -i \left\langle \left[\sigma_i^x(t), \sigma_j^x(t') \right] \right\rangle_{\text{SS}} \\ &= -i \sum_k e^{-ik(i-j)} \chi_k(t-t'). \end{aligned} \tag{9.49b}$$

In the frequency domain, the $C_k(\omega)$ and $\chi_k(\omega)$ take the form

$$C_k(\omega) = -\frac{8\left(\Gamma_k^2\left(4\omega^2 - 32\Delta J_k - \bar{\Gamma}_k^2\right) + \left(4\omega^2 + \bar{\Gamma}_k^2\right)^2\right)}{\Gamma_k\left(\Gamma_k^4 + 2\Gamma_k^2\left(4\omega^2 - \bar{\Gamma}_k^2\right) + \left(4\omega^2 + \bar{\Gamma}_k^2\right)^2\right)}, \tag{9.50}$$

and

$$i\chi_k(\omega) = \frac{128\Delta\omega\Gamma_k}{\Gamma_k^4 + 2\Gamma_k^2\left(4\omega^2 - \bar{\Gamma}_k^2\right) + \left(4\omega^2 + \bar{\Gamma}_k^2\right)^2}. \tag{9.51}$$

Fourier transforming these expressions back to the time domain reveals the explicit temporal decay governed by the Liouvillian gap. The steady-state correlation function reads

$$C_k(t) = \frac{e^{\frac{-\Gamma_k|t|}{2}}}{\bar{\Gamma}_k}\left[\frac{\Gamma_k\bar{\Gamma}_k + 16(J_k-\Delta)\Delta}{\Gamma_k+\bar{\Gamma}_k}e^{\frac{-\bar{\Gamma}_k|t|}{2}} + \frac{\Gamma_k\bar{\Gamma}_k - 16(J_k-\Delta)\Delta}{\Gamma_k-\bar{\Gamma}_k}e^{\frac{\bar{\Gamma}_k|t|}{2}}\right], \tag{9.52}$$

while the response function takes the form

$$\chi_k(t) = \mathrm{sgn}(t)\frac{4\Delta}{\bar{\Gamma}_k}e^{-|\frac{t}{2}|\Gamma_k}\left[e^{-|\frac{t}{2}|\bar{\Gamma}_k} - e^{|\frac{t}{2}|\bar{\Gamma}_k}\right]. \tag{9.53}$$

9.2.8 Higher-Order Expansions

In order to probe the mean-field bistability region, it is necessary to go beyond the Gaussian approximation developed in Section 9.2.6 and capture the non-linear interactions which dominate near the phase transition. It follows that we must expand the full exact action in Eq. (9.26) to higher powers of the auxiliary fields. Absorbing a factor of $\sqrt{N}$ into the fields for consistent bookkeeping, the full action may be put on the form

$$\mathcal{S}_\sigma = \int_t \sum_k \vec{m}_{-k}^T D_k^{\mathrm{K}} \vec{m}_k - i\sum_{j=1}^{N} \ln\left(1 + \sum_{p=2,4,6\ldots}^{\infty} \mathcal{D}_{j,p}\right), \tag{9.54}$$

where p denotes the order of the expansion. Because the underlying unperturbed Liouvillian preserves the global $\mathbb{Z}_2$ symmetry of the Ising model, all odd-order terms in the expansion ($p = 1, 3, 5, \ldots$) evaluate to zero.

The p-th order expansion term, $\mathcal{D}_{j,p}$, describes the p-body interactions of the Keldysh fields mediated by the local spin dynamics at site j. It is explicitly given by

$$\mathcal{D}_{j,p} = \frac{1}{N^{p/2}}\sum_{\boldsymbol{k}}\sum_{\boldsymbol{\alpha},\boldsymbol{\mu}}\int_{\boldsymbol{t}} \overline{u}^{\boldsymbol{\alpha},\boldsymbol{\mu}}_{j,p,\boldsymbol{k}}(\boldsymbol{t})\prod_{n=1}^{p} m^{\alpha_n}_{k_n,\mu_n}(t_n). \tag{9.55}$$

Here, we utilize the shorthand notation for the momentum sums $\sum_{\boldsymbol{k}} \equiv \sum_{k_1\ldots k_p}$ and the time-ordered integrals $\int_{\boldsymbol{t}} \equiv \int_{-\infty}^{\infty} dt_1 \int_{-\infty}^{t_1} dt_2 \cdots \int_{-\infty}^{t_{p-1}} dt_p$. The indices α_n specify the field components $\alpha_n \in \{x, y\}$, whereas μ_n labels the classical/quantum components of the fields $\mu_n \in \{c, q\}$.

The effective p-point vertex function in the time domain, $\overline{u}^{\alpha,\mu}_{j,p,\boldsymbol{k}}(\boldsymbol{t})$, is defined via a time-ordered trace over the single-site nonequilibrium steady state (the vacuum state $|\mathrm{vac}\rangle\rangle$)

$$\begin{aligned}\overline{u}^{\alpha,\mu}_{j,p,\boldsymbol{k}}(\boldsymbol{t}) &= \overline{\mathrm{Tr}}\left[\mathcal{T}\prod_{n=1}^{p} ie^{ik_n j}\hat{\Sigma}^{\alpha_n}_{j,\mu_n}(t_n)\right] \\ &= \left(\prod_{n=1}^{p} ie^{ik_n j}\right)\overline{\mathrm{Tr}}\left[\hat{\Sigma}^{\alpha_1}_{j,\mu_1}\,\hat{\mathbb{U}}^{t_1}_{t_2}\,\hat{\Sigma}^{\alpha_2}_{j,\mu_2}\,\ldots\,\hat{\mathbb{U}}^{t_{p-1}}_{t_p}\hat{\Sigma}^{\alpha_p}_{j,\mu_p}\right],\end{aligned} \tag{9.56}$$

where the single-site unperturbed propagator governing the free time-evolution between interactions in the disorder phase is $\hat{\mathbb{U}}^{t}_{t'} = \exp\left[(t-t')\hat{\mathbb{L}}^{\sigma}_{1,j}\right]$. The single-site trace is formally defined as $\overline{\mathrm{Tr}}[\bullet] = \langle\langle\hat{I}|\bullet|\mathrm{vac}\rangle\rangle$.

The Taylor expansion of the logarithm in Eq. (9.54) systematically generates the connected diagrams (cumulants) of the theory. The scaling of the prefactors is crucial: the factor of $1/N$ inherent to the $p = 2$ (quadratic) term exactly cancels with the overall factor of N emerging from the spatial lattice sum $\sum_j$. For higher-order interacting terms ($p > 2$), the expansion yields residual prefactors scaling as $N^{1-p/2}$. This $1/N$ suppression confirms the validity of the large-N saddle-point approximation and dictates the perturbative hierarchy of the higher-order corrections.

To evaluate these vertices, we transform to frequency space via $\overline{u}(\boldsymbol{\omega}) = \int_{\boldsymbol{t}} e^{-i\sum_n \omega_n t_n}\overline{u}(\boldsymbol{t})$. Utilizing the resolvent form of the unperturbed propagator

$$\hat{\mathbb{U}}(\omega) = \int_0^\infty dt\, e^{t(\hat{\mathbb{L}}^{\sigma}_{1,j} - i\omega)} = -(\hat{\mathbb{L}}^{\sigma}_{1,j} - i\omega)^{-1}, \tag{9.57}$$

the vertex function takes its final algebraic form

$$\overline{u}^{\alpha,\mu}_{j,p,\boldsymbol{k}}(\boldsymbol{\omega}) = \left(\prod_{n=1}^{p} ie^{ik_n j}\right)\delta(\tilde{\omega}_p) \times \overline{\mathrm{Tr}}\left[\hat{\Sigma}^{\alpha_1}_{j,\mu_1}\,\hat{\mathbb{U}}(\tilde{\omega}_1)\,\hat{\Sigma}^{\alpha_2}_{j,\mu_2}\,\ldots\,\hat{\mathbb{U}}(\tilde{\omega}_{p-1})\,\hat{\Sigma}^{\alpha_p}_{j,\mu_p}\right]. \tag{9.58}$$

Here, $\tilde{\omega}_n = \sum_{n'=1}^{n}\omega_{n'}$ represents the cumulative frequency flowing through the propagator at step n. The Dirac delta function $\delta(\tilde{\omega}_p)$, where $\tilde{\omega}_p = \sum_{n=1}^{p}\omega_n = 0$, strictly enforces overall energy conservation at the interaction vertex.

Equipped with this generalized expansion, we can now project the action onto the critical eigenbasis (ϕ, ζ) defined in Section 9.2.6 to construct the low-energy effective potential and classify the phase transitions.

9.3 Phase Diagram in the Infinite-Range Limit

To demonstrate the utility of this field-theoretic formalism, we apply it to the infinite-range limit. In this regime, both the coherent Ising coupling and the collective dissipation are completely non-local and uniform across the lattice, such that $J_{ij} = J_0$ and $\Gamma_{ij} = \Gamma_0$. In the momentum representation, this restricts the interactions entirely to the zero-momentum mode: $J_k = J_0\delta_{k,0}$ and $\Gamma_k = \Gamma_0\delta_{k,0}$.

In this limit, spatial fluctuations are suppressed, and the saddle-point evaluation of the Keldysh action becomes exact in the thermodynamic limit. However, properly capturing the critical scaling and the phase boundary of the first-order transition within the bistability region fundamentally requires analyzing the higher-order terms of the full action—a task that lies beyond the reach of standard mean-field analysis.

9.3.1 Integrating the Massive Modes

As established in Section 9.2.6, the critical dynamics at $\Gamma_0 \approx \Gamma_c$ are entirely dominated by the gapless soft mode ϕ, while the ζ mode remains massive with a finite mass δ. Our primary objective in this section is to trace out these fast-relaxing ζ fluctuations to derive a low-energy effective partition function, Z_ϕ, formulated solely in terms of the order-parameter field ϕ. To systematically decouple these modes, we formally partition the full action into a pure ϕ component ($\mathcal{S}_\phi$), a pure ζ component ($\mathcal{S}_\zeta$), and their interactions, expanding up to the sixth order

$$\mathcal{S} = \mathcal{S}^{(2)} + \mathcal{S}^{(4)} + \mathcal{S}^{(6)} + \dots, \tag{9.59}$$

where each term scales as $\mathcal{S}^{(p)} \propto O(N^{1-p/2})$. By factoring out the bare Gaussian weight of the massive field, $e^{i\mathcal{S}_\zeta^{(2)}}$, we can exactly rewrite the full partition function as a path integral over the fields ϕ, weighted by an expectation value over the ζ fluctuations

$$\begin{aligned} Z &= \int \mathcal{D}[\phi_{c/q}, \zeta_{c/q}] e^{i\mathcal{S}} \\ &= \int \mathcal{D}[\zeta_{c/q}] e^{i\mathcal{S}_\zeta^{(2)}} \int \mathcal{D}[\phi_{c/q}] e^{i(\mathcal{S}-\mathcal{S}_\zeta^{(2)})} \\ &= \int \mathcal{D}[\phi_{c/q}] \langle e^{i(\mathcal{S}-\mathcal{S}_\zeta^{(2)})} \rangle_\zeta. \end{aligned} \tag{9.60}$$

Here, $\langle \dots \rangle_\zeta$ denotes the expectation value with respect to the free massive action.

To absorb this expectation value back into the exponent and derive an effective action, we evaluate it using a cumulant expansion. Taking the Taylor series of the exponential up to second order in the interaction terms, we obtain[1]

$$Z = \int \mathcal{D}[\phi_{c/q}] e^{i(\mathcal{S}_\phi^{(2)} + \mathcal{S}_\phi^{(4)} + \mathcal{S}_\phi^{(6)})} \Big\langle 1 + i(\mathcal{S}^{(4)} - \mathcal{S}_\phi^{(4)}) + i(\mathcal{S}^{(6)} - \mathcal{S}_\phi^{(6)}) - \frac{1}{2}(\mathcal{S}^{(4)} - \mathcal{S}_\phi^{(4)})^2 - (\dots) \Big\rangle_\zeta . \tag{9.61}$$

At this stage, we can drastically simplify the expression by analyzing the large-N scaling of these fluctuation corrections. Tracking the $1/N$ dependence reveals that, aside from the term $\langle -\frac{1}{2}(\mathcal{S}^{(4)} - \mathcal{S}_\phi^{(4)})^2 \rangle_\zeta$—which specifically generates an essential correction to the sextic ($p = 6$) interaction term—all other fluctuation corrections produce terms that are at least $O(1/N)$ smaller than their tree-level counterparts and can be systematically discarded.

By re-exponentiating the remaining terms, we isolate the low-energy physics into the partition function Z_ϕ

$$Z_\phi = \int \mathcal{D}[\phi_{c/q}] e^{i\mathcal{S}_{\text{eff}}[\phi]}, \tag{9.62}$$

which is now governed entirely by the effective action

$$\mathcal{S}_{\text{eff}}[\phi] \approx \mathcal{S}_\phi^{(2)} + \mathcal{S}_\phi^{(4)} + \mathcal{S}_\phi^{(6)} + \frac{i}{2}\langle (\mathcal{S}^{(4)} - \mathcal{S}_\phi^{(4)})^2 \rangle_\zeta . \tag{9.63}$$

This establishes the mathematical foundation for treating the system in terms of the critical field ϕ, where the final term represents the necessary corrections generated by integrating-out the massive modes.

9.3.2 The Effective Action and Langevin Dynamics

In the low-frequency, long-wavelength limit near the critical point, the scaling dimensions for the classical and quantum fields are $[\phi_c] = 1/2$ and $[\phi_q] = -1/2$. Keeping only the most relevant tree-level terms in the time domain, the effective action reads

$$\mathcal{S}_\sigma^{\text{eff}} = \int_t \phi_q(-\gamma\partial_t - r)\phi_c + \frac{D}{2}\phi_q^2 - \frac{u}{2N}\phi_c^3\phi_q - \frac{v}{3N^2}\phi_c^5\phi_q + \dots , \tag{9.64}$$

[1] Although the interaction term $(\mathcal{S} - \mathcal{S}_\zeta^{(2)})$ may contain mixed quadratic terms of the form $\phi_q\zeta_q$, such terms may be safely neglected. Contracting them under first-order perturbation theory only generates terms that are at least quadratic in the quantum field ϕ_q, which do not contribute to the classical effective potential governing the steady state evaluated in Eq. (9.69).

where the quadratic coefficients, extracted from the matrix $\mathcal{S}_\phi^{(2)}(k=0,\omega)$, represent the mass ($r$), friction ($\gamma$), and Keldysh noise ($D$) of the soft mode

$$r = -P_\phi^{\mathrm{R}}(k=0,\omega=0) = \frac{32J_0(\Gamma_0^2-\Gamma_c^2)}{(16\Delta^2+\Gamma_0\Gamma_c)^2-16\Delta^2(\Gamma_0^2-\Gamma_c^2)}, \tag{9.65a}$$

$$\gamma = -i[\partial_\omega P_\phi^{\mathrm{R}}(k=0,\omega)]_{\omega=0} = 128J_0\Gamma_0\frac{(16\Delta^2+\Gamma_0\Gamma_c)^2-\Gamma_0(\Gamma_0-\Gamma_c)(16\Delta^2+\Gamma_0\Gamma_c)}{[(16\Delta^2+\Gamma_0\Gamma_c)^2-16\Delta^2(\Gamma_0-\Gamma_c)^2]^2}, \tag{9.65b}$$

$$D = P_\phi^{\mathrm{K}}(k=0,\omega=0) = 256iJ_0\Gamma_0\frac{(16\Delta^2+\Gamma_0\Gamma_c)^2+16\Delta^2\Gamma_0^2+2\Gamma_0\Gamma_c-\Gamma_c^4}{[(16\Delta^2+\Gamma_0\Gamma_c)^2-16\Delta^2(\Gamma_0-\Gamma_c)^2]^2}. \tag{9.65c}$$

Once again, these coefficients are evaluated in the limit $\varepsilon \to 0$. The quartic- (u) and sextic-order (v) coupling constants in the static limit ($\omega \to 0$) evaluate to

$$u = \frac{\Delta^4-(\Gamma_c/4)^4}{8J_0^2\Delta^5}, \tag{9.66a}$$

$$v = \frac{3}{32J_0\Delta^6}\left[\frac{12}{J_0^2}(\Gamma_c/4)^4+(\Gamma_c/4)^2-\Delta^2\right]. \tag{9.66b}$$

With the relevant parameters defined, we can map this effective action onto a classical stochastic process. To do this, we apply a Hubbard-Stratonovich transformation to decouple the quadratic noise term ϕ_q^2. This introduces an auxiliary white-noise field $f(t)$, allowing the action in Eq. (9.64) to be recast as [269]

$$\begin{aligned}\mathcal{S}_\sigma^{\mathrm{eff}} = &\int_t\left[(-\gamma\partial_t-r)\phi_c-\frac{u}{2N}\phi_c^3-\frac{v}{3N^2}\phi_c^5+\sqrt{2}f(t)\right]\phi_q\\ &-\int_t\frac{1}{D}f(t)^2,\end{aligned} \tag{9.67}$$

Finally, upon integrating out the quantum field ϕ_q, we arrive at

$$\gamma\partial_t\phi_c = -r\phi_c-\frac{u}{2N}\phi_c^3-\frac{v}{3N^2}\phi_c^5+f(t), \tag{9.68}$$

where $\langle f(t)\rangle = 0$, and $\langle f(t)f(t')\rangle = \frac{-iD}{2}\delta(t-t')$. The previous equation provides a Langevin description of a classical damped motion of the order parameter ϕ_c relaxing in an effective potential given by

$$V_{\mathrm{eff}}(\phi_c) = \frac{r}{2}\phi_c^2+\frac{u}{8N}\phi_c^4+\frac{v}{18N^2}\phi_c^6. \tag{9.69}$$

The steady-state macroscopic magnetization is then found by minimizing this potential, $\langle\sigma^x\rangle \propto \min[V_{\mathrm{eff}}(\phi_c)]$.

9.3.3 Criticality, Scaling, and the Phase Diagram

With the fully established effective potential $V_{\text{eff}}(\phi_c)$ in hand, we can now classify the nonequilibrium steady states and extract the critical scaling exponents. The macroscopic steady-state magnetization is directly proportional to the global minimum of the potential, $\langle \sigma^x \rangle \propto \phi_0$, where ϕ_0 satisfies

$$\left.\frac{\partial V_{\text{eff}}}{\partial \phi_c}\right|_{\phi_0} = \phi_0 \left(r + \frac{u}{2N}\phi_0^2 + \frac{v}{3N^2}\phi_0^4 \right) = 0. \tag{9.70}$$

The roots of this equation dictate the value of the order parameter, governed by the tuning parameter r and the effective interaction vertices.

9.3.3.1 Continuous Transition and Standard Scaling ($\beta = 1/2$)

When the transverse field is sufficiently strong ($\Delta > J_0$), the exact bare quartic coupling u remains strictly positive ($u > 0$). In this regime, the sextic term v represents a sub-leading irrelevant perturbation near the critical point, and the our model behaves as a standard ϕ^4 theory.

For $\Gamma_0 > \Gamma_c$, the mass parameter $r > 0$, and the only real root is the trivial paramagnetic state, $\phi_0 = 0$. However, as the collective dissipation dips below the critical threshold ($\Gamma_0 < \Gamma_c$), the mass parameter r becomes negative, destabilizing the origin. The system continuously breaks the $\mathbb{Z}_2$ symmetry, acquiring a finite steady-state magnetization

$$\phi_0 = \sqrt{\frac{-2Nr}{u}} \propto (\Gamma_0 - \Gamma_c)^{1/2}. \tag{9.71}$$

This confirms that along the continuous phase boundary, the order parameter sustains a standard critical scaling exponent of $\beta = 1/2$.

9.3.3.2 Bistability and the First-Order Transition

Conversely, when the coherent interactions dominate ($\Delta < J_0$), the exact tree-level evaluation of the quartic coupling changes sign, becoming strictly negative ($u < 0$). In our analysis, the positive, sextic term $v > 0$ ensures the potential remains bounded from below, stabilizing the theory.

However, the negative quartic term fundamentally alters the landscape of the effective potential, creating a regime where the system possesses three distinct extrema: a minimum at $\phi = 0$, as well as symmetric minima at finite $\pm\phi_0$, and unstable maxima separating them. This manifests physically

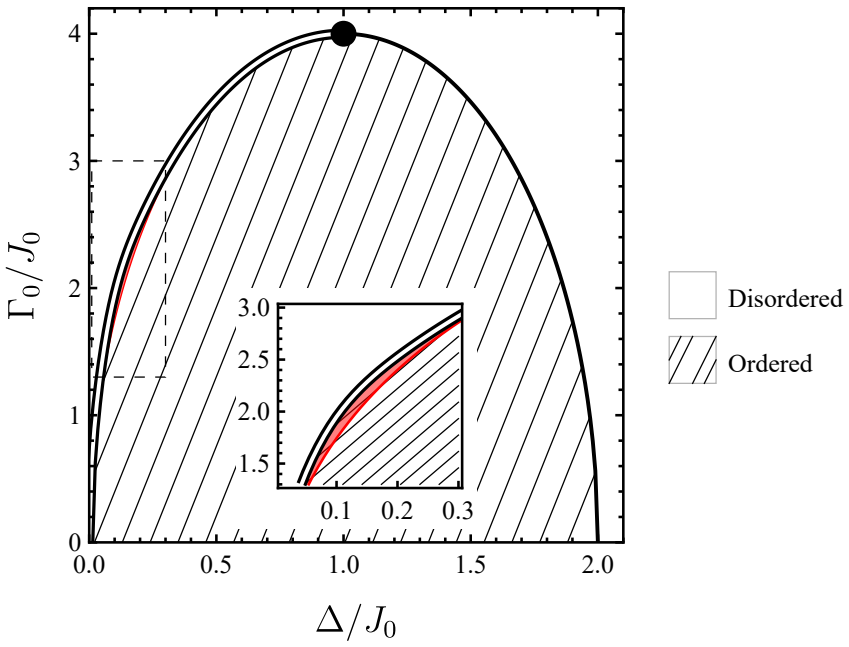

Figure 9.2 Phase diagram of the infinite-range driven-dissipative Ising model in the limit $\varepsilon \to 0$ near the critical phase boundary. The solid boundary at $\Delta/J_0 > 1$ corresponds to a second-order (continuous) phase transition, whereas the boundary labeled by double lines ($\Delta/J_0 < 1$) corresponds a first-order phase transition line. The two lines meet at a tricritical point at $\Delta/J_0 = 1$. The area shaded in red and magnified in the inset represents the ordered part of the mean-field bistable region.

as a region of bistability as shown in Fig. 9.1. Consequently, crossing the phase boundary in this parameter regime results in an abrupt, discontinuous jump in the order parameter, characteristic of a first-order phase transition. The first-order transition boundary is labeled by double lines in Fig. 9.2. The fact that the transition happens very close to Γ_c is due to the fact that $v \gg u$ in that region.

9.3.3.3 The Tricritical Point ($\beta = 1/4$)

The point where the first-order transition line terminates and the continuous second-order critical line begins defines a tricritical point. This point corresponds to the condition $r = u = 0$. From our field-theoretic derivation, this precise point occurs exactly at $\Delta = J_0$ when taking the limit $\varepsilon \to 0$. At the tricritical point, the bare quartic coupling identically vanishes ($u = 0$) and the leading non-linear fluctuation is governed entirely by the sextic term. The effective potential flattens considerably into $V_{\text{eff}} \approx \frac{r}{2}\phi_c^2 + \frac{v}{18N^2}\phi_c^6$. Minimizing this tricritical potential reveals a fundamentally different universal scaling behavior. The order parameter continuously emerges from the origin,

but scales as

$$\phi_0 = \left(\frac{-3N^2 r}{v}\right)^{1/4} \propto (\Gamma_0 - \Gamma_c)^{1/4}. \tag{9.72}$$

The critical exponent shifts from $\beta = 1/2$ along the continuous line to $\beta = 1/4$ at the tricritical point. This emergent scaling behavior is shown in Fig. 9.3.

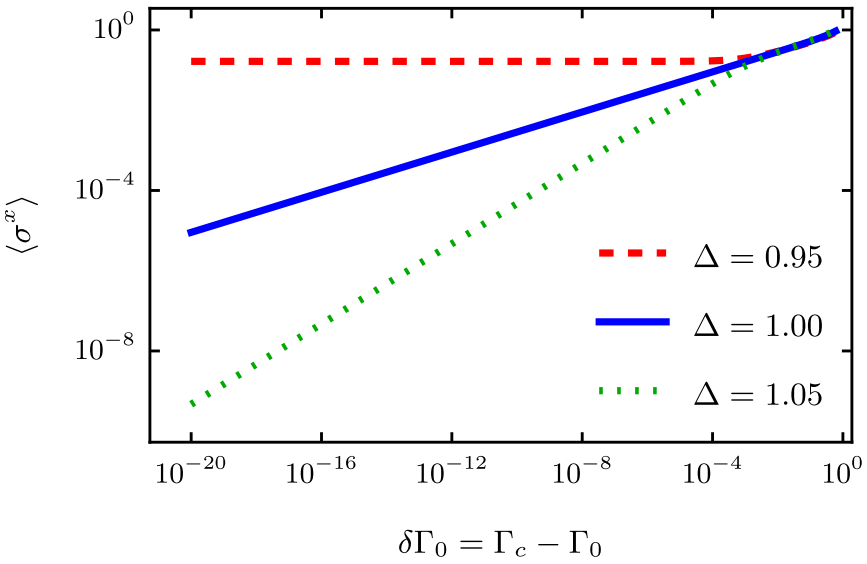

Figure 9.3 Magnetization in the steady state obtained by minimizing the effective potential in Eq. (9.69) in the limit $\varepsilon \to 0$ and setting $J_0 = 1$ for multiple values of Δ near the tricritical point. At $\Delta = 1.05$, the magnetization $\langle \sigma^x \rangle \approx (3.176)\ \delta\Gamma^{0.488}$, while at the tricritical point, $\langle \sigma^x \rangle \approx (0.917)\ \delta\Gamma^{0.250}$. The extracted exponent of $\beta = 1/4$ at the tricritical point confirms the shift to a universality class governed by the ϕ^6 theory.

The phase boundary is quantitatively studied in Fig. 9.4, which shows the jump in the order parameter within the bistable region. To clarify the phase boundaries: the dashed line denotes the bare critical condition where the effective mass vanishes ($r = 0$). The solid line is a mean-field boundary marking the upper limit of the bistable region; above this line, the system is strictly in the disordered phase. Consequently, the mean-field first-order phase transition is constrained to occur within the bistable region between these two lines. By leveraging the effective field theory and evaluating the expansion coefficients u and v, we can explicitly resolve the steady-state magnetization and pinpoint the exact location of the first-order transition, visible as the sharp transition between the ordered (green) and disordered (blue) regimes.

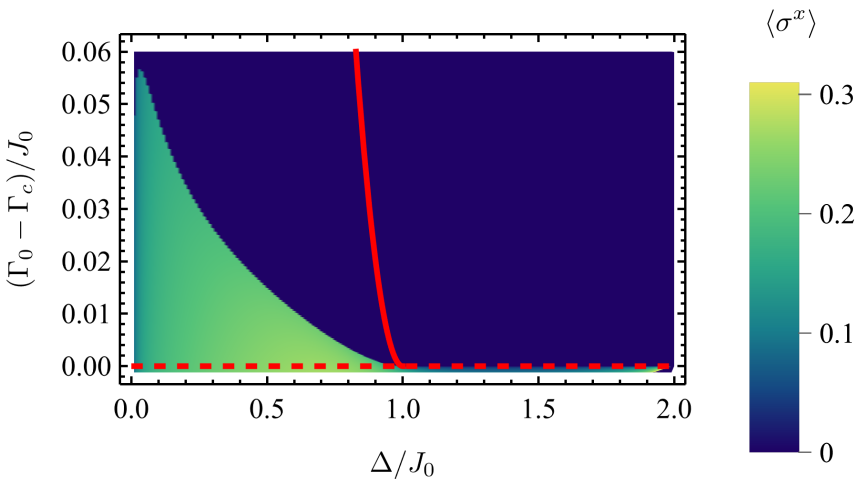

Figure 9.4 Phase diagram of the infinite-range driven-dissipative Ising model in the limit $\varepsilon \to 0$ near the critical phase boundary. The horizontal axis represents the normalized detuning Δ/J_0, while the vertical axis shows the deviation from the critical dissipation strength, $(\Gamma_0 - \Gamma_c)/J_0$. The color gradient encodes the steady-state magnetization $\langle\sigma^x\rangle$. The area between the dashed line at $(\Gamma_0 - \Gamma_c) = 0$ and the solid line corresponds to the mean-field bistability region. This region ($\Delta/J_0 < 1$) hosts a first-order phase transition; this turns into a second-order (continuous) transition for $\Delta/J_0 > 1$, with the two regimes meeting at a tricritical point at $\Delta/J_0 = 1$.

This result highlights the power of the Keldysh functional integral approach developed in this chapter. While a mean-field approximation can identify a bistable region, it requires the powerful machinery of the field theory to characterize fluctuations and identify the phase boundary.

9.4 Conclusion and Outlook

In this chapter, we have constructed a rigorous Keldysh functional integral formalism to describe the nonequilibrium steady states of the long-range driven-dissipative quantum Ising models. By mapping the spin-1/2 algebra to a bosonic field theory with a hard-core constraint and subsequently executing a Hubbard-Stratonovich decoupling, we isolated the critical soft modes governing the critical dynamics. Notably, going beyond the semiclassical mean-field limit, our field-theoretic approach revealed that integrating out the massive quantum fields generates an effective classical potential that captures the NESS criticality. This mechanism accurately identifies the emergence of a tricritical point and the ensuing first-order phase transition driven by collective dissipation.

Building upon this robust theoretical foundation, several compelling avenues for future research naturally emerge:

1. **Power-Law Dissipation and Interaction Profiles:**

   While the present analysis focused primarily on the analytically tractable infinite-range (all-to-all) limit, modern quantum simulation platforms—such as trapped ions and waveguide-QED systems—often exhibit interactions and correlated dissipation that decay algebraically with distance ($J_{ij} \propto 1/|i-j|^{\alpha}$ and $\Gamma_{ij} \propto 1/|i-j|^{\gamma}$). A direct extension of our work is to evaluate the momentum-dependent perturbative corrections for these power-law profiles. A critical objective will be to map how the finite spatial range alters the structure of the effective potential $V_{\text{eff}}(\phi_c)$. Specifically, we aim to determine whether there exists a strict upper bound on the decay exponent γ beyond which the first-order transition may be washed out, thereby restricting the nonequilibrium bistability to geometries with sufficiently long-range dissipation.

2. **Continuous Symmetries and Non-Reciprocal Dissipation:**

   The formalism developed here for the 1D quantum Ising model can be readily generalized to encompass systems with even more generic Hamiltonians, such as open XX or XY models. It may even be extended to study spin systems in higher spatial dimensions. Furthermore, in our analysis, we assumed strict spatial reciprocity in the dissipative coupling ($\Gamma_{ij} = \Gamma_{ji}$). Breaking this symmetry to introduce non-reciprocal dissipation—an increasingly relevant paradigm in chiral quantum optics and topological photonics [277–279]—could fundamentally alter the NESS. Investigating how non-reciprocity competes with long-range coherent interactions could unveil novel dynamical phases, such as steady-state chiral currents or continuously time-crystals [280–283].

3. **Alternative Field-Theoretic Representations (Schwinger Bosons):**

   From a methodological standpoint, our approach enforces the spin-1/2 algebra by introducing an infinite on-site hard-core repulsion ($U \to \infty$) into the bosonic Hamiltonian *prior* to formulating the path integral. While effective, an alternative, potentially more elegant formalism could be developed utilizing the Schwinger boson representation [284–286]. This involves mapping the local spin operators to a two-species bosonic algebra ($\sigma^{\uparrow} = \hat{a}^{\dagger}\hat{b}$, $\sigma^{z} = \frac{1}{2}(\hat{a}^{\dagger}\hat{a} - \hat{b}^{\dagger}\hat{b})$), while

enforcing the strict local Hilbert space constraint ($\hat{a}^\dagger \hat{a} + \hat{b}^\dagger \hat{b} = 1$) within the functional integral. Developing this Schwinger-Keldysh path integral would bypass the need for an infinite nonlinear interaction penalty, as well as the Hubbard-Stratonovich transformation potentially offering a more controlled framework.

APPENDIX 9A

MEAN-FIELD SOLUTION

The mean field solution for the model introduced in Section 9.1 becomes exact in the limit of infinite-range coherent coupling ($J_r = J_0$) and infinite-range collective dissipation ($\Gamma_r = \Gamma_0$). In this case, we can re-write the Hamiltonian as

$$\hat{H}_\infty = -\frac{J_0}{N}\hat{S}_x^2 + \Delta\hat{S}_z, \tag{9A.1}$$

where $\hat{S}_\alpha = \sum_{i=1}^{N}\sigma_i^\alpha$ are the total spin operators. The dissipation part is governed by two channels represented by the jump operators

$$\hat{L}_i^{\text{loc}} = \sqrt{\varepsilon}\sigma_i^{\downarrow} \quad \text{, for } i = 1, 2, ..., N, \tag{9A.2a}$$

$$\hat{L}^{\text{glob}} = \sqrt{\Gamma_0/N}\hat{S}_{\downarrow}. \tag{9A.2b}$$

We can then develop a mean-field solution in the steady state using the Heisenberg equations of motion. To first order (ignoring terms of $O(1/N)$), we find

$$\frac{\mathrm{d}\langle\hat{O}\rangle}{\mathrm{d}t} = i\left\langle[\hat{H}_\infty, \hat{O}]\right\rangle + \hat{\mathcal{D}}_{\text{loc}}^{\dagger}(\hat{O}) + \hat{\mathcal{D}}_{\text{glob}}^{\dagger}(\hat{O}), \tag{9A.3}$$

where

$$\hat{\mathcal{D}}_{\text{loc}}^{\dagger}(\hat{O}) = \sum_{i=1}^{N}\hat{L}_i^{\text{loc}\dagger}\hat{O}\hat{L}_i^{\text{loc}} - \frac{1}{2}\{\hat{L}_i^{\text{loc}\dagger}\hat{L}_i^{\text{loc}}, \hat{O}\} \tag{9A.4a}$$

$$\hat{\mathcal{D}}_{\text{glob}}^{\dagger}(\hat{O}) = \hat{L}^{\text{glob}\dagger}\hat{O}\hat{L}^{\text{glob}} - \frac{1}{2}\{\hat{L}^{\text{glob}\dagger}\hat{L}^{\text{glob}}, \hat{O}\} \tag{9A.4b}$$

For the operators $\sigma^{x/y/z}$, the first two terms have already been reported in Ref. [269]. Incorporating the collective dissipation channel, the full mean-field equations read

$$\partial_t\langle\sigma^x\rangle = -2\Delta\langle\sigma^y\rangle - \frac{\varepsilon}{2}\langle\sigma^x\rangle + \frac{\Gamma_0}{2}\langle\sigma^x\rangle\langle\sigma^z\rangle, \tag{9A.5a}$$

$$\begin{aligned}\partial_t\langle\sigma^y\rangle = {} & 4J_0\langle\sigma^x\rangle\langle\sigma^z\rangle + 2\Delta\langle\sigma^x\rangle \\ & - \frac{\varepsilon}{2}\langle\sigma^y\rangle + \frac{\Gamma_0}{2}\langle\sigma^y\rangle\langle\sigma^z\rangle,\end{aligned} \tag{9A.5b}$$

$$\begin{aligned}\partial_t\langle\sigma^z\rangle = {} & -4J_0\langle\sigma^x\rangle\langle\sigma^z\rangle - \varepsilon(1 + \langle\sigma^z\rangle) \\ & - \frac{\Gamma_0}{2}(\langle\sigma^x\rangle^2 + \langle\sigma^y\rangle^2).\end{aligned} \tag{9A.5c}$$

The steady state solutions ($\partial_t \langle\sigma^x\rangle = \partial_t \langle\sigma^y\rangle = \partial_t \langle\sigma^z\rangle = 0$) are given by the trivial state $\langle\boldsymbol{\sigma}\rangle_{\rm SS} = (0, 0, -1)$ and the four ordered branches

$$\langle\sigma^x\rangle_{\rm SS} = \frac{s_1}{J_0\Gamma_0}\sqrt{4s_2\Lambda + J_0\Delta[\Gamma_0(\varepsilon + \Gamma_0) - 16J_0\Delta]} \tag{9A.6a}$$

$$\langle\sigma^y\rangle_{\rm SS} = -s_1\frac{(4J_0^2\Delta^2 - s_2\Lambda)}{J_0\Gamma_0\Delta^2}|\langle\sigma^x\rangle_{\rm SS}| \tag{9A.6b}$$

$$\langle\sigma^z\rangle_{\rm SS} = \frac{4s_2\Lambda + J_0\Delta(\Gamma_0\varepsilon - 16J_0\Delta)}{J_0\Gamma_0^2\Delta}, \tag{9A.6c}$$

where $\Lambda = \sqrt{J_0^2\Delta^3(16J_0^2\Delta - \Gamma_0^2\Delta - 2J_0\Gamma_0\varepsilon)}$ and $s_1, s_2 \in \{+1, -1\}$ denote the four ordered solution branches, as defined in Section 9.2.5. The mean-field is therefore in exact agreement with the saddle-point solution presented in Section 9.2.5. Interestingly, the total spin is not conserved even as $\varepsilon \to 0$.

In order to determine the phase boundaries and the stability of these steady states, we perform a linear stability analysis. By expanding the semiclassical equations of motion, Eq. (9A.5), around the steady-state solutions to linear order, $\langle\sigma^\alpha\rangle = \langle\sigma^\alpha\rangle_{\rm SS} + \delta\sigma^\alpha$, we construct the corresponding 3×3 Jacobian matrix. A steady-state configuration is dynamically stable to small fluctuations if all eigenvalues of the Jacobian have strictly non-positive real parts.

Applying this stability criterion to both the disordered normal phase ($\langle\boldsymbol{\sigma}\rangle_{\rm SS} = (0, 0, -1)$) and the ordered branches yields the phase diagrams presented in Fig. 9A.1. The parameter space, governed by the transverse field Δ/J_0 and collective dissipation Γ_0/J_0, generally exhibits three distinct regimes: a normal phase, a symmetry-broken ordered phase, and a region of bistability. In the bistable regime, both the disordered and ordered macroscopic states act as stable attractors of the nonequilibrium dynamics. As illustrated in the sequence of plots, increasing the local dissipation rate ε progressively suppresses the cooperative effects, causing the bistability region to shrink until it completely disappears for sufficiently large ε.

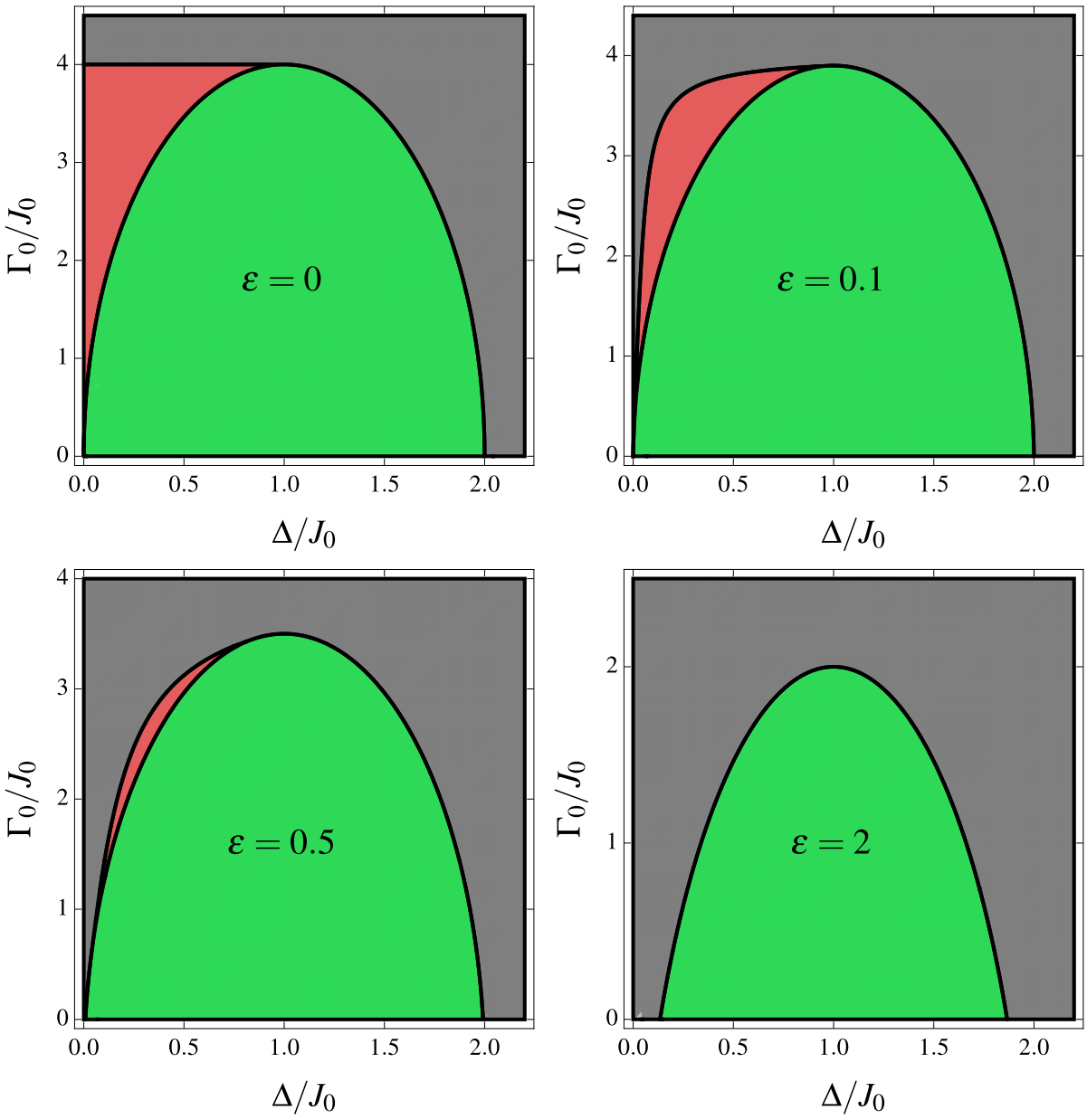

Figure 9A.1 Nonequilibrium mean-field phase diagrams of the long-range Ising model subject to both collective and local dissipation. The stability boundaries are mapped as a function of the scaled transverse field Δ/J_0 and collective dissipation Γ_0/J_0 for varying local dissipation strengths ε. The parameter space is divided into a stable disordered normal phase (gray), a stable ordered phase (green), and a bistability region (red) where both states are dynamically stable. The bistability region, characteristic of a first-order dissipative phase transition, diminishes and ultimately vanishes as the local dissipation ε is increased.

CHAPTER 10

THE DRIVEN-DISSIPATIVE SPIN-BOSON MODEL

Traditionally, quantum phase transitions characterize low-temperature equilibrium phenomena in many-body physics, but observing them in nonequilibrium settings remains a significant challenge. A key platform for exploring nonequilibrium physics is driven open quantum systems, where the coherent evolution governed by a Hamiltonian is inherently at odds with Markovian loss induced by the surrounding environment [49, 52]. Typically, the interplay between continuous driving and dissipation destroys these delicate quantum transitions, pushing the system toward an effectively classical, thermalized state [287–293]. This classical crossover happens because the system's noise profile usually resembles $A(\omega) = \gamma|\omega| + \Gamma$, meaning that at low frequencies, the frequency-independent white noise (Γ) originating from the Markovian bath completely washes out the quantum-mechanical colored noise.

Breaking from this conventional wisdom, our recent preprint demonstrates that Markovian dissipation can actually stabilize a robust quantum phase transition instead of destroying it [294]. We investigate a variant of the spin-boson model, a paradigmatic quantum impurity model originally introduced to capture the effective low-energy physics of a particle tunneling between two potential wells in the presence of an environment that continuously performs measurements on the system [33, 295]. In this setup, the model features a two-level system (the spin) interacting with a continuum of bosonic modes forming an Ohmic bath. In the rotating frame of the drive, the system's Hamiltonian is expressed as

$$\hat{H} = -\frac{\Delta}{2}\sigma^x + \sum_k \omega_k \hat{a}_k^\dagger \hat{a}_k + \frac{\sigma^z}{2}\sum_k \lambda_k(\hat{a}_k + \hat{a}_k^\dagger). \tag{10.1}$$

The interaction between the spin and the bath is governed by the spectral function $J(\omega) = \pi \sum_k \lambda_k^2 \delta(\omega - \omega_k)$. Assuming an Ohmic bath profile, the spectral function takes the specific form

$$J(\omega) = 2\pi\alpha\omega\Theta(\omega_c - \omega)\,, \tag{10.2}$$

where α denotes the dimensionless coupling strength and ω_c is the high-frequency ultraviolet cutoff.

In its standard formulation, the Ohmic spin-boson model is known to undergo a quantum phase transition (at zero-temperature) into a localized state where spin tunneling is entirely suppressed [33, 295]. This is happens as a consequence of the tunneling rate getting normalized by the low-frequency bosonic excitations in the bath. Assuming a large cutoff ($\omega_c \gg \Delta$), this critical point is located at $\alpha_c = 1 + \mathcal{O}(\Delta/\omega_c)$.

This critical behavior is often analyzed by mapping the quantum system to a classical one. By integrating out the bosonic degrees of freedom, the system maps exactly onto a one-dimensional classical Ising model extended along imaginary time τ. In this case, the Feynman-Vernon influence functional yields an effective action for the classical spin trajectories $S(\tau) \in \{+1, -1\}$ [295]. The resulting action takes the form

$$S_{\text{eff}} = -\frac{1}{2}\int d\tau \int d\tau' S(\tau)K(\tau - \tau')S(\tau') \tag{10.3}$$

where the memory kernel $K(\tau)$ is given in terms of the spectral function of the bath

$$K(\tau) = \int_0^\infty d\omega J(\omega) e^{-\omega|\tau|}. \tag{10.4}$$

For an Ohmic bath at zero temperature, this integral directly yields the long-range coupling $K(\tau) \propto 1/\tau^2$. While standard 1D classical models with short-range interactions are always disordered, the $1/\tau^2$ long-range coupling circumvents this restriction, allowing a phase transition to occur [33, 296–298]. Specifically, a Berezinskii-Kosterlitz-Thouless (BKT) transition, characterized by a sudden, discontinuous jump in the order parameter (magnetization) [299–303]. Notably, the long-range nature of this interaction on the imaginary-time axis stems from the low-frequency bath modes. If a finite temperature is introduced, it imposes an upper bound on the imaginary time integration (the inverse temperature β), effectively truncating the long-range correlations and destroying the phase transition entirely.

Crucially, we consider the case where the bath is at zero temperature, but the bosons are subject to a Markovian loss that is strictly proportional to their frequency, effectively vanishing at low frequencies (soft dissipation). This dissipative dynamics is captured by the Lindblad jump operators

$$\hat{L}_k = \sqrt{\kappa_k}\hat{a}_k, \tag{10.5}$$

where we assume

$$\kappa_k = r\omega_k, \tag{10.6}$$

with r the constant of proportionality.

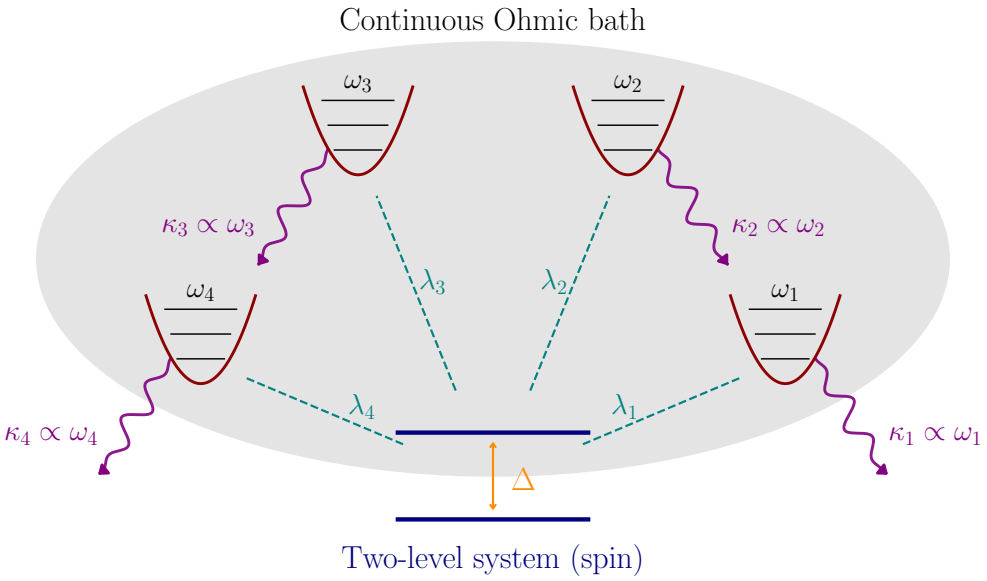

Figure 10.1 Schematic representation of the driven-dissipative spin-boson model. A central two-level system (spin) is coupled to an Ohmic bath of bosonic modes. Unlike the standard model, the bosons here are subject to a Markovian loss rate $\kappa_k = r\omega_k$ that vanishes at low frequencies (soft dissipation). This frequency-dependent dissipation stabilizes a localization phase transition in the nonequilibrium steady state.

While a bath with constant decay rates essentially acts as a heat bath destroying the BKT phase transition, we show that under soft Markovian dissipation, a localization phase transition re-emerges in the nonequilibrium steady state. To establish the existence and nature of this transition, our collaborative work in Ref. [294] employs a variational polaron ansatz alongside extensive time-evolving block decimation (TEBD) simulations. These methods confirm that the driven-dissipative system undergoes a sharp localization transition characterized by a nontrivial purification: the steady state at the critical point becomes a pure quantum state, stabilized by the strong renormalization of the spin's tunneling dynamics by low-frequency bosonic modes. This stands as a rare counterexample to the standard expectation that interacting driven-dissipative systems always behave semi-classically.

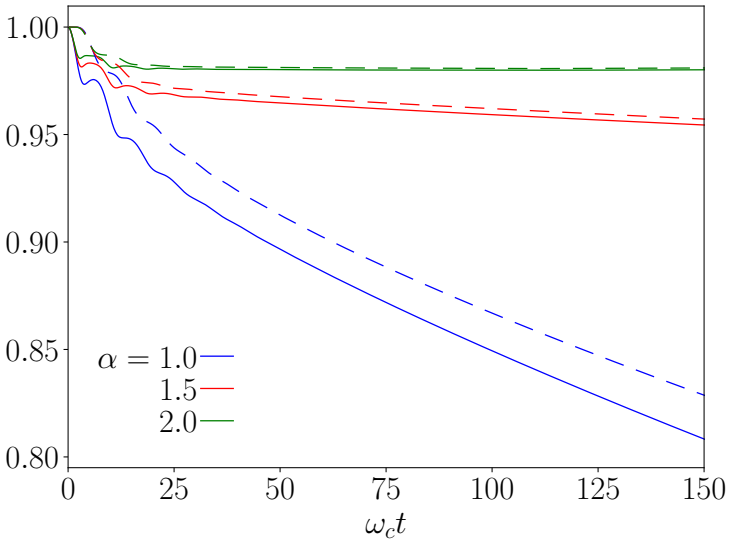

Figure 10.2 Magnetization $\langle \sigma^z(t) \rangle$ (solid lines) and purity (dashed lines) as a function of time for different values of α; we take $\Delta = 1, \omega_c = 10$, $r = 0.5$. For $\alpha = 2$, the magnetization quickly approaches a constant close to unity, signaling a localization phase transition. The purity follows a similar trend as the magnetization, with the spin-boson system remaining almost perfectly pure at the transition. Figure adapted from Ref. [294]. The TEBD simulations and data visualization for this figure were conducted by co-author Naushad A. Kamar.

In order to emphasize the quantum nature of the single spin-1/2 impurity model, we aim to contrast the results in Fig. 10.2 with a mean-field limit to fully appreciate the mechanics at play. My primary contribution to this research addresses exactly this by analyzing the mean-field behavior of a large-spin variant of the same model. The following section details this theoretical framework, demonstrating that macroscopic classical fluctuations, rather than quantum ones, dominate in the large-spin limit.

10.1 Large Spin Limit: Quantum vs. Classical Behavior

To highlight the *quantum* nature of the spin-1/2 driven-dissipative spin-boson model, it is instructive to consider an alternative mean-field limit where the bosonic bath is coupled to a large collective spin. This section details the field-theoretic analysis of this large-spin model, demonstrating that, in contrast to the single spin-1/2 case, taking the large-spin limit results in a quantum-to-classical crossover. In the mean-field limit, the large-spin model exhibits purely classical critical fluctuations and a vanishing purity at the critical point.

The full Hamiltonian of the large-spin system is given by

$$\hat{H} = \Delta \hat{S}_z + \sum_k \omega_k \hat{a}_k^\dagger \hat{a}_k + \frac{\hat{S}_x}{\sqrt{N}} \sum_k \lambda_k (\hat{a}_k^\dagger + \hat{a}_k). \tag{10.7}$$

Compared to Eq. (10.1), we have performed a $-\pi/2$ rotation around the $y-$axis, which takes $\hat{S}_z \to \hat{S}_x$, and $\hat{S}_x \to -\hat{S}_z$. Here, N is the total number of spins. The dissipative dynamics are governed by the Lindblad master equation with jump operators linear in the bosonic annihilation operators: $\hat{L}_k = \sqrt{\kappa_k}\hat{a}_k$, where the soft dissipation rate is $\kappa_k = r\omega_k$.

Deep in the normal phase (for large Δ), we perform a Holstein-Primakoff transformation [163]

$$\hat{S}_z = \hat{b}^\dagger \hat{b} - N/2, \quad \hat{S}^+ \approx \hat{b}^\dagger \sqrt{N}, \quad \hat{S}_x = \frac{\hat{S}^+ + \hat{S}^-}{2}. \tag{10.8}$$

In the thermodynamic limit ($N \to \infty$), taking only the quadratic terms yields the continuous bosonic Hamiltonian

$$\hat{H} = \Delta \hat{b}^\dagger \hat{b} + \sum_k \omega_k \hat{a}_k^\dagger \hat{a}_k + (\hat{b}^\dagger + \hat{b}) \sum_k g_k (\hat{a}_k^\dagger + \hat{a}_k), \tag{10.9}$$

where we redefined the coupling parameter $g_k = \lambda_k/2$.

10.2 Keldysh Field Theory Analysis

To systematically integrate out the bath modes and capture the spin fluctuations in the nonequilibrium steady state, we formulate the problem using the Keldysh path integral formalism. We replace the bosonic operators $\hat{b}$ and $\hat{b}^\dagger$ with fields (c-numbers) defined on the forward and backward time branches, and subsequently rotate them into the Keldysh classical (c) and quantum (q) fields, $b_{c/q} = (b_+ \pm b_-)/\sqrt{2}$. The bath modes $\hat{a}_k$ are treated identically. Since the Hamiltonian is quadratic under the Holstein-Primakoff (HP) approximation, we can exactly integrate out the bosonic bath modes.

The resulting effective action for the HP boson takes the form

$$S[\{b, b^*\}] = \int_\omega v^\dagger(\omega) \begin{pmatrix} 0 & P^{\mathrm{A}}(\omega) \\ P^{\mathrm{R}}(\omega) & P^{\mathrm{K}}(\omega) \end{pmatrix} v(\omega)\,, \tag{10.10}$$

where the Nambu-style field vector is $v(\omega) = (b_c(\omega), b_c^*(-\omega), b_q(\omega), b_q^*(-\omega))^T$. Here we utilize the shorthand notation $\int_\omega = \int_{-\infty}^{\infty} \frac{d\omega}{2\pi}$. The inverse retarded and advanced Green's functions are

given by

$$P^{\mathrm{R}}(\omega) = [P^{\mathrm{A}}(\omega)]^{\dagger} = \begin{pmatrix} \Sigma(\omega) + \omega - \Delta & \Sigma(\omega) \\ \Sigma(\omega) & \Sigma(\omega) - \omega - \Delta \end{pmatrix}, \tag{10.11}$$

while the Keldysh component reads

$$P^{\mathrm{K}}(\omega) = d(\omega) \begin{pmatrix} 1 & 1 \\ 1 & 1 \end{pmatrix}. \tag{10.12}$$

where the self energy function $\Sigma(\omega)$ and the function $d(\omega)$ are defined in terms of the bath spectral function as

$$\Sigma(\omega) = -\frac{1}{2} \int_{\tilde{\omega}} J(\tilde{\omega}) \Big[\frac{1}{(\omega - \tilde{\omega}) + i\kappa(\tilde{\omega})} - \frac{1}{(\omega + \tilde{\omega}) + i\kappa(\tilde{\omega})} \Big], \tag{10.13a}$$

$$d(\omega) = i \int_{\tilde{\omega}} \kappa(\tilde{\omega}) J(\tilde{\omega}) \Big[\frac{1}{(\omega - \tilde{\omega})^2 + \kappa^2(\tilde{\omega})} + \frac{1}{(\omega + \tilde{\omega})^2 + \kappa^2(\tilde{\omega})} \Big]. \tag{10.13b}$$

Given the structure of the action, it is evident that a superradiant phase transition occurs when $\det P^{\mathrm{R}}(\omega = 0, \Delta = \Delta_c) = 0$, which corresponds to

$$\Delta_c = 2\Sigma(\omega = 0) = \frac{2\alpha\omega_c}{1 + r^2}. \tag{10.14}$$

10.3 Critical Fluctuations

Unlike the spin-boson model, a continuous phase transition occurs for any α when $\Delta = \Delta_c \propto \alpha$. Furthermore, this transition is fundamentally a superradiant phase transition where taking the large-spin plays the role of taking the thermodynamic limit. Here, we are interested in the critical nature of the phase transition. To understand the critical behavior, we first break the fields into their real and imaginary parts by defining

$$\phi_{c/q}(t) = 2\,\mathrm{Re}\, b_{c/q}(t), \qquad \zeta_{c/q}(t) = 2\,\mathrm{Im}\, b_{c/q}(t). \tag{10.15}$$

One can see that the fields $\zeta_{c/q}$ are gapped, and we can integrate them out close to the critical point. We then find an effective Keldysh action depending only on $\phi_{c,q}$ as

$$\mathcal{S}[\phi_{c/q}] = \int_{\omega} \begin{pmatrix} \phi_c(\omega) \\ \phi_q(\omega) \end{pmatrix}^{\dagger} \begin{pmatrix} 0 & P^{\mathrm{A}}_{\phi}(\omega) \\ P^{\mathrm{R}}_{\phi}(\omega) & P^{\mathrm{K}}_{\phi}(\omega) \end{pmatrix} \begin{pmatrix} \phi_c(\omega) \\ \phi_q(\omega) \end{pmatrix}, \tag{10.16}$$

where

$$P^{\mathrm{R}}_{\phi}(\omega) = [P^{\mathrm{A}}_{\phi}(\omega)]^{*} = \Sigma(\omega) - \frac{\Delta}{2} + \frac{\omega^2}{2\Delta}, \tag{10.17a}$$

$$P^{\mathrm{K}}_{\phi}(\omega) = d(\omega). \tag{10.17b}$$

To characterize the phase transition, we must evaluate the variance of the macroscopic order parameter, $\hat{S}_x$. Within the Keldysh formalism, these steady-state statistical fluctuations are dictated directly by the two-point correlation function of the classical field component, ϕ_c

$$\frac{\langle \hat{S}_x^2 \rangle}{N} = \frac{1}{4}\int_{\omega} \langle \phi_c^2(\omega) \rangle = -\frac{i}{4}\int_{\omega} \frac{P^{\mathrm{K}}_{\phi}(\omega)}{\left|P^{\mathrm{R}}_{\phi}(\omega)\right|^2}. \tag{10.18}$$

Approaching the critical point ($\Delta \to \Delta_c$), the low-frequency contribution diverges as $P^{\mathrm{R}}_{\phi}(\omega \to 0)$ vanishes, while $P^{\mathrm{K}}_{\phi}(\omega \to 0)$ remains finite. The integral in Eq. (10.18) is calculated numerically and shown in Fig. 10.3, where we find that the spin excitations diverge as $1/(\Delta - \Delta_c)$ upon approaching the critical point. This scaling is compatible with classical rather than quantum fluctuations where one would expect $1/\sqrt{\Delta - \Delta_c}$.

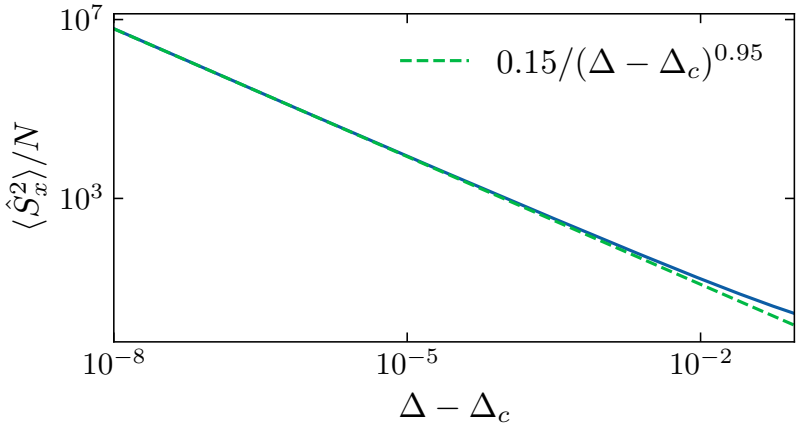

Figure 10.3 Spin fluctuations near the critical point Δ_c. Here, we take $\alpha = 1$, $r = 1/2$, $\omega_c = 10$. $\langle \hat{S}_x^2 \rangle / N$ is calculated numerically from Eq. (10.18) showing fluctuations to follow a classical critical scaling $\langle \hat{S}_x^2 \rangle / N \sim 1/(\Delta - \Delta_c)$.

10.4 Purity and Quantum Entanglement

To conclusively underscore the classical nature of this mean-field transition, we calculate the quantum purity and entanglement properties of the steady state. Because the effective Hamiltonian

in the Holstein-Primakoff approximation is quadratic, the steady state of the system is strictly Gaussian. Consequently, its purity can be computed efficiently and directly from the covariance matrix σ via the relation $\mu = 1/\sqrt{\det \sigma}$.

To perform this calculation, it is more convenient to work in the 1D lattice representation introduced in appendix 10A. In this basis, the large spin (now mapped to a soft-core Holstein-Primakoff boson) is coupled to a finite bosonic tight-binding lattice of size L [304], where the Hamiltonian is given by

$$\hat{H} = -\frac{\Delta}{2}\sigma^x + \frac{\sigma^z}{2}c_0(\hat{d}_0 + \hat{d}_0^\dagger) + \sum_{n=0}^{\infty}\omega_n \hat{d}_n^\dagger \hat{d}_n + \sum_{n=0}^{\infty} t_n(\hat{d}_n^\dagger \hat{d}_{n+1} + h.c.). \tag{10.19}$$

The mapping is exact in the limit $L \to \infty$. We define the covariance matrix σ in terms of the position and momentum operators, $\hat{x}_i = \frac{1}{\sqrt{2\omega_i}}(\hat{d}_i^\dagger + \hat{d}_i)$ and $\hat{p}_i = i\sqrt{\frac{\omega_i}{2}}(\hat{d}_i^\dagger - \hat{d}_i)$, spanning the full set of modes including the spin. We denote the full set of modes ($\hat{d}$) defined on the 1D lattice by the vector $\underline{\hat{d}}_{\text{sys}} = (\hat{d}_0, ..., \hat{d}_{L-1}, \hat{b})$.

For a Gaussian system, the purity can be computed as [305]

$$\mu = \frac{1}{\sqrt{\det \sigma}}, \tag{10.20}$$

where the covariance matrix σ is defined as

$$\sigma = \begin{pmatrix} \langle\{\underline{\hat{x}}, \underline{\hat{x}}\}\rangle & \langle\{\underline{\hat{x}}, \underline{\hat{p}}\}\rangle \\ \langle\{\underline{\hat{p}}, \underline{\hat{x}}\}\rangle & \langle\{\underline{\hat{p}}, \underline{\hat{p}}\}\rangle \end{pmatrix}, \tag{10.21}$$

Utilizing the third quantization formalism developed in Ref. [158, 159] and discussed in Section 4.2, we can put the Hamiltonian on the matrix form

$$\mathbf{H}' = \left(\begin{array}{ccccc} & & & & -ic_0 \\ & & \mathbf{H} & & 0 \\ & & & & \vdots \\ & & & & 0 \\ \hline ic_0 & 0 & \cdots & 0 & \Delta \end{array}\right), \tag{10.22}$$

which includes the coupling of the chain to the large spin. The matrix $\mathbf{H}$ encodes all the boson-boson coupling on the discrete chain

$$\mathbf{H}_{\alpha,\beta} = \delta_{\alpha,\beta}\,\omega_{\alpha-1} + \delta_{\alpha,\beta-1}\,t_{\alpha-1} + \delta_{\alpha,\beta+1}\,t_{\alpha-2}. \tag{10.23}$$

Similarly, we define the matrix $\mathbf{M}'$ with dimensions $(L+1)\times(L+1)$

$$\mathbf{M}' = \left(\begin{array}{ccc|c} & & & 0 \\ & \mathbf{M} & & \vdots \\ & & & 0 \\ \hline 0 & \cdots & 0 & 0 \end{array}\right), \tag{10.24}$$

which accounts for the dissipation terms. The zeros in $\mathbf{M}'$ are due to dissipation not acting directly on the spin. Dissipation within the chain is captured by the matrix

$$\mathbf{M} = \sum_{n=0}^{L-1} \underline{l}_{1,n} \otimes \underline{l}^*_{1,n} + \sum_{n=0}^{L-2} \underline{l}_{2,n} \otimes \underline{l}^*_{2,n}, \tag{10.25}$$

where the j-th element of the vectors encodes the decay rate of the corresponding jump operator

$$(\underline{l}_{1,n})_j = \sqrt{r}\sqrt{\kappa_{1,n}}\delta_{n,j}, \tag{10.26a}$$

$$(\underline{l}_{2,n})_j = \sqrt{r}\sqrt{\kappa_{2,n}}(\delta_{n,j} + \delta_{n+1,j}). \tag{10.26b}$$

Finally, we can define the matrix $\mathbf{X}' = \frac{1}{2}\begin{pmatrix} i(\mathbf{H}')^* + \mathbf{M}' & 0 \\ 0 & -i\mathbf{H}' + (\mathbf{M}')^* \end{pmatrix}$, which captures the full properties of the system. Solving the Lyapunov equation [159]

$$\mathbf{X}'\mathbf{Z} + \mathbf{Z}\mathbf{X}' = 0, \tag{10.27}$$

allows us to compute the solution matrix

$$\mathbf{Z} = \begin{pmatrix} \langle \underline{\hat{d}}_{\text{sys}} \otimes \underline{\hat{d}}_{\text{sys}} \rangle & \langle : \underline{\hat{d}}_{\text{sys}} \otimes \underline{\hat{d}}^\dagger_{\text{sys}} : \rangle \\ \langle \underline{\hat{d}}^\dagger_{\text{sys}} \otimes \underline{\hat{d}}_{\text{sys}} \rangle & \langle \underline{\hat{d}}^\dagger_{\text{sys}} \otimes \underline{\hat{d}}^\dagger_{\text{sys}} \rangle \end{pmatrix} = \begin{pmatrix} \mathbf{Z}_{11} & \mathbf{Z}_{12} \\ \mathbf{Z}_{21} & \mathbf{Z}_{22} \end{pmatrix}. \tag{10.28}$$

The elements of the matrix $\mathbf{Z}$ are directly related to the elements of the covariance matrix, σ. We note that

$$\langle\{\underline{\hat{x}}, \underline{\hat{x}}\}\rangle_{ij} = 2\langle\hat{x}_i\hat{x}_j\rangle = \frac{1}{\sqrt{\omega_i\omega_j}}(\mathbf{Z}_{11} + \mathbf{Z}_{12} + \mathbf{Z}_{21} + \mathbf{Z}_{22} + \mathbf{I})_{ij}, \tag{10.29a}$$

$$\langle\{\underline{\hat{p}}, \underline{\hat{p}}\}\rangle_{ij} = 2\langle\hat{p}_i\hat{p}_j\rangle = \sqrt{\omega_i\omega_j}(-\mathbf{Z}_{11} + \mathbf{Z}_{12} + \mathbf{Z}_{21} - \mathbf{Z}_{22} + \mathbf{I})_{ij}, \tag{10.29b}$$

$$\langle\{\underline{\hat{x}}, \underline{\hat{p}}\}\rangle_{ij} = \langle\hat{x}_i\hat{p}_j + \hat{p}_j\hat{x}_i\rangle = i\sqrt{\frac{\omega_j}{\omega_i}}(-\mathbf{Z}_{11} + \mathbf{Z}_{12} - \mathbf{Z}_{21} + \mathbf{Z}_{22})_{ij}, \tag{10.29c}$$

$$\langle\{\underline{\hat{p}}, \underline{\hat{x}}\}\rangle_{ij} = \langle\{\underline{\hat{x}}, \underline{\hat{p}}\}\rangle_{ji}. \tag{10.29d}$$

Upon evaluating σ for large bath sizes (up to $L = 1000$), we find that the purity rapidly vanishes upon approaching the critical point from the normal phase. Specifically, the purity collapse follows a steep power law in $\Delta - \Delta_c$ with an exponent ≈ 6, scaling as $\mu \sim (\Delta - \Delta_c)^6$.

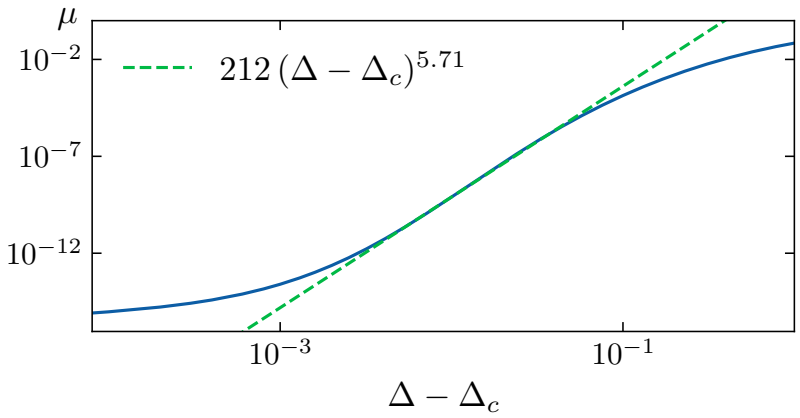

Figure 10.4 Purity in the steady state. We set the parameters $\alpha = 1$, $r = 1/2$, $\omega_c = 10$, and consider a bosonic bath of size $L = 1000$. Purity quickly vanishes upon approaching the critical point, following a power law in $\Delta - \Delta_c$ with an exponent of approximately 6, and levels off very close to the critical point due to finite-size effects.

To further probe the underlying quantum correlations, we examine the system's phase-space uncertainty and look for signatures of spin-squeezing. Physically, spin squeezing occurs when the variance of one collective spin component is reduced below the standard quantum limit (the isotropic variance of a coherent spin state), at the inevitable expense of increased variance in an orthogonal component [306–308]. It is a well-established macroscopic signature of quantum entanglement in collective spin systems [309, 310].

For our Gaussian continuous-variable system, the variances of the principal spin quadratures are exactly quantified by the ordinary eigenvalues of the 2×2 spin sub-system covariance matrix, σ_{spin}. In our normalization, the standard quantum limit (Heisenberg uncertainty) corresponds to an eigenvalue of exactly 1. True quantum squeezing would therefore require the minimum eigenvalue of σ_{spin} to drop below 1.

Crucially, calculating the eigenvalues of the spin sub-system reveals no such quantum squeezing. As the system approaches criticality, the minimum eigenvalue does not drop below the vacuum limit; instead, it takes a bounded constant value of ≈ 2.22 exactly at the critical point. Because this minimum variance remains strictly above the standard quantum limit, the state is heavily anti-squeezed by the dissipative environment. In stark contrast, the largest eigenvalue exhibits a purely classical power-law divergence, scaling as $1/(\Delta - \Delta_c)$, representing macroscopic thermal-like fluctuations of the order parameter; see the left panel in Fig. 10.5.

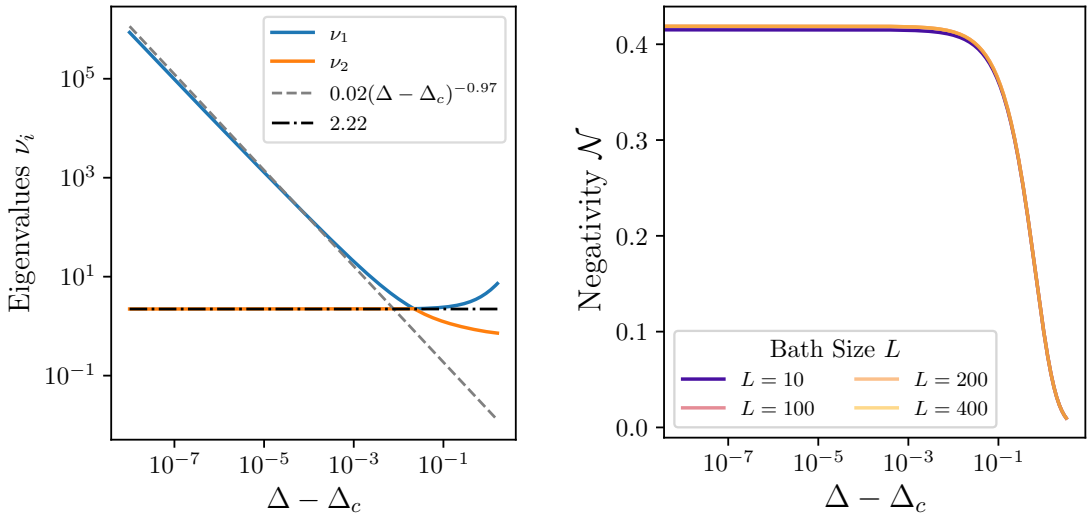

Figure 10.5 Left panel: eigenvalues of the covariance matrix σ_{spin} of the spin sub-system as a function of Δ. The minimum eigenvalue remains bounded at ≈ 2.22 at the critical point (strictly above the standard quantum limit of 1, indicating no squeezing), while the maximum eigenvalue diverges. The system parameters are fixed at ($\alpha = \omega_c = 2r = 1$). The eigenvalues are calculated using the results obtained in Section 10.3 in the thermodynamic limit. Right panel: bipartite entanglement negativity $\mathcal{N}$ between the large spin and the bosonic bath as a function of the distance to the critical point ($\Delta - \Delta_c$) for multiple bath sizes L. The negativity remains strictly bounded ($\mathcal{N} \approx 0.42$), reflecting a lack of divergent quantum correlations at the macroscopic transition.

The thermal, anti-squeezed nature of this covariance matrix severely constrains the available quantum entanglement in the system. To quantify this mixed-state entanglement, we compute the entanglement negativity $\mathcal{N}$, a computable measure of bipartite entanglement derived from the Peres-Horodecki positive partial transpose (PPT) criterion [311, 312]. For Gaussian states, the PPT criterion is elegantly formulated in phase space [313]. The partial transposition with respect to a subsystem (in this case, the macroscopic spin) corresponds simply to time reversal on that subsystem, which flips the sign of its momentum operator ($p_{\text{spin}} \to -p_{\text{spin}}$).

The negativity is then completely determined by the symplectic eigenvalues $\{\tilde{\nu}_j\}$ of this partially transposed covariance matrix $\tilde{\sigma}$ [305, 314]. Because the standard quantum limit in our normalization corresponds to $\tilde{\nu}_j = 1$, the entanglement negativity is explicitly evaluated as

$$\mathcal{N} = \sum_j \max\left(0, \frac{1}{\tilde{\nu}_j} - 1\right). \tag{10.30}$$

Computing the bipartite entanglement negativity between the collective spin and the bosonic bath, we find it reaches a maximum bounded value of only $\mathcal{N} \approx 0.42$, which is to be expected for a Gaussian state where negativity is bounded by the minimum squeezing eigenvalue shown in Fig. 10.5 ($1/2.22 \approx 0.45$). This lack of divergent entanglement negativity, coupled with the complete collapse of the purity and the absence of spin-squeezing in the NESS, conclusively demonstrates that while the interacting single spin-$1/2$ model stabilizes a true pure-state quantum phase transition, its macroscopic mean-field analog is invariably driven into an effectively classical, highly mixed state at criticality.

In conclusion, this chapter has demonstrated that soft Markovian dissipation can uniquely stabilize a pure-state quantum phase transition in the driven-dissipative spin-boson model. In order to establish the quantum nature of this phenomenon, we contrasted the single spin-$1/2$ impurity against a macroscopic large-spin mean-field limit. By employing Keldysh field theory alongside exact third quantization techniques, we showed that the macroscopic large-spin model invariably collapses into a highly mixed state at criticality. This transition is dominated by purely classical, thermal-like fluctuations that scale as $1/(\Delta - \Delta_c)$. The absence of quantum spin-squeezing and the strictly bounded bipartite entanglement negativity further corroborate this classical crossover.

Consequently, the survival of a localized, pure steady state in the single-spin system represents a non-trivial departure from the standard expectation that driven-dissipative interacting systems behave semi-classically.

APPENDIX 10A

CHAIN MAPPING AND DISSIPATIVE LATTICE DYNAMICS

To facilitate numerical simulations and exact analytical treatments of the bath, we map the continuous bosonic environment to a semi-infinite tight-binding chain. We apply the method presented in Ref. [304] which derives the tight-binding coefficients for the chain using orthogonal polynomials. While this method is inspired by the foundational numerical renormalization group (NRG) method established by K.G. Wilson in Ref. [315], it allows us to handle any spectral density without the discretization errors typical of standard numerics.

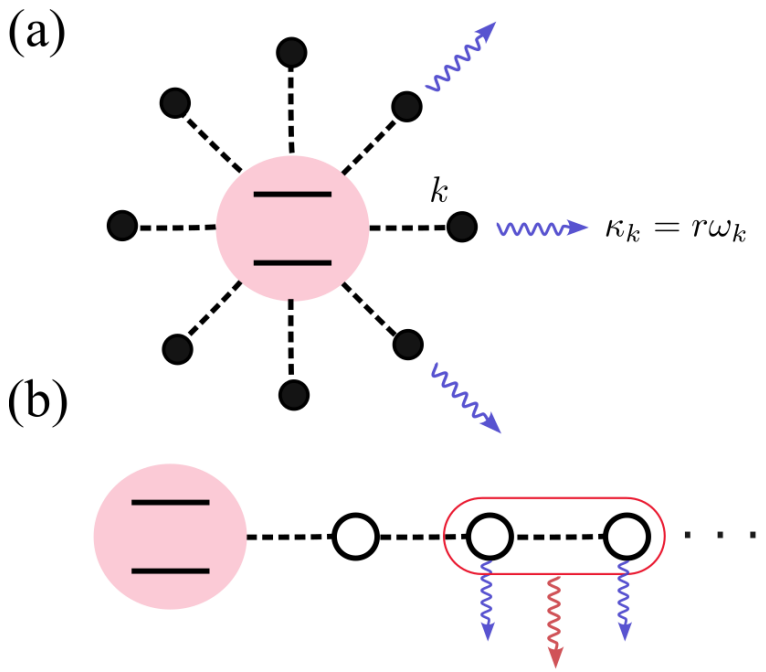

Figure 10A.1 Schematic picture depicting the spin-boson model with bosons subject to Markovian loss. (a) The top panel shows the spin-boson model where the spin (two-level system) is coupled to bosonic modes (solid circles). Bosons are subject to a mode-dependent loss, $\kappa_k = r\omega_k$, vanishing with the frequency. (b) The bottom panel depicts the model in a transformed basis where the spin is coupled to a bosonic lattice (open circles). The Markovian loss takes the form of single- and correlated two-site dissipation. Figure adapted from Ref. [294].

In the absence of dissipation, the original Hamiltonian transforms into a nearest-neighbor interacting model [304]

$$\hat{H} = -\frac{\Delta}{2}\sigma^x + \frac{\sigma^z}{2}c_0(\hat{d}_0 + \hat{d}_0^\dagger) + \sum_{n=0}^{\infty}\omega_n \hat{d}_n^\dagger \hat{d}_n + \sum_{n=0}^{\infty} t_n(\hat{d}_n^\dagger \hat{d}_{n+1} + h.c.), \tag{10A.1}$$

where $\hat{d}_n(\hat{d}_n^\dagger)$ are the bosonic annihilation (creation) operators at site n of the lattice. For an Ohmic bath with spectral function $J(\omega) = 2\pi\alpha\omega\Theta(\omega_c - \omega)$, the parameters are defined as [304]

$$c_0 = \frac{\sqrt{\alpha}}{2}\omega_c, \quad \omega_n = \frac{\omega_c}{2}\left(1 + \frac{1}{(1+2n)(3+2n)}\right), \quad t_n = \frac{\omega_c(1+n)(2+n)}{(3+2n)(5+2n)}\sqrt{\frac{5+2n}{3+2n}}. \tag{10A.2}$$

Under the soft Markovian dissipation $\kappa_k = r\omega_k$, the dissipative superoperator can be mapped into the same lattice basis. This transformation generates both single-site and correlated two-site jump operators

$$\hat{L}_{1,n} = \sqrt{\kappa_{1,n}}\hat{d}_n, \quad \hat{L}_{2,n} = \sqrt{\kappa_{2,n}}(\hat{d}_n + \hat{d}_{n+1}), \tag{10A.3}$$

where the lattice decay rates are $\kappa_{1,n} = r(\omega_n - t_n - t_{n-1})$ and $\kappa_{2,n} = rt_n$, with $t_{-1} \equiv 0$.

APPENDIX 10B

RESPONSE AND CORRELATION FUNCTIONS WITH MODIFIED DISSIPATION

In the numerical simulation of the driven-dissipative spin-boson model using matrix product states (MPS) and the time-evolving block decimation (TEBD) algorithm, the primary computational bottleneck is the unbounded local Hilbert space of the bosonic modes. To represent the state computationally, the local bosonic Hilbert space must be truncated to a large dimension d_b.

In the 1D semi-infinite chain representation, the central spin couples directly and exclusively to the first site of the bosonic chain ($n = 0$) in Eq. (10A.1). Consequently, the bosonic population at this boundary site can become highly excited. Capturing the dynamics and the subsequent phase transition accurately would require a prohibitively large d_b on this specific site, limiting the system sizes and coupling strengths we can reliably simulate.

To alleviate this bottleneck and accelerate numerical convergence, we utilize a tweaked model where the soft Markovian dissipation is turned off exclusively on the first bath site ($n = 0$). By setting the local dissipation rates to zero at the boundary ($\kappa_{1,0} = \kappa_{2,0} = 0$), we significantly relax the required size of d_b. Physically, because the $n = 0$ site remains strongly coupled via the hopping amplitude t_0 to the rest of the highly dissipative bulk, boundary excitations are rapidly transported away, ensuring the central spin still experiences the effective Markovian environment.

In the following sections, we demonstrate that this local modification does not alter the fundamental qualitative nature of the Ohmic bath. Specifically, it preserves the characteristic asymptotic $1/t^2$ power-law decay of the bath's temporal correlation functions.

10B.1 Third Quantization of the Bosonic Lattice

Turning off dissipation at $n = 0$ prevents us from representing the bath in terms of independent, decoupled momentum modes. We instead employ algebraic third quantization techniques in the bosonic operator space [159] to exactly solve for the bath correlations.

We consider a bosonic lattice of size L, and write the bosonic Hamiltonian (absent the coupling to the spin) in a compact quadratic form as

$$\hat{H}_B = \underline{\hat{d}}^\dagger \cdot \mathbf{H}\, \underline{\hat{d}}\,, \tag{10B.1}$$

where $\underline{\hat{d}} = (\hat{d}_0, \hat{d}_1, \ldots, \hat{d}_{L-1})^T$ is a vector of bosonic annihilation operators, and the matrix elements of $\mathbf{H}$ are given by the standard tight-binding parameters of the mapped Ohmic bath in Eq. (10.23).

To construct the dissipative Liouvillian, we utilize the same single-site and correlated two-site Markovian jump operators defined in Section 10.4, encoded by the dissipation matrix $\mathbf{M}$ and the associated coupling vectors $\underline{l}_{1,n}$ and $\underline{l}_{2,n}$.

It is important to emphasize the distinction between this setup and the one used in Section 10.1 (specifically for purity calculations). In Section 10.1, we constructed the $(L+1)\times(L+1)$ matrices $\mathbf{H}'$ and $\mathbf{M}'$ to find the steady state of the *coupled* system (the bath plus the Holstein-Primakoff boson). Here, we are explicitly characterizing the intrinsic memory kernel of the *uncoupled* bath. Therefore, the matrices $\mathbf{H}$ and $\mathbf{M}$ used here are strictly of dimension $L \times L$ and do not include the interaction c_0 or the spin's detuning Δ.

To analyze the exact nonequilibrium dynamics of the bath, we need a framework that treats dissipation on the same footing as coherent evolution. We achieve this by mapping the density matrix onto a doubled ''Liouville-Fock'' space. Physically, this allows the Liouvillian superoperator $\hat{\mathbb{L}}_B$, which governs bosonic part of the master equation to be diagonalized just like a standard Hamiltonian.

In this doubled space, operators must be distinguished based on whether they act on the density matrix from the left (the ''upper'' or u branch), or from the right (the ''lower'' or l branch). To isolate the dissipative modes, we define a new set of superoperators following the notation in Ref. [159]

$$\begin{aligned} \underline{\hat{d}}_0 &= \underline{\hat{d}}^u, \quad \underline{\hat{d}}'_0 = \underline{\hat{d}}^{u*} - \underline{\hat{d}}^{l*}, \\ \underline{\hat{d}}_1 &= \underline{\hat{d}}^{l*}, \quad \underline{\hat{d}}'_1 = \underline{\hat{d}}^{l} - \underline{\hat{d}}^{u}. \end{aligned} \tag{10B.2}$$

While the primed operators are not the Hermitian conjugates of the unprimed operators (e.g., $(\hat{d}_{0,j})^\dagger \neq \hat{d}'_{0,j}$), they obey the canonical bosonic commutation relations, e.g., $[\hat{d}_{0,j}, \hat{d}'_{0,k}] = \delta_{j,k}$. Because the Liouvillian is non-Hermitian, its left and right eigenmatrices differ, necessitating this biorthogonal operator basis. With these definitions, the bosonic part of the Liouvillian takes the

vectorized quadratic form

$$\hat{\mathbb{L}}_B = \underline{\hat{d}}_0' \cdot (-i\mathbf{H} - \mathbf{M}^*)\, \underline{\hat{d}}_0 + \underline{\hat{d}}_1' \cdot (i\mathbf{H}^* - \mathbf{M})\, \underline{\hat{d}}_1 \,. \tag{10B.3}$$

We can even write this Liouvillian in a more compact form by introducing the $4L \times 4L$ matrix $\mathbf{S}$ such that

$$\hat{\mathbb{L}}_B = \underline{\hat{c}} \cdot \mathbf{S}\, \underline{\hat{c}} - \mathrm{Tr}\{\mathbf{M}\}, \tag{10B.4}$$

where $\underline{\hat{c}} = (\underline{\hat{d}}_0, \underline{\hat{d}}_1, \underline{\hat{d}}_0', \underline{\hat{d}}_1')^T$ and $\mathbf{S} = \begin{pmatrix} 0 & -\mathbf{X} \\ -\mathbf{X}^T & 0 \end{pmatrix}$. The coupled coherent and dissipative dynamics are entirely encapsulated within the central matrix $\mathbf{X}$

$$\mathbf{X} = \frac{1}{2}\begin{pmatrix} i\mathbf{H}^* + \mathbf{M} & 0 \\ 0 & -i\mathbf{H} + \mathbf{M}^* \end{pmatrix}. \tag{10B.5}$$

Assuming the matrix $\mathbf{X}$ is diagonalizable, we introduce the matrices $\mathbf{P}$ and $\mathbf{\Delta}$ that satisfy $\mathbf{XP} = \mathbf{P\Delta}$, where $\mathbf{\Delta} = \mathrm{diag}\{\Delta_1, ..., \Delta_{2L}\}$ contains the complex eigenvalues of $\mathbf{X}$. By transforming to the eigenmodes $\underline{\hat{\zeta}}$ using $\underline{\hat{d}} = (\mathbf{P}^T)^{-1}\underline{\hat{\zeta}}$ and $\underline{\hat{d}}' = \mathbf{P}\underline{\hat{\zeta}}'$, the Liouvillian is brought to a diagonal form

$$\hat{\mathbb{L}}_B = -2\sum_{r=1}^{2L} \Delta_r \hat{\zeta}_r' \hat{\zeta}_r \,. \tag{10B.6}$$

This final diagonal form is highly intuitive: the complex nonequilibrium bath has been exactly mapped to a set of independent, non-Hermitian harmonic oscillators. The real parts of the complex eigenvalues Δ_r dictate the exponential decay rates of these collective modes, while the imaginary parts represent their oscillation frequencies. Furthermore, the nonequilibrium steady state (NESS) physically corresponds to the true ''vacuum'' of this doubled space. The unprimed normal modes annihilate this vacuum ($\hat{\zeta}_r \,|\mathrm{NESS}\rangle\rangle = 0$ and $\langle\langle \mathbb{I}|\, \hat{\zeta}_r' = 0$), mathematically ensuring that any transient excitation created in the bath will eventually decay, relaxing the system back to its steady state.

10B.2 Exact Spectral Function and Asymptotic Decay

Using this diagonalized basis, we can compute the correlation function of the bath exactly. We define the characteristic bath correlator using the local position operator at the boundary site, $\hat{X}(t) = (\hat{d}_0(t) + \hat{d}_0^\dagger(t))/2$

$$C(t) = 2\alpha\omega_c^2 \left\langle \hat{X}(t)\hat{X}(0) \right\rangle \,. \tag{10B.7}$$

Applying the third quantization mapping, $C(t)$ is evaluated exactly in terms of the eigenvalues and eigenvectors of the Liouvillian

$$C(t) = \frac{\alpha\omega_c^2}{2} \sum_{r=1}^{2L} \left[(\mathbf{P}^T)^{-1}_{1,r} + (\mathbf{P}^T)^{-1}_{1+L,r} \right] \mathbf{P}_{1,r} e^{-2\Delta_r t} \,. \tag{10B.8}$$

The real and imaginary parts of $C(t)$ correspond to the symmetrized correlation function $C^{\mathrm{sym}}(t) = \mathrm{Re}\, C(t)$ and the response function $\chi(t) = \mathrm{Im}\, C(t)$, respectively.

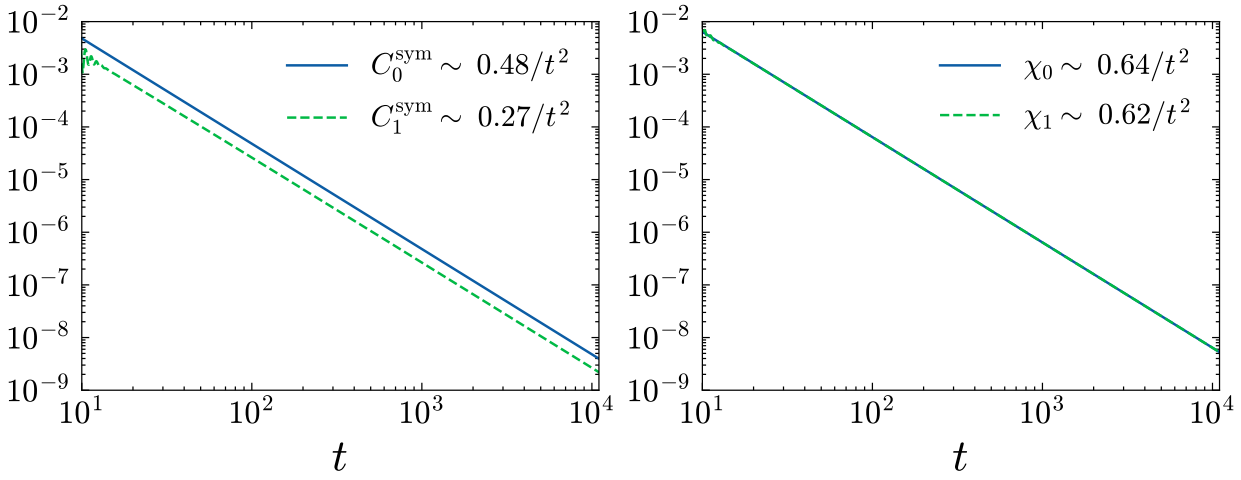

Figure 10B.1 Bath characteristic correlator $C(t)$ as a function of time with the parameters $\alpha = 1$, $r = 1/2$, $\omega_c = 10$ and a bosonic lattice size of $L = 4000$. The left panel shows the symmetrized correlation function $C^{\mathrm{sym}}_{0/1}(t)$, and the right panel shows the response function $\chi_{0/1}(t)$. The subscript 0 indicates dissipation on all sites, while subscript 1 indicates dissipation is removed from the site $n = 0$. Both models robustly maintain the $1/t^2$ asymptotic power-law decay.

When soft dissipation ($\kappa_k = r\omega_k$) is applied to all sites uniformly, this correlator must scale asymptotically as $1/t^2$. To verify our tweaked model, we numerically construct the matrices for extremely large bath sizes up to $L = 4000$ while explicitly setting the dissipation rates on the first site to zero ($\kappa_{1,0} = \kappa_{2,0} = 0$). As shown in Fig. 10B.1, the exact diagonalization results conclusively demonstrate that turning off dissipation on the first site does not alter the defining $1/t^2$ asymptotic power-law decay of either the response or correlation functions. The primary effect of removing the boundary site's dissipation is simply a rescaling of the decay coefficients. Consequently, the long-range temporal correlations necessary to stabilize the localization phase transition remain intact, justifying the use of the tweaked model to achieve numerical convergence in the MPS simulations.

BIBLIOGRAPHY

[1] H. Spohn and J. L. Lebowitz, ‘‘Irreversible Thermodynamics for Quantum Systems Weakly Coupled to Thermal Reservoirs’’, in *Advances in Chemical Physics* (John Wiley & Sons, Ltd, 1978), pp. 109–142.

[2] G. T. Landi and M. Paternostro, ‘‘Irreversible entropy production: From classical to quantum’’, Rev. Mod. Phys. **93**, 035008 (2021).

[3] L. Boltzmann, ‘‘Further Studies on the Thermal Equilibrium of Gas Molecules’’, in *The Kinetic Theory of Gases*, Vol. 1, History of Modern Physical Sciences (Published by Imperial College Press and distributed by World Scientific Publishing Co., July 2003), pp. 262–349.

[4] J. C. Maxwell, ‘‘IV. On the dynamical theory of gases’’, Phil. Trans. R. Soc., 49–88 (1867).

[5] N. Bogoliubov, ‘‘Kinetic Equations’’, J. Phys. **10** (1946).

[6] M. Born and H. S. Green, ‘‘A general kinetic theory of liquids I. The molecular distribution functions’’, Proc. A **188**, 10–18 (1946).

[7] J. G. Kirkwood, ‘‘The Statistical Mechanical Theory of Transport Processes I. General Theory’’, J. Chem. Phys. **14**, 180–201 (1946).

[8] J. Yvon, *La théorie statistique des fluides et l’équation d’état*, Actualités scientifiques et industrielles 203 (Hermann, Paris, 1935).

[9] O. E. Lanford, ‘‘Time evolution of large classical systems’’, in *Dynamical Systems, Theory and Applications*, Vol. 38 (Jan. 1975), pp. 1–111.

[10] T.-Y. Wu, ‘‘Boltzmann’sH theorem and the Loschmidt and the Zermelo paradoxes’’, Int J Theor Phys **14**, 289–294 (1975).

[11] H. Price, *Time’s Arrow and Archimedes’ Point: New Directions for the Physics of Time* (Oxford University Press, Oxford, New York, Dec. 1997).

[12] A. Einstein, ‘‘Über die von der molekularkinetischen Theorie der Wärme geforderte Bewegung von in ruhenden Flüssigkeiten suspendierten Teilchen’’, Ann. Phys. **322**, 549–560 (1905).

[13] M. von Smoluchowski, ‘‘Zur kinetischen Theorie der Brownschen Molekularbewegung und der Suspensionen’’, Ann. Phys. **326**, 756–780 (1906).

[14] G. E. Uhlenbeck and L. S. Ornstein, ‘‘On the Theory of the Brownian Motion’’, Phys. Rev. **36**, 823–841 (1930).

[15] P. Langevin, ‘‘Paul Langevin’s 1908 paper ‘‘On the Theory of Brownian Motion’’ [‘‘Sur la théorie du mouvement brownien,’’ C. R. Acad. Sci. (Paris) 146, 530–533 (1908)]’’, Am. J. Phys. **65**, 1079–1081 (1997).

[16] L. Onsager, ‘‘Reciprocal Relations in Irreversible Processes. I.’’, Phys. Rev. **37**, 405–426 (1931).

[17] L. Onsager, ‘‘Reciprocal Relations in Irreversible Processes. II.’’, Phys. Rev. **38**, 2265–2279 (1931).

[18] H. B. G. Casimir, ‘‘On Onsager’s Principle of Microscopic Reversibility’’, Rev. Mod. Phys. **17**, 343–350 (1945).

[19] H. B. Callen and T. A. Welton, ‘‘Irreversibility and Generalized Noise’’, Phys. Rev. **83**, 34–40 (1951).

[20] M. S. Green, ‘‘Markoff Random Processes and the Statistical Mechanics of Time-Dependent Phenomena. II. Irreversible Processes in Fluids’’, J. Chem. Phys. **22**, 398–413 (1954).

[21] R. Kubo, ‘‘Statistical-Mechanical Theory of Irreversible Processes. I. General Theory and Simple Applications to Magnetic and Conduction Problems’’, J. Phys. Soc. Jpn. **12**, 570–586 (1957).

[22] H. Nyquist, ‘‘Thermal Agitation of Electric Charge in Conductors’’, Phys. Rev. **32**, 110–113 (1928).

[23] J. B. Johnson, ‘‘Thermal Agitation of Electricity in Conductors’’, Phys. Rev. **32**, 97–109 (1928).

[24] D. J. Evans, E. G. D. Cohen, and G. P. Morriss, ‘‘Probability of second law violations in shearing steady states’’, Phys. Rev. Lett. **71**, 2401–2404 (1993).

[25] G. Gallavotti and E. G. D. Cohen, ‘‘Dynamical Ensembles in Nonequilibrium Statistical Mechanics’’, Phys. Rev. Lett. **74**, 2694–2697 (1995).

[26] C. Jarzynski, ‘‘Nonequilibrium Equality for Free Energy Differences’’, Phys. Rev. Lett. **78**, 2690–2693 (1997).

[27] G. E. Crooks, ‘‘Entropy production fluctuation theorem and the nonequilibrium work relation for free energy differences’’, Phys. Rev. E **60**, 2721–2726 (1999).

[28] J. Liphardt et al., ‘‘Equilibrium Information from Nonequilibrium Measurements in an Experimental Test of Jarzynski’s Equality’’, Science **296**, 1832–1835 (2002).

[29] D. Collin et al., ‘‘Verification of the Crooks fluctuation theorem and recovery of RNA folding free energies’’, Nature **437**, 231–234 (2005).

[30] W. H. Zurek, ‘‘Decoherence, einselection, and the quantum origins of the classical’’, Rev. Mod. Phys. **75**, 715–775 (2003).

[31] A. O. Caldeira and A. J. Leggett, ‘‘Path integral approach to quantum Brownian motion’’, Physica A: Statistical Mechanics and its Applications **121**, 587–616 (1983).

[32] A. O. Caldeira and A. J. Leggett, ‘‘Quantum tunnelling in a dissipative system’’, Annals of Physics **149**, 374–456 (1983).

[33] A. J. Leggett et al., ‘‘Dynamics of the dissipative two-state system’’, Rev. Mod. Phys. **59**, 1–85 (1987).

[34] M. B. Plenio and S. F. Huelga, ‘‘Dephasing-assisted transport: quantum networks and biomolecules’’, New J. Phys. **10**, 113019 (2008).

[35] A. Ishizaki and G. R. Fleming, ‘‘Theoretical examination of quantum coherence in a photosynthetic system at physiological temperature’’, Proc. Natl. Acad. Sci. **106**, 17255–17260 (2009).

[36] A. G. Redfield, ‘‘On the Theory of Relaxation Processes’’, IBM J. Res. Dev. **1**, 19–31 (1957).

[37] G. Lindblad, ‘‘On the generators of quantum dynamical semigroups’’, Commun.Math. Phys. **48**, 119–130 (1976).

[38] V. Gorini, A. Kossakowski, and E. C. G. Sudarshan, ‘‘Completely positive dynamical semigroups of N-level systems’’, J. Math. Phys. **17**, 821–825 (1976).

[39] F. Haake and M. Lewenstein, ‘‘Adiabatic drag and initial slip in random processes’’, Phys. Rev. A **28**, 3606–3612 (1983).

[40] P. Gaspard and M. Nagaoka, ‘‘Slippage of initial conditions for the Redfield master equation’’, J. Chem. Phys. **111**, 5668–5675 (1999).

[41] G. Schaller and T. Brandes, ‘‘Preservation of positivity by dynamical coarse graining’’, Phys. Rev. A **78**, 022106 (2008).

[42] H.-P. Breuer, E.-M. Laine, and J. Piilo, ‘‘Measure for the Degree of Non-Markovian Behavior of Quantum Processes in Open Systems’’, Phys. Rev. Lett. **103**, 210401 (2009).

[43] W. E. Lamb, ‘‘Theory of an Optical Maser’’, Phys. Rev. **134**, A1429–A1450 (1964).

[44] H. Haken, *Laser Theory* (Springer, Berlin, Heidelberg, 1984).

[45] H. Haken, ''Cooperative phenomena in systems far from thermal equilibrium and in nonphysical systems'', Rev. Mod. Phys. **47**, 67–121 (1975).

[46] J. H. Shirley, ''Solution of the Schrödinger Equation with a Hamiltonian Periodic in Time'', Phys. Rev. **138**, B979–B987 (1965).

[47] H. Sambe, ''Steady States and Quasienergies of a Quantum-Mechanical System in an Oscillating Field'', Phys. Rev. A **7**, 2203–2213 (1973).

[48] J. F. Poyatos, J. I. Cirac, and P. Zoller, ''Quantum Reservoir Engineering with Laser Cooled Trapped Ions'', Phys. Rev. Lett. **77**, 4728–4731 (1996).

[49] F. Verstraete, M. M. Wolf, and J. I. Cirac, ''Quantum computation and quantum-state engineering driven by dissipation'', Nat. Phys. **5**, 633–636 (2009).

[50] J. T. Barreiro et al., ''An open-system quantum simulator with trapped ions'', Nature **470**, 486–491 (2011).

[51] H. Krauter et al., ''Entanglement Generated by Dissipation and Steady State Entanglement of Two Macroscopic Objects'', Phys. Rev. Lett. **107**, 080503 (2011).

[52] S. Diehl et al., ''Quantum states and phases in driven open quantum systems with cold atoms'', Nat. Phys. **4**, 878–883 (2008).

[53] M. Müller, S. Diehl, G. Pupillo, and P. Zoller, ''Engineered open systems and quantum simulations with atoms and ions'', in *Advances in atomic, molecular, and optical physics*, Vol. 61, edited by P. Berman, E. Arimondo, and C. Lin, Advances in Atomic, Molecular, and Optical Physics (Academic Press, 2012), pp. 1–80.

[54] I. M. Georgescu, S. Ashhab, and F. Nori, ''Quantum simulation'', Rev. Mod. Phys. **86**, 153–185 (2014).

[55] C. Monroe et al., ''Programmable quantum simulations of spin systems with trapped ions'', Rev. Mod. Phys. **93**, 025001 (2021).

[56] A. Browaeys and T. Lahaye, ''Many-body physics with individually controlled Rydberg atoms'', Nat. Phys. **16**, 132–142 (2020).

[57] S. Ebadi et al., ''Quantum phases of matter on a 256-atom programmable quantum simulator'', Nature **595**, 227–232 (2021).

[58] A. A. Houck, H. E. Türeci, and J. Koch, ''On-chip quantum simulation with superconducting circuits'', Nat. Phys. **8**, 292–299 (2012).

[59] A. Blais, A. L. Grimsmo, S. M. Girvin, and A. Wallraff, ‘‘Circuit quantum electrodynamics’’, Rev. Mod. Phys. **93**, 025005 (2021).

[60] M. Fitzpatrick et al., ‘‘Observation of a dissipative phase transition in a one-dimensional circuit QED lattice’’, Phys. Rev. X **7**, 011016 (2017).

[61] A. Keesling et al., ‘‘Quantum Kibble–Zurek mechanism and critical dynamics on a programmable Rydberg simulator’’, Nature **568**, 207–211 (2019).

[62] R. Blatt and C. F. Roos, ‘‘Quantum simulations with trapped ions’’, Nat. Phys. **8**, 277–284 (2012).

[63] H. Bernien et al., ‘‘Probing many-body dynamics on a 51-atom quantum simulator’’, Nature **551**, 579–584 (2017).

[64] J. Kasprzak et al., ‘‘Bose–Einstein condensation of exciton polaritons’’, Nature **443**, 409–414 (2006).

[65] E. M. Kessler et al., ‘‘Dissipative phase transition in a central spin system’’, Phys. Rev. A **86**, 012116 (2012).

[66] F. Vicentini et al., ‘‘Critical slowing down in driven-dissipative Bose-Hubbard lattices’’, Phys. Rev. A **97**, 013853 (2018).

[67] F. Minganti, A. Biella, N. Bartolo, and C. Ciuti, ‘‘Spectral theory of Liouvillians for dissipative phase transitions’’, Phys. Rev. A **98**, 042118 (2018).

[68] L. M. Sieberer, M. Buchhold, and S. Diehl, ‘‘Keldysh field theory for driven open quantum systems’’, Rep. Prog. Phys. **79**, 096001 (2016).

[69] E. G. Dalla Torre, E. Demler, T. Giamarchi, and E. Altman, ‘‘Quantum critical states and phase transitions in the presence of non-equilibrium noise’’, Nat. Phys. **6**, 806 (2010).

[70] R. Rota, F. Minganti, C. Ciuti, and V. Savona, ‘‘Quantum critical regime in a quadratically driven nonlinear photonic lattice’’, Phys. Rev. Lett. **122**, 110405 (2019).

[71] M. Žnidarič, ‘‘Exact solution for a diffusive nonequilibrium steady state of an open quantum chain’’, J. Stat. Mech. Theory Exp. **2010**, L05002 (2010).

[72] E. Altman et al., ‘‘Quantum Simulators: Architectures and Opportunities’’, PRX Quantum **2**, 017003 (2021).

[73] J. Preskill, ‘‘Quantum computing in the NISQ era and beyond’’, Quantum **2**, 79 (2018).

[74] F. Wagner, D. J. Egger, and F. Liers, ‘‘Optimized Noise Suppression for Quantum

Circuits'', Inf. J. Comput. **37**, 22–41 (2025).

[75] D. Qin, X. Xu, and Y. Li, ''An overview of quantum error mitigation formulas'', Chinese Phys. B **31**, 090306 (2022).

[76] Z. Cai et al., ''Quantum error mitigation'', Rev. Mod. Phys. **95**, 045005 (2023).

[77] M. Ippoliti et al., ''Many-Body Physics in the NISQ Era: Quantum Programming a Discrete Time Crystal'', PRX Quantum **2**, 030346 (2021).

[78] H. E. Stanley and V. K. Wong, ''Introduction to Phase Transitions and Critical Phenomena'', Am. J. Phys. **40**, 927–928 (1972).

[79] P. W. Anderson, ''More Is Different'', Science **177**, 393–396 (1972).

[80] L. Landau, ''The Theory of Phase Transitions'', Nature **138**, 840–841 (1936).

[81] L. D. Landau and E. M. Lifshitz, *Statistical Mechanics* (Elsevier, 1980).

[82] S. Sachdev, *Quantum phase transitions*, Second edition (Cambridge University Press, Cambridge ; New York, 2011).

[83] X.-G. Wen, *Quantum Field Theory of Many-Body Systems : From the Origin of Sound to an Origin of Light and Electrons*, Oxford Graduate Texts (OUP Oxford, Oxford, Jan. 2004).

[84] L. D. Landau, ''On the Theory of Phase Transitions'', in *Collected Papers of L.D. Landau* (Pergamon, Jan. 1965), pp. 193–216.

[85] P. C. Hohenberg and A. P. Krekhov, ''An introduction to the Ginzburg–Landau theory of phase transitions and nonequilibrium patterns'', Physics Reports, An Introduction to the Ginzburg–Landau Theory of Phase Transitions and Nonequilibrium Patterns **572**, 1–42 (2015).

[86] P. M. Chaikin and T. C. Lubensky, *Principles of Condensed Matter Physics* (Cambridge University Press, Cambridge, Jan. 1995).

[87] D. J. Amit and V. Martin-mayor, *Field Theory, The Renormalization Group, And Critical Phenomena: Graphs To Computers (3rd Edition)* (World Scientific Publishing Company, Singapore, SG, 2005).

[88] P. Weiss, ''L'hypothèse du champ moléculaire et la propriété ferromagnétique'', J. Phys. Theor. Appl. **6**, 661–690 (1907).

[89] L. S. Ornstein and F. Zernike, ''Accidental deviations of density and opalescence at the critical point of a single substance'', KNAW Proc. **17 II** (1914).

[90] K. G. Wilson and J. Kogut, ‘‘The renormalization group and the ϵ expansion’’, Physics Reports **12**, 75–199 (1974).

[91] L. Onsager, ‘‘Crystal Statistics. I. A Two-Dimensional Model with an Order-Disorder Transition’’, Phys. Rev. **65**, 117–149 (1944).

[92] K. G. Wilson, ‘‘Renormalization Group and Critical Phenomena. I. Renormalization Group and the Kadanoff Scaling Picture’’, Phys. Rev. B **4**, 3174–3183 (1971).

[93] C. G. Callan, ‘‘Broken Scale Invariance in Scalar Field Theory’’, Phys. Rev. D **2**, 1541–1547 (1970).

[94] K. G. Wilson and M. E. Fisher, ‘‘Critical Exponents in 3.99 Dimensions’’, Phys. Rev. Lett. **28**, 240–243 (1972).

[95] S. L. Sondhi, S. M. Girvin, J. P. Carini, and D. Shahar, ‘‘Continuous quantum phase transitions’’, Rev. Mod. Phys. **69**, 315–333 (1997).

[96] P. Pfeuty, ‘‘The one-dimensional Ising model with a transverse field’’, Annals of Physics **57**, 79–90 (1970).

[97] R. B. Stinchcombe, ‘‘Ising model in a transverse field. I. Basic theory’’, J. Phys. C: Solid State Phys. **6**, 2459 (1973).

[98] P. Jordan and E. Wigner, ‘‘Über das Paulische Äquivalenzverbot’’, Z. Physik **47**, 631–651 (1928).

[99] M. Suzuki, ‘‘Relationship between d-Dimensional Quantal Spin Systems and (d+1)-Dimensional Ising Systems: Equivalence, Critical Exponents and Systematic Approximants of the Partition Function and Spin Correlations’’, Prog Theor Phys **56**, 1454–1469 (1976).

[100] R. H. Dicke, ‘‘Coherence in Spontaneous Radiation Processes’’, Phys. Rev. **93**, 99–110 (1954).

[101] B. M. Garraway, ‘‘The Dicke model in quantum optics: Dicke model revisited’’, Philos Trans A Math Phys Eng Sci **369**, 1137–1155 (2011).

[102] F. Damanet, A. J. Daley, and J. Keeling, ‘‘Atom-only descriptions of the driven-dissipative Dicke model’’, Phys. Rev. A **99**, 033845 (2019).

[103] K. Hepp and E. H. Lieb, ‘‘On the superradiant phase transition for molecules in a quantized radiation field: the dicke maser model’’, Annals of Physics **76**, 360–404 (1973).

[104] P. Kirton, M. M. Roses, J. Keeling, and E. G. Dalla Torre, ‘‘Introduction to the Dicke

Model: From Equilibrium to Nonequilibrium, and Vice Versa'', Adv. Quantum Technol. **2**, 1800043 (2019).

[105] M. Vojta, ''Quantum phase transitions'', Rep. Prog. Phys. **66**, 2069 (2003).

[106] J. A. Hertz, ''Quantum critical phenomena'', Phys. Rev. B **14**, 1165–1184 (1976).

[107] S. Chakravarty, B. I. Halperin, and D. R. Nelson, ''Two-dimensional quantum Heisenberg antiferromagnet at low temperatures'', Phys. Rev. B **39**, 2344–2371 (1989).

[108] L. Zhu, M. Garst, A. Rosch, and Q. Si, ''Universally Diverging Grüneisen Parameter and the Magnetocaloric Effect Close to Quantum Critical Points'', Phys. Rev. Lett. **91**, 066404 (2003).

[109] M. Garst and A. Rosch, ''Sign change of the Grüneisen parameter and magnetocaloric effect near quantum critical points'', Phys. Rev. B **72**, 205129 (2005).

[110] H. v. Löhneysen et al., ''Non-Fermi-liquid behavior in a heavy-fermion alloy at a magnetic instability'', Phys. Rev. Lett. **72**, 3262–3265 (1994).

[111] J. Custers et al., ''The break-up of heavy electrons at a quantum critical point'', Nature **424**, 524–527 (2003).

[112] G. R. Stewart, ''Non-Fermi-liquid behavior in d- and f-electron metals'', Rev. Mod. Phys. **73**, 797–855 (2001).

[113] P. Coleman, C. Pépin, Q. Si, and R. Ramazashvili, ''How do Fermi liquids get heavy and die?'', J. Phys.: Condens. Matter **13**, R723 (2001).

[114] Q. Si, S. Rabello, K. Ingersent, and J. L. Smith, ''Locally critical quantum phase transitions in strongly correlated metals'', Nature **413**, 804–808 (2001).

[115] J. Zaanen, ''Why the temperature is high'', Nature **430**, 512–513 (2004).

[116] A. Legros et al., ''Universal T-linear resistivity and Planckian dissipation in overdoped cuprates'', Nat. Phys. **15**, 142–147 (2019).

[117] A. Polkovnikov, K. Sengupta, A. Silva, and M. Vengalattore, ''Colloquium: Nonequilibrium dynamics of closed interacting quantum systems'', Rev. Mod. Phys. **83**, 863–883 (2011).

[118] T. W. B. Kibble, ''Topology of cosmic domains and strings'', J. Phys. A: Math. Gen. **9**, 1387 (1976).

[119] W. H. Zurek, ''Cosmological experiments in superfluid helium?'', Nature **317**, 505–508

(1985).

[120] A. Polkovnikov, ‘‘Universal adiabatic dynamics in the vicinity of a quantum critical point’’, Phys. Rev. B **72**, 161201 (2005).

[121] W. Zurek, ‘‘Cosmic strings in laboratory superfluids and the topological remnants of other phase transitions’’, Acta Phys. Pol. B (1993).

[122] W. H. Zurek, ‘‘Cosmological experiments in condensed matter systems’’, Physics Reports **276**, 177–221 (1996).

[123] I. Chuang, R. Durrer, N. Turok, and B. Yurke, ‘‘Cosmology in the Laboratory: Defect Dynamics in Liquid Crystals’’, Science **251**, 1336–1342 (1991).

[124] R. Carmi, E. Polturak, and G. Koren, ‘‘Observation of Spontaneous Flux Generation in a Multi-Josephson-Junction Loop’’, Phys. Rev. Lett. **84**, 4966–4969 (2000).

[125] K. Pyka et al., ‘‘Topological defect formation and spontaneous symmetry breaking in ion Coulomb crystals’’, Nat Commun **4**, 2291 (2013).

[126] S. Ulm et al., ‘‘Observation of the Kibble–Zurek scaling law for defect formation in ion crystals’’, Nat Commun **4**, 2290 (2013).

[127] N. Navon, A. L. Gaunt, R. P. Smith, and Z. Hadzibabic, ‘‘Critical dynamics of spontaneous symmetry breaking in a homogeneous Bose gas’’, Science **347**, 167–170 (2015).

[128] B. Gardas, J. Dziarmaga, W. H. Zurek, and M. Zwolak, ‘‘Defects in Quantum Computers’’, Sci Rep **8**, 4539 (2018).

[129] P. Titum and M. F. Maghrebi, ‘‘Nonequilibrium criticality in quench dynamics of long-range spin models’’, Phys. Rev. Lett. **125**, 040602 (2020).

[130] M. Srednicki, ‘‘The approach to thermal equilibrium in quantized chaotic systems’’, J. Phys. A: Math. Gen. **32**, 1163 (1999).

[131] M. Rigol, V. Dunjko, and M. Olshanii, ‘‘Thermalization and its mechanism for generic isolated quantum systems’’, Nature **452**, 854–858 (2008).

[132] L. D’Alessio, Y. Kafri, A. Polkovnikov, and M. Rigol, ‘‘From quantum chaos and eigenstate thermalization to statistical mechanics and thermodynamics’’, Adv. Phys. **65**, 239–362 (2016).

[133] C. Gogolin and J. Eisert, ‘‘Equilibration, thermalisation, and the emergence of statistical mechanics in closed quantum systems’’, Rep. Prog. Phys. **79**, 056001 (2016).

[134] S. Bhattacharyya, S. Dasgupta, and A. Das, ''Signature of a continuous quantum phase transition in non-equilibrium energy absorption: Footprints of criticality on higher excited states'', Sci. Rep. **5**, 16490 (2015).

[135] S. Roy, R. Moessner, and A. Das, ''Locating topological phase transitions using nonequilibrium signatures in local bulk observables'', Phys. Rev. B **95**, 041105 (2017).

[136] P. Titum et al., ''Probing ground-state phase transitions through quench dynamics'', Phys. Rev. Lett. **123**, 115701 (2019).

[137] S. Paul, P. Titum, and M. Maghrebi, ''Hidden quantum criticality and entanglement in quench dynamics'', Phys. Rev. Res. **6**, L032003 (2024).

[138] P. Richerme et al., ''Non-local propagation of correlations in quantum systems with long-range interactions'', Nature **511**, 198–201 (2014).

[139] P. Jurcevic et al., ''Quasiparticle engineering and entanglement propagation in a quantum many-body system'', Nature **511**, 202–205 (2014).

[140] S. Braun et al., ''Emergence of coherence and the dynamics of quantum phase transitions'', Proc. Natl. Acad. Sci. **112**, 3641–3646 (2015).

[141] H. J. Carmichael, ''Breakdown of Photon Blockade: A Dissipative Quantum Phase Transition in Zero Dimensions'', Phys. Rev. X **5**, 031028 (2015).

[142] W. Casteels, R. Fazio, and C. Ciuti, ''Critical dynamical properties of a first-order dissipative phase transition'', Phys. Rev. A **95**, 012128 (2017).

[143] K. Baumann, C. Guerlin, F. Brennecke, and T. Esslinger, ''Dicke quantum phase transition with a superfluid gas in an optical cavity'', Nature **464**, 1301–1306 (2010).

[144] J. J. Sakurai and J. Napolitano, *Modern quantum mechanics*, 3rd ed (Cambridge University Press, Cambridge, 2021).

[145] M. A. Nielsen and I. L. Chuang, *Quantum computation and quantum information*, 10. printing (Cambridge Univ. Press, Cambridge, 2009).

[146] M. A. Schlosshauer, *Decoherence and the Quantum-To-Classical Transition*, Frontiers Collection (Springer Berlin Heidelberg, Berlin, Heidelberg, 2007).

[147] H.-P. Breuer and F. Petruccione, *The Theory of Open Quantum Systems* (Oxford University Press, Jan. 2007).

[148] R. Alicki, *Quantum Dynamical Semigroups and Applications*, 2nd ed, Lecture Notes in Physics Ser v.717 (Springer Berlin / Heidelberg, Berlin, Heidelberg, 2007).

[149] J. Preskill, *Lecture Notes for Physics 229:Quantum Information and Computation* (CreateSpace Independent Publishing Platform, Jan. 2015).

[150] M. M. Wolf, F. Verstraete, M. B. Hastings, and J. I. Cirac, ‘‘Area Laws in Quantum Systems: Mutual Information and Correlations’’, Phys. Rev. Lett. **100**, 070502 (2008).

[151] H. Carmichael, *An Open Systems Approach to Quantum Optics: Lectures Presented at the Université Libre de Bruxelles October 28 to November 4, 1991*, edited by H. Araki et al., Vol. 18, Lecture Notes in Physics Monographs (Springer, Berlin, Heidelberg, 1993).

[152] J. Marino and S. Diehl, ‘‘Driven markovian quantum criticality’’, Phys. Rev. Lett. **116**, 070407 (2016).

[153] M.-D. Choi, ‘‘Completely positive linear maps on complex matrices’’, Linear Algebra and its Applications **10**, 285–290 (1975).

[154] A. Jamiołkowski, ‘‘Linear transformations which preserve trace and positive semidefiniteness of operators’’, Reports on Mathematical Physics **3**, 275–278 (1972).

[155] J. R. Johansson, P. D. Nation, and F. Nori, ‘‘QuTiP: An open-source Python framework for the dynamics of open quantum systems’’, Computer Physics Communications **183**, 1760–1772 (2012).

[156] J. R. Johansson, P. D. Nation, and F. Nori, ‘‘QuTiP 2: A Python framework for the dynamics of open quantum systems’’, Computer Physics Communications **184**, 1234–1240 (2013).

[157] H. Weimer, A. Kshetrimayum, and R. Orús, ‘‘Simulation methods for open quantum many-body systems’’, Rev. Mod. Phys. **93**, 015008 (2021).

[158] T. Prosen, ‘‘Third quantization: a general method to solve master equations for quadratic open Fermi systems’’, New J. Phys. **10**, 043026 (2008).

[159] T. Prosen and T. H. Seligman, ‘‘Quantization over boson operator spaces’’, J. Phys. A: Math. Theor. **43**, 392004 (2010).

[160] M. O. Scully and M. S. Zubairy, *Quantum Optics* (Cambridge University Press, 1997).

[161] C. Joshi, F. Nissen, and J. Keeling, ‘‘Quantum correlations in the one-dimensional driven dissipative XY model’’, Phys. Rev. A **88**, 063835 (2013).

[162] M. Ali, N. A. Kamar, A. Seif, and M. Maghrebi, ‘‘Signatures of Quantum Phase Transitions in Driven Dissipative Spin Chains’’, Phys. Rev. Lett. **136**, 060404 (2026).

[163] T. Holstein and H. Primakoff, ‘‘Field Dependence of the Intrinsic Domain Magnetization

of a Ferromagnet'', Phys. Rev. **58**, 1098–1113 (1940).

[164] I. R. Senitzky, ''Dissipation in Quantum Mechanics. The Harmonic Oscillator'', Phys. Rev. **119**, 670–679 (1960).

[165] M. Lax, ''Quantum Noise. IV. Quantum Theory of Noise Sources'', Phys. Rev. **145**, 110–129 (1966).

[166] G. W. Ford, M. Kac, and P. Mazur, ''Statistical Mechanics of Assemblies of Coupled Oscillators'', J. Math. Phys. **6**, 504–515 (1965).

[167] A. McDonald and A. A. Clerk, ''Third quantization of open quantum systems: Dissipative symmetries and connections to phase-space and Keldysh field-theory formulations'', Phys. Rev. Res. **5**, 033107 (2023).

[168] C. Weedbrook et al., ''Gaussian quantum information'', Rev. Mod. Phys. **84**, 621–669 (2012).

[169] T. Barthel and Y. Zhang, ''Solving quasi-free and quadratic Lindblad master equations for open fermionic and bosonic systems'', J. Stat. Mech. **2022**, 113101 (2022).

[170] P. C. Parks, ''A. M. Lyapunov's stability theory—100 years on'', IMA J Math Control Info **9**, 275–303 (1992).

[171] A. Kamenev, *Field theory of non-equilibrium systems*, Second edition (Cambridge, United Kingdom New York, NY Cambridge University Press, 2023).

[172] R. P. Feynman, ''Space-Time Approach to Non-Relativistic Quantum Mechanics'', Rev. Mod. Phys. **20**, 367–387 (1948).

[173] R. P. Feynman, *Quantum mechanics and path integrals*, International Series in Pure and Applied Physics. (McGraw-Hill, New York : 1965).

[174] T. Matsubara, ''A New Approach to Quantum-Statistical Mechanics'', Prog. Theor. Phys. **14**, 351–378 (1955).

[175] A. Abrikosov, *Methods of quantum field theory in statistical physics*, Revised English edition / translated and edited by Richard A. Silverman., Selected Russian Publications in the Mathematical Sciences. (Dover Publications, New York : 1975).

[176] M. Gell-Mann and F. Low, ''Bound States in Quantum Field Theory'', Phys. Rev. **84**, 350–354 (1951).

[177] J. Schwinger, ''The special canonical group*'', Proc. Natl. Acad. Sci. **46**, 1401–1415 (1960).

[178] J. Schwinger, ‘‘Brownian Motion of a Quantum Oscillator’’, J. Math. Phys. **2**, 407–432 (1961).

[179] L. V. Keldysh, ‘‘Diagram technique for nonequilibrium processes’’, in *Selected Papers of Leonid V Keldysh* (World Scientific Publishing Company, 1965), pp. 47–55.

[180] M. Suzuki, ‘‘Generalized Trotter’s formula and systematic approximants of exponential operators and inner derivations with applications to many-body problems’’, Commun.Math. Phys. **51**, 183–190 (1976).

[181] D. Paz and M. Maghrebi, ‘‘Time-reversal symmetry breaking and emergence in driven-dissipative Ising models’’, SciPost Phys. **12**, 066 (2022).

[182] R. Bellman, *Dynamic programming*. Rand Corporation Research Study. (Princeton University Press, Princeton : 1957).

[183] V. V. Albert and L. Jiang, ‘‘Symmetries and conserved quantities in Lindblad master equations’’, Phys. Rev. A **89**, 022118 (2014).

[184] R. B. Lehoucq, D. C. Sorensen, and C. Yang, *ARPACK Users' Guide: Solution of Large-scale Eigenvalue Problems with Implicitly Restarted Arnoldi Methods* (SIAM, Jan. 1998).

[185] W. H. Press and S. A. Teukolsky, *Numerical Recipes* (Cambridge University Press, Sept. 2007).

[186] J. Dalibard, Y. Castin, and K. Mølmer, ‘‘Wave-function approach to dissipative processes in quantum optics’’, Phys. Rev. Lett. **68**, 580–583 (1992).

[187] R. Dum, P. Zoller, and H. Ritsch, ‘‘Monte Carlo simulation of the atomic master equation for spontaneous emission’’, Phys. Rev. A **45**, 4879–4887 (1992).

[188] H. J. Carmichael, ‘‘Quantum trajectory theory for cascaded open systems’’, Phys. Rev. Lett. **70**, 2273–2276 (1993).

[189] M. B. Plenio and P. L. Knight, ‘‘The quantum-jump approach to dissipative dynamics in quantum optics’’, Rev. Mod. Phys. **70**, 101–144 (1998).

[190] J. Eisert, M. Cramer, and M. B. Plenio, ‘‘Colloquium: Area laws for the entanglement entropy’’, Rev. Mod. Phys. **82**, 277–306 (2010).

[191] U. Schollwöck, ‘‘The density-matrix renormalization group in the age of matrix product states’’, Ann. Phys. **326**, 96–192 (2011).

[192] J. C. Bridgeman and C. T. Chubb, ‘‘Hand-waving and interpretive dance: an introductory

course on tensor networks'', J. Phys. A: Math. Theor. **50**, 223001 (2017).

[193] S. R. White, ''Density matrix formulation for quantum renormalization groups'', Phys. Rev. Lett. **69**, 2863–2866 (1992).

[194] E. Mascarenhas, H. Flayac, and V. Savona, ''Matrix-product-operator approach to the nonequilibrium steady state of driven-dissipative quantum arrays'', Phys. Rev. A **92**, 022116 (2015).

[195] J. Cui, J. I. Cirac, and M. C. Bañuls, ''Variational matrix product operators for the steady state of dissipative quantum systems'', Phys. Rev. Lett. **114**, 220601 (2015).

[196] A. De et al., ''Non-equilibrium critical scaling and universality in a quantum simulator'', Nat Commun **16**, 7939 (2025).

[197] L. Deslauriers et al., ''Zero-point cooling and low heating of trapped $^{111}Cd^{+}$ ions'', Phys. Rev. A **70**, 043408 (2004).

[198] M. Cetina et al., ''Control of Transverse Motion for Quantum Gates on Individually Addressed Atomic Qubits'', PRX Quantum **3**, 010334 (2022).

[199] G. Pagano et al., ''Quantum approximate optimization of the long-range Ising model with a trapped-ion quantum simulator'', Proc. Natl. Acad. Sci. **117**, 25396–25401 (2020).

[200] W. L. Tan et al., ''Domain-wall confinement and dynamics in a quantum simulator'', Nat. Phys. **17**, 742–747 (2021).

[201] M. Kac and C. J. Thompson, ''Critical Behavior of Several Lattice Models with Long-Range Interaction'', J. Math. Phys. **10**, 1373–1386 (1969).

[202] H. Deng et al., ''Condensation of Semiconductor Microcavity Exciton Polaritons'', Science **298**, 199–202 (2002).

[203] M. H. Szymań ńska, J. Keeling, and P. B. Littlewood, ''Nonequilibrium quantum condensation in an incoherently pumped dissipative system'', Phys. Rev. Lett. **96**, 230602 (2006).

[204] T. Byrnes, N. Y. Kim, and Y. Yamamoto, ''Exciton–polariton condensates'', Nat. Phys. **10**, 803–813 (2014).

[205] S. R. Rodriguez et al., ''Interaction-induced hopping phase in driven-dissipative coupled photonic microcavities'', Nat. Commun. **7**, 11887 (2016).

[206] S. R. K. Rodriguez et al., ''Probing a dissipative phase transition via dynamical optical hysteresis'', Phys. Rev. Lett. **118**, 247402 (2017).

[207] P. Schindler et al., ‘‘Quantum simulation of dynamical maps with trapped ions’’, Nat. Phys. **9**, 361–367 (2013).

[208] J. G. Bohnet et al., ‘‘Quantum spin dynamics and entanglement generation with hundreds of trapped ions’’, Science **352**, 1297–1301 (2016).

[209] T. Peyronel et al., ‘‘Quantum nonlinear optics with single photons enabled by strongly interacting atoms’’, Nature **488**, 57–60 (2012).

[210] O. Firstenberg et al., ‘‘Attractive photons in a quantum nonlinear medium’’, Nature **502**, 71–75 (2013).

[211] C. Carr et al., ‘‘Nonequilibrium phase transition in a dilute rydberg ensemble’’, Phys. Rev. Lett. **111**, 113901 (2013).

[212] N. Malossi et al., ‘‘Full counting statistics and phase diagram of a dissipative rydberg gas’’, Phys. Rev. Lett. **113**, 023006 (2014).

[213] H. Labuhn et al., ‘‘Tunable two-dimensional arrays of single Rydberg atoms for realizing Quantum Ising models’’, Nature **534**, 667–670 (2016).

[214] L. Shirizly, G. Misguich, and H. Landa, ‘‘Dissipative dynamics of graph-state stabilizers with superconducting qubits’’, Phys. Rev. Lett. **132**, 010601 (2024).

[215] R. Ma et al., ‘‘A dissipatively stabilized Mott insulator of photons’’, Nature **566**, 51–57 (2019).

[216] X. Mi et al., ‘‘Stable quantum-correlated many-body states through engineered dissipation’’, Science **383**, 1332–1337 (2024).

[217] J. D. Guimarães et al., ‘‘Noise-assisted digital quantum simulation of open systems using partial probabilistic error cancellation’’, PRX Quantum **4**, 040329 (2023).

[218] P. Sierant et al., ‘‘Dissipative Floquet Dynamics: from Steady State to Measurement Induced Criticality in Trapped-ion Chains’’, Quantum **6**, 638 (2022).

[219] C. Haack et al., ‘‘Probing non-equilibrium dissipative phase transitions with trapped-ion quantum simulators’’, ArXiv Prepr., arXiv:2311.06199 (2023).

[220] B. Žunkovič, ‘‘Closed hierarchy of correlations in Markovian open quantum systems’’, New J. Phys. **16**, 013042 (2014).

[221] K. Kawabata, R. Sohal, and S. Ryu, ‘‘Lieb-schultz-mattis theorem in open quantum systems’’, Phys. Rev. Lett. **132**, 070402 (2024).

[222] J. M. Torres, ‘‘Closed-form solution of Lindblad master equations without gain’’, Phys. Rev. A **89**, 052133 (2014).

[223] T. Prosen and I. Pižorn, ‘‘Quantum phase transition in a far-from-equilibrium steady state of an XY spin chain’’, Phys. Rev. Lett. **101**, 105701 (2008).

[224] T. Prosen, ‘‘Exact nonequilibrium steady state of a strongly driven open XXZ chain’’, Phys. Rev. Lett. **107**, 137201 (2011).

[225] M. Foss-Feig et al., ‘‘Solvable family of driven-dissipative many-body systems’’, Phys. Rev. Lett. **119**, 190402 (2017).

[226] D. Roberts and A. A. Clerk, ‘‘Exact solution of the infinite-range dissipative transverse-field ising model’’, Phys. Rev. Lett. **131**, 190403 (2023).

[227] Z. Cai and T. Barthel, ‘‘Algebraic versus Exponential Decoherence in Dissipative Many-Particle Systems’’, Phys. Rev. Lett. **111**, 150403 (2013).

[228] I. Bouchoule, B. Doyon, and J. Dubail, ‘‘The effect of atom losses on the distribution of rapidities in the one-dimensional Bose gas’’, SciPost Phys. **9**, 044 (2020).

[229] F. Lange, Z. Lenarčič, and A. Rosch, ‘‘Pumping approximately integrable systems’’, Nat. Commun. **8**, 15767 (2017).

[230] Z. Lenarčič, F. Lange, and A. Rosch, ‘‘Perturbative approach to weakly driven many-particle systems in the presence of approximate conservation laws’’, Phys. Rev. B **97**, 024302 (2018).

[231] F. Lange, Z. Lenarčič, and A. Rosch, ‘‘Time-dependent generalized Gibbs ensembles in open quantum systems’’, Phys. Rev. B **97**, 165138 (2018).

[232] G. Perfetto, F. Carollo, J. P. Garrahan, and I. Lesanovsky, ‘‘Quantum reaction-limited reaction-diffusion dynamics of annihilation processes’’, Phys. Rev. E **108**, 064104 (2023).

[233] G. Perfetto, F. Carollo, J. P. Garrahan, and I. Lesanovsky, ‘‘Reaction-limited quantum reaction-diffusion dynamics’’, Phys. Rev. Lett. **130**, 210402 (2023).

[234] F. Riggio, L. Rosso, D. Karevski, and J. Dubail, ‘‘Effects of atom losses on a one-dimensional lattice gas of hard-core bosons’’, Phys. Rev. A **109**, 023311 (2024).

[235] I. Bouchoule and J. Dubail, ‘‘Breakdown of tan’s relation in lossy one-dimensional bose gases’’, Phys. Rev. Lett. **126**, 160603 (2021).

[236] I. Bouchoule, L. Dubois, and L.-P. Barbier, ‘‘Losses in interacting quantum gases: Ultraviolet divergence and its regularization’’, Phys. Rev. A **104**, L031304 (2021).

[237] F. Gerbino, I. Lesanovsky, and G. Perfetto, ‘‘Large-scale universality in quantum reaction-diffusion from Keldysh field theory’’, Phys. Rev. B **109**, L220304 (2024).

[238] I. Ulčakar and Z. Lenarčič, ‘‘Generalized Gibbs ensembles in weakly interacting dissipative systems and digital quantum computers’’, SciPost Phys. **19**, 068 (2025).

[239] J. Lloyd et al., ‘‘Quasiparticle cooling algorithms for quantum many-body state preparation’’, ArXiv Prepr., 2404.12175 (2024).

[240] C.-E. Bardyn and A. İmamoğlu, ‘‘Majorana-like Modes of Light in a One-Dimensional Array of Nonlinear Cavities’’, Phys. Rev. Lett. **109**, 253606 (2012).

[241] M. J. Hartmann, F. G. S. L. Brandão, and M. B. Plenio, ‘‘Strongly interacting polaritons in coupled arrays of cavities’’, Nat. Phys. **2**, 849–855 (2006).

[242] M. J. Hartmann, F. G. S. L. Brandão, and M. Plenio, ‘‘Quantum many-body phenomena in coupled cavity arrays’’, Laser Photonics Rev. **2**, 527–556 (2008).

[243] A. D. Greentree, C. Tahan, J. H. Cole, and L. C. L. Hollenberg, ‘‘Quantum phase transitions of light’’, Nat. Phys. **2**, 856–861 (2006).

[244] D. G. Angelakis, M. F. Santos, and S. Bose, ‘‘Photon-blockade-induced Mott transitions and *XY* spin models in coupled cavity arrays’’, Phys. Rev. A **76**, 031805 (2007).

[245] S. Schmidt and J. Koch, ‘‘Circuit QED lattices: Towards quantum simulation with superconducting circuits’’, Ann. Phys. **525**, 395–412 (2013).

[246] E. Lieb, T. Schultz, and D. Mattis, ‘‘Two soluble models of an antiferromagnetic chain’’, Annals of Physics **16**, 407–466 (1961).

[247] P. Calabrese, F. H. L. Essler, and M. Fagotti, ‘‘Quantum quench in the transverse field Ising chain: I. Time evolution of order parameter correlators’’, J. Stat. Mech. Theory Exp. **2012**, 07016 (2012).

[248] J. M. Deutsch, ‘‘Quantum statistical mechanics in a closed system’’, Phys. Rev. A **43**, 2046–2049 (1991).

[249] M. Srednicki, ‘‘Chaos and quantum thermalization’’, Phys. Rev. E **50**, 888–901 (1994).

[250] M. Rigol, ‘‘Quantum quenches and thermalization in one-dimensional fermionic systems’’, Phys. Rev. A **80**, 053607 (2009).

[251] J. Eisert, M. Friesdorf, and C. Gogolin, ‘‘Quantum many-body systems out of equilibrium’’, Nat. Phys. **11**, 124–130 (2015).

[252] L. Vidmar and M. Rigol, ‘‘Generalized Gibbs ensemble in integrable lattice models’’, J. Stat. Mech. Theory Exp. **2016**, 064007 (2016).

[253] M. Rigol, ‘‘Fundamental asymmetry in quenches between integrable and nonintegrable systems’’, Phys. Rev. Lett. **116**, 100601 (2016).

[254] K. Sengupta, S. Powell, and S. Sachdev, ‘‘Quench dynamics across quantum critical points’’, Phys. Rev. A **69**, 053616 (2004).

[255] E. Barouch and B. M. McCoy, ‘‘Statistical Mechanics of the XY Model. II. Spin-Correlation Functions’’, Phys. Rev. A **3**, 786–804 (1971).

[256] A. Haldar et al., ‘‘Signatures of quantum phase transitions after quenches in quantum chaotic one-dimensional systems’’, Phys. Rev. X **11**, 031062 (2021).

[257] K. Binder, ‘‘Finite size scaling analysis of Ising model block distribution functions’’, Z. Für Phys. B Condens. Matter **43**, 119–140 (1981).

[258] T. Shirai and T. Mori, ‘‘Thermalization in open many-body systems based on eigenstate thermalization hypothesis’’, Phys. Rev. E **101**, 042116 (2020).

[259] P.-Y. Zhao, K. Ding, and S. Yang, ‘‘Chebyshev pseudosite matrix product state approach for the spectral functions of electron-phonon coupling systems’’, Phys. Rev. Res. **5**, 023026 (2023).

[260] N. A. Kamar and M. Maghrebi, ‘‘Splitting the local Hilbert space: Matrix product state based approach to large local dimensions’’, Phys. Rev. B **110**, 075114 (2024).

[261] Z. Lenarčič, O. Alberton, A. Rosch, and E. Altman, ‘‘Critical Behavior near the Many-Body Localization Transition in Driven Open Systems’’, Phys. Rev. Lett. **125**, 116601 (2020).

[262] I. Reichental, A. Klempner, Y. Kafri, and D. Podolsky, ‘‘Thermalization in open quantum systems’’, Phys. Rev. B **97**, 134301 (2018).

[263] Z. Lenarčič, E. Altman, and A. Rosch, ‘‘Activating Many-Body Localization in Solids by Driving with Light’’, Phys. Rev. Lett. **121**, 267603 (2018).

[264] D. Porras and J. I. Cirac, ‘‘Effective Quantum Spin Systems with Trapped Ions’’, Phys. Rev. Lett. **92**, 207901 (2004).

[265] J. W. Britton et al., ‘‘Engineered two-dimensional Ising interactions in a trapped-ion quantum simulator with hundreds of spins’’, Nature **484**, 489–492 (2012).

[266] H. Ritsch, P. Domokos, F. Brennecke, and T. Esslinger, ‘‘Cold atoms in cavity-generated

dynamical optical potentials'', Rev. Mod. Phys. **85**, 553–601 (2013).

[267] J. S. Douglas et al., ''Quantum many-body models with cold atoms coupled to photonic crystals'', Nat. Photon. **9**, 326–331 (2015).

[268] A. Asenjo-Garcia et al., ''Exponential Improvement in Photon Storage Fidelities Using Subradiance and ''Selective Radiance'' in Atomic Arrays'', Phys. Rev. X **7**, 031024 (2017).

[269] D. A. Paz and M. F. Maghrebi, ''Driven-dissipative Ising model: An exact field-theoretical analysis'', Phys. Rev. A **104**, 023713 (2021).

[270] J. Marino, ''Universality Class of Ising Critical States with Long-Range Losses'', Phys. Rev. Lett. **129**, 050603 (2022).

[271] K. Seetharam, A. Lerose, R. Fazio, and J. Marino, ''Dynamical scaling of correlations generated by short- and long-range dissipation'', Phys. Rev. B **105**, 184305 (2022).

[272] J. Gelhausen and M. Buchhold, ''Dissipative Dicke model with collective atomic decay: Bistability, noise-driven activation, and the nonthermal first-order superradiance transition'', Phys. Rev. A **97**, 023807 (2018).

[273] L. Garbe et al., ''Dissipation-induced bistability in the two-photon Dicke model'', Sci Rep **10**, 13408 (2020).

[274] J. Klinder et al., ''Dynamical phase transition in the open Dicke model'', Proc. Natl. Acad. Sci. **112**, 3290–3295 (2015).

[275] P. Strack and S. Sachdev, ''Dicke Quantum Spin Glass of Atoms and Photons'', Phys. Rev. Lett. **107**, 10.1103/PhysRevLett.107.277202 (2011).

[276] V. D. Vaidya et al., ''Tunable-Range, Photon-Mediated Atomic Interactions in Multimode Cavity QED'', Phys. Rev. X **8**, 011002 (2018).

[277] P. Lodahl et al., ''Chiral quantum optics'', Nature **541**, 473–480 (2017).

[278] H. Pichler, S. Choi, P. Zoller, and M. D. Lukin, ''Universal photonic quantum computation via time-delayed feedback'', Proc Natl Acad Sci U S A **114**, 11362–11367 (2017).

[279] T. Ozawa et al., ''Topological photonics'', Rev. Mod. Phys. **91**, 015006 (2019).

[280] A. Metelmann and A. A. Clerk, ''Nonreciprocal Photon Transmission and Amplification via Reservoir Engineering'', Phys. Rev. X **5**, 021025 (2015).

[281] S. Choi et al., ''Observation of discrete time-crystalline order in a disordered dipolar

many-body system'', Nature **543**, 221–225 (2017).

[282] F. Iemini et al., ''Boundary Time Crystals'', Phys. Rev. Lett. **121**, 035301 (2018).

[283] P. Kongkhambut et al., ''Observation of a continuous time crystal'', Science **377**, 670–673 (2022).

[284] J. Schwinger, *On Angular Momentum*, tech. rep. (Harvard Univ.; Nuclear Development Associates, Inc. (US), United States, 1952).

[285] D. P. Arovas and A. Auerbach, ''Functional integral theories of low-dimensional quantum Heisenberg models'', Phys. Rev. B **38**, 316–332 (1988).

[286] A. Auerbach, *Interacting Electrons and Quantum Magnetism*, edited by J. L. Birman et al., Graduate Texts in Contemporary Physics (Springer, New York, NY, 1994).

[287] E. G. D. Torre et al., ''Keldysh approach for nonequilibrium phase transitions in quantum optics: Beyond the Dicke model in optical cavities'', Phys. Rev. A **87**, 023831 (2013).

[288] B. Öztop, M. Bordyuh, Ö. E. Müstecaplıoğlu, and H. E. Türeci, ''Excitations of optically driven atomic condensate in a cavity: theory of photodetection measurements'', New J. Phys. **14**, 085011 (2012).

[289] M. F. Maghrebi and A. V. Gorshkov, ''Nonequilibrium many-body steady states via Keldysh formalism'', Phys. Rev. B **93**, 014307 (2016).

[290] M. Wouters and I. Carusotto, ''Absence of long-range coherence in the parametric emission of photonic wires'', Phys. Rev. B **74**, 245316 (2006).

[291] A. Mitra, S. Takei, Y. B. Kim, and A. J. Millis, ''Nonequilibrium quantum criticality in open electronic systems'', Phys. Rev. Lett. **97**, 236808 (2006).

[292] J. T. Young, A. V. Gorshkov, M. Foss-Feig, and M. F. Maghrebi, ''Nonequilibrium fixed points of coupled ising models'', Phys. Rev. X **10**, 011039 (2020).

[293] L. M. Sieberer, M. Buchhold, J. Marino, and S. Diehl, ''Universality in driven open quantum matter'', Rev. Mod. Phys. **97**, 025004 (2025).

[294] N. A. Kamar, M. Ali, and M. Maghrebi, *Markovian dissipation can stabilize a (localization) quantum phase transition*, May 2025.

[295] U. Weiss, *Quantum Dissipative Systems (Fourth Edition)* (World Scientific Publishing Company, Singapore, 2012).

[296] D. J. Thouless, ''Long-Range Order in One-Dimensional Ising Systems'', Phys. Rev. **187**,

732–733 (1969).

[297] P. W. Anderson and G. Yuval, ‘‘Some numerical results on the Kondo problem and the inverse square one-dimensional Ising model’’, J. Phys. C: Solid State Phys. **4**, 607 (1971).

[298] F. J. Dyson, ‘‘An Ising ferromagnet with discontinuous long-range order’’, Commun.Math. Phys. **21**, 269–283 (1971).

[299] P. W. Anderson, G. Yuval, and D. R. Hamann, ‘‘Exact Results in the Kondo Problem. II. Scaling Theory, Qualitatively Correct Solution, and Some New Results on One-Dimensional Classical Statistical Models’’, Phys. Rev. B **1**, 4464–4473 (1970).

[300] V. J. Emery and A. Luther, ‘‘Low- temperature properties of the Kondo Hamiltonian’’, Phys. Rev. B **9**, 215–226 (1974).

[301] M. Aizenman, J. T. Chayes, L. Chayes, and C. M. Newman, ‘‘Discontinuity of the magnetization in one-dimensional $1/|x\text{-}y|^2$ Ising and Potts models’’, J Stat Phys **50**, 1–40 (1988).

[302] G. De Filippis et al., ‘‘Quantum phase transitions in the spin-boson model: Monte Carlo method versus variational approach à la Feynman’’, Phys. Rev. B **101**, 180408 (2020).

[303] J. M. Kosterlitz, ‘‘Kosterlitz–Thouless physics: a review of key issues’’, Rep. Prog. Phys. **79**, 026001 (2016).

[304] A. W. Chin, Á. Rivas, S. F. Huelga, and M. B. Plenio, ‘‘Exact mapping between system-reservoir quantum models and semi-infinite discrete chains using orthogonal polynomials’’, J. Math. Phys. **51**, 092109 (2010).

[305] G. Adesso, A. Serafini, and F. Illuminati, ‘‘Extremal entanglement and mixedness in continuous variable systems’’, Phys. Rev. A **70**, 022318 (2004).

[306] M. Kitagawa and M. Ueda, ‘‘Squeezed spin states’’, Phys. Rev. A **47**, 5138–5143 (1993).

[307] D. J. Wineland et al., ‘‘Spin squeezing and reduced quantum noise in spectroscopy’’, Phys. Rev. A **46**, R6797–R6800 (1992).

[308] L. Pezzè et al., ‘‘Quantum metrology with nonclassical states of atomic ensembles’’, Rev. Mod. Phys. **90**, 035005 (2018).

[309] A. Sørensen, L.-M. Duan, J. I. Cirac, and P. Zoller, ‘‘Many-particle entanglement with Bose–Einstein condensates’’, Nature **409**, 63–66 (2001).

[310] J. Ma, X. Wang, C. P. Sun, and F. Nori, ‘‘Quantum spin squeezing’’, Physics Reports **509**, 89–165 (2011).

[311] A. Peres, ‘‘Separability Criterion for Density Matrices’’, Phys. Rev. Lett. **77**, 1413–1415 (1996).

[312] M. Horodecki, P. Horodecki, and R. Horodecki, ‘‘Separability of mixed states: necessary and sufficient conditions’’, Physics Letters A **223**, 1–8 (1996).

[313] R. Simon, ‘‘Peres-Horodecki Separability Criterion for Continuous Variable Systems’’, Phys. Rev. Lett. **84**, 2726–2729 (2000).

[314] G. Vidal and R. F. Werner, ‘‘Computable measure of entanglement’’, Phys. Rev. A **65**, 032314 (2002).

[315] K. G. Wilson, ‘‘The renormalization group: Critical phenomena and the Kondo problem’’, Rev. Mod. Phys. **47**, 773–840 (1975).